SAPIENZA
UNIVERSITÀ DI ROMA

INRS Institut national de la recherche scientifique

Advanced time-of-flight diagnostics for real-time characterization of ions accelerated by high energy lasers.

Prof. Daniele Del Re

Dottorato di Ricerca in Fisica degli Acceleratori – XXXIII Ciclo

Candidate

Martina Salvadori
ID number 1805427

Thesis Advisor

Prof. Mauro Migliorati
Prof. Patrizio Antici

External Advisor

Dr. Fabrizio Consoli

January 2021

Alla mia famiglia.

Abstract

Time-Of-Flight (TOF) methods are very effective to detect ions accelerated in laser-plasma interactions, but they show significant limitations when used in experiments with high energy and intensity lasers, where both high-energy ions and remarkable levels of ElectroMagnetic Pulses (EMPs) in the radiofrequency-microwave range are generated.

In this joined-doctoral thesis, performed at the La Sapienza University in Rome, at the institut national de la recherche scientifique (INRS) in Montréal and at ENEA Centro Ricerche Frascati, an advanced diagnostic technique for the characterization of protons accelerated by intense laser-matter interactions with high-energy and high-intensity lasers has been implemented.
The proposed method exploits and improves the advantages given by TOF technique coupled to Chemical Vapor Deposition diamond detectors and features high sensitivity, high energy resolution and high radiation hardness. Thanks to the optimization of the acquisition system and to the careful setup of the TOF line, high signal-to-noise ratios in environments heavily affected by remarkable EMP fields have been achieved.

In the first part of the work a brief overview of laser-matter interaction is given, with particular emphasis to processes leading to particle acceleration. Then, the main diagnostic techniques available for the characterization of secondary sources produced by laser-matter interaction are presented. Here the TOF technique is introduced and analyzed when coupled with different kinds of detectors, including diamonds. The choice of the latter is justified by their physical properties. Various types of diamond structures and electrode layouts have been tested and their performances characterized for application as detectors to be employed in TOF lines.

The second part of the work is dedicated to a detailed description of the proposed advanced technique and to examples of its effectiveness in reducing the EMP noise and in enhancing the dynamic range, when employed in real experimental scenarios. A novel procedure to retrieve a calibrated proton spectrum from the performed measurements is here also proposed and discussed. Eventually, the developed technique is applied for detecting laser-plasma accelerated particles produced in different application scenarios and in the most variable laser-matter interaction conditions and the concept of a new multi-layer detector is also described.

Résumé

Les méthodes de temps de vol (TOF) sont très efficaces pour détecter les ions accélérés dans les interactions laser-plasma, mais elles présentent des limites importantes lorsqu'elles sont utilisées dans des expériences avec des lasers à haute énergie et à haute intensité, où sont générés à la fois des ions à haute énergie et des niveaux remarquables d'impulsions électromagnétiques (EMP) dans la gamme radiofréquence-micro-ondes.

Dans cette thèse de doctorat en cotutelle, réalisée à l'Université La Sapienza de Rome, à l'institut national de la recherche scientifique (INRS) de Montréal et à l'ENEA Centro Ricerche Frascati, une technique de diagnostic avancée pour la caractérisation des protons accélérés par des interactions laser-matière intenses avec des lasers de haute énergie et de haute intensité a été mise en œuvre.
La méthode proposée exploite et améliore les avantages donnés par la technique TOF couplée à des détecteurs diamantés à dépôt chimique en phase vapeur et se caractérise par une grande sensibilité, une résolution énergétique élevée et une grande dureté de rayonnement. Grâce à l'optimisation du système d'acquisition et à la mise en place minutieuse de la ligne TOF, des rapports signal/bruit élevés ont été obtenus dans des environnements fortement affectés par des champs EMP remarquables.

Dans la première partie du travail, un bref aperçu de l'interaction laser-matière est donné, avec un accent particulier sur les processus conduisant à l'accélération des particules. Ensuite, les principales techniques de diagnostic disponibles pour la caractérisation des sources secondaires produites par l'interaction laser-matière sont présentées. Ici, la technique TOF est introduite et analysée lorsqu'elle est couplée à différents types de détecteurs, y compris les diamants. Le choix de ces derniers est justifié par leurs propriétés physiques. Différents types de structures de diamant et d'agencements d'électrodes ont été testés et leurs performances ont été caractérisées en vue d'une application en tant que détecteurs à utiliser dans les lignes TOF.

La deuxième partie du travail est consacrée à une description détaillée de la technique avancée proposée et à des exemples de son efficacité pour réduire le bruit EMP et améliorer la gamme dynamique, lorsqu'elle est utilisée dans des scénarios expérimentaux réels. Une nouvelle procédure permettant de récupérer un spectre de protons calibré à partir des mesures effectuées est également proposée et discutée ici. Enfin, la technique développée est appliquée pour détecter les particules accélérées par laser-plasma produites dans différents scénarios d'application et dans les conditions d'interaction laser-matière les plus variables, et le concept d'un nouveau détecteur multicouche est également décrit.

Introduction

Soon after the development of the first operational ruby laser[1], the requirements coming from the different fields of possible applications acted as main driving stimulus for the laser technology improvement[2]. In the last decades, among the several branches pushing toward the development and commissioning of laser systems with always increasing power and repetition rate, were the laser-driven particle acceleration[3] and the Inertial Confinement Fusion (ICF)[4,5]. Since the first theoretical prevision of the two mechanisms, high power laser facilities have flourished around the world covering a variety of laser-matter interaction regimes related to them.
Several laser systems were built with the aim of reaching ignition. To this purpose, they are mostly based on Nd: phosphate glass active media and work in the UV-range exploiting its third harmonic ($\lambda_{1\omega}$ =1054 nm, $\lambda_{3\omega}$ = 351 nm). Remarkable examples are the National Ignition Facility (NIF) in USA[6] and the Laser Mega-Joule (LMJ) in France[7]. In particular, NIF has 192 beams and is able to deliver 1.8 MJ at 500 TW[6]. The facility was designed to achieve the ignition of a deuterium-tritium nuclear fusion target exploiting the indirect drive scheme, but it has also enabled the studies of all the phenomena related to high energy density physics[8,9].
The field of laser-driven particle acceleration, on the other hand, experienced a noteworthy evolution after the introduction of the Chirped-Pulse-Amplification (CPA) mechanism. This technique, developed by Donna Strickland and Gérard Mourou in 1985, has then allowed to compress the temporal duration of the laser down to few tens of femtoseconds, reaching ultra-high power ranging from terawatt to petawatt[10].
The advancement in the laser technology paved the way to the birth of many facilities designed to provide high power lasers for a broad range of applications and fundamental research. Nowadays more than 50 Petawatt class laser are already operational or in construction phase[11,12]. Some of these are shown in the map of Figure I.1.

The growth in the availability of powerful lasers enabled a fast expansion and evolution of the researches on laser-matter interaction. This progression has been necessarily accompanied by the development of dedicated diagnostic systems able to precisely characterize the laser-plasma interactions. In the last decades, plenty of new techniques and devices have been developed and tested to investigate all the different aspects. Indeed, the multiple requirements they have to satisfy heavily depend on the features of the specific interaction regime to be investigated.
Because of the impact that a well characterized laser-accelerated ion beam can have on a variety of different applications[13], from nuclear fusion[14,15] to medical treatments[16,17] to mention a few examples, a large portion of the developed diagnos-

Figure I.1. Some of the laser facilities worldwide.

tic systems has been dedicated to the accurate measurement of the main features of the so-accelerated particles[18].

These usually present high currents and a large energy spread. A suitable detector for them should be able to provide fast acquisition time, real-time operation, high dynamic range, high sensitivity, high energy resolution and angular-resolved characterization. This last requirement is usually satisfied so far by employing stacks of passive detectors such as Imaging Plates (IP)[19], solid state nuclear track detectors[20] and radiochromic films (RCF)[21]. The latters, for instance, are sensitive to impinging particles and change color because of the incoming flux. They allow to reconstruct the beam divergence, but are characterized by intrinsic low energy resolution (of the order of 1 MeV), are not sensitive to low energy particles (<1 MeV) and do not distinguish between different ion species. Electrostatic-magnetostatic spectrometers of the Thomson type[22], on the other hand, allow to have ion-species discrimination according to their different charge to mass ratio, but do not have any angular resolution. Another method to retrieve information about the spectrum of accelerated particles is the Time Of Flight (TOF) technique[23,24], where a time-resolved particle detector (e.g. a semiconductor based detector or a scintillator) is placed at a known distance. The signal produced by the detector is recorded by using an oscilloscope. Since particles with different velocity take different times to travel to the detector, there is a direct correspondence between the time of detection and the particle energy.

It is well known that, with growing laser energies and intensities, a sensible growth in the electromagnetic pulses (EMP) generated during the laser-matter interaction was also experienced[25,26]. These electromagnetic fields may hinder the operation and safety of any electronic device in the proximity of the target. Hence, the capability

of the diagnostic system to be operated in environments highly affected by these electromagnetic fields has great importance.
Among the aforementioned diagnostic systems, those able to work un-affected in such harsh environments are generally employing passive detectors. But this poses strong limitations in exploiting the possibilities of the high-repetition rate facilities, which would require an on-line characterization of the interaction. Indeed, passive detectors are compatible with single-shot laser systems, but the current push from the laser-plasma community is, of course, the use and development of high-repetition rate laser systems with real-time on-line monitoring. These allow to increase the particle flux and the statistics, by accumulation of subsequent comparable shots, and open the way to many different interesting applications.
For this reason, in recent years a strong effort has been profusely spent to develop a reliable and accurate diagnostic system able to efficiently characterize the features of the laser accelerated particles and simultaneously cope with the strong EMP presence, which will be even higher for future high energy and intensity lasers[26]. A detector based on the analysis of the acoustic waves generated by the energy dissipated into a water volume by the accelerated ion bunch, called I-BEAT, has been lately proposed as an example of high repetition-rate and EMP robust diagnostics[27]. Despite its promising features, the I-BEAT has been applied only to a few laser-plasma acceleration experiments employing Ti:Sapphire lasers with maximum energy reaching 30 J. On the contrary, TOF technique shows promising characteristics for being a suitable candidate to this difficult task.

The aim of this PhD thesis was the study, the development and the application of on-line diagnostic systems for detecting laser-plasma accelerated ions produced in different scenarios and in the most varying laser-matter interaction conditions. A detailed description of the resulting TOF technique is here discussed and presented together with an accurate procedure to retrieve calibrated proton spectra characterized by high dynamic range, high sensitivity and high energy resolution. Despite the technique itself cannot provide information on the beam angular distribution, the compactness of the detection system allows to easily place several line-of-flights around the chamber, providing a simultaneous measurement of the proton beam from different angles that can be used to reconstruct the angular distribution of the accelerated particles. Moreover, this technique can be easily applied to get real-time information on accelerated ions and is suitable for high repetition-rate experiments.

Structure of the Thesis

The thesis is structured as follows.

- Chapter 1: In the first chapter a brief introduction to laser produced plasmas is provided. Particular emphasis is given to the mechanisms leading to the production of energetic ions and electrons, as well as to the variety of applications that would benefit from an accurate characterization of the accelerated particles.
- Chapter 2: A detailed analysis of the requirements that an ideal diagnostic system has to satisfy is here presented together with a comprehensive description of the existing techniques and of their limitations.
- Chapter 3: Among all the different possibilities for time-of-flight diagnostics the choice of diamond detectors is justified for this purpose. In this chapter a detailed characterization of the detectors employed in the experimental activity performed during this doctoral project is presented and discussed.
- Chapter 4: This is the core of the present work and it describes the optimized TOF technique implemented to work in environments highly affected by electromagnetic noise. The full procedure going from the data acquisition to their analysis is presented and discussed.
- Chapter 5: The developed detection method is applied to different laser-matter interaction regimes. The technique has indeed been applied during several experimental campaigns at which I had the possibility to join, or to work on the data, during the PhD course. For each investigated regime, it is highlighted each particular aspect or issue addressed by the advanced TOF technique presented throughout the previous chapters.

Contents

Chapter 1

Laser-matter interaction driving particle acceleration

In 1957 Veksler proposed a new principle for the acceleration of particles[28]. Instead of using an external source to generate the accelerating electric field, as in conventional accelerators, he introduced the idea of a "coherent acceleration" mechanism where the accelerating electric field is provided by the accelerated bunch itself. Each particle would thus be affected by an electric field proportional to the number of particles being accelerated, with the possibility to achieve very high electric field gradients[28]. In his work, Veksler suggested for the first time the possibility to use a plasma as a medium for particle acceleration and he foresaw some of the characterizing features of ion acceleration driven by laser-plasma interaction. Among these: the automatic synchronization between the particles in motion and the accelerating field, the localization of the latter only in the region where accelerated charges are, and the possibility to accelerate quasi-neutral bunches of particles.
The earliest experimental observations of ion emission produced by laser-matter interaction came a few years later[29], after the development of the first operational ruby laser in 1960[1]. Since then, the advent of high-power lasers has enabled the production of more energetic particles. In the 90's several research groups reported on the measurements of ions having energies of a few MeV obtained by irradiation of different kinds of targets[30–32]. Nevertheless, the properties of the accelerated ions (i.e. an almost isotropic emission and a low brilliance) were still far from being interesting for applications, if compared to those offered by a conventional accelerator. The turning point in laser-driven ion acceleration came in 2000 when laser systems with intensities ranging from 3×10^{18} W cm^{-2} to 3×10^{20} W cm^{-2} and a short temporal duration (of the order of hundreds of femtoseconds) where used to irradiate micrometric solid targets either of metallic or plastic material, producing intense bunches of tens of MeV protons[33–36]. In 2001 Wilks[37] presented a model to explain the results obtained during these experiments. In the paper he suggested that a cloud of energetic electrons is produced at the irradiated side of the target by the impinging laser radiation interacting with the pre-plasma (i.e. the plasma generated by the pedestal of the laser). These electrons expand at both sides of the target producing the space-charge field driving proton accelerations. He hypothesized that at the front side of the target, i.e. the irradiated one, the distribution of protons was

almost spherical since ions were contained in the expanding plasma plume. At the rear side of the target, on the other hand, protons presented a flat, sharp density gradient leading to higher energies and to a beam-like shape. The newly described process was here named by Wilks "Target Normal Sheath Acceleration" (TNSA).

This first chapter gives an outline of the vast topic of laser-matter interactions driving particle acceleration, describing the variety of mechanisms that can take place in the different interaction regimes. To this purpose, Section 1.1 is dedicated to a brief theoretical description of the main characteristics of a laser-produced plasma focusing on concepts that are useful to the comprehension of the different laser-driven acceleration mechanisms. This is followed by Section 1.2, where a summary of the main characteristics of the laser-driven ion sources is given. Then, in Section 1.3, the topic of the electromagnetic pulses produced during laser-matter interaction is introduced. They can produce great interference during the experiments and have to be properly considered also when evaluating laser-driven ion sources for different applications. The latter are briefly reviewed in Section 1.4.

1.1 High-power lasers interacting with matter

A high power laser impinging onto a solid target may induce its ionization. To obtain laser-induced ionization, the laser intensity has to overcome the so called atomic intensity[38,39] $I_a = 3.5 \times 10^{16}$ W cm^{-2}. This is defined as the intensity at which the electric field of the laser beam matches the one felt by the electron in the first Bohr orbit of the hydrogen atom, namely 5.1×10^9 V cm^{-1}. Laser pulses providing intensities of the order of I_a are sufficiently strong to induce the ionization of the irradiated material[38]. Nevertheless, ionization of solid targets can occur also for laser intensities that are orders of magnitudes lower than I_a. This is due to more complex phenomena such as tunnel ionization or multi-photon ionization which lower the ionization intensity threshold[39]. Thus, lasers having $I_L \sim 10^9$ W cm^{-2} are still able to ionize the irradiated target turning its surface into the plasma state. A plasma, indeed, can be described as a low density ionized gas in which the forces acting between near particles are much lower than the long range Coulomb force[40]. Namely a plasma consists of a quasi-neutral ionized gas of charged and neutral particles presenting a collective behavior[41]. The terms quasi-neutral refers to the fact that, thanks to charge compensation mechanism, the plasma presents a globally neutral behavior. However this feature takes place only on large volumes and time scales. Indeed, it is possible to define a distance within which the charge neutralization fails, this is called Debye screening length and can be expressed as[40]:

$$\lambda_D = \sqrt{\frac{\epsilon_0 k_B T_e}{n_e q_e^2}} = \frac{v_{th}}{\omega_p}. \tag{1.1}$$

where ϵ_0 is the vacuum permittivity, k_B is the Boltzmann constant, T_e is the electronic temperature, n_e is the electronic plasma density, q_e is the electronic charge and v_{th} is the electron thermal velocity. Typically the Debye screening length in laboratory plasmas can range from hundreds of Amstrong up to hundreds of μm.

The quantity ω_p, present in equation (1.1), is another important parameter characterizing the plasma and is related to the so-called plasma frequency f_p by the relation $f_p = \omega_p/2\pi$. It indicates the frequency at which the electrons oscillate as a response to any perturbation to the initial electron density distribution. These electrons oscillations are called Langmuir waves and their frequency is given by[40]:

$$\omega_p = \sqrt{\frac{n_e q_e^2}{m_e \epsilon_0}} \tag{1.2}$$

where m_e is the electron mass.
Since we are mainly interested in studying the laser-produced plasma, it is of interest to describe the conditions under which a monochromatic plane electromagnetic wave with frequency ω_L and wave-vector k_L is able to propagate into this medium. To this purpose it is useful to consider the dispersion relation of a electromagnetic wave traveling into a plasma under the condition that no external magnetic field is applied. This can be retrieved starting from the Ampere's law of a conductor:

$$\nabla \wedge \mathbf{H} = \mathbf{J}_{cond} + \frac{\partial}{\partial t}\mathbf{D} \tag{1.3}$$

where $\mathbf{H}$ is the magnetic field vector, $\mathbf{J}_{cond}$ is the current density vector and $\mathbf{D}$ is the dielectric displacement field vector. By applying the curl operator to both sides of the previous equation, it becomes:

$$\nabla^2\mathbf{H} = \sigma\mu\frac{\partial}{\partial t}\mathbf{H} + \frac{n^2}{c^2}\frac{\partial^2}{\partial t^2}\mathbf{H} \tag{1.4}$$

where $\sigma = \sigma_0/[1 - i(\omega_L/\nu_{ei})]$ is the conductivity with $\sigma_0 = n_e q_e^2/m_e\nu_{ei}$ and ν_{ei} is the electron-ion collision frequencies, μ is the magnetic permittivity and n the refractive index. Using the complex representatives formalism, equation 1.4 leads to the following dispersion relation[42]:

$$k_L^2 = -i\omega_L\sigma\mu + \omega_L^2\frac{n^2}{c^2} \tag{1.5}$$

In the approximation of a non collisional plasma, i.e. a plasma dominated by long-range electromagnetic force rather than collisions, equation (1.5) becomes[42]:

$$\omega_L^2 = \omega_p^2 + k_L^2 c^2 \tag{1.6}$$

From the dispersion relation it is possible to see that the wave-vector k_L^2 can be expressed as a function of the difference $(\omega_L^2 - \omega_p^2)$:

$$k_L^2 = \frac{\omega_L^2 - \omega_p^2}{c^2} \tag{1.7}$$

This equation states that only when the laser radiation has a frequency larger than ω_p the electromagnetic wave propagation can occur, otherwise the wave-vector becomes imaginary, the wave does not propagate, and the field amplitude decreases exponentially. Given equation (1.2), this condition can be expressed in terms of

the plasma density, defining the so-called critical density at which any further electromagnetic wave propagation is inhibited:

$$n_{cr} = \frac{m_e \epsilon_0 \omega_L^2}{q_e^2} \simeq \frac{1.1 \times 10^{21}}{(\lambda_L[\mu\text{m}])^2} \text{ cm}^{-3} \tag{1.8}$$

where λ_L is the wavelength of the impinging laser. Different laser systems will thus have different critical densities. For instance Nd:phosphate glass lasers, working at 1.054 μm fundamental wavelength present a critical density $n_{cr} \sim 10^{21}$ cm^{-3} whereas laser systems based on Ti:sapphire technology, having $\lambda = 0.8$ μm present a critical density $n_{cr} \sim 1.7 \times 10^{21}$ cm^{-3}.
In those regions where $n_e > n_{cr}$ the plasma is referred as *overdense* and the incident electromagnetic wave vanishes within a distance called skin depth, given by the relation[43]

$$\delta_s \simeq \frac{c}{\sqrt{\omega_p^2 - \omega_L^2}} \tag{1.9}$$

In those regions where $n_e < n_{cr}$ the plasma is said to be *underdense* and the laser is able to propagate.

A laser-produced plasma presents a peculiar density profile evolving over time which can be described by a steep front due to the shock induced by the radiation ablation front and a tail of decreasing density due to the plasma plume expansion[44]. Therefore, according to the laser pulse temporal duration, the type of interaction will be substantially different since the plasma with which the laser interacts will be changing in time. Indeed, considering the interaction of an ultrashort laser pulse with matter, it is reasonable to model the density distribution as a step function since the plasma does not have the time to undergo a significant expansion. On the other hand, laser pulses of sufficient duration (i.e. hundreds of ps or more) will produce the mentioned density gradient before the end of the laser pulse itself, making the interaction with the expanding plasma possible.

1.1.1 Long pulses and moderate intensity laser regime

A long laser pulse having sufficient intensity to ionize the material with which it is interacting transforms the target surface into plasma state and continues to interact with it during its hydrodynamic expansion. At the target surface, an ablation plasma sheath is created which expands in vacuum with the ion sound speed $c_s = \sqrt{k_b(ZT_e + T_i)/m_i}$ where T_i, Z and m_i are the ion temperature, the charge number and the mass of the ion[45]. Typical values of the expansion velocities range between 10^7 and 10^8 cm/s. The so-generated plasma plume shows an exponentially decreasing density profile so that the impinging electromagnetic wave interacts with a plasma with a long-density scale length, namely[45]:

$$L_n = \frac{n_e}{\nabla n_e} \gg \lambda_L \simeq c_s \tau_L \tag{1.10}$$

where τ_L is the laser temporal duration.
For laser intensities ranging from 10^9 W cm^{-2} up to 10^{14} W cm^{-2} and a pulse length

of hundreds of ps up to hundreds of ns, the main absorption mechanism taking place is the Inverse Bremsstrahlung Absortion (or collisional absorption). For intensities higher than 10^{14} W cm^{-2} the resonance absorption also starts to play a major role. In both cases the laser interacts directly with plasma electrons which then transfer the acquired energy to ions.

Inverse Bremstrahlung Absorption

In the Inverse Bremstrahlung Absorption mechanism the electromagnetic waves induce electron oscillations which are then damped by the electron-ion collisions providing the energy transfer from the laser to the plasma which heats up. The collisional absorption coefficient k_{ib} can be obtained from the linear momentum balance of the electronic fluid, written in the complex formalism:

$$-i\omega_L m_e \mathbf{u_e} = -q_e \boldsymbol{\mathcal{E}} - \nu_{ei} m_e \mathbf{u_e} \tag{1.11}$$

where $\mathbf{u_e}$ is the electrons velocity, $\boldsymbol{\mathcal{E}}$ the electric field and on the right side is included the electron-ion collisional term. From equation (1.11) the expression for the electron velocity can be obtained and used to write the plasma current density:

$$\mathbf{J} = q_e n_e \mathbf{u_e} = \frac{i\epsilon_0 \omega_p^2}{\omega + i\nu_{ei}} \boldsymbol{\mathcal{E}} \tag{1.12}$$

Exploiting the Ohm's law $\mathbf{J} = \sigma \boldsymbol{\mathcal{E}}$ and using the Maxwell equations it is possible to retrieve the dispersion relation for a collisional plasma:

$$\omega_L^2 = k_L^2 c^2 + \omega_p^2 \left(1 - \frac{i\nu_{ei}}{\omega_L}\right) \tag{1.13}$$

Comparing the latter with equation (1.6) the presence of the damping term ν_{ei}/ω_L is highlighted. Taking the real part of equation (1.13) the collisionless dispersion relation is retrieved whilst considering its imaginary part and explicating the electro-ion collision frequency, the coefficient for collisional absorption can be obtained[45]:

$$k_{ib} \propto \frac{Z n_e^2}{T_e^{3/2}(1 - n_e/n_{cr})^{1/2}} \tag{1.14}$$

From this relation it is easy to see that the collisional absorption decreases with temperature and increases with Z and density. Then, when laser light interacts with inhomogeneous plasmas, this kind of absorption takes place mostly near the critical surface n_{cr}.

For growing laser intensities, due to the strong dependence on the Coulomb cross section which decreases with electron velocity, the collisional absorption mechanism becomes progressively ineffective. Indeed the electrons, under the action of an electric field, acquire a quiver velocity proportional to the electric field amplitude $\mathcal{E}_0$ of the laser. Thus for growing laser intesities, also the electron velocity increases. In this frame, the Resonance Absorption mechanism starts to play a major role.

Resonance Absorption

The Resonance Absorption mechanism relies on the excitation of Langmuir waves near the critical surface and in the subsequent conversion into thermal plasma energy through their damping by collisions, Landau damping[40] or wave breaking[40].
A necessary condition to be able to excite these plasma modes is to have an obliquely impinging "p" polarized electromagnetic wave. In this way the associated electric field lies on the plane of incidence with a component in the direction of the density gradient as shown in Figure 1.1. The majority of the electromagnetic wave will be reflected back as it reaches the plasma density $n_e = n_{cr}cos^2(\theta)$, being θ the angle of incidence of the electromagnetic wave, with the exception of a small evanescent wave. The latter, thanks to the "p" polarization, has a component which oscillates along the direction of the plasma density gradient and can excite plasma Langmuir waves. Indeed the associated electric field acts on the electrons of the plasma inducing charge separation between the displaced electrons and the ions which, due to the higher mass are weakly affected by the electric field in comparison to the lighter electrons. The ions will thus drag back the electrons which will start to oscillate with the characteristic frequency ω_p. These oscillations can travel in the overdense plasma regions and through their damping transfer the laser energy to the plasma. Since Langmuir waves can be effectively excited in the proximity of the critical density where $\omega_L \sim \omega_p$, an optimal angle of incidence must be sought for which laser light is able to penetrate as near as possible to the critical surface without loosing the component of the electric field parallel to the density gradient.

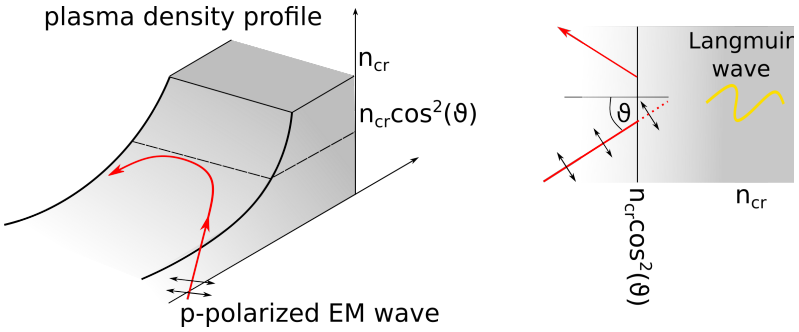

Figure 1.1. Langmuir waves excitation at the critical surface by an impingng "p" polarized electromagnetic wave. In the sketch a darker gray is used to indicate higher densities.

Ponderomotive Force

The aforementioned processes refer to the near critical and overcritical regions of the plasma which are readily formed at the first instants of the interaction. Nevertheless, within the long temporal duration of the laser pulse here considered, the plasma undergoes a significant expansion giving the possibility to the laser itself to interact with extended underdense regions.
Here the electromagnetic wave interacts with charged particles which experience an inhomogeneous electromagnetic field and are subjected to a nonlinear force, called the ponderomotive force. The latter can be represented as the gradient of

the ponderomotive potential time-averaged over a field period Φ_p and that can be expressed as[39,43]:

$$\Phi_p = \frac{q^2}{4m\omega_L^2}|\boldsymbol{\mathcal{E}}|^2 \tag{1.15}$$

where q and m are the particle charge and mass respectively. The ponderomotive force is thus generated by the gradient of the laser beam intensity profile and plays a major role for high intensity lasers[43]

$$\mathbf{F_p} = -\nabla\Phi_p = -\frac{q^2}{4m\omega_L^2}\nabla\boldsymbol{\mathcal{E}}^2 \propto -\frac{\nabla I_L}{m\omega_L^2} \tag{1.16}$$

where it has been exploited the relation of proportionality between the laser intensity and the square of the electric field amplitude $I_L \propto \boldsymbol{\mathcal{E}}^2$. Since the ponderomotive force depends on the inverse of particle mass, its action will be almost negligible on ions whereas it will strongly affect the electron motion. Given the typical intensity profile of a Gaussian beam, electrons will be pushed outwards, generating an electron depletion channel along the direction of laser propagation as shown in Figure 1.2.a. Since the refractive index depends on the plasma frequency which in turn depends on the electron density, the density gradient generated by the displacement of electrons produces a varying refractive index which will decrease towards the edges of the depletion channel where a greater density of electrons is found. This acts like a lens focusing the impinging radiation providing to maintain high focusing and intensity over a longer distance than the typical laser values given by the Raleygh length. When the described phenomenon involves the whole laser beam it is called self-focusing. If the laser focal spot is not homogeneous and presents some "hot-spots", namely several small portion of the beam presenting a higher intensity than the surrounding, the beam undergoes the filamentation process, where multiple highly focused and intense filaments will be produced as shown in Figure 1.2.b.

Parametric Instabilities

In long density scale length plasmas, some peculiar physical phenomena are commonly observed. These processes are grouped together under the name of parametric instabilities. These phenomena lead to the formation of ionic and electronic plasma waves with consequent plasma heating due to their damping. One of them that can bring a relevant contribution to the energy transfer is the Two Plasmon Decay[46]. The latter happens in proximity of the plasma surface where $n_e = n_{cr}/4$. Here an incident electromagnetic wave of frequency ω can decay into two plasma waves, identified as the blue and red plasmon. Indeed the two oscillate with blue and red-shifted frequencies with respect to $\omega/2$. The recombination of one of the plasmon with the incoming electromagnetic wave gives rise to the characteristic three-half harmonic emission which, if detected, constitutes a clear signature of the occurrence of the TPD instability.
Two other parametric instabilities can be excited during the interaction of the electromagnetic wave with the underdense plasma: the Stimulated Raman and Brillouin Scattering[5,42]. The first can be only developed in those regions where the electronic

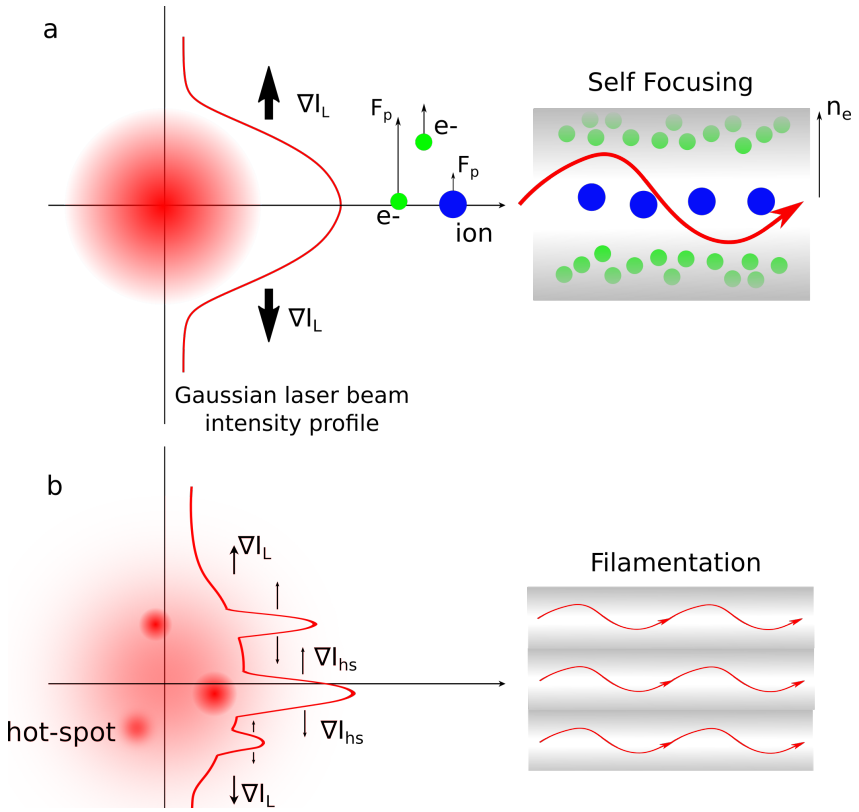

Figure 1.2. (a) The intensity profile of a Gaussian beam impinging on a plasma. The particles are affected by the so called Ponderomotive force, whose amplitude is directly proportional to the laser intensity gradient and inversely to the particle mass. The resulting displacement of electrons induces a variation in the refractive index which leads to the phenomenon of self focusing. (b) If the laser beam profile is not Gaussian but still presents some regions at higher intensit, a similar process leads to the phenomenon of filamentation.

density is lower than $n_{cr}/4$ and it consists in a back-scattering of the impinging electromagnetic wave by an electronic density fluctuation. The backscattered wave can interfere with the incident light producing a variation in the wave pressure which can reinforce the electron density perturbation triggering a positive feed-back loop. The Brillouin scattering phenomenon is similar to the Raman scattering phenomenon with the exception that it involves ionic plasma waves rather than electronic oscillations.

Generation of suprathermal ions

In this long-pulse regime, multiple phenomena can take place leading to the production of ion populations having different energies. For low intensities, in the range of $\sim 10^{11}$ W cm^{-2}, the inverse bremstrahlung absorption leads to the plasma heating and to the formation of thermal ions that expands in vacuum. For growing laser intensities ($> 10^{14}$ W cm^{-2}), the Resonance Absorption mechanism starts to play

a major role, followed by the possible excitation of parametric instabilities in the case that the required specific conditions are met. These produce energetic electrons that, being lighter than ions, expand in vacuum with a greater velocity. For a very simple description of the mechanism leading to the formation of suprathermal ions in this regime, it is possible to think that the displacement of electrons will generate an electric field due to charge separation, providing the force acting on ions $F = \mathcal{E} Z_i q_e / A_i m_p$ where Z_i is the ion atomic number and A_i the atomic mass. In the hypothesis of a uniform acceleration motion, assuming that the process takes place in a length L_{acc} the ions are going to acquire a velocity

$$v_i = \left(\frac{2\mathcal{E} q_e L_{acc}}{m_p} \frac{Z_i}{A_i} \right)^{1/2} \tag{1.17}$$

so that the fastest ions will be protons, having the highest charge-over-mass ratio.

1.1.2 Short pulses and high intensity laser regime

In 90's, the advent of ultra high-peak power, short pulse lasers[10] (sub ps, tens of fs) allowed to reach intensities on target exceeding 10^{17} W cm^{-2}. In the ideal case, the short temporal duration of the pulse would make the interaction with a steep electron density gradient, given by the over-dense solid target interface with vacuum, possible. However, in a real laser system, the short pulse is characterized by the presence of preceding lower power laser pulses. Usually, several contributions should be taken into account. If in the system a regenerative amplifier is employed, a leakage pulse has to be expected ~ 10 ns before the main pulse, with a contrast ratio, i.e. the ratio of its intensity over the one of the main pulse, of 10^{-5} and a duration similar to the one of the main pulse. One more contribution is due to the Amplified Spontaneous Emission (ASE) which has a contrast of $10^{-6} - 10^{-10}$ and a duration of few ns. Then, there is also the pedestal which can have ps or even ns temporal duration, providing 10^{-4} or 10^{-7} times the intensity of the main pulse. Eventually it is also possible to have some prepulses a few tens or hundreds of ps before the main pulse presenting a duration similar to the main pulse and variable contrast ratio. For the mentioned high intensity laser-systems, this preceding light is able to produce a plasma, so that the following main peak will interact with an expanding plasma with a smoother density profile.
At this stage the interaction is similar to that described in the previous section, but when the main intense peak hits the plasma it can lead to new phenomena involving relativistic effects. To distinguish the two different regimes of interaction, i.e. relativistic or non relativistic, it is useful to introduce the dimensionless parameter a_0 defined as the ratio among the electron quiver velocity on the speed of light. Thus if $a_0 \sim 1$ the relativistic effects cannot be neglected. For practical use a_0 can be more conveniently expressed in terms of the laser irradiance as:

$$a_0^2 = n \frac{I_L \lambda_L^2}{1.37 \times 10^{18}} \tag{1.18}$$

where n changes according to the laser polarization: it is equal to 1 for linear and 2 for circular polarization. The laser intensity I_L is expressed in W cm^{-2} and the

laser wavelength λ_L is expressed in μm. For example, a Ti:sapphire laser system, having a wavelength of ~ 0.8 μm, will induce relativistic effects for an intensity $I_L \sim 2 \times 10^{18}$ W cm^{-2}.
In this regime several interesting effects can occur. One of them is the relativistic self focusing. Due to the relativistic electron motion, the phenomenon of self focusing is reinforced by the dependence of the relativistic electron mass on the velocity. Along the beam propagation direction, electrons will have maximum velocity which decreases moving outwards. Correspondingly, the first will have a higher relativistic electron mass than the latter. Thus ω_p will be minimum at the center and maximum outside, leading to a varying refractive index which decreases towards the edges of the plasma channel[43].
Similarly, the mentioned variation of ω_p affects also the critical density value which is increased by a factor equal to the relativistic parameter γ, inducing the so-called self induced transparency or relativistic transparency[43].
Moreover the laser beam can be properly treated in order to increase the contrast ratio, i.e. lowering the intensity on target brought by the preceding light. In this way the ultra short, high intensity main laser pulse will be able to interact with a sharper density gradient leading to new absorption phenomenon. Nevertheless, the laser energy transfer still relies on the electron heating.

Electron heating processes

Assuming that the ionization and the heating of the target occur rapidly enough to neglect the hydrodynamic expansion, it is possible to consider the interaction with a plasma presenting a steep electron density profile. As already discussed, due to the strong dependence of the Coulomb cross section from the electron velocity, as the latter grows the collisional absorption becomes ineffective. Hence, in this regime, laser energy-transfer can efficiently occur only via collisionless mechanisms.
One of the processes leading to the electron heating is the sheath inverse bremsstrahlung. Electrons oscillating in the laser field tend to escape into the vacuum but, due to the so-generated thin charge separation layer, they are electrostatically confined by the back-holding electric field produced by the sheath. The process can be described as the electrons were instantaneously reflected by the sheath field. The reflection has an effect similar to a collision, leading to a non vanishing energy gain[47].
It is possible to estimate the amplitude of the back-holding electric field $\mathcal{E}_{sheath}$ considering that it has to be strong enough to restrain electrons of energy $k_b T_e$, hence $q_e \mathcal{E}_{sheath} \lambda_D = k_b T_e$ which leads to $\mathcal{E}_{sheath} = k_b T_e / q_e \lambda_D$[43].
Similarly to collisional absorption, also the Resonance Absorption model, discussed for moderate intensity laser interaction with matter, is no more suitable to describe the interaction in the high intensity regime. Indeed, it holds for long-density-scale-length plasmas where it is possible to consider the density nearly uniform over the oscillation amplitude and a local plasma frequency can be defined, requirement that is no longer satisfied in this regime.
Nevertheless, having an intense laser pulse with oblique incidence and p-polarization impinging on a solid surface is the base for the vacuum heating absorption model introduced by Brunel in 1987[48]. In this model the "p" component of the impinging electric field pulls the electrons out in vacuum for about half a cycle. The elec-

trons acquire a kinetic energy that can be expressed as a function of the quiver electron velocity, thus depending on the electric field amplitude. Then, re-entering into the plasma due to the oscillating electric field, they deliver the acquired energy. For driving this process, the external electric field has to be intense enough to suppress the back-holding electric field generated by the sheath field due to charge separation induced at the target surface. This implies having the component of the electric field perpendicular to the target surface satisfying the condition $\mathcal{E}_\perp = 2\mathcal{E}_0 sin(\theta) > k_b T_e/(q_e \lambda_D)$ leading to $\mathcal{E}_0^2 sin^2(\theta) > (n_e k_b T_e)/\epsilon_0$. From this relation it is possible to infer that the radiation pressure is generally greater than the thermal plasma pressure, meaning that the ponderomotive force is able to effectively counteract the thermal expansion maintaining the condition of a step boundary density profile[43].
Similarly to Resonance Absorption, vacuum heating cannot occur for normal incidence or s polarized lasers since there is no component of the electric field perpendicular to the density gradient. In this condition the magnetic field can play a major role inducing electron oscillations and leading to the $\mathbf{J} \times \mathbf{B}$ heating[39,49]. The electron dynamics is similar to the one described in the vacuum heating with the exception that the driving magnetic force oscillates at $2\omega_L$ instead of ω_L, thus leading to generation of hot electrons twice per laser cycle.

Ion Acceleration Models

The hot-electron generation is of fundamental importance for ion acceleration since the laser pulse energy is transferred to ions in an indirect way, being mediated by electrons.
In the described absorption mechanisms, energetic electrons are generated at the front side of the target when the laser pulse hits its surface. In the simple model that we are going to discuss here, we assume that, once a quasi-equilibrium state has been reached, the electrons are characterized by a spectrum which presents a low-energy background population with a high energy Maxwellian tail. The mean kinetic energy of the latter is usually referred to as hot electron temperature $k_B T_{hot}$. These electrons are pushed inside the target, generating a strong current density that can reach values up to[43] 10^8 A m^{-2} as schematically depicted in Figure 1.3.a. This high current has to be locally neutralized by a return current, otherwise the electric field resulting from the charge unbalance would be strong enough to hinder the hot electrons propagation[3] (Figure 1.3.b). This return current is provided in metal by cold electrons which are present in the conduction band or, in the case of insulator, produced by coillisional ionization[50]. Eventually, a portion of the hot electrons is able to escape from the rear side of the target. Electrons that do not have sufficient energy are retained at the back surface by the positively charged ions that are left in the target. Due to the charge separation produced by the negatively charged electron cloud and the positively charged ions, a strong electric sheath field is created at the rear target surface (Figure 1.3.c).
At this stage, protons and heavier ions, contained in contaminants located on the target rear surface (for instance hydrocarbons released by vacuum pumping process) start to be accelerated by the sheath electric field and expand into the vacuum at the rear side of the target (Figure 1.3.d). This is the base of sheath acceleration

models that include the Target Normal Sheath Acceleration (TNSA) mechanism.

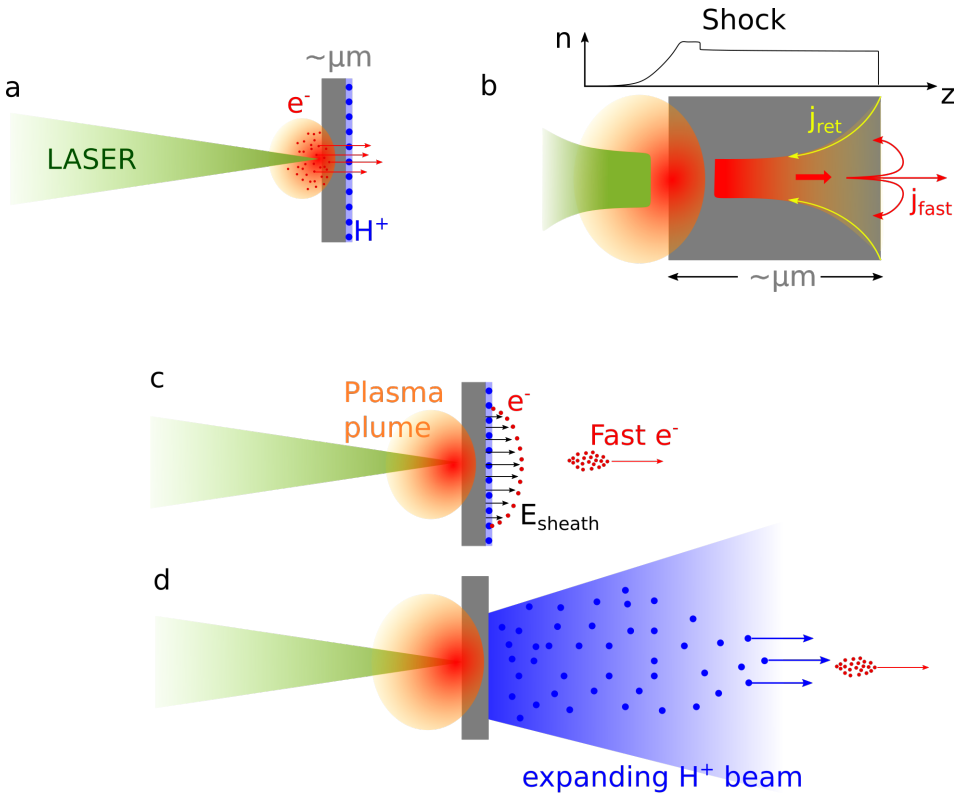

Figure 1.3. The evolution of the TNSA mechanism: (a) A high power laser impinging on a solid surface generates a plasma and accelerates electrons which are pushed inside the target, (b) the light pressure leads to a density profile steepening (shown at the top) and to an in-ward travelling shockwave that heats and ionizes the target. The electrons propagating towards the rear side of the target constitute a current j_{fast}. Due to binary collisions, the propagation inside the material leads to a spatial broadening of the electron distribution.(c) Electrons with sufficient energy are able to escape from the rear side of the target, the induced charge separation generates a sheath field which backholds slower electrons providing also the accelerating field for ions (d) Protons, having the highest charge to mass ratio are those most effectively accelerated.

Following an argument similar to the one adopted for vacuum heating discussion, it is possible to relate the sheath field $\mathcal{E}_{sheath}$ to the hot electron temperature. Indeed it has to be strong enough to retain the escaping electron having energy $k_B T_{hot}$ thus:

$$\mathcal{E}_{sheath} \simeq \frac{k_B T_{hot}}{q_e l_s} \simeq \frac{k_B T_{hot}}{q_e \lambda_D} \tag{1.19}$$

where l_s is the extension of the sheath typically of the order of the Debye length λ_D. This first simple estimation allows to understand the strong relation between the electron heating process and the final accelerated ion energies E_i that can be expressed as: $E_i = Z q_e U_{sheath} = Z q_e \mathcal{E}_{sheath} \lambda_D \propto 2 Z k_B T_{hot}$ being Z the atomic number of the ion and U_{sheath} the electric potential associated to the sheath electric field. For typical values of laser-plasma acceleration experiment employing ultrashort and ultra intense laser, this sheath field can reach values up to 6×10^8 V m^{-1} and

will be mostly directed along the normal to the target rear surface. Ions will be thus accelerated perpendicularly to the surface presenting high collimation.
Being based on the generation of an electrostatic potential, the acceleration process will be more effective on protons, since they present the highest Z/A ratio, being A the atomic mass number. The heavier ions population provides the positive charge generating the accelerating field via charge separation. Nevertheless if the proton number is not sufficient to balance the charge of escaping electrons, at later times, also heavier ions can be accelerated.
The described process leads to a proton beam with peculiar characteristics. The energy spectrum is typically broadband up to a maximum energy and the particle number per MeV can be approximated with a quasi-exponential distribution presenting a sharp cutoff in its correspondence. The spatial and angular distribution is strongly dependent on the electron sheath spatial distribution, hence on the target properties such as resistivity and surface roughness which can affect the electron propagation.
it is worth to mention that the electron heating happening at the front surface of the target, in addition to drive the TNSA mechanism, contributes also to generate an electrostatic field at the target irradiated side, resulting in an accelerated ion beam in the backward direction[34].
Since TNSA process is routinely achievable in modern laser experiments, it has been extensively studied in the last decades. Nevertheless it is not the only process that can lead to ion acceleration. Indeed several other processes have been investigated. For instance, if the target thickness is smaller than the laser wavelength, the laser pulse can be intense enough to blow out all the electrons of the target. This will generate a strong repulsive Coulomb force among the positively charged ions left in the target leading to its Coulomb explosion. In this scheme the ion acceleration is driven by their own space-charge field. Usually it is achieved by irradiation of small clusters formed in low-temperatures gas-jets[51].
At extremely high level of laser intensities ($I_L > 10^{20}$ W cm^{-2}), the Radiation Pressure Acceleration mechanism (RPA) can be observed[52]. Here the laser pulse interacting with a steep boundary overdense plasma pushes and piles up electrons into the skin layer, i.e the laser penetration depth, thanks to the action of the ponderomotive force. This generates a static field that acts on the ions which are thus accelerated at the front side. If the target is thick enough the electromagnetic wave can further enter the target and push the high density ion layer (Hole Boring Regime)[53]. On the other hand, if the irradiated target is sufficiently thin all the ions can be accelerated before the end of the laser pulse. In such a case, the laser is able to accelerate ions to higher energies since there is no more a background screening plasma (Light Sail Regime)[3].
A further process that has been investigated is the Collisionless Shock Acceleration mechanism[54] which exploits the reflection of ions at the front of the collisionless electrostatic shock wave generated into the plasma by the impinging radiation.

1.2 Laser driven ion-source characteristics

The aforementioned various mechanisms lead to the production of ion sources with peculiar characteristics. The main investigated features have been determined by the requirements of different possible applications. The most studied aspects concern the maximum achievable energy and the accelerated particle spectra. Noteworthy importance is also given to the ion source size, to its opening angle and to the quality of the accelerated ion bunch. The latter, in accelerator physics, is commonly described by its emittance.
In the following Section, an up-to-date summary of the many interesting features of laser-driven ion sources that have been identified in several experiments during the last decades is presented.

1.2.1 Energy spectrum

Among the various characterizing parameters of the laser-driven accelerated ion bunches, the most investigated has always been the achievable maximum energy. Over the years several experiments were conducted in order to optimize the target composition and geometry (thickness, shape, surface texture and so on) trying to push the proton energy spectrum towards higher limits. Figure 1.4 shows different calibrated spectra obtained from the interaction of laser systems delivering tens of Joules onto a solid target, for a pulse duration of hundreds of fs[55]. The reported spectra set the world record in maximum proton energy at the time of their publication.

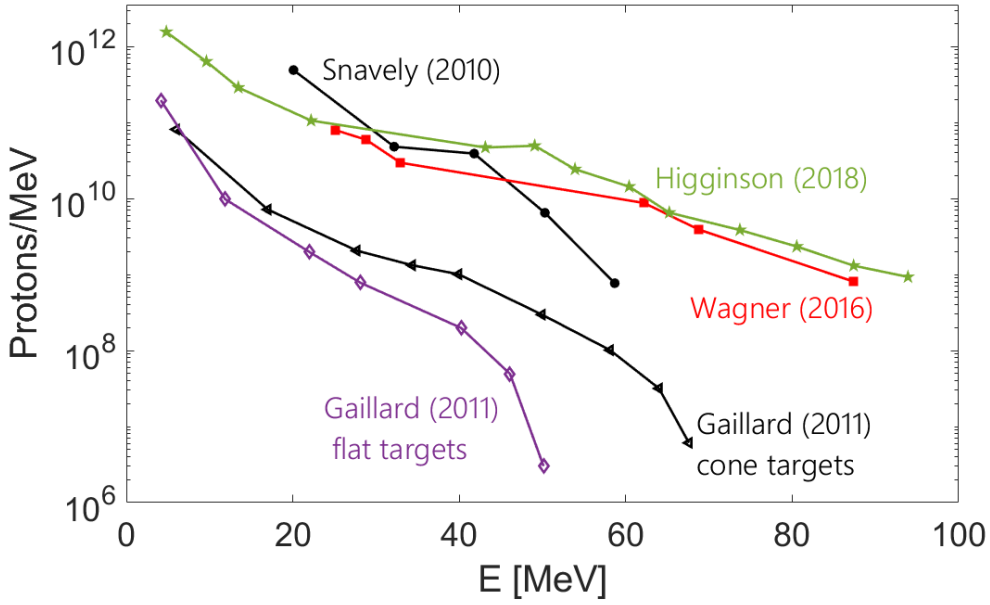

Figure 1.4. Proton energy spectra from three experiments reporting new world records in the cut-off energy at the time of publication. Adapted from *Bolton et al.*[55].

Next to the target engineering, also various irradiation schemes (different polarization, multi-pulse ecc.) were tested and laser system themselves optimized. The

investigation of different laser-matter interaction regimes led to results obtained exploiting different acceleration mechanisms among those previously cited or even to hybrid acceleration schemes. To the author knowledge, the current record in maximum achievable energy has been set in 2018 exploiting an hybrid radiation pressure - sheath acceleration scheme irradiating ultra-thin foils with hundreds of Joules linearly polarized laser pulse. Here, proton energy spectrum with 94 MeV cutoff was measured and a laser to proton conversion efficiency of $\sim 12\%$ achieved[56].

Even though the maximum energy is a crucial parameter for an effective employment in some fields like hadron therapy, some other applications require to have a limited proton energy spread. Hence, since the laser-matter interaction typically generates wide energy spectrum, a branch of laser-driven accelerator community focuses to achieve proton sources with a small energy spread of the order of few per cent. A first demonstration of the feasibility of a quasi-monoenergetic proton beam has been experimentally achieved in 2006 irradiating microstructred target with a 10 TW laser pulse (0.8 J, 80 fs). The target consisted in a 5 μm titanium foil with $0.2 - 0.5$ μm thick polymethylmethacrylate (PPMA) microdots. The proton contamination, unavoidable in vacuum condition, was removed by several shots of nanosecond ablation laser just before the main pulse irradiation. The obtained proton spectrum had a maximum energy of 1.2 MeV with a relative bandwidth of $\sim 40\%$[57].
Nevertheless, the most promising type of interaction in order to achieve monoenergetic proton bunches is actually represented by the interaction of picosecond laser pulses with ultra-thin targets exploiting the relativistic transparency regime, or, if interacting with gas targets, the collisionless shock acceleration mechanism. The latter, in 2012, led to 20 MeV protons with 1% energy spread detection when multi-TW Neptune CO_2 laser interacted wih a gas jet[54].

1.2.2 Beam source size and opening angle

As already mentioned in Section 1.1.2, the acceleration processes based on the irradiation of thin foils and the subsequent generation of a sheath field, generally produce the emission of proton bunches from both the irradiated surface and the rear side of the target[34].
The proton bunch source size at the rear target side is usually larger than the laser irradiation area at the front. An explanation of this phenomenon can be found assuming a ballistic propagation of the electrons generated at the front surface, one of the condition under which the TNSA isothermal model is developed. The divergence of the electon beam leads to the generation of a sheath field larger than the focal spot size. Nevertheless this approach is strongly simplified and the assumption of a ballistic electron propagation has been demonstrated to be faulty for millimeters thick targets[13]. The accelerated proton beam is diverging and the highest energy portion of the bunch appears to be emitted from a ~ 10 μm spot located behind the actual source, usually identified as the virtual source point. This higher energy component is located near the target normal axis: as the radial distance from this increases, the particle energy gradually decreases[13]. For lower energies the source size progressively increases reaching up to ~ 200 μm diameter. In Fig. 1.5.a this

trend is highlighted for experiments performed with three different laser systems: TRIDENT ($E_L = 18.7$ J, $\tau_L = 600$ fs, $I_L = 9.1 \times 10^{18}$ W cm^{-2} and an ASE contrast ratio better than 10^{-6} at 1.2 ns before the main pulse), LULI-100 TW ($E_L = 18$ J, $\tau_L = 350$ fs, $I_L = 3 \times 10^{19}$ W cm^{-2} and a contrast ratio of 10^{-6} at 500 ps before the main pulse) and Z-Petawatt ($E_L = 40$ J, $\tau_L < 1$ ps, $I_L > 9.2 \times 10^{19}$ W cm^{-2} and 10^{-7} pre-pulse contrast). The energy dependence of the source size is well described by a Gaussian distribution[58]

$$E = \exp\left\{\frac{-[4\ln(2)x]^2}{\sigma^2}\right\} \tag{1.20}$$

being x the source size and 2σ the FWHM.

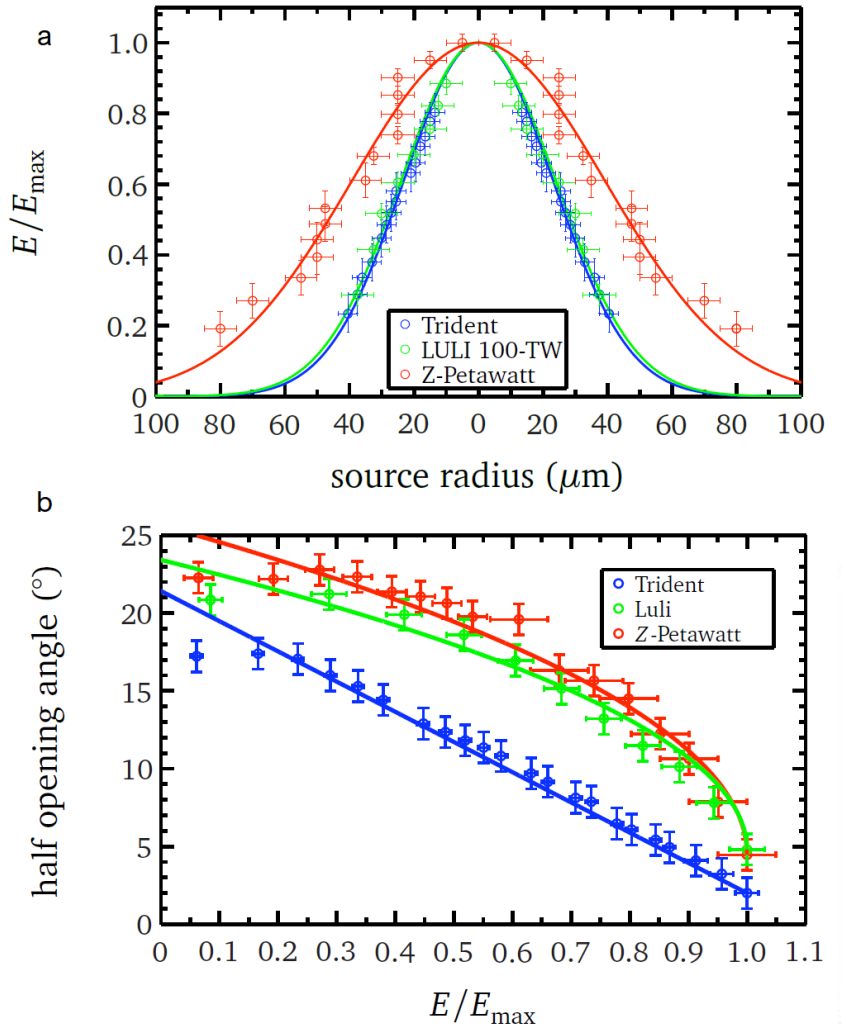

Figure 1.5. (a) Energy resolved source size and (b) Energy dependence on the half-opening angle obtained in three different laser facilities: Trident (blue), LULI 100 TW (green) and Z-Petawatt (red) having an intensity of 9.1×10^{18} W cm^{-2}, 3×10^{19} W cm^{-2} and $> 9.2 \times 10^{19}$ W cm^{-2} respectively. From *Roth et al.*[58]

.

Source size information is complementary to that on the opening angle of the beam. Protons with the highest energy are emitted with the smallest opening angle ($\sim 5^\circ$ half angle) which rapidly increases for protons at lower energies. The trend of the opening angle as a function of the normalized proton energy for the three aforementioned laser facilities is shown in Fig. 1.5.b. The opening angle increases for decreasing energy, reaching a maximum and staying constant for $E_p \sim 0.3E_{max}$. The slope of the curve is determined by the initial hot electron sheath shape at the target surface. A parabolic hot-electron sheath results in a linear dependence whereas a sheath with a Gaussian shape will lead to a strongly curved opening angle[59].

1.2.3 Emittance

The emittance of accelerated ion beams is a figure of merit commonly used in accelerator physics to determine the beam geometric features. It often represents a constraint for beam quality for several applications which usually require a low beam emittance[60].
To describe the evolution of the particle beam is usually convenient to introduce its representation in the phase space where each particle is identified by a point in a six dimensional space with coordinates (w, p_w) being w the spatial coordinate and p_w the associated canonical momentum with $w = \{x, y, z\}$. At a given time, the particle bunch can thus be represented by N points, being N the number of accelerated particles. The beam dynamics is then described with respect to a reference particle which moves on an ideal trajectory. In each point of this trajectory, identified by the coordinate s, it is possible to define a Cartesian frame which moves with the reference particle. In this Cartesian frame the reference particle will be always located at the origin and its momentum will be parallel to the z axis, As schematically shown in Figure 1.6.a. The displacement of each particle from this optimal path is well described by its divergence given by the ratio $w' = p_w/p_z$.
The beam dynamics is thus conveniently represented in the so-called trace space (w, w'). Under the hypothesis of uncorrelated motion in the three orthogonal planes, it is possible to work in the projected trace spaces (x, x'), (y, y'), (z, z'). Taking as reference the transverse trace space (x, x') and solving the equation of motion of the particles in the bunch (described by the Hill's equation) it is possible to derive the parameter[60]:

$$\epsilon = \gamma(s)x^2(s) + 2\alpha(s)x(s)x'(s) + \beta(s)x'^2(s) \tag{1.21}$$

Equation 1.21 represents an ellipse in the transverse plane which encloses all the N points associated to the particles of the bunch and it is defined as the geometrical emittance of the beam. As shown in Figure 1.6.b, the Courant-Snyder parameters α, β and γ describe the shape of the ellipse defining its geometrical features. In particular, it is possible to define the beam transverse dimension and its divergence as $\sigma_x = \sqrt{\beta\epsilon}$ and $\sigma_{x'} = \sqrt{\gamma\epsilon}$ respectively. The latter is usually employed as a beam quality parameter; the lower the divergence, the better the particle beam.

The just defined geometrical emittance ϵ is conserved under the hypothesis that only linear forces are acting on the system and if the longitudinal momentum is constant, i.e. if the particles of the beam are not accelerated. For this reason it

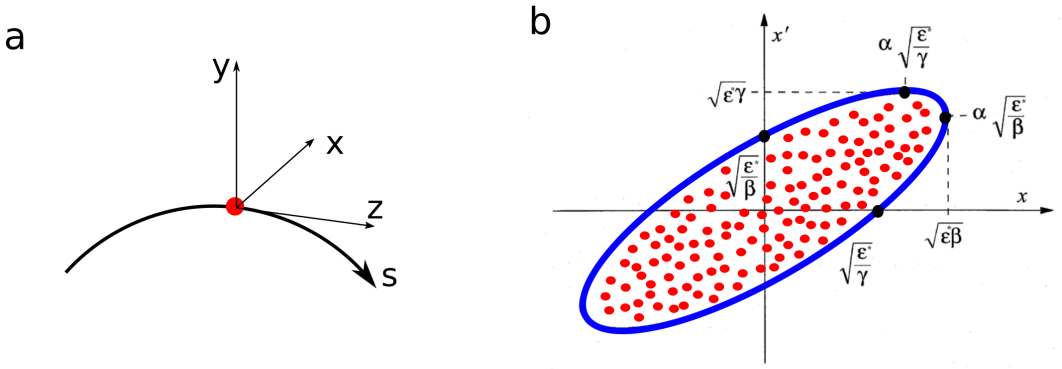

Figure 1.6. (a) Coordinate system used to describe the beam dynamics. An ideal trajectory is defined with respect to which the particles motion is described. (b) The area covered by the particles in the transverse phase plane is given by the geometrical transverse emittance, the Courant-Snyder parameters highlight its geometrical features.

has been introduced the more practical root mean square emittance given by the relation[60]:

$$\epsilon_{rms} = \gamma x + \alpha x x' + \beta x'^2 \tag{1.22}$$

with the associated transverse dimension $\sigma_x = \sqrt{\beta\epsilon_{rms}}$ and divergence $\sigma_{x'} = \sqrt{\gamma\epsilon_{rms}}$. Eventually to take into account also the particle energy and the beam energy spread the normalized emittance is introduced, which in the paraxial approximation hypothesis[60], can be related both to the geometrical and the root mean square emittance by the relation $\epsilon_n = \beta\gamma\epsilon_{g,rms}$.
A typical value for the emittance in conventional (radio-frequency based) accelerators is ~ 0.5 mm mrad. Several factors contribute to the overall emittance of a beam: its thermal spread, the driving accelerating field and the space charge forces. In laser-driven sources, the latter are strongly mitigated thanks to the co-moving electrons providing a neutralization of the charges. Moreover the sheath field evolves self-consistently with the ions producing an ideal accelerating structure. Hence the only component that actively contributes to the emittance is the thermal one. These are some of the reasons that make it possible for laser driven sources to have an emittance order of magnitudes lower than those achievable with accelerators[21]. Nevertheless, the high energy spread typical of the laser-driven sources, leads to an effective emittance growth even over short distances from the laser-plasma interaction point. This effect is mitigated when aiming for acceleration of monochromatic beams, but in all the other cases, despite the better performance of the laser-driven sources in terms of emittance at source, the issue of the beam transport remains an open challenge.

1.2.4 Beam Power and Intensity

The combination of short duration and high flux of the proton-bunch leads to remarkably high values of proton beam current, power and intensity. These three factors are of utmost importance for many applications. Their characterization and the knowledge of their behavior with distance from target is often a key issue to evaluate the feasibility of employing laser-driven ion sources. Assuming to have

a laser pulse energy of 1 J with 1% laser-to-proton conversion efficiency, a total number of protons $\sim 10^{11}$/shot and a source size of 100 μm for a duration of 1 ps, the peak current is of 10 kA for a current density of 100 MA cm^{-2}. Thus, at the source, the proton beam power and intensity reach the values of 10 GW and $\sim 10^{14}$ W cm^{-2} respectively. However, the beam is divergent and, as the distance from the source increases, the mentioned values rapidly decrease[13].

1.2.5 Acceleration of multiple ion species

Together with protons, also heavier ions such as carbon, nitrogen, oxygen are accelerated. They are commonly present as pollutant on the target surface, but since protons have the highest charge to mass ratio, in usual conditions they take most of the energy from the accelerating field. Then the cloud of accelerated protons partially screens the electric field generated by the electrons hindering the acceleration of heavier ions which indeed acquire much lower energies. Nevertheless, if the contamination layer containing protons and light ions is removed, heavy ions can be efficiently produced from the same laser source. Target resistive heating up to hundreds of celsius has proven to be an effective method to get rid of hydrogen contaminants and led to an improvement in carbon ion acceleration. Heavier ions have been efficiently accelerated heating a thermally stable tungsten target coated with the material of interest up to 1200 Celsius. The irradiation of these targets showed an enhancement of a factor of five in maximum achieved energy and a factor of ten in the conversion efficiency with respect to non-heated targets[61,62]

1.3 Laser produced electromagnetic pulses

During laser-target interaction, Electromagnetic Pulses (EMP) in the radiofrequency-microwave range are regularly detected. They are produced on a wide set of experimental condition, for laser pulses duration ranging from femtosecond to nanosecond[26]. The EMP intensity can be so high to represent a serious threat to any electronic device. They attract the interest of many research groups for finding methodologies to reduce them or to build diagnostics with high hardness to EMPs, or looking toward the possibility for employing them in a number of applications[63,64]. In laser-matter interactions, the electromagnetic emission is mainly produced by charge separation and the subsequent target polarization. The EMP can present broadband frequencies ranging from MHz up to THz domain according to both laser and target characteristics. Among the principal sources of EMP production there are the electron ejection and the subsequent generation of the return currents[26,65,66]. As discussed in the previous sections, the laser impinging on a solid target leads to the production of energetic electrons characterized by a temperature T_{hot}. These electrons, escaping from the solid target (both from its front and rear side), produce target charging up to MV potentials depending on their temperature. Also the maximum charge accumulated on the target depends on T_{hot} and can be estimated as $Q_e \simeq C_t k_B T_{hot}/q_e$ where C_t is the target capacitance. The energy of the impinging laser E_L, together with the conversion efficiency to hot electrons η_L, also limits the maximum achievable accumulated charge $Q_e \leq q_e \eta_L E_L / k_B T_{hot}$. According to laser energy and focusing condition, Q_e value ranges from few nC up to tens of μC.

The timing of charge accumulation and storage into the target influences the temporal characteristics of the current, which in turn defines the spectral domain and the field amplitude of the emitted electromagnetic pulses. For sub-ps laser systems, the target charging process is temporally separated from the discharge process. On the other hand, for longer pulses the electron ejection and return currents generation tend to balance each other, leading to the establishment of the target potential without a remarkable charge accumulation. The emission related to electron ejection will produce EMP in the THz frequency domain, whereas the electromagnetic emission related to relaxation processes will lead to EMPs in the GHz frequency domain.
In terms of interference with the electronic devices used for on-line particle detection, the electromagnetic emission in the GHz range is the one to take into account. Indeed it is the one that strongly affects the performance of the detector used.
In the following sections a basic description of the main phenomenon leading to the EMP emission in the GHz range is given.

1.3.1 EMP production by return currents: GHz emission

Emissions in the frequency domain lower than 30-100 GHz is ascribable to timescales longer than 30-100 p,s which are related to the relaxation of the accumulated charge. This is triggered effectively by laser pulses in the fs-ps range although significative fields can be produced also by ns pulses.
A commonly employed target in laser-matter experiments can be schematized as a metallic disc with a diameter d_t supported by a metallic stalk of few centimeters length ℓ_s as depicted in Figure 1.7.

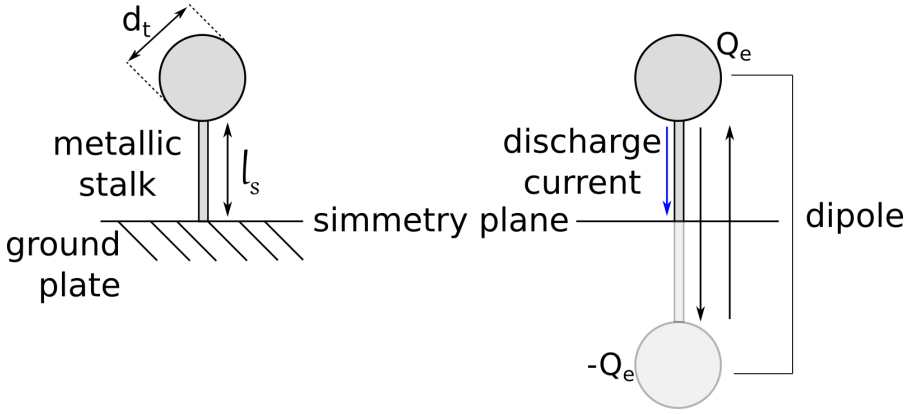

Figure 1.7. A schematic representation of the target (a disk of diameter d_t) and the metallic stalk standing on the experimental chamber floor. When a charge Q_e is accumulated on the target, a discharge current flows through the stalk causing the EMP generation. As shown on the right, the system become electrically equivalent to an oscillating dipole.

As already mentioned, for short laser pulses, a charge Q_e is produced on the target before the discharge current is formed. The current flows from the target through the stalk to the ground and then it comes back to the target. It is thus generated an oscillating current along the stalk. This forms a linear antenna which, since in the case of interest the pulse length of the feed-in current is shorter than the antenna length, has the characteristic wavelength of emission equal to four times

the length of the stalk. For a typical length of 10 cm, the main emission frequency will be $\omega = \pi c/2\ell_s \simeq 4.7$ GHz. It is possible to estimate the total energy emitted in the GHz domain to be[26]:

$$E_{GHz} \simeq 0.1\sqrt{\frac{\mu_0}{\epsilon_0}}\frac{c}{d_t}Q_e^2 \tag{1.23}$$

which results to be of the same order of magnitude of that emitted in THz domain in experiments with fs-ps laser pulses but can have much stronger effects on the electronic devices. In order to mitigate the emission in this particular spectral range, many groups proposed different possibilities to reduce the velocity of the propagation of the current into the stalk employing a dielectric material or shaping it into a complex geometry[25,26].

1.3.2 Description of EMP signals in time and frequency domain

The electromagnetic field inside an experimental chamber, established during and after the laser-matter interaction, results from the superimposition of the emitted EMPs with their multiple reflections. Indeed, in a real experimental setup, the emitted electromagnetic radiation is going to be reflected by the multitude of conducive objects placed inside the chamber as well by the walls of the chamber[67]. Moreover, as discussed in the previous section, for each EMP wavelength the expanding plasma represents a time-varying volumetric distribution of overcritical regions reflecting the impinging radiation[68]. Hence a detailed analysis would require an extendend numerical simulation. Nevertheless, analytical expressions can be found in the simplified hypothesis of a hollow experimental chamber with a simple geometrical shape. Under this assumption it is possible to write the analytical expression of the electric and magnetic fields inside a vacuum chamber[26,67,69]:

$$\begin{cases} \mathbf{E} = \sum\limits_{i=1}^{+\infty} A_i\mathbf{E}_i + \sum\limits_{i=1}^{M-1} A_i^0\mathbf{E}_i^0 + \sum\limits_{i=1}^{+\infty} B_i\mathbf{s}_i \\ \\ \mathbf{B} = \sum\limits_{i=1}^{+\infty} C_i\mathbf{H}_i + \sum\limits_{i=1}^{P-1} C_i^0\mathbf{H}_i^0 + \sum\limits_{i=1}^{+\infty} D_i\mathbf{g}_i \end{cases} \tag{1.24}$$

where $\mathbf{E}_i$ and $\mathbf{H}_i$ are the solenoidal electric and magnetic egeinvectors, $\mathbf{E}_i^0$ and $\mathbf{H}_i^0$ are the harmonic electric and magnetic eigenvectors, associated with M separate boundary parts and with a P-times connected volume, and $\mathbf{s}_i$ and $\mathbf{g}_i$ are the irrotational electric and magnetic eigenvectors.
These equations contain an infinite number of modes, but only few of them are effectively excited by the sources.This means that only a finite set of coefficient is non-zero. Moreover, given an EMP with a broadband spectrum, the chamber acts like a microwave filter, leading to the fast decay of all non-resonant harmonics while maintaining for a longer time the resonant modes. For an ideal δ-function emission, the non-resonant modes decay exponentially with a characteristic decay time $\tau_{decay} = 2Q_i/\omega_{i_{EMP}}$ dependent by the quality factor Q_i of the experimental chamber, here seen as a resonant cavity.
The time domain measurements of EMPs performed in different laser facilities present thus a complex structure and are effectively described adopting the amplitude

envelope approach[67] characterizing the amplitude variation of the signal. The amplitude envelope of a signal $x(t)$ is defined as:

$$AE(t) \equiv \left| x(t) + \frac{i}{\pi}\mathcal{P}\left(\int_{-\infty}^{\infty} \frac{x(\tau)}{t-\tau} d\tau \right) \right| \tag{1.25}$$

where the second term is the Hilbert transform of the signal and $\mathcal{P}$ stands for the Cauchy principal value of the integral. In laser-plasma experiments, the typical time-domain signal is reported in Figure 1.8.a and its amplitude envelope is reported in Figure 1.8.b. It is possible to see an oscillating signal modulated by a fast rising edge followed by slower decay. In terms of the Amplitude Envelope approach this signal is well described by the difference of two exponential functions characterized by different time constants, multiplied by the Heaviside step function $\theta(t)$:

$$f(t) = \left[A_0 \exp\left(-\frac{t}{\tau_f} \right) - B_0 \exp\left(-\frac{t}{\tau_r} \right) \right] \theta(t) \tag{1.26}$$

Moreover, since the spectral content of EMP changes over time, it can be described with a time-frequency analysis using the Short-Time Fourier Transform (STFT) which, given a window function w being zero outside a specific time interval, is defined as:

$$F_x^w(t,f) \equiv \int_{-\infty}^{+\infty} x(\tau) w(\tau - t) e^{2\pi i f \tau} d\tau \tag{1.27}$$

with the associated spectrogram defined as:

$$S_x^w(t,f) \equiv |F_s^w(t,f)|^2 \tag{1.28}$$

The spectral content of the signal reported in Figure 1.8.a is shown in Fig. 1.8.c.

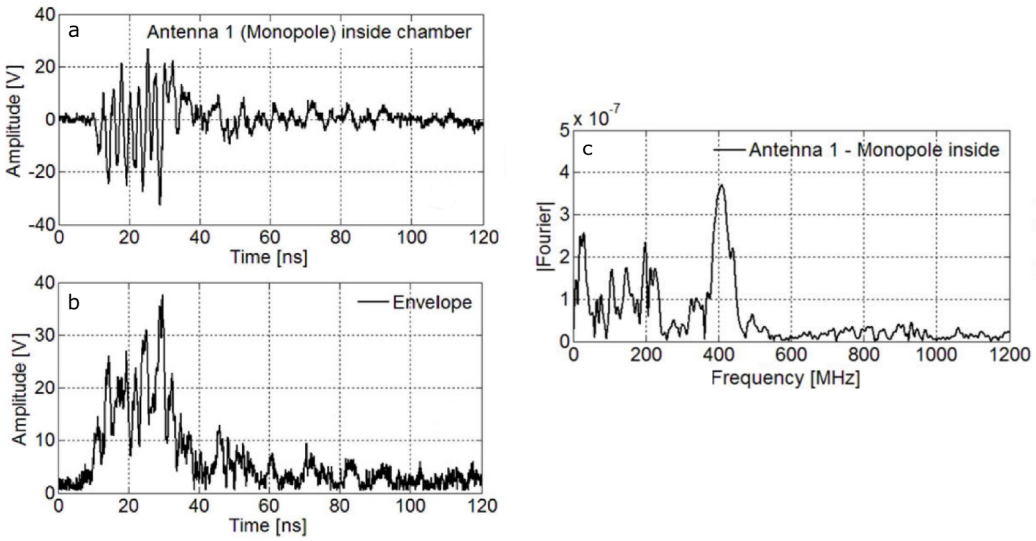

Figure 1.8. (a) A typical raw signal collected during a shot performed at the ABC laser facility operating with 3 ns laser pulses. (b) The amplitude envelope of the signal reported in (a) and its spectral content (c). From *Consoli et al.*[26]

1.4 Laser-driven ion sources for applications

The unique properties of laser-driven accelerated ions, such as the high number of protons per shot (up to $\simeq 10^{13}$ and more), the short initial temporal duration of the proton bunch ($\simeq 10^{-12}$ s)[70], the high laser to proton energy conversion efficiency achievable in the PW interaction[71], the collimation within a cone angle of few tens of degrees and the possibility to focus the beam with a proper shaping of the target[72–74], make this source appealing for many applications. Moreover, the emission of protons is accompanied by a co-moving electron cloud ensuring charge neutralization and limiting the space-charge detrimental effects[13]. On the other hand, the stability of this kind of source remains an issue for several applications. The fluctuations in the ion energy spectrum, the size of the source and its angular beam profile need a shot-to-shot detailed characterization in order to be of actual practical use.
Nevertheless, laser-driven ion beams have soon attracted the interest in the field of medicine and they were indeed proposed for oncological ion beam therapy (IBT)[75]. A strong effort is ongoing to demonstrate the feasibility of this proposition, trying to reach the necessary ion beam parameters. Even though the pathway to its employment in clinical environments is still long and presents some challenges, the effectiveness in tumor treatments has been investigated by conducting cell irradiation experiments, which led to promising results[16,17]. A more detailed overview of the medical application of laser-driven sources is given in Section 1.4.1.
A laminar beam of highly energetic charged particles with pulse initial duration down to few ps is extremely appealing also for diagnosing transient phenomena. Indeed, laser-driven protons have been used as probes for the investigation of the electric field in laser-produced plasmas, as briefly discussed in Section 1.4.2. Thanks to the high temporal and spatial resolution, due to the combination of the short duration

pulse and low emittance, their employment allowed to detect relativistic solitons generated in laser plasma[76] and to picture the accelerating Debye sheath in the TNSA process as well as the subsequent ion expansion[77]. Laser-driven ion sources have been investigated also for applications in material science. Very recently it has been introduced as an alternative source for particle-induced X-ray Emission (PIXE) spectroscopy of materials[78]. A description of this technique is given in Section 1.4.3. Moreover, soon after the first observation, laser-accelerated protons have been proposed for the fast-ignition scheme in Inertial Confinement Fusion (ICF). This led to a wide study on the optimization of the beam focusing and control to effectively employ them to create a hot spot in Inertial Confinement Fusion targets[5]. In more recent years, they were also proposed as projectiles for triggering proton-boron fusion reaction. In Section 1.4.4 a description of these two approaches is reported.

1.4.1 Medical Application

One of the major applications of laser-accelerated ion in the medical field for tumor treatments. In hadrontherapy, energetic carbon ions and protons are used to destroy the DNA of the tumoral cells while minimizing the dose received by the surrounding healthy tissue. The employment of hadrons is justified by their energy deposition distribution in matter, which is characterized by a maximum dose deposition at the end of their path, with a minimum fluctuation in the penetration depth. Despite the evidence of its effectiveness in cancer treatment, hadrontherapy accessibility is still limited to a few percent of the patients. This is mainly due to the huge costs for construction and maintenance of the necessary structures and equipment associated to complex accelerators. A laser-based approach would allow to increase the compactness of the system, lowering the overall costs[79]. For instance, the possibility to generate ions in the treatment room, may reduce the cost related to the ion-beam transport. Furthermore, with respect to conventional ion sources, laser driven ions present some intrinsic advantages such as a typical ultra short beam pulse and a high dose for single pulse, as well as the possibility to work at high repetition rate. Nevertheless, both the high divergence, the broad energy spectrum and the instability of the laser-target interaction, still represent non-negligible drawbacks for their clinical application. Proper energy selectors need to be developed and a primary task is to control the stability of the laser-target interaction and to be able to characterize the dose and the fluency delivered to the patient. Possible solutions to these issues have been already proposed both by means of target engineering[80,81] and ion optics[82,83] able to focus and energy-select the emitted ion beam.
Another task to accomplish before a laser-based ion source could replace a conventional accelerator, is the enhancement of the maximum achievable energy. Indeed the energies typically required for effectively treating tumoral cells are higher than the currently available maximum laser-driven proton energy. For instance for lung tumors, typically located at $\sim$ 13 cm in depth, 130 MeV/nucleon ion beams are necessary. The progresses in the last years, both in laser systems and in target design, strongly improved this aspect, making it possible to reach the lower energy threshold for medical application, represented by the treatment of eye tumor, for which energies of $\sim$ 60 MeV are sufficient. Nevertheless, further developments are needed.

Eventually, the simultaneous emission of electrons, γ rays and X-rays can represent an issue if not taken into account. With a careful design of a proper transport line they can be an interesting opportunity for mixed field tumor irradiation schemes[84]. The strong interest in this field led to the spreading of several research projects[85] and to the commissioning and construction of experimental areas dedicated to the investigation of possible solutions for a medical employment of laser-based sources[86–88].

1.4.2 Proton radiography

Proton radiography relies on the variation in the velocities (i.e. energy and direction) of the impinging protons that, propagating through the sample, interact with its atoms and with the local electromagnetic fields. Particles passing through different sections of an object that presents various density, will undergo a different set of scattering events acquiring distinct final velocities[89].
In the last fifty years, ion beams produced with conventional accelerators have been successfully used to radiograph both static and moving sample and transient events. Nevertheless, small source size, low emittance and short duration of laser-driven sources have greatly expanded the possibilities of proton probing and radiography, in terms of both spatial and temporal resolution. As shown in Section 1.2.2, the protons accelerated by the TNSA process can be described as emitted by a virtual point-like source located at the front side of the irradiated target. This intrinsically provides a high spatial resolution when applied to imaging. Indeed, it automatically satisfies the requirements of a point projection imaging scheme with a magnification of the image defined only by the geometrical distances. This high resolution allows to resolve details with spatial dimension of few microns. Moreover, the short duration of the proton bunch offers the possibility to investigate transient phenomena evolving in a few picoseconds, such as the evolution of the magnetic and electric fields in a laser-produced plasma[77].

1.4.3 Laser driven Ion Beam Analysis: PIXE

Ion Beam Analysis (IBA) is a modern branch of techniques devoted to the characterization of materials. IBA has a wide range of applicability, from fundamental science to cultural heritage, where it is of crucial importance to avoid any damage to the investigated samples. The technique, already commonly used with conventional proton sources such as compact cyclotrons or small Van de Graaff accelerators, is able to provide a complete chemical analysis of the irradiated material. In this method, energetic and heavy charged particles are sent onto the surface of the sample to generate inner-shell vacancies. The subsequent de-excitation of the vacancies results in the emission of characteristic radiation that can be measured and whose wavelengths represent a fingerprint of each chemical element present in the analyzed specimen. In Particle induced X-ray emission (PIXE) the impinging particles are more often protons or alfa particles and the emitted radiation falls in the X-ray range. The classical employment of conventional accelerators as ion sources poses some limitations to applicability of the technique in many fields and also to the wide range of information that could be retrieved. Two of the main institutions

devoted to cultural heritage studies and using conventional proton accelerator are the AGLAE located at the French Louvre Laboratory and the italian INFN-LABEC laboratory located in Florence. They can provide proton energies ranging from 1 up to 5 MeV, beam currents from 10 pA up to nA and spot sizes ~ 10 μm that can be defocused up to 500 μm to investigate larger areas of the sample. Such energies limit the depth of the sample to be effectively investigated to a layer of ~ 20 μm. This is usually the thickness of surface patina or bronze cancer (cuprite, malachite), limiting the analysis to the deteriorated layers of the investigated sample. The reduced dimension of the focal spot allows for high resolution but, on the other hand, multiple measurements are required if the whole surface of the sample has to be investigated. Due to the low beam current, each of these measurements requires long time of exposition to completely retrieve the information needed. These two factors lead to a long analysis time that can produce damages to the sample.
The employment of laser-driven sources presents thus some advantages. Currently available multi-TW table-top laser systems can generate intensities on target up to 10^{20} W cm^{-2} providing proton energies in the range of 15-20 MeV, with currents in the kA regime. In addition, the laser-driven ion source allows to easily change the energy range of the accelerated ions by tuning the energy of the impinging laser, with major advantages in terms of flexibility. Moreover, the issue of radiation protection is limited to a region surrounding the interaction point, resulting in a higher manageability of the system.
On the other hand, the source presents some peculiar characteristics that need to be properly addressed. Among these, the accelerated proton bunch has a wide energy spread and is preceded by a strong emission of hot electrons. In recent years these issues have been already investigated both with numerical analysis and dedicated experiments[90,91]. The results are promising and demonstrate the future feasibility of a compact and versatile laser-driven apparatus for Ion Beam Analysis.

1.4.4 Nuclear Fusion: fast ignition and proton boron scheme.

Fast ignition was proposed as an advanced scheme both for indirect and direct drive traditional approaches where the ignition occurs in a central hot spot following a pulse compression of the whole deuterium-tritium pellet (central hot spot ignition)[5]. To overcome the issues related to hydrodynamic instabilities formation, which requires an extremely high symmetry in the irradiation scheme, it was proposed to separate the pulse compression process from the ignition stage. In the fast ignition scheme, ignition relies on an external driver which creates the hot spot in a shorter time than the typical pellet disassembly time[92]. In the original proposal, the driver was identified with laser-driven multi-MeV electrons[93]. In subsequent studies it was shown that the smooth energy deposition profile of electrons in matter was not ideal to create a localized hot-spot.
Soon after the observation of laser-driven fast proton beam generation, protons were suggested as an alternative to electrons for being used as external drivers[94]. The main advantage consisted in the peculiar energy deposition function presenting a sharp peak, i.e. the Bragg peak, at the maximum penetration depth. Besides the localized energy deposition, other advantages were the low emittance of the beam and its focusability via proper target shaping. Moreover, the exponential energy

spectrum of the laser-driven protons resulted to be an optimum for the hot-spot heating. Indeed, the first protons to reach the compressed fuel will be the more energetic ones. As the target temperature starts to rise, the stopping power is reduced, thus the protons with lower energies, reaching the target at later times, will be stopped at roughly similar depth. This leads to the major portion of the proton beam depositing its energy in the same fuel volume[95].
The ignition conditions are well established and are the same both for electrons and for protons. Radiation-hydrodynamic models show that in fast ignition the required temperatures and areal densities are $T = 5 - 10$ keV for $\rho r = 0.3 - 0.5$ g cm^{-2} respectively. The mentioned effects of the quasi-thermal distribution of protons energies added a requirement in their temporal spread. All protons must arrive within the 20 ps inertial confinement time so the source to hot-spot distance should be < 1 mm to take full advantage of the useful spread of energies. In addition to this, simulations suggested that, for a given fuel density, the minimum energy required for ignition increases with the distance between the driver source and the pellet core. In order to reduce this distance, it was suggested to employ a cone shaped holder with an integrated parabolic curved foil to use as target for laser irradiation and focused proton beam production. The foil thickness should be chosen to protect the rear surface from the laser pre-pulse. This limits the laser to proton energy conversion efficiency; thus harmonic conversion of the short laser pulse can be employed to increase the contrast and to allow irradiation of thinner foils. The cone has to be thick enough to prevent the penetration of the shock wave produced by the imploding plasma. This introduces an additional energy loss for protons that have to cross the cone tip for reaching the fuel. In Figure 1.9.a the conceptual design of these targets together with suitable parameters for fast ignition is depicted.

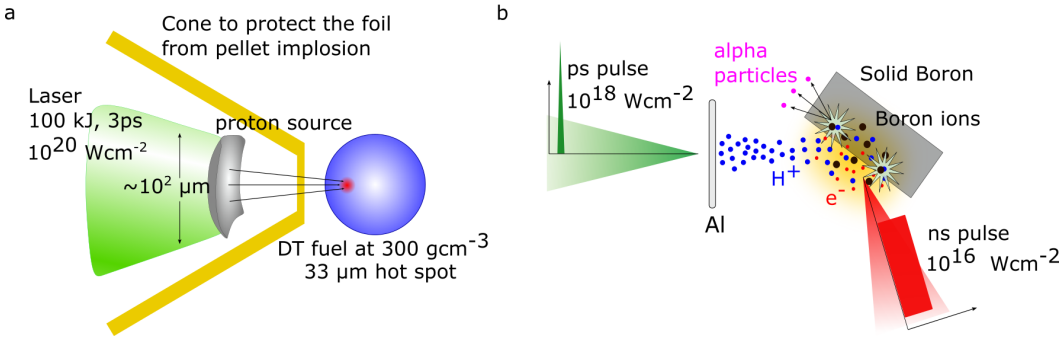

Figure 1.9. (a) Conceptual scheme for fast ignition driven by protons. The reduced distance between the DT fuel and the target employed as proton source requires to protect the latter from the pellet implosion. For this reason the cone-shaped shield is employed. The bent target profile is necessary to obtain a focused accelerated proton beam, as uniform as possible. (b) The scheme for the pB fusion reaction triggered by laser-driven protons. A solid boron target is first ionized with a long pulse. A short laser pulse is then used to irradiate a thin metallic foil to produce energetic protons sent on the boron plasma to trigger the pB fusion reaction.

Alternative fuels to the Deuterium-Tritium (DT) mixture have been also investigated. One of the more appealing is the p + ^{11}B $\rightarrow 3\alpha$ + 8.7 MeV fusion reaction which, despite the lower cross section and energy gain with respect to the

conventional D +T $\rightarrow \alpha$ + n + 17.59 MeV reaction, presents the possibility to exclude fast neutron production, allowing to get safer and cleaner future power plants. Two main schemes were investigated to trigger this reaction[96]. One approach is to exploit the protons accelerated via the TNSA mechanism by sending them to a boron plasma produced by another laser-pulse[97,98] or to a solid boron target[14]. In Figure 1.9.b a schematic representation of this arrangement is shown for an experiment performed at the LULI laser system. Here a ns laser was used to ionize the boron target and a ps pulse with intensity 6×10^{18} Wcm^{-2} was employed to produce the accelerated protons from a foil target. This scheme led to an α particle yield of 9×10^6 α/sr/shot[97]. A similar scheme was used in experiments at LFEX with boron targets and demonstrated particle yield of 5×10^9 α/sr/shot[99]. In this approach, the most favorable condition to trigger the reaction is given by a resonance in the pB cross section for proton energies of 614 keV.
A systematic study on the characteristics of various laser-driven proton sources that could be effectively employed to trigger fusion reactions has shown that the most promising source in terms of high proton yield at comparatively low laser power is the cryogenic hydrogen target[100]. In order to fully exploit the peculiar energy distribution of the laser-driven proton source, a novel lithium-boron hybrid target design was also proposed. The idea was to combine the pB fusion reaction together with the p + ^{7}Li $\rightarrow 2\alpha$ + 17.2 MeV enabling to achieve a maximum fusion yield by taking advantage of the energy spread of the accelerated protons. Indeed, with the BLi hybrid target the useful energy range to trigger fusion reactions would go from 0.4 and 4 MeV rather than relying only on resonances, and still involving neutron-less fusion reactions[100].
Another scheme involves the irradiation of solid target doped with boron atoms[15,101]. This was the first to be experimentally investigated in 2005 by irradiating boroated plastic targets with ps laser pulses with an intensity of 2×10^{18} W cm^{-2}. It led to a maximum alpha particle yield of 10^5 α/sr/shot[101,102]. The same scheme was used in 2013 irradiating with a sub-ns laser an hydrogenated silicon target doped by boron through ion implantation and enriched with hydrogen. This experiment led to a maximum alpha particle yield of 10^9 α/sr/shot[15]. Very recently the irradiation of a boron nitride thick target with a sub-ns pulse for an intensity on target of 3×10^{16} W cm^{-2}, led to the production of an alpha particle yield of 1.3×10^{11} α/sr/shot[103].

Chapter 2

Diagnostic techniques for the characterization of accelerated particles in laser-matter experiments

The development of laser systems with increasing performances has allowed to investigate new laser-matter interaction regimes. This has been necessarily accompanied by the spreading of a plethora of diagnostic techniques devoted to the characterization of one or more aspects of the laser-produced plasma and the emitted particles.
In the previous chapter a list of the main characteristics of the laser-driven accelerated ions has been presented. Among these, the very short time duration of the exposition, the high currents, the collimation and the large energy spread of particles. It is therefore straightforward to enumerate a series of requirements that the ideal diagnostic system should satisfy. It should be able to provide fast acquisition times, high dynamic ranges, high sensitivities, high energy resolutions and angular-resolved characterizations. Moreover, as discussed in the previous chapter, in order to be effectively employed in some applications, the laser-driven ion sources should be operated at a high-repetition rate. This presents some challenges both from the targetry point of view and from the diagnostic systems one. Indeed, the shot-to-shot variability of the interaction requires a beam characterization for each shot. In high-repetition-rate facilities this means a detection system able to work on-line, to give a real-time feedback of the ion bunch parameters. The necessity to have an on-line characterization of the beam poses an additional requirement to the detector.

It has been shown that the laser-matter interaction is capable to produce strong electromagnetic pulses (EMPs) which hinder the employment of any electronic device near the experimental chamber. This issue is more severe as the laser energy and intensity increase. Hence, an ideal high-repetition rate detection system should behave also great insensitivity to EMPs.

In the following sections an overview of the main diagnostic techniques currently available for ion diagnostics is provided. The first part of the chapter is dedicated

to all the detectors that require a post-processing procedure before being able to extract any information and that, for their intrinsic nature, cannot provide an on-line characterization of the beam. These techniques employ radiochromic films or Imaging Plate stacks, both described in Section 2.1. Then, in Section 2.2, solid state nuclear detectors are presented and, in Section 2.3, the principles of nuclear activation techniques are described. The second part of the chapter is instead dedicated to methodologies that can be employed for on-line diagnostics. These include electrostatic-magnetostatic spectrometers, introduced in Section 2.4, and the Time-of-Flight technique, discussed in Section 2.5.

2.1 Film detectors

A widely used technique to retrieve the spatial distribution of the accelerated proton bunch, together with their spectrum, is the employment of film detectors such as radiochromic film[104] or imaging plates[19]. The main advantage of this technique is the high resolution and the insensitivity to the electromagnetic noise, allowing it to be used near the interaction point.
The main drawback of the technique is that the exposed film needs to be scanned and to undergo a post-processing procedure before giving any quantitative information. This would not allow to employ them for an on-line diagnostic in a high-repetition rate facility. Nevertheless, it provides reliable information both on the spatial and on the energy distribution, and its compactness allows to place several stacks around the interaction point to investigate the particle emission from different angles.

2.1.1 Radiochromic Film (RCF)

Radiochromic films consist of colorless polyester foils with embedded self-developing active layers which darken upon exposure to ionizing radiation. The coloration is due to the polymerization at which the active layer, made of crystalline polyacetylenes (in particular dyacetylenes), undergoes after irradiation[104]. According to the specific dyacetylene monomer used, the coloration of the film can turn from blue to red.
Several types of RCF have been manufactured over the years to meet the different needs coming from the various application fields. The currently available models are the HD-810, MD-V2-55 and EBT, which have been the latest RCF films to be developed. They differ for the polyester sheets and active layer thickness, as well for the composition of the latter. Their nominal suitable dose ranges are $0.001 - 8$ Gy for EBT, $2 - 100$ Gy for MD-V2-55 and $10 - 400$ Gy for HD-810[18].
The coloration of exposed RCF films can be appreciated also by human eye, providing a fast evaluation of qualitative nature. Nevertheless, to retrieve quantitative information on the ionizing radiation causing the darkening, precise optical light intensity measurements are needed. The degree of coloration is measured in terms of optical density (OD) which is defined as[104]:

$$\mathrm{OD} = \mathrm{Log}\left(\frac{I_0}{I}\right), \tag{2.1}$$

where I_0 is the incident light intensity and I is the light transmitted through the exposed film. For employing them for dosimetry application, it is therefore of crucial

importance to have a known relation between the OD and the dose absorbed by the film. This can be obtained with suitable film calibration providing the dose, for a given energy and type of radiation, as a function of OD[105–112].
RCFs present a broad absorption spectrum with different responses for the same dose[104]. For Photons, this results in a significantly different sensitivity of the film according to the different wavelengths. Therefore, by adopting a multichannel approach, scanning the image in full colors, it is possible to increase the dynamic range of the dose measurement, by exploiting the film response in the three color channels Red, Green and Blue[104].

Radiochromic film Imaging Spectroscopy (RIS)

For the characterization of laser-driven proton emission, both spatial and spectral information are needed. They can be obtained by means of the Radiochromic film Imaging Spectroscopy[21] technique. This allows to determine the source size, the divergence and the transverse emittance of the proton beam and it provides a space and energy-resolved proton distribution.
In this technique, RCFs are placed in a stack and it is possible to attribute an energy range to each layer according to the position occupied in the stack. The technique relies on the energy deposition of the impinging radiation and thus cannot distinguish between ion species, X-rays or electrons, apart from their different stopping power. The latter are more penetrant than ions, resulting in a faint background signal that can be identified and taken into account. Heavier ions can be distinguished from protons thanks to the dependence of the stopping power on Z^2. Hence heavier ions will be stopped within the first layers of the stack, whereas protons will be able to cross multiple layers according to their energies. Thanks to the localized energy deposition of ions in matter, it is possible to know at which depth, hence in which layer of the stack, a proton will be stopped depositing most of its energy.
In order to enhance the effectiveness in reconstructing the spectrum and in distinguishing the different ion populations, it is also possible to include filters of proper thickness and material between each layer of the stack. This will contribute to stop the heavier ions in the very first layer of the stack and it can also reduce the background due to soft X-rays detection.

In Figure 2.1.a a sequence of RCF films is shown after being exposed to a proton beam driven by the PHELIX laser. They were capable to show that the most energetic portion of the emitted protons is localized in a narrow surface near the target normal, whereas the divergence increases for lower energies. The technique provides thus a spatially and energy resolved measurement of the impinging proton bunch. Each layer of the film stack provides a 2D image of the proton beam for a given energy range defined by the layer number.

The other parameters can be extrapolated with high spatial resolution if, in combination with the stacked foils, micro-structured targets are employed. The micro grooves at the target rear surface generate beamlets in the laser-accelerated proton beam. The beam expands while propagating, enhancing the separation of these beamlets which are recorded in the RCF as intensity modulations resulting in a line pattern, as shown in Figure 2.1.b. Measuring the number of visible lines as

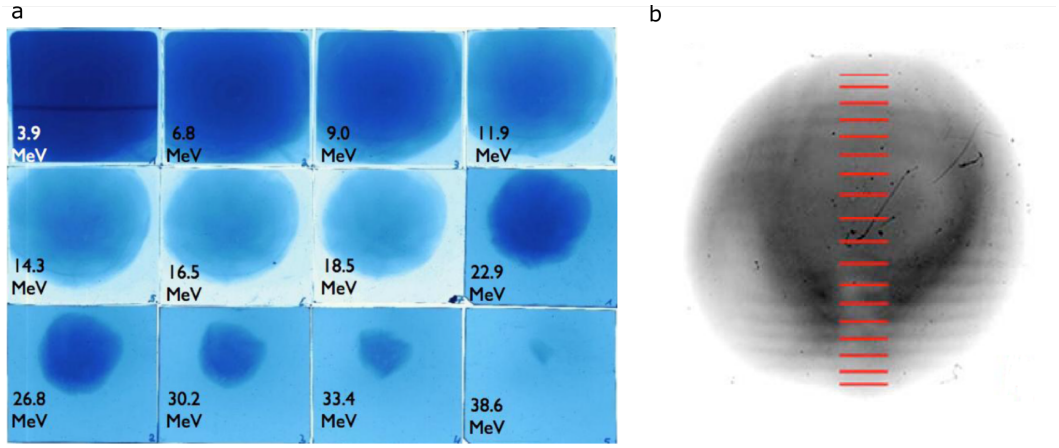

Figure 2.1. (a) Sequence of RCF employed in a stack after being exposed to the proton beam driven by PHELIX laser facility. For each layer the corresponding energy range is reported.[18] (b) The line pattern resulting from the microstructured targets irradiation. From *Nürnberg et al*[21]

well as the distances from each other, it is possible to obtain the real source size, i.e. the proton emission zone at the target surface, and to retrieve the virtual source size located at the front side where the protons seem to be generated.
The data reported in Figure 1.5 about source size, opening angle and emittance were obtained using this technique and following the procedure described by *Cowan et al.*[113] and *Nürnberg et al.*[21].

2.1.2 Imaging Plates (IP)

Imaging Plate detectors are based on the photo-stimulated luminescence (PSL) phenomenon, i.e. the storage of information in an excited state of the substance which is then retrieved by stimulating the de-excitation of the state by light irradiation[19]. Many substances show this property, but after an extensive study a barium fluorohalide compound containing a small amount of bivalent Europium (BaFX:Eu^{2+}, X = Cl, Br, I) was identified as having the strongest PSL response and chosen for being used in detectors[19]. When ionizing radiation impinges on this kind of compound, it can produce an $F^{\dagger}$ color center, i.e. a defect in the crystalline structure which absorbs a specific wavelength in the visible range. A color center is formed when an electron fills a vacancy left in the crystal structure. This state is meta-stable and, if irradiated with the proper radiation, the electron will be released again and the energy surplus will be emitted as photons. In the BaFX:Eu^{2+} compound, the europium is called the activator, since its presence provides the electrons producing the F color centers. When the compound is exposed to ionizing radiation, an electron from Eu^{2+} is excited and released in the conduction band where it is captured by a vacancy and forms the meta-stable F center which stores the information on the impinging radiation. When exposed to suitable visible radiation the electron is released again and absorbed by the previously-generated Eu^{3+} with the subsequent

†from the German term *"Farbenzenter"*

emission of a photon in the UV range and the possibility to retrieve the information stored as schematically shown in Figure 2.2.a.

Imaging plates are made depositing the BaFX:Eu^{2+} crystal grains on a polyester support film. After exposition, they can be read with proper scanners which usually employ a laser-diode to de-excite the meta-stable F state. The emitted radiation is then detected and converted in an electric signal which is digitized in a format with up to 16 bit resolution.
The base structure of an imaging plate consists of a 160 μm magnetic layer and a support polyester layer over which the sensitive photo-luminescent crystal is deposited. On top of this, a protective layer may be present. The thickness of each layer depends on the IP model. Fujifilm is one of the major IPs producer and provides indeed four main different IP types: BAS-TR, BAS-SR, BAS-MS and BAS-ND type. The latter is meant for neutron detection, whereas the first three are suitable for ions detection and are commonly used in the laser-driven accelerator community. As shown in Figure 2.2.b, each of them presents a different response for the impinging radiation[114] according to their layer structure and atomic composition: BAS-MS is equipped with a 9 μm protective layer and a 115 μm sensitive layer which composition is $BaFBr_{0.85}I_{0.15}$. BAS-SR presents a thinner protective layer and a thicker sensitive one, 6 μm and 120 μm respectively. The composition of its active layer is BaFBr. BAS-TR does not have a protective layer and has an atomic composition of the sensitive layer equal to the BAS-MS type, but with a reduced thickness of 50 μm.
All of them are characterized by high sensitivity and very high dynamic ranges, spanning over 8 order of magnitudes.[115]. Their response for proton irradiation has been characterized over a wide energy range[114,116–118], enabling quantitative measurements.

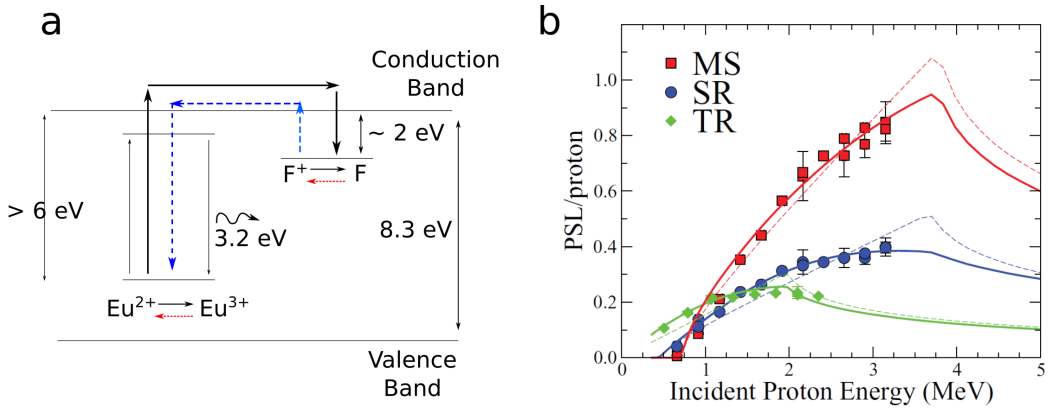

Figure 2.2. (a) The process of image storage and reading from an Imaging Plate. (b) Response of the three different IPs types as a function of proton energy. From *Bonnet et al.*[114]

2.1.3 IPs Fading time and RCF full-development

Both for RCF and IPs it is important to choose the proper time for the scanning procedure. Indeed RCF may take some time to develop full color which typically reaches saturation after 24 h[104]. On the other hand, the image information stored in the "memory" of the IP sensitive layer starts to fade with the passage of time. This means that the amount of photo-stimulated light emission changes over time[19]. This fading process is faster soon after the exposure (half an hour) and then it starts to slow down until it is almost negligible. This effect has to be taken into account when aiming for quantitative measurements and usually it is a good practice to perform the scanning procedure after that the first fast decrement of the signal has already happened and, for each exposed film, it should be always done with the same delay from the irradiation time.

2.2 Solid state nuclear track detector

Another widely used technique to detect and characterize laser-plasma interaction products employs solid state nuclear track detectors (SSNTD). They can be divided into two main categories according to the detecting media. Natural mineral crystals and polymers (CR39, PM-355, allyl diglycol carbonate). Those commonly used in ionizing radiation detection fall in the second category[20]. In these materials the impinging radiation causes the breaking of long polymer chains, damaging the film in localized spots. During the etching procedure, these weakened regions will be prone to a faster deterioration with respect to the undamaged material. This leads to a non-uniform film thinning revealing the tracks left by the impinging radiation. These tracks can be detected by means of a confocal optical microscope.
Chemical etching is usually performed by means of an aqueous solution of NaOH with concentrations ranging from a molarity of 1 to 12 and a controlled temperature going from 40 to 70 °C. In this bath two processes contribute to bring out the latent tracks: chemical dissolution of the impinging radiation trails and, at a lower rate, the dissolution of the bulk material. According to the thickness of the detector, the final tracks can result in etched-trough holes or, in the case of a thick detector, in superficial grooves.
Knowing the etching rate and its duration, which usually takes several hours, the energy of the impinging particle can be inferred by the track dimension[20]. Additional information can be extrapolated from the track shape. A circular pit is generated when particles enter the surface at normal incidence, otherwise an ellipse is generated, whose ellipticity and orientation provide information on the direction of incidence[119]. Due to the statistical nature of the etching procedure, the energy resolution offered by the employment of this technique is not very high. Indeed, even for a monochromatic particle beam, the size of the pits will distribute in an histogram-like distribution rather than on a sharp peak. Nevertheless, the resolution of the measurement can be improved by employing a multi-step etching procedure, in this way a resolution of 0.1 MeV can be achieved when stacks of CR39 film are used or the SSNTD is filtered with foils of proper material and thickness[120]. A typical example of the track generated on the solid state nuclear detector during laser-driven proton acceleration experiments is shown in Figure 2.3 together with the associated energy distribution

of the detected protons[121].
Solid state nuclear detectors present thus some advantages. They are insensitive to electromagnetic noise in the radiofrequency-microwave regime (EMPs) and do not require any in-situ electronic device, resulting suitable to perform measurements in highly EMP polluted environments. They allow for an angularly-resolved measurement of the accelerated particles and the contribution of fast electrons and X-rays does not hinder the quality of the measurement significantly. Moreover, the employment of filters of proper material and thickness, covering the detector surface, helps to cut the contribution of heavier ions producing unwanted tracks[96]. On the other hand, the process required to retrieve the data is quite long and time consuming, especially for the necessity to perform an etching procedure that can last up to several hours.

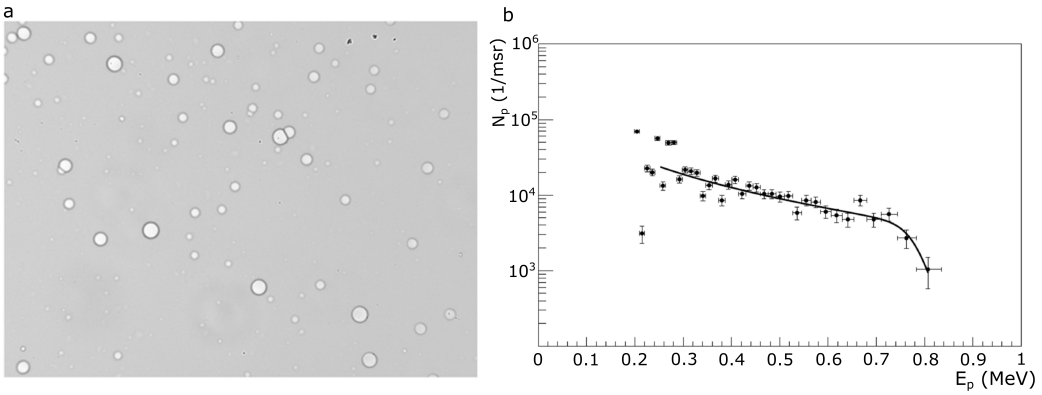

Figure 2.3. (a) Pits associated with protons impinging on the detector at normal incidence. (b) The associated proton energy distribution. From *Seimetz et al.*[121].

2.3 Nuclear activation

The acceleration of energetic ions can induce nuclear reactions in a secondary target. For instance, protons in the energy range from a few and up to several tens of MeV may induce emission of nucleons or, if more energetic (hundreds of MeV), can induce fission and spallation reactions. By monitoring the products of such reactions it is possible to retrieve the spectral properties of the impinging ion beam. Hence, nuclear activation has been used since the first experiments as a diagnostic technique.
To rhis purpose, some well-known nuclear reactions are chosen and a suitable secondary target is placed along the ion beam path. The selection of the secondary target material depends on: the type of ion of interest, the reaction activation energy, the knowledge of the cross section $\sigma(E)$, the half-life of the decay products. Moreover it is required the availability of a sample with a high density of the stable parent nucleus, so to guarantee a proper amount of reactions induced by impinging protons. For measurements of accelerated proton, proton-induced reactions in ^{63}Cu are usually adopted. This reaction has a threshold energy $E_{threshold} = 4.15$ MeV and results in the production of ^{63}Zn which decays by positron emission. The annihilation of the positrons emits 511 keV photons which can be detected using NaI scintillator

detectors[122] or high resolution GE-crystal gamma-ray spectrometers.
The number of reactions N induced by protons can be expressed as:

$$N = N_0 \int_{E_{threshold}}^{\infty} \sigma(E) n_p(E) dE \tag{2.2}$$

where N_0 is the total number of irradiated nuclei in the secondary target, and $n_p(E)$ is the incident proton energy distribution per unit area. If every other parameter in (2.2) is known, it is possible to estimate the proton energy spectrum by measuring the number of induced reactions.
The technique can be applied by using a single copper foil[123] or stacked foils[122]. In the latter case, as for RCF and IP stacking procedure discussed in Section 2.1, it will be possible to extend the analysis to a wider range of energies.
Spectrally and spatially resolved proton beam profile can be retrieved by means of the nuclear activated imaging spectroscopy (NAIS) technique[124]. This technique relies on the activation of stacked copper foils and its auto-radiography which is impressed on IP detectors. As in Radiochromic film Imaging Sectroscopy (RIS), each layer is related to an energy range; lower-energy protons are stopped in the first copper foils whereas the more energetic are able to penetrate deeper. Each copper foil is activated according to the energy of the impinging protons. The photons emitted by the decay reactions are detected by IP detectors. The PSL value is then related to the activity within the copper foil and thus to the proton-induced reaction yield from which it is possible to retrieve their energy spectrum. Experimental results obtained from the irradiation of a stack of Cu foils are reported in Figure 2.4.

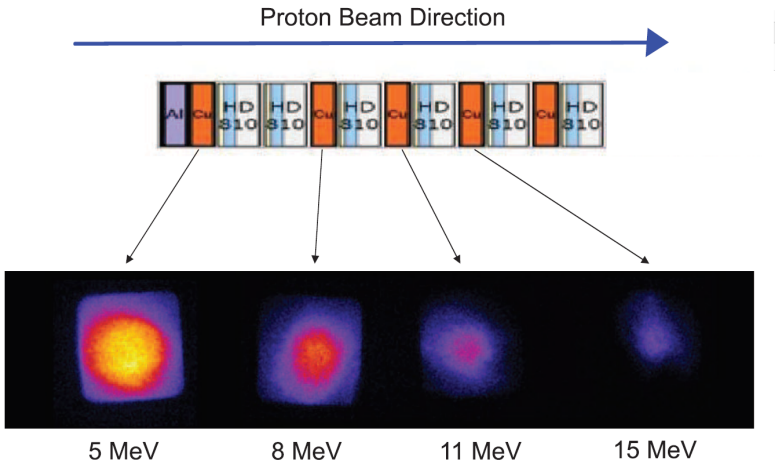

Figure 2.4. The stack of copper foils used for the nuclear activation technique. In the experiment each layer was alternated to a RCF to compare the results obtained with the NAIS technique with those given by RIS method. Below the autoradiography of each activated copper layer using IPs. From *Gunther et al.*[124].

2.4 Electrostatic - Magnetostatic spectrometers

Electrostatic and magnetostatic spectrometers allow to retrieve the energy of a charged particle exploiting the relation between its energy and the deflection at which it is subjected traveling through an electrostatic or magnetostatic field. In Figure 2.5 it is depicted a simple scheme of this kind of spectrometers, illustrating its working principle. The relation linking the particle kinetic energy and the deflection

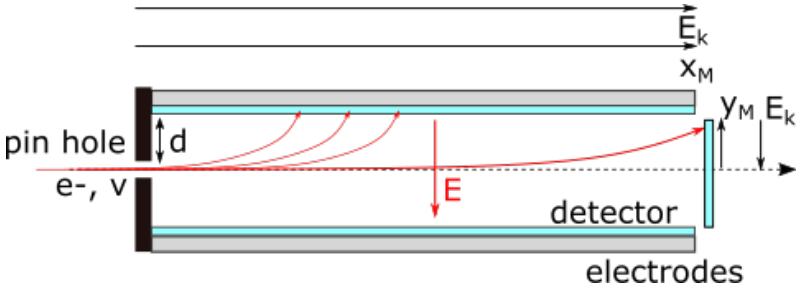

Figure 2.5. Electrostatic spectrometer. As an example, the trajectories of electrons with different energies are shown.

in an electrostatic spectrometer can be easily obtained from the equation of motion. As shown in Figure 2.5, the detectors can be placed either perpendicular to the particle original trajectory or along its path. This allows to extend the range of the investigated energies. At a non-relativistic regime, the relation between the energy E_k of a particle and the deflection y_M in the detector can be expressed as:

$$E_k = \frac{1}{4}\frac{qE}{y_M}L \tag{2.3}$$

where E is the applied electric field and, if the spectrometer does not comprehend any free drift space (as the one depicted in Figure 2.5), L is the distance from the detector plane to the pin-hole. For the detectors along the particle path the deflection is given in terms of the coordinate x_M:

$$E_k = \frac{1}{4}x_M^2\frac{qE}{d} \tag{2.4}$$

where d is the distance from the detector to the spectrometer axis as shown in Figure 2.5. None of these two equations depend on the mass of the incoming particle. Thus, this diagnostic is very useful when dealing with a single particle type, for instance for electron spectrometers, but it does not allow to distinguish among the contribution of different ionic species.
Similar equations can be obtained for a magnetostatic spectrometer, where a magnetic field perpendicular to the particle trajectory is applied, but in this case the particle mass affect the deflection.
On the other hand, spectrometers of the Thomson type[22], exploiting the action of a superimposed electric and magnetic field, enable to obtain simultaneous information on the distribution of accelerated ions as a function of their energy and charge to mass ratio. The main components of a Thomson spectrometer (TS) are an entrance pin-hole followed by a region where both an electric and a magnetic field are applied.

Hereinafter the space where these field are applied is identified as the spectrometer. In the simplest scheme, the electric and magnetic fields are provided by parallel rectangular electrodes and permanent magnets. Then, at a proper distance, a detector is placed to reveal the deflected particles. According to the experimental needs, the detector can be either a passive one, such as an Imaging Plate or a CR39, or an active one to allow on-line measurements. The latter is usually a micro-channel plate (MCP)[125] coupled with a phosphor screen which produces an image collected by a CCD and saved. A simple scheme of a conventional TS is depicted in Figure 2.6.a.

An ion bunch entering through the pin-hole will thus be affected by an electric field

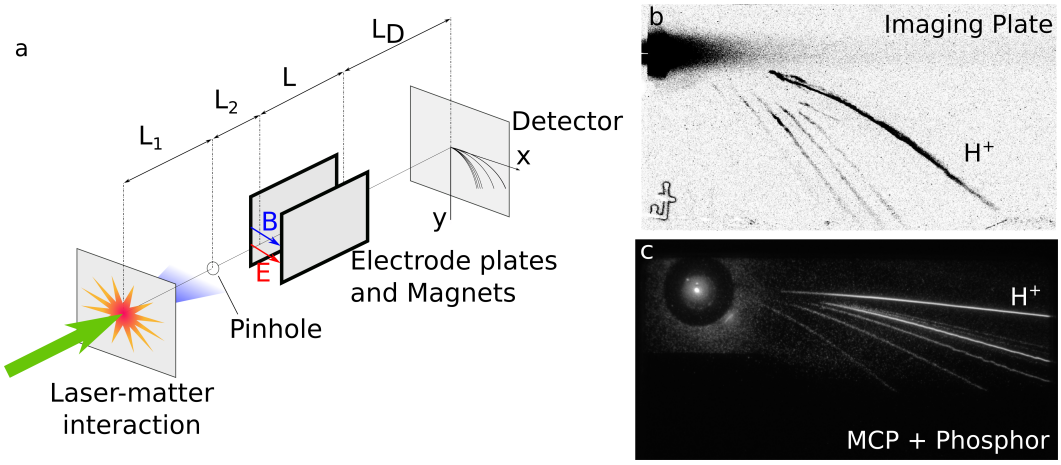

Figure 2.6. (a) The scheme of a Thomson spectrometer (b) Traces collected by a TS equipped with an Imaging Plate (c) Traces collected by a TS equipped with an MCP coupled to a phosphor screen.

E orthogonal to its motion which will provide different deflection according to the charge over mass ratio of each ion type. Moreover, the magnetic field B, parallel to the electric one, will provide a differentiation according to the ions momentum. Then, the deflected particles travel through the drift space of length L_D increasing their mutual separation until they reach the detector site. For an ion propagating along the z direction with velocity v_z, assuming uniform electric and magnetic fields are applied for a length L, the equations of motion can be written as[18,22]:

$$\begin{cases} x = \frac{Ze}{Am_p}\frac{BL}{v_z}\left(\frac{L}{2}+L_D\right) \\ y = Am_p\frac{EL}{v_z^2}\left(\frac{L}{2}+L_D\right) \end{cases} \tag{2.5}$$

where A is the atomic mass, Z the atomic number and m_p the proton mass. From these equation it is possible to obtain:

$$y(x) = \frac{Am_p}{Ze}\frac{E}{B^2}\frac{1}{L\left(\frac{L}{2}+L_D\right)}x^2 \tag{2.6}$$

The collected traces have indeed a typical parabolic shape as shown in Figure 2.6.b,c. Each parabola is related to a specific Z/A ratio and each point in the

parabola corresponds to a different energy. Since the laser-accelerated ion bunch is characterized by different ion species, each with a broad energy distribution, the signal will appear as several parabolas originated from a common point. This is identified by the straight trajectory followed by X-rays and neutral particles.
The resolution is mainly determined by the pinhole diameter. Larger pinholes allow to have an enhanced sensitivity but the traces of each parabola will be larger, limiting the capability to resolve different ion species, specially at higher energies, i.e. near to the origin[96]. The width, δ, of the trace is determined by the distance between the source to the pinhole L_1 and the one from the pinhole to the region affected by the electric and the magnetic fields L_2 and it can be expressed as $\delta = d(L_1 + L_2)/L_1$[96].
Another issue is related to the magnetic and electric fields themselves. Indeed they are never completely uniform along the spectrometer length. To take this effect into account, in equation (2.5) it is useful to employ two field integrals in place of the values E and B[126,127]. These are defined as:

$$\begin{cases} I_B = \int_0^L B(z)dz = \bar{B}L \\ I_E = \int_0^L E(z)dz = \bar{E}L \end{cases} \tag{2.7}$$

Once the traces have been carefully fitted with a parabolic curve defined by equation (2.6) with the proper values of the electric and magnetic field, they should be correctly associated to the correspondent ion species and, if a calibrated detector has been used, the spectrum can be retrieved.

Thomson spectrometers are thus valuable methods to obtain quantitative information on the accelerated ion species and their energy distribution. For this reason in the past decades Thomosn spectrometers have been widely used in laser-plasma experiments and several optimization to the scheme here presented have been designed.
For high-resolution multi-MeV ion detection, it has been proposed the employment of non-parallel electrodes. This guarantees a higher electric field value at the entrance of the spectrometer and a greater opening at the very end so to avoid that deflected ions may hit the electrode plates[128]. In experiments where a high sensitivity is required, for instance when monitoring pB fusion reaction products, a practical solution is to get nearer to the interaction point. This requires a compact spectrometer and a high insensitivity to the electromagnetic noise[96,129] characterizing the target surroundings. Indeed, EMPs can superimpose to the fields in the spectrometer causing oscillating parabolic traces which would hinder a detailed analysis. One main disadvantage in the TS employment is the lack of information about the angular distribution of the incoming ions. One possibility is to have multiple probing points exploiting the same electrodes and magnets using a slit with several pinholes instead of the single-pinhole approach[130].

2.5 Time-Of-Flight technique

The Time-Of-Flight technique (TOF) was first proposed as an upgrade of mass spectrometers[23,24]. This Ion "Velocitron"[23] measured the particle velocity and was based on the measurement of the time needed by a particle to travel through a given

distance. Being the velocity related to the mass and energy of the particle, if the latter are known, the mass is easily retrievable. The very same approach can be applied to compute the energy of a particle of known mass. indeed, TOF has been a widely used diagnostic to characterize the laser-accelerated ion beams since the first observations[131].
As shown in Figure 2.7, the time-resolved signal produced by radiation and particle collection usually presents a broad ion contribution preceded by a narrower peak. The latter is generated by the detection of X-rays, ultraviolet radiation and fast electrons emitted at the interaction instant and is referred as *photopeak*. According to the specific interaction regime and experimental conditions, the amplitude of the photopeak and that of the ion signal can differ for orders of magnitude. TOF signals are thus intrinsically characterized by a high-dynamic range and require detection techniques suitable to appreciate the whole of it. Indeed, to retrieve the ion energy, both the temporal position of the photopeak and of the ion signal are needed. For a given distance d_{TOF} between the ion source and the detector, the time of flight t_{TOF} can be estimated using as absolute time reference the photopeak detection time t_{ph}.

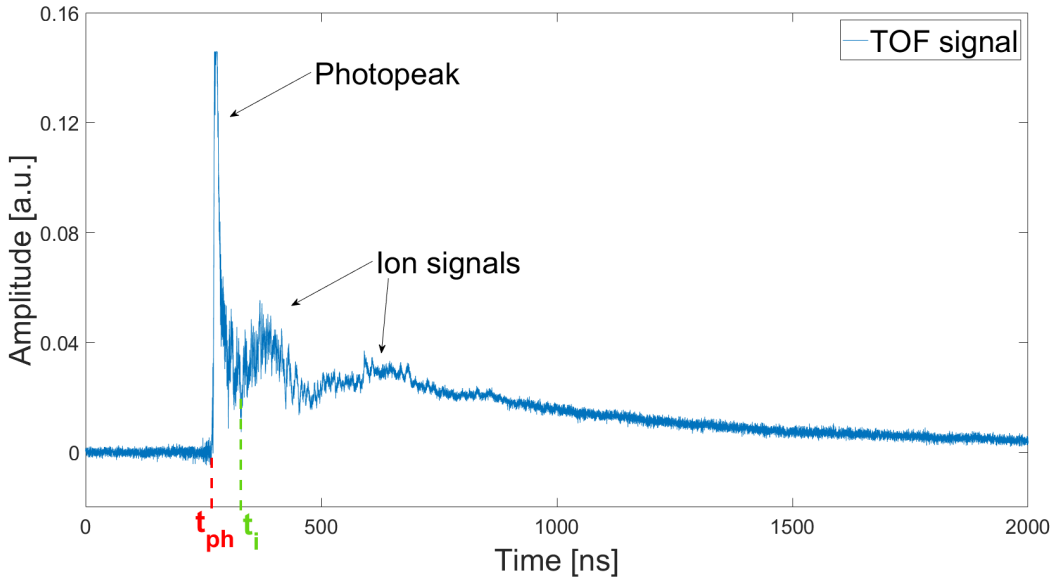

Figure 2.7. A typical signal collected performing time of flight measurements. The first peak is the photopeak, its width is determined mainly by UV and slow-electrons contribution. At later times the ion signal contribution is visible.

Being c the speed of light, the time needed for photons to reach the detector is given by d_{TOF}/c and the interaction instant can be retrieved as $t_{start} = t_{ph} - d_{TOF}/c$. The time needed by a certain particle to cross the same distance can thus be written as:

$$t_{TOF} = t_i - \left(t_{ph} - \frac{d_{TOF}}{c}\right) \tag{2.8}$$

where t_i is the particle detection time. From this, for ions of known species, it is possible to obtain the kinetic energy $E_i = m_i\,(\gamma - 1)\;\; c^2$ where m_i is the detected

ion rest mass and γ is the relativistic parameter given by:

$$\gamma = \left(1 - \beta^2\right)^{-1/2} = \left(1 - \frac{{d_{TOF}}^2}{c^2 \left(t_{TOF}\right)^2}\right)^{-1/2} \tag{2.9}$$

For the investigated regime, the previous equation can be simplified. Indeed for ion energies in the range of 0.1-100 MeV, the relativistic correction can be neglected and the classical expression for the kinetic energy can be used.

In order to fully profit of the benefits that TOF technique can offer, it is necessary to use some caution to manage the contribution to the signal provided by the electrons impinging onto the detector. It is possible to make a distinction among fast and slow electrons which will affect the measurement in two different manners. The contribution of fast electrons is going to be overlapped to the photopeak signal and thus will have a negligible effect on the characterization of the ions. On the other hand, slow electrons are co-propagating with ions and thus can have time-of-flight equal, or similar, to that of ions. They can thus hinder the precise measurement of the minimum TOF of the ions, i.e. the ions having maximum energy, and also cause an overestimation of their number. This effect is more severe when electrostatic detectors are used, whereas it is almost negligible when the measurements is performed by means of semiconductor detectors. Indeed, as will be discussed in the following sections, the semiconductor detectors produce a signal whose amplitude is proportional to the amount of energy deposited inside it. Therefore, the contribution of one electron that is co-propagating with one ion, thus having an energy order of magnitudes lower than the ion, will give a negligible effect on the final signal amplitude. Since in common laser-driven acceleration scenario the amount of electrons reaching the detector is comparable to the amount of ions, the contribution of slow electrons to the signal can be neglected.
In any case, this issue can be treated by means of small permanent magnets which bend the electrons trajectory so to not intercept the detector surface, or applying a thin filter, usually an aluminum foil, which cuts the contribution of UV radiation and slow electrons. The filter application can also be useful to isolate the protons signal from that of heavier ions. TOF technique on its own does not distinguish among the contribution of different charge-states or ion types. The filter application can help to cut the slower ions which would otherwise be superimposed to the proton signal.
By means of the aforementioned methods, and by using a detector whose response to ion exposition is well known, it is possible to exploit the TOF technique to retrieve the proton calibrated spectrum[132–134]. To this purpose, over the years several detectors were used in the time-of-flight scheme. They can be grouped in three categories according to the detection principle: electrostatic detectors[135], scintillators coupled with vacuum phototubes[136] and semiconductor detectors[135].

2.5.1 Electrostatic detectors

Within the electrostatic detectors group, the Faraday cups are those more commonly used in TOF measurements. They consist in a conductive cup designed to collect

ions: when charged particles impinge on the metallic surface, this gains a small net charge generating a current which can be measured.
The separation between ion and electron components is usually provided by a static electric field applied between the grounded entrance grid and the biased collector or between the entrance grid and a control biased grid[131], depending on the specific detector design as shown in Figure 2.8.

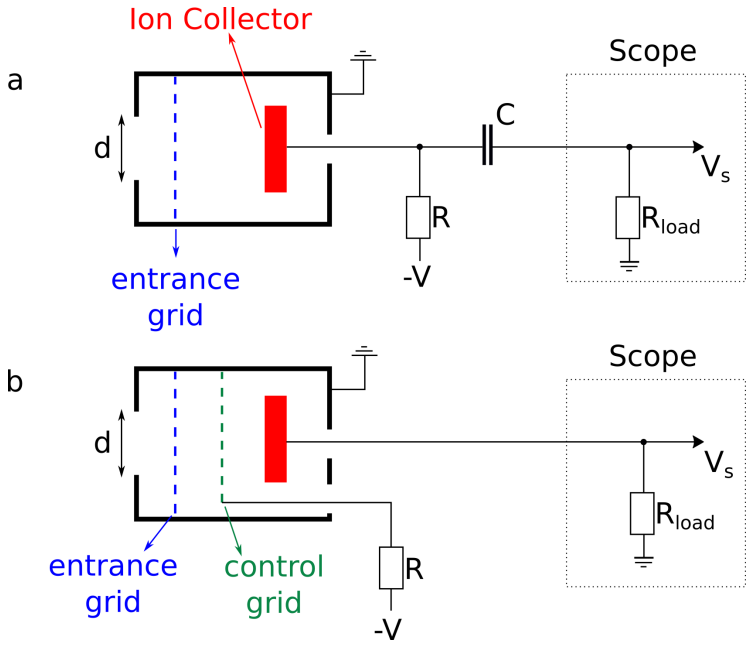

Figure 2.8. Two different designs for charge collectors usually adopted in TOF measurements. The two differ for the item devoted to the electron and ion component separation: in (a) the electric field arises from the biased ion collector and the grounded entrance grid; in (b) the electrostatic field is generated between the grounded entrance grid and the biased control grid.

When ions reach the collector, they can also produce a secondary electron emission. If this contribution is not suppressed by any other means, it has to be properly taken into account when estimating the number of ions impinging on the detector. Indeed, the current signal of the collector I_c will be produced by the combination of the ion current I_i and the secondary electron current I_e, namely[131]:

$$I_c = I_i + I_e = q_e \epsilon v S \sum_{j=0}^{z_{max}} [z_j(t) + \gamma_j(t)] n_{i,j}(t) \tag{2.10}$$

where ϵ is the transparency of the entrance grid, v is the plasma velocity, S the area of the entrance pin-hole, γ_j, z_j and $n_{i,j}$ are the secondary ion-electron emission coefficient, the charge state and the ion density of the j-th ion species respectively. At a given moment, the ion current in the entrance grid I_i can be written as[131]:

$$I_i(t) = \frac{V(t)}{\epsilon R_{load}(1 + \bar{\gamma}(t)/\bar{z}(t))} = \frac{dQ}{dt} = q_e \frac{d[N(t)\bar{z}(t)]}{dt} \tag{2.11}$$

where $V(t)$ is the voltage amplitude of the collector, $\bar{\gamma}(t)$ is the average secondary io-electron emission coefficient, $\bar{z}(t)$ is the average charge state of ions, $N(t)$ the number of ions and R_{load} is the load resistance. Once that all the contribution are properly considered it is therefore possible to retrieve the expression for the time distribution of ion charge[131].
The time resolved signal provided by these detectors operated in time-of-flight scheme allows to reconstruct the energy distribution of the impinging particles exploiting the previous relations. Moreover, if their charge state is known, the total number of impinging particles in the unit time can be also retrieved from the measurement of the generated current.
Given the properties of the just described electrostatic detectors, they results particularly suitable when dealing with high fluxes of low-energy ions. Indeed the amplitude of the generated signal will be proportional to the charge of the detected particle regardless its energy.

2.5.2 Scintillators coupled with vacuum tubes

A plastic scintillator is here used to convert the incoming ions in fluorescence light that can be detected by a photo multiplier tube operated in current mode and linked to a fast oscilloscope. A schematic representation of the detection system is given in Figure 2.9 together with a typical TOF signal acquired with this kind of detectors. An aluminum filter is employed to reduce the amount of both scattered laser light and UV radiation impinging on the scintillators and causing an unwanted background signal which gives a threshold on minimum ion energy. From the time-resolved signal it is possible to retrieve the ion energy following the argument previously discussed. The energy resolution is linked to the temporal resolution of the detection system, which is given by the slower response among the scintillating time ($\sim 1-3$ ns depending on the scintillator used) and the photo-multiplication tube temporal response that can reach values ≤ 1 ns.
The number of particles for each energy interval can also be computed if the energy dependent response curve of the whole detection system (Filter + scintillator + PMT) is known. It can be determined by exposing the system to particles of controlled flux, type and energy produced by a conventional particle accelerator. This detection system is usually characterized by a high efficiency, thus it would be suitable even for low-fluxes of particles characterized by moderate-low energies. Indeed, in this case a PMT with a high amplification value is preferred at expenses of temporal resolution. Nevertheless, there are some limitation both on the maximum amplification value that is possible to use (in order to avoid the PMT saturation due to the photopeak detection) and on the minimum detectable particle energy. Indeed, since it is necessary to limit the contribution given by the visible light emitted during laser-matter interaction as well as to prevent the amplification of any scattered laser light, a proper filter has to be placed before the scintillator, limiting the minimum proton energies that are able to reach the detection system[136,137].

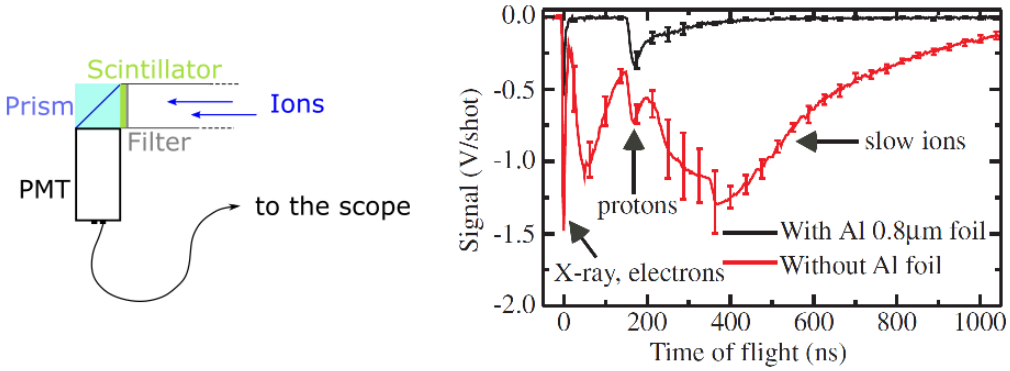

Figure 2.9. Experimental set up for a TOF line equipped with a plastic scintillator coupled with a photomultiplier tube and the acquired signal when no filter is placed in front of the scintillator (red) compared to the one collected with the employment of a filter to cut UV contribution (black). From *Nakamura et al.*[136].

2.5.3 Semiconductor detectors

Charged particles, impinging on a semiconductor detector surface, penetrate inside the material creating electron-holes pairs. These pairs, in presence of an external electric field, move apart one from the other, generating a current that can be measured. The intensity of this signal is proportional to the amount of energy lost inside the material. The charge generated by N_i particles of energy E_i impinging on this type of detector is[132]:

$$Q_i = N_i \frac{q_e E_i}{\epsilon_g} \tag{2.12}$$

where q_e is the electronic charge and ϵ_g is the average energy needed to create a free electron hole pair inside the detector in use (13.1 eV for diamond detectors[138], 7.7 eV for Silicon Carbide[139], 3.62 eV for Silicon and 2.95 eV for Germanium). When employed in a TOF line, the charge collected by the electrodes generates the time-resolved signal $V(t)$. Given the temporal resolution Δt of the diagnostic system employed for the TOF measurement, it is possible to divide the time axis in a series of consecutive intervals having width equal to Δt. For each temporal interval $(t_i, t_{i+1} = t_i + \Delta t)$, associated to a specific energy range (E_i, E_{i+1}), it is possible to estimate the number of impinging particles:

$$N_i = \frac{Q_i \epsilon_g}{\bar{E}_i q_e} \tag{2.13}$$

where $\bar{E}_i = \sqrt{E_i E_{i+1}}$ is the average energy associated to the interval and the measured charge Q_i is given by:

$$Q_i = \int_{t_i}^{t_{i+1}} I(t)dt = \int_{t_i}^{t_{i+1}} \frac{V(t)}{R} dt \tag{2.14}$$

with $V(t)$ the measured signal amplitude and R the impedance of the acquiring system.
Semiconductor detectors results thus particulary suitable for the characterization of

fast-ions. Moreover, since their response is proportional to the amount of energy deposited inside their bulk by the incoming ion, they can provide high signal also for low-fluxes of energetic particles.

Despite the Time-Of-Flight technique does not provide an intrinsic angular distribution, the compactness of the system equipped with semiconductor detectors or Faraday cups may allow to place several TOF lines even within a small solid angle, thus allowing to retrieve information on the spatial distribution of the emitted particles.

2.6 The requirements for a diagnostic ideal for ion detection in laser-plasma experiments

It is useful to list the requirements that an ideal diagnostic has to satisfy for being fruitfully employed in the characterization of laser-accelerated ion beams.
In the previous chapter, it was shown that these beams have characteristic spatial and energy distributions that can be useful to identify the different acceleration mechanisms taking place during the interaction. The ideal diagnostic system should thus be able to provide reliable information regarding both the spectra of the emitted particles and their angular distribution. Moreover, the aforementioned applications often require to work accumulating multiple shots (i.e. Ion Beam Analysis) and to have an on-line accurate characterization of the emitted ion beams (i.e. medical applications). Both these requirements call for diagnostics able to work at high repetition rate and to provide prompt beam characterization.
To identify the diagnostics that could be promising candidates to better suit all these requirements, it is useful to resume all the main characteristics of the discussed systems. Their dynamic range, spatial and temporal resolution are reported in Table 2.1. The minimum time needed to retrieve the raw data collected by each diagnostic is also reported there. In Table 2.2 all the mentioned requirements for an ideal diagnostic system for ion detection in laser-plasma experiments are listed and for each of them is shown which diagnostic is able to satisfy it.
TOF technique seems to be promising for employment as on-line diagnostic system able to provide prompt information about the laser-plasma interaction. It also allows to retrieve the spectra of the detected particles and results to be very handy especially if used with compact detectors.
Nevertheless, to fulfill all the mentioned tasks while working at high repetition rate, it is necessary to develop a methodology for data acquisition and analysis able to cope with the presence of strong electromagnetic pulses while ensuring an high dynamic range and the possibility to retrieve a calibrated proton spectrum. To properly address these problems it was necessary to perform a detailed analysis of all the different steps from the signal acquisition to the spectrum computation.

It is possible to identify three main knots characterizing the whole technique:

1. Signal acquisition;

2. Detector knowledge and detailed characterization;

Table 2.1. The performance of each discussed diagnostic technique is resumed here in terms of dynamic range, spatial resolution, temporal resolution and the time needed to retrieve the data. The reported values are intended for the best possible performance nowadays available. In the case of RCF and IP is indicated the spatial resolution achievable with an ideal scanner, between brackets instead is given the value for existing scanners). RCF = Radiochromic Film; IP = Imaging Plate; SSNTD = Solid State Nuclear Track Detector, NA = Nuclear Activation; TS = Thomson Spectrometer, TOF = Time-Of-Flight.

	Dynamic Range [dB]	Spatial Resolution [μm]	Temporal Resolution	Data Availability
RCF	~ 50	2.5 (10)	No	24 h
IP	~ 80	10 (25)	No	1-2 h
SSNTD	~ 120	5	No	1-12 h
NA	> 100	$<$ mm	No	up to few hours
TS passive	~ 80	10	No	1 - 24 h
TS active	~ 45	25	hundreds ns	$\sim$ ms
TOF	~ 70	No	< 1 ns	$\sim$ ms

Table 2.2. Requirements for an ideal diagnostic system for ion detection in laser-plasma experiments and existing diagnostic systems capabilities

	RCF	IP	SSNTD	TS passive	TS active	TOF	NA
Angular distribution	✓	✓	✓	✗	✗	?	✓
Maximum Energy	✓	✓	✓	✓	✓	✓	✓
spectra reconstruction	✓	✓	✓	✓	✓	✓	✓
High repetion rate	✗	✗	✗	✗	✓	✓	✗
EMP resistant	✓	✓	✓	✓	✗	?	✓

3. Signals analysis.

1. Signal acquisition The signal has to be acquired providing high-dynamic range, necessary to appreciate with a good precision the position of the photopeak without loosing the information on the emitted particles. The diagnostic set up (TOF line, detector and acquisition system) has to be arranged to avoid electromagnetic pulses coupling to the system itself.

2. Detector knowledge and detailed characterization. The characteristic behavior of the chosen detector has to be known in terms of signal generation and response for each particle type and energy to be detected in the experiment.

3. Signals analysis. Once the signal has been acquired, it has to be processed taking into account several factors. Indeed, the system set-up, in particular the transmission line, can have a non negligible influence on the original signal. Eventually, the time domain signal can be converted in an energy distribution of impinging particles and then to their spectrum thanks to the detector characterization.

The detailed discussion of these three points is given in the following chapters.

First of all, in Chapter 3, the properties of semiconductor detectors are briefly reviewed and the characterization of the chosen diamond detectors is provided. This is followed by Chapter 4 where the implementation of a new methodology allows to enhance the dynamic range of the measurement. The difficulties related to the presence of strong electromagnetic noise pollution are also discussed and addressed by means of an accurate set up which allows to obtain clean signals even in facilities characterized by a very high level of EMPs. In the Chapter it is also presented a novel procedure used to retrieve the proton number by taking into account the detector response.

Chapter 3

Diamond detectors for TOF

In Chapter 2 it has been shown how Time-of-Flight measurements can be performed with three kinds of detectors: electrostatic detectors, scintillators coupled with photo-multiplying tubes and semiconductor detectors. For both the electrostatic detectors and semiconductor detectors it was briefly presented how it is possible to retrieve the number of particles generating the signal so to reconstruct the spectrum. The aim of this chapter is to provide a brief overview of the available semiconductor detectors, focusing on the properties of the Chemical Vapor Deposition (CVD) diamond detectors which are those employed in the experimental activity of this doctoral thesis. In Section 3.1 the working principle of semiconductor detectors is reviewed and the main parameters are compared for the different available detectors based on germanium, silicium, silicium carbide, gallium arsenide and CVD diamond. A good knowledge of the detector characteristics affects the spectrum computation both for the energy and for the particles number estimation. Then, in Section 3.2 and 3.3 a complete characterization of the detectors employed in the experiments carried out during this PhD course is presented. The results obtained in this chapter will be fundamental to analyze the data collected in the different experimental campaigns and later described in Chapter 5.

3.1 Semiconductor detectors

The mechanism leading to a signal production when an energetic particle is revealed by a semiconductor detector is schematized in Figure 3.1 and can be described with two subsequent phases[140]:

1. Through the interaction with bound electrons, the impinging particle releases its energy into the bulk of the semiconductor-based device leading to the generation of free electrons and lattice vacancies (holes).

2. Under the action of a suitable external electric field, the produced electrons and holes move apart one from the other towards the electrodes where they can be collected. If not enough voltage is applied, the generated electron-hole pairs quickly recombine without contributing to the signal generation.

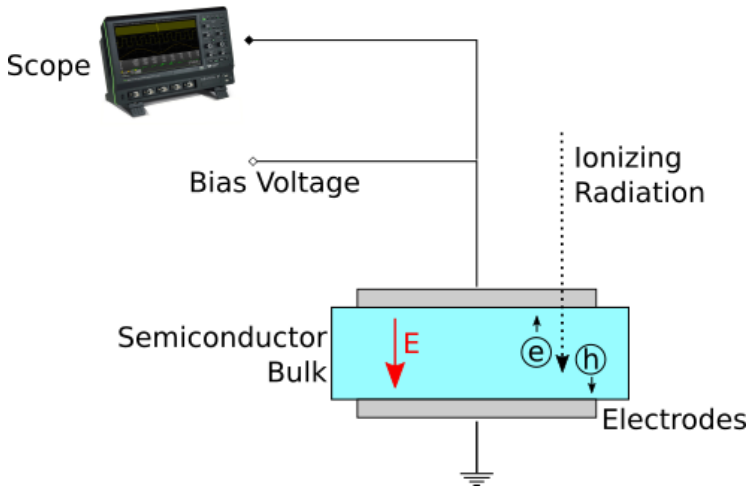

Figure 3.1. Schematic representation of the signal generation process inside a semiconductor-based particle detector.

Both these processes depend on specific characteristics of the semiconductor in use[141]:

1. When an energetic particle enters into a semiconductor crystal and is completely stopped inside it, the amount of generated free electron-hole pairs is independent from the nature of the impinging particle and depends solely on its energy[142].
   In particular, for a given particle energy, the number of produced electron-hole pairs is determined by the radiation-ionization-energy ϵ_g. The latter is peculiar of the specific semiconductor in use and it is strongly related to the band-structure of the material[143].
   Similarly to insulators, semiconductor materials are characterized by a set of forbidden energy levels separating the valence and the conduction band[141]. The presence of this energy gap, known also as band-gap, does not allow the charges to move freely around the lattice. On the contrary, in conductors the band structure does not include any gap[141]. The main difference between insulators and semiconductors relies on the width of the energy gap E_g. Insulators present band-gaps larger than 10 eV whereas semiconductors are usually characterized by band-gaps of few eV[141], as shown in Table 3.1.
   This difference implies that in semiconductor materials electrons are more easily excited from the valence band to the conduction band with respect to insulators. Indeed, the minimum energy required to induce the electron excitation is given by E_g. Nevertheless, the excited state is meta-stable, hence if no additional energy is provided to the excited electrons, they will soon recombine with the holes created in the valence band, releasing the surplus of energy via photon emission or phonon excitation[141].
   The process leading to the effective production of an e-h pair is more complex than the bare electron excitation and includes other phenomena which have to be taken into account in the energy balance[142]. In a simple model described by *Shocley et al.*[142] three main energy consumption processes taking place

during the ionization and leading to the final pair production are identified, as described below.
The excitation of electrons requires an energy E_g. Before the ionization happens, a portion of energy is converted into lattice vibration exciting phonons and eventually the produced pair must account for a certain kinetic energy. In a first approximation, the radiation-ionization-energy must thus take all these processes into account. As proven from various measurements[144], ϵ_g will have a value sensibly greater than the band-gap energy to which is related both from theoretical consideration[142,145] and empirical models[143]. This is also highlighted in the values reported in Table 3.1.

Table 3.1. Main characteristic parameters of the commonly-used semiconductors for particle detection at room temperature[138,146]. In the case of diamond, the values of electron and holes mobility are intended for a single crystal CVD-diamond.

	Ge	Si	GaAS	4H-SiC	diamond
Bandgap (eV)	0.66	1.126	1.43	3.26	5.45
e-h pair generation energy ϵ_g (eV)	2.96	3.67	4.18	7.8	13.1
Electron mobility μ_e (cm^2/Vs)	3900	1500	8500	1000	2200
Hole mobility μ_h (cm^2/Vs)	1900	450	400	50	1600
Saturation velocity (10^7 cm/s)	0.6	1	1.2	2	2.7
Relative dielectric constant ϵ_r	16	11.9	13.1	10	5.5
Breakdown field (MV/cm)	0.1	0.3	0.4	2	10

2. Once generated, the electron-hole pairs have to travel towards the electrodes to be collected and to propagate their signal. The force moving the electrons and holes is provided by an applied external electric field.
In a first approximation, the relationship between the charge carriers drift velocity v_d and the applied electric field $\mathcal{E}$ is given by $v_d = \mu_{e,h}\mathcal{E}$ where $\mu_{e,h}$ is the carrier mobility, which in general is different for electrons and holes[140,147]. This relation holds for moderate values of the applied electric field, up to $\sim 5 \times 10^4$ V m^{-1}. Up to this value, the drift velocity can thus be increased in an almost linear trend by increasing the applied electric field. Then, the carrier mobility starts to decrease due to the growth of scattering events between the charge carriers and the crystal lattice[148].This effect limits the maximum achievable drift velocity to a certain value called "saturation velocity" v_s[138].
The dependence of the charge carrier drift velocity on the applied electric field has been proven to be well described by the relation[138]:

$$v_d = \frac{\mu_{e,h}\mathcal{E}}{1 + \frac{\mu_{e,h}\mathcal{E}}{v_s}} \tag{3.1}$$

In the majority of semiconductors, the saturation velocity is usually reached for values of the electric field $\sim 10^6$ V m^{-1} and it has values of the order of 10^7 cm s^{-1}. The drift velocity, together with the detector active layer thickness, contributes to determine the minimum collection time.
Concerning the amplitude of the generated signal, another effect to take into

account is that not the whole produced charge is always collected by the electrodes. Indeed, recombination and trapping processes can lead to the loss of a portion of it. These effects are quantified by the charge collection efficiency (CCE) which depends on the detector material and also on the electrodes geometry. Therefore it has to be determined for the specific detector in use.

The first materials to be investigated for being applied as semiconductor particle detectors were silicium and germanium, soon after followed by gallium arsenide. Due to their quite small band-gap, they are sensitive to thermal noise and, if employed in laser-plasma experiments, their operation for detecting ionizing radiation is hindered by the remarkable level of visible radiation emitted during the interaction.
In more recent years, technology advancements allowed to produce sensors based on wide band gap semiconductors such as silicon carbide and diamonds.
Compared to regular semiconductors, the wider band-gaps give a better signal-to-noise ratio. Moreover, their saturation velocity is sensibly higher, as well as the breakdown electric field, allowing to work with higher values of applied voltage. Their strong chemical bonds allow them to tolerate high radiation flux doses without considerable degradation of their properties, making them particularly suitable for manufacturing detectors to monitor ionizing radiation[138].
In Table 3.1 the interesting parameters for the commonly-used semiconductors employed for particle detectors are reported.

During the experimental work of this thesis, measurements were performed with CVD diamond detectors. The choice arises mainly from the physical properties of this type of diamond which results particularly suitable for the application in laser-plasma environments and provides some improvement even in comparison with those of the silicon carbide (SiC), which already allows to obtain advanced detectors[146].
In fact, with respect to the latter, diamond has a wider band gap (5.5 eV versus 3.2 eV) providing a further lower sensitivity to incoming soft X-rays that can saturate the detector and hinder ions detection.
The wider band-gap also allows to design detectors with lower sensibility to thermal noise providing a higher signal-to-noise ratio and allowing their employment at room temperature.
The lower dielectric constant (5.7 vs 10) yields a smaller capacitance in transverse geometry which leads to better noise performances.
Diamonds have also a higher breakdown field ($\simeq$ 10 MV/cm versus $\simeq$ 2 MV/cm), which allows them to be operated with higher internal electric field. Eventually, diamonds present also a slightly higher saturation velocity of charge carriers $\simeq 2.7 \times 10^7$ cm/s versus $\simeq 2 \times 10^7$ resulting in a faster temporal response[138,146].
For all the mentioned reasons the performance of diamond detectors is expected to be comparable, and in some cases better, to that of the SiC detectors.
On the other hand, SiC detectors are superior in terms of production costs. Indeed during the fabrication process of diamond detectors, the wafer used as substrate has limited dimensions (ranging from 3×3 mm^2 to 5×5 mm^2); each detector has thus to be produced singularly. On the contrary, it is possible to use wider SiC wafers that are going to be cut later on to obtain multiple detectors in one production

process. This sensibly lowers the overall production costs of the latter that result to be cheaper with respect to CVD diamond detectors.

In the following sections a detailed characterization of the CVD diamond detectors used in the experimental activity performed during this PhD thesis is presented. Both single crystal and polycrystalline structures have been used and in the following the main differences among them will be highlighted.

3.2 Single crystal diamond detectors

The very high purity and crystalline quality of homoepitaxial single crystal diamonds guarantees a considerably high value of carrier mobility and charge collection efficiency (CCE).
The synthetic single-crystal diamonds employed in the experiments performed during this thesis project were designed and fabricated at Tor Vergata University. They consist of 50 μm thick layer, grown by microwave enhanced plasma chemical vapor deposition technique on a commercial low-cost High Pressure High Temperature (HPHT) substrate, with dimension $4 \times 4 \times 0.5$ mm^3.
Two types of diamond detectors, having different electrode layout, were used. The sandwich configuration (SC in the following), shown in Figure 3.2.a, has the intrinsic diamond enclosed between a 100 nm thick metal contact made of Cr (2.1×2.1 mm) and a layer of heavy boron-doped diamond used as backing contact. This layout provides an almost constant CCE throughout all the 50 μm thickness of the detector[149].
The interdigital electrode configuration (IEC), shown in Figure 3.2.b, has superficial Cr contacts of 50 nm thickness and 20 μm width with a spacing of 20 μm, fabricated by standard photolithography technique[150]. In this case, despite the thickness of 50 μm of the intrinsic diamond, the region where the charges are efficiently collected is limited to a shallow layer by the superficial positioning of the electrodes. Therefore, the CCE of the interdigit diamond detector has a maximum value for all those low-energy radiation and particles completely stopped near its surface and will start to decrease for more penetrant ones[151].
The IEC shows also an improvement in the time response velocity of charge collection also thanks to the very low capacitance[152] and for low-energy particles this leads to better temporal resolution than the SC configuration.
Both the detectors were mounted in ad-hoc holders designed for shielding the electric connections from EMPs, as shown in Figure 3.2.

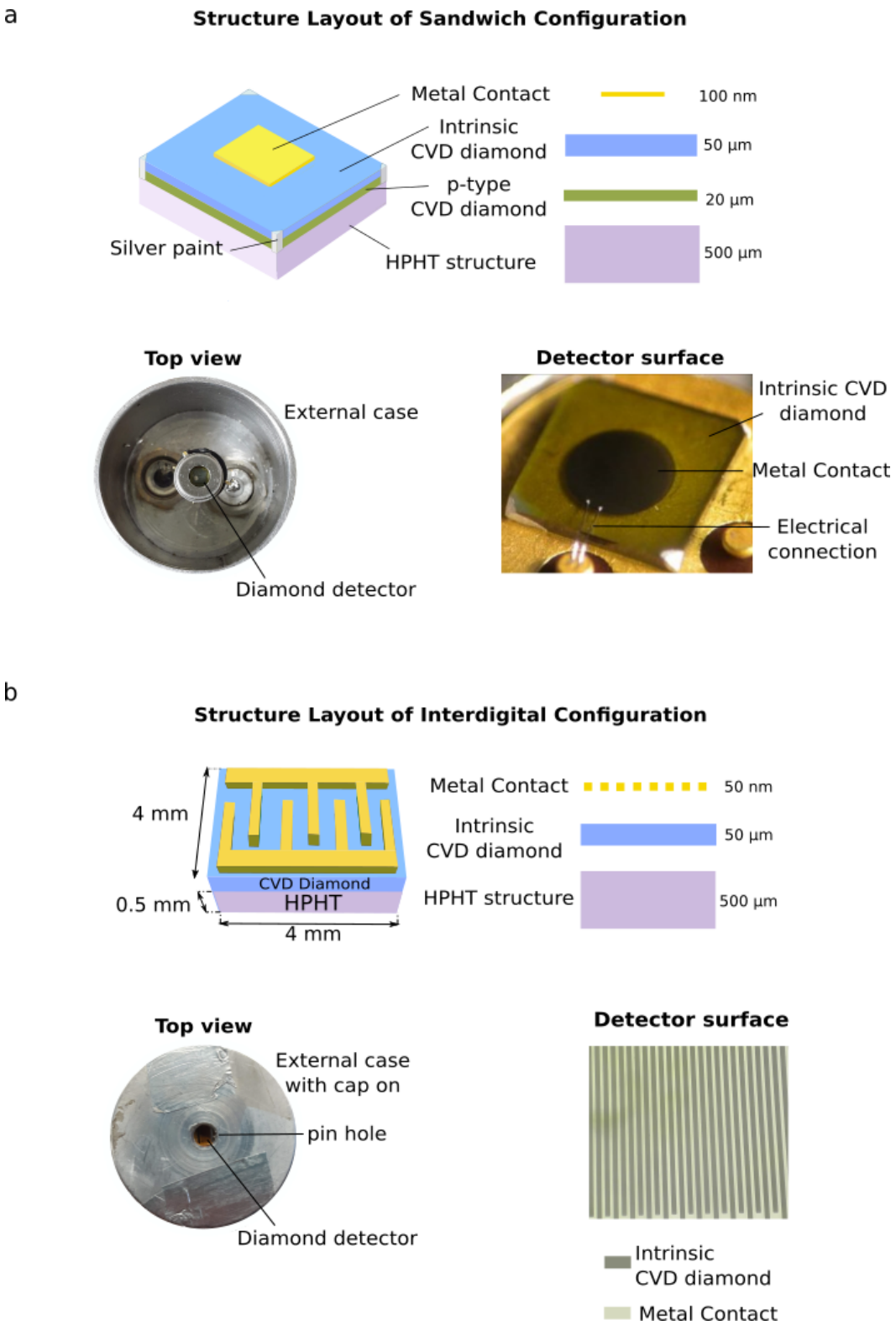

Figure 3.2. The two types of single crystal diamonds used in the experiments: (a) a schematic representation of the diamond with electrodes in sandwich configuration (SC) and under this scheme a picture of the SC detector mounted in the holder without the protective cap and an example of the detector surface in the SC configuration. (b) The layout of the interdigital configuration (IEC) and below the IEC detector mounted in the holder with the protective cap and an example of the detector surface in the IEC configuration.

3.2.1 Detector characterization

The complete detector devices were preliminary tested by exposing them, under vacuum, to the 5.486 MeV α particles produced by a radioactive ^{241}Am source. This allowed to retrieve information about the detector temporal response and efficiency. The CCE is defined as the ratio between the collected charge Q and the charge Q_0 generated inside the detector due to the incoming radiation. When α particles pass through the sensitive volume of the detector, their energy is deposited into it. As previously explained, the energy necessary to generate a free electron-hole pair is determined by the radiation-ionization-energy ϵ_g, which for diamonds is equal to 13.1 eV[144]. Thus, a particle of $E = 5.486$ MeV, depositing all its energy in the detector, generates a total charge $Q_0 = \frac{eE}{\epsilon_g} = \frac{eE}{13.1} = 6.7 \times 10^{-14}$ C inside it. By measuring the effective charge collected by the detector it is possible to estimate the CCE for α particles collection. Given the peculiar energy deposition of ions in matter[153], the majority of the particle energy is going to be released at a localized depth in the detector, defined by the penetration length of the 5.486 MeV α particle in the diamonds, i.e. at ~ 15 μm from the detector surface.

Temporal response

To appreciate the temporal response by single particle detection, the outputs of the diamond detectors were connected to the biasing fast amplifier DBA-IV (gain $G = 46$ dB, bandwidth = 2.5 GHz) and then to the LECROY 620 Zi scope (bandwidth = 2 GHz, sample rate = 20 GS/s). A scheme of the measurement set-up is shown in Figure 3.3.
The fast amplifier was necessary to bias the detector and also to increase the amplitude of the fast-varying signal to levels detectable by the scope.

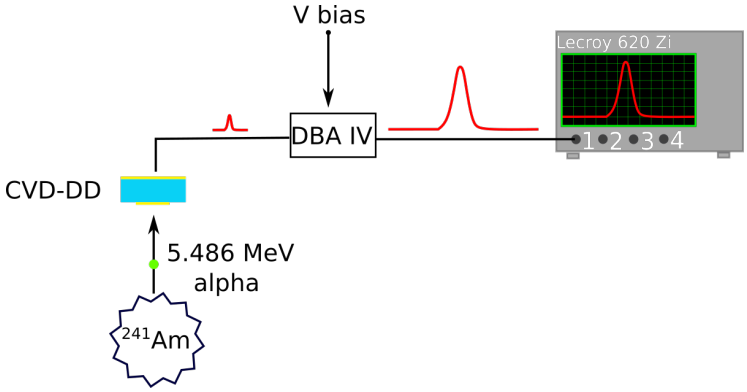

Figure 3.3. The set-up employed for the measurement of the diamond detector temporal response.

The output signals collected by the IEC and the SC detectors are reported in Figure 3.4.a and 3.4.b, respectively. They are obtained by averaging over several acquisitions (i.e. 100 pulses), with both diamonds biased at +150 V.
In order to properly chose the feeding voltage, different measurement sessions where performed one after the other supplying for each an increasing bias to the diamond

detectors. Thanks to this procedure it was possible to evaluate the voltage needed to reach the velocity saturation regime, namely the value of the voltage for which its further increment does not produce neither a growth in the collected charge or an improvement in the temporal response. For the detectors under testing this regime was already achieved with a bias of 50 V.
The collected charge has been retrieved using the relation[132]: $Q_\alpha = \frac{1}{RG}\int_{t_i}^{t_f} V(t)\,dt$, where $R = 50\ \Omega$ is the impedance of the acquisition system, $G = 199.5$ the gain of the amplifier and $V(t)$ the output signal. From the acquired pulses, the full width at half maximum (FWHM), the collected charge (Q_α) and the CCE were then calculated for both the detectors and then reported in Table 3.2.
In particular, a FWHM of about 500 ps is observed, demonstrating a high intrinsic response velocity of both the diamond detectors. The obtained values seem to suggest that both the detectors have comparable time characteristics. Nevertheless it has to be considered that, as previously mentioned, the alpha particles employed for the characterization are stopped at $\sim 15\ \mu$m from the detector surface. In the IEC detector, at this depth, the amplitude of the electric field acting on the charge carriers already started to decrease, leading to a lower drift velocity and thus to a slower temporal response. The response of the SC detector, on the other hand, is constant throughout its thickness. Thus, for low energy particles stopped near the detector surface, the response of the IEC detector can be sensibly higher than the SC one.

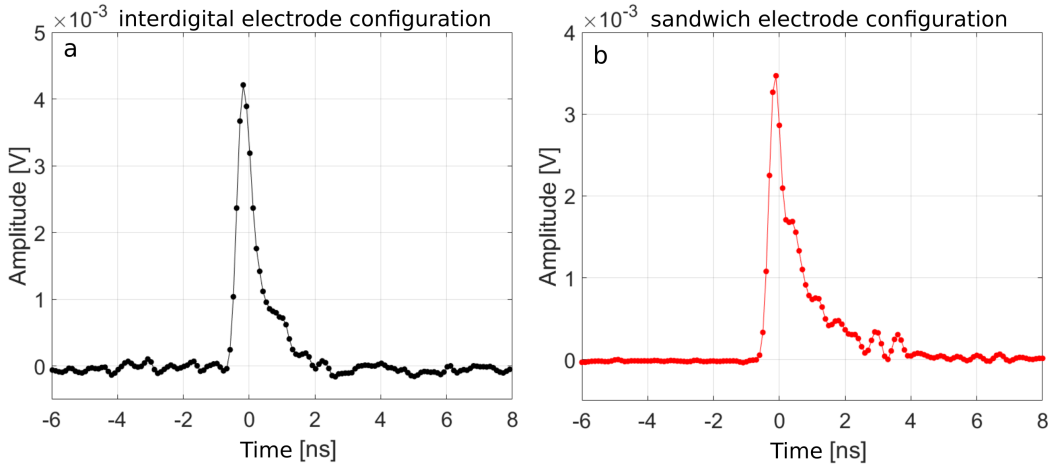

Figure 3.4. Signals obtained exposing the diamond detectors in IEC (a) and in SC (b) configurations to the α particles produced by the americium decay. From these signals the detectors temporal response was estimated by measuring their FWHM and a first estimation of the CCE was obtained by integrating the signals to compute the collected charges.

Charge Collection Efficiency estimation

To refine the estimation of the CCE, an additional measurement was performed. The output signals of the diamonds, generated by exposition to monochromatic α particles, were processed by a conventional charge-sensitive electronic chain shown in

Table 3.2. Estimated values for the temporal response and CCE for the single crystal diamonds both in IEC and SC configuration.

Electrode type	Bias (V)	FWHM (ps)	Q_α (C)	CCE (%)
SC	+150	(460±50)	$(6.6 \pm 0.1)\times10^{-14}$	(98±1)
IEC	+150	(520±50)	$(4.7 \pm 0.3) \times10^{-14}$	(70±4)

Figure 3.5. The output signal was first integrated by a charge sensitive preamplifier (ORTEC 142A). The resulting voltage pulse was sent to a shaping amplifier (ORTEC 671). The gain and the shaping time of the amplifier were fixed to 200 and 6 μs respectively. Finally, a multichannel analyser (MCA) (ORTEC Easy MCA 8k) connected to a computer was employed to obtain a pulse height spectrum (PHS). A scheme of the set-up is shown in Figure 3.5.

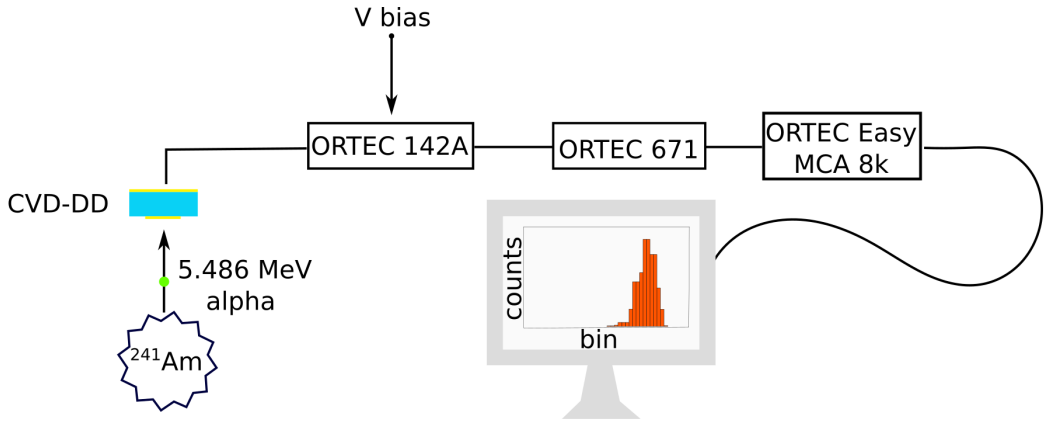

Figure 3.5. The set-up for the measurement of the diamond detector charge collection efficiency employing a calibrated electronic chain to retrieve a pulse height spectrum.

The MCA, operated in the pulse-height-analyzer mode, sorted the input pulses in different bins according to their amplitude. As previously discussed, a particle with a given energy will produce a certain amount of charges inside the detector, defined by the radiation-ionization-energy ϵ_g.
In the case of an ideal detector having 100% CCE all the produced charge would be collected by the electrodes generating a signal of a certain amplitude. Therefore, particles having different energies will produce signals with different amplitudes. In the PHS this will result in a distribution of peaks located at different bins.
What happens in a real detector is that not all the produced charge is going to be collected by the electrodes, due to recombination and trapping processes taking place during the carrier motion. Hence, the amplitude of the output signal will decrease by a certain factor proportional to the CCE. This will result in a shift of the peak in the PHS spectrum with respect to the ideal 100% CCE case which in our measurements has been defined through the calibration of the electronic chain exploiting a well-characterized Si detector.
In Figure 3.6 the PHS obtained after an exposition time of 300 seconds with the detectors biased at +150 V is reported. The estimated CCE is given in Table 3.3

and it is consistent with the one evaluated with the previous method.

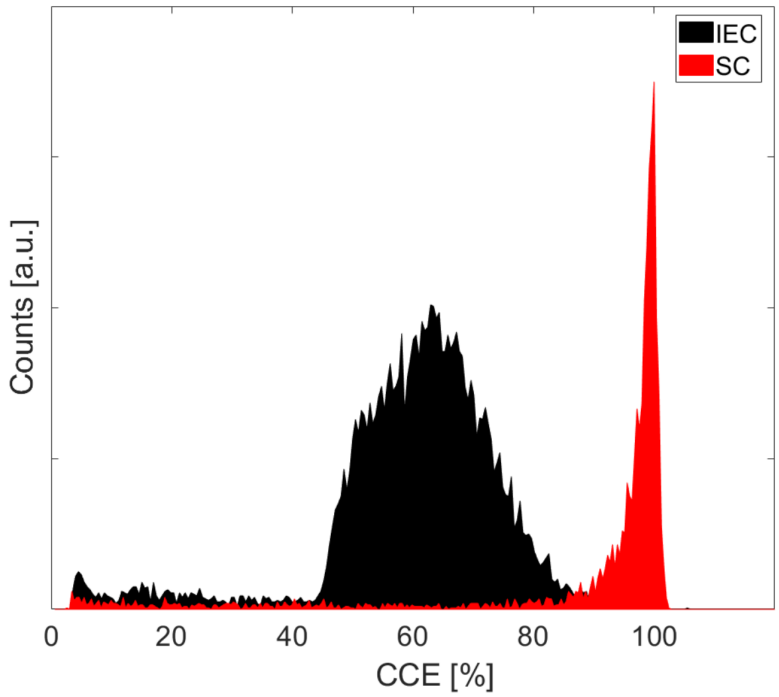

Figure 3.6. Pulse Height Spectrum (PHS) obtained for the diamond detectors in the IEC and SC configuration.

From the obtained PHS it is also possible to retrieve an additional information regarding the intrinsic energy resolution of the two exposed detectors. Indeed, the width of each bin of the MCA is associated to a certain amount of charge which can be set before starting the measurement. In the analyzed case, it was chosen to work with bins of 3×10^{-16} C width.
Ideally, the detection of monochromatic particles should generate a signal only in one of the bins, the height of the peak being dependent on the number of detected events. Clearly, this is not the case of the spectra shown in Figure 3.6 where a distribution of peaks of different height is reported. The obtained signal can be interpreted as follows: as already mentioned the detector was exposed to the americium for a time of 300 s, given the activity of the radioactive sample, this results in the detection of multiples events. Each of these events produces in the detector a certain amount of charges which are then collected according to the detector CCE and should thus produce a single peak located in one bin of the PHS. Nevertheless, it is necessary to take into account another factor which is the homogeneity of the detector response[138]. Charge trapping, statistical fluctuation of the charge generation process, energy loss straggling, inhomogeneity of the film thickness and varying electronic parameters strongly affect the detector response[138]. The amplitude of the output signal can thus be different even for particles having the same energy, causing a widening of the pulse height distribution. In Figure 3.6 this effect is quantitatively evaluated by the PHS spectrum whose FWHM provides information on the energy response.

The performed measurements show that the SC has a sensibly greater energy resolution than the IEC detector, the obtained values for the analyzed detectors are reported in Table 3.3 as uncertainties on the measured CCE. Nevertheless, it is worth

Table 3.3. Characteristic values obtained during the tests performed to measure the charge collection efficiency and the energy resolution of the investigated type of electrode configuration.

Electrode type	Bias (V)	CCE (%)
SC	+150	(99 ± 2)
IEC	+150	(68 ± 18)

to notice that, when these detectors are employed in a TOF scheme, the energy of the impinging particle is retrieved by measuring the time needed by the particle to travel from the source to the detector. The energy resolution of the measurement is thus defined only by the temporal response of the detector and to the length of the TOF line. Therefore, despite the IEC detector showed sensibly lower intrinsic energy resolution than the SC detector, since it has a similar temporal response, it leads to an overall energy resolution comparable to the one of SC when used in TOF technique.
On the other hand, what is affected by the highlighted lower intrinsic energetic resolution, is the particle number estimation. Indeed, equation (2.14) which, for each energy, links the signal amplitude to the number of particles generating it, is based on the assumption that a particle depositing a certain amount of energy E_i in the detector will always trigger a signal of the same amplitude. If this hypothesis falls, which is the case highlighted by the FWHM in the PHS, it means that for the same particle energy E_i it is possible to have a signal amplitude $I \pm \Delta I$ leading to an intrinsic ΔN_i, from equation (2.13), depending on the detector characteristics.

The superficial positioning of the electrodes in the IEC configuration requires a further investigation to properly characterize the detector response in terms of the CCE. Indeed, the applied electric field will not be constant throughout the thickness of the 50 μm diamond but it will decrease with increasing depth.
With the performed characterization, employing alpha particles of 5.486 MeV, the detector response was tested for a particle releasing the majority of its energy at 15 μm from the detector surface. In order to have a detailed estimation of the CCE variation along the thickness of the IEC detector, an additional characterization was carried out by Tor Vergata University at the AN2000 microbeam facility of the National Laboratories of Legnaro (Italy) using proton beams of energy respectively 0.3 MeV, 1 MeV, 1.4 MeV and 2 MeV. The beam was focused to a spot size of ∼5 μm on the sensitive electrodes of diamond. As evaluated by the SRIM Monte Carlo Simulation code[153], the range of protons with the mentioned energies in diamond varies from 1.5 μm to 25 μm.
An electronic chain consisting of a charge-sensitive preamplifier ORTEC142A and an ORTEC572 shaping amplifier was used similarly to what it has been shown in the scheme in Figure 3.5. The calibration of the electronic chain was performed using a precision pulse generator ORTEC419 relating the pulse heights provided by a reference Si detector with those from the diamond device. The CCE of the

detector as a function of the investigated proton energies is reported in Figure 3.7. As expected, for low energy protons, which are stopped near the surface where the

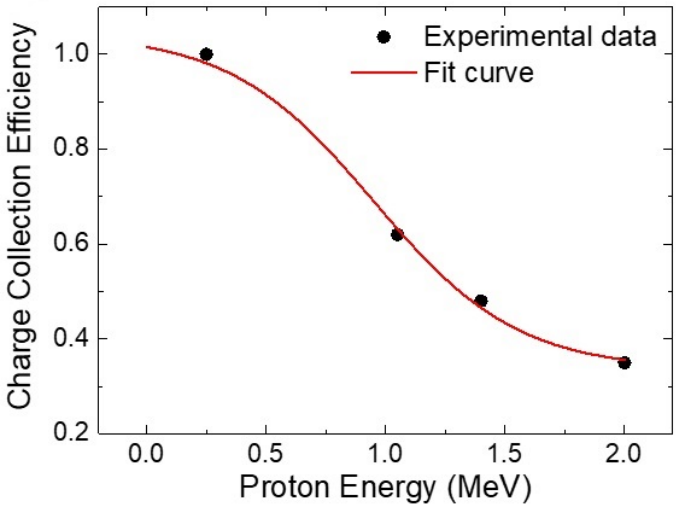

Figure 3.7. Charge Collection Efficiency of the IEC diamond detector as a function of energy. From *Salvadori et al.*[154]

electric field is more intense, the induced charge is practically equal to the generated charge (CCE = 100 %). On the other hand, for protons having higher energies, charges are generated in regions where a weak electric field is present, and therefore the CCE of the detector decreases. The experimental data reported in Figure 3.7.b are well fitted by a non-linear curve having the following expression:

$$\mathrm{CCE}(E_p) = \frac{0.71}{1 + e^{(\frac{E_p - 9.1\times10^5}{3.1\times10^5})}} + 0.33 \tag{3.2}$$

By considering that equal CCE is obtained for other particles having the same range in the detector, from these measurements it is possible to determine the CCE also for other ion species.

Effective area estimation

The effective area of the two single crystal diamonds was estimated with the Ion Beam Induced Charge (IBIC) mapping[155] of the detector surface. The knowledge of the effective area of the detectors is important because it is used to calculate the solid angle covered by detector when employed in experiments. Moreover, the IBIC technique allows also to estimate the intrinsic energy resolution of the detector under investigation which is relevant to understand the uncertainty on the computation of particles number.
The measurements were performed at the Ruđer Bošković Institute (RBI) ion microprobe facility (croatia) and were carried out by the group of Tor Vergata University. The surface of the diamond detectors in the two electrode configurations was irradiated by a raster scanning with a focused 1.5 MeV proton beam (~ 1 μm in diameter), in order to assess the charge collection efficiency with high spatial resolution. For

each scanned point the collected charge was computed and compared with the one generated inside the diamonds, to compute the CCE point-by-point and estimate the effective active surface of the two diamond detectors.
Figure 3.8.a and 3.8.b show the IBIC 2D maps measured over the sensitive surface of the IEC and SC detector, respectively. The color-map refers to the associated estimated CCE.
It is possible to see that the IEC detector shows an inhomogeneous response along the superficial interdigitated contacts. This is highlighted in the IBIC map which shows a periodic structure, where a high CCE (represented by a bright green in Figure 3.8.a) is alternated with a low CCE region (in Figure 3.8 the absence of signal is represented in white). Such behavior can be explained by considering the geometry of the Schottky[156] interdigitated electrodes, which results in the formation of a depletion region underneath the anodes[151]. In particular, the CCE maxima in Figure 3.8.a are measured around the interdigitated electrodes where a positive bias is applied, whereas a smaller CCE (almost zero) contribution is observed at the grounded electrodes.
On the other hand, the SC detector shows a quite uniform sensitivity (highlighted by the uniform light blue in Figure 3.8.b), well contained inside the superficial Schottky Cr contact. Therefore, it is possible to infer that a signal is induced by the drift of charge carriers in the depletion region below the Cr electrode, whereas free carriers generated elsewhere do not induce detectable signals.
From these IBIC measurements, the effective area of the IEC detector results to be approximately 2 mm^2 whereas that of SC about 4.5 mm^2, i.e. almost the whole Cr electrode size.

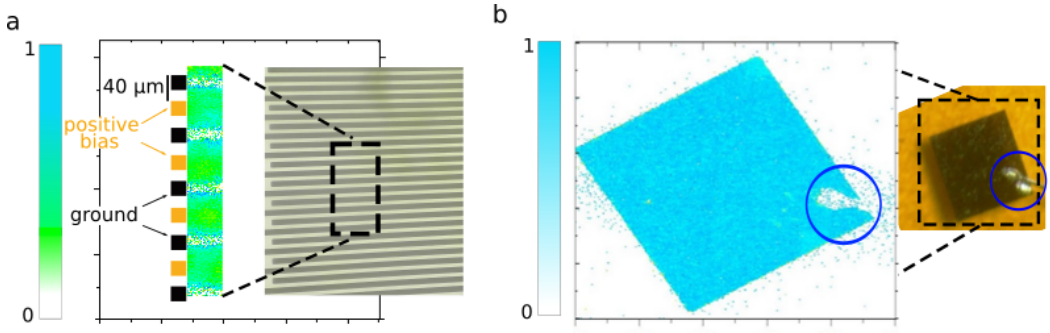

Figure 3.8. (a) IBIC mapping of a portion of the IEC detector surface. Bright green stands for a high CCE whereas the zero signal is represented by white regions. The black and orange squares indicate the corresponding position of the electrodes on the detector surface. (b) IBIC mapping of the SC detector surface, an area of 500 μm $\times$ 500 μm was scanned so to include the whole Cr electrode and a portion of the surrounding diamond surface. The light blue indicates region of high CCE whereas white stands for absence of signal. From *Verona et al.*[157]

3.3 Large area polycrystalline diamond detector

A polycrystalline diamond is made of many small crystal grains randomly oriented. The size of these grains depends on various factors as the synthesis conditions, the type of substrate and the layer thickness. According to the grain size, the diamonds can be classified as ultra-nano-crystalline (grain size < 10 nm), nano-crystalline (10-50 nm) or micro-crystalline (< 500 μm).
The boundaries between these grains act as scattering centers limiting the carrier mobility as well as the charge collection efficiency[138,158]. Thus detectors based on polycrystalline structure will be characterized by lower temporal resolution, which will reduce the energy resolution in TOF measurements. On the other hand, they are the only solution if detectors with large areas are needed for instance to cover a larger solid angle.
The polycrystalline detector used in the experiments carried out during this PhD thesis was a type IIa-electronic grade polycrystalline diamond, i.e. a diamond characterized by a very low concentration of impurities (less than 5 ppm) mainly represented by nitrogen and engineered for large area passive detectors. Among the diamond detectors at our disposal it has indeed the largest surface. It presents a 15×15 mm area for a thickness of 150 μm.
To exploit the full thickness of the deposited diamond, electrodes were mounted in a sandwich configuration as shown in Figure 3.9.a. This allowed to collect the charges generated throughout the whole body of the detector with an almost constant charge collection efficiency, so to effectively detect protons up to 5.8 MeV, fully stopped inside the detector active layer as derived from SRIM simulations[153].
The wafer was then placed in an ad-hoc holder made in stainless steel, shown in Figure 3.9.b, with electrical connection properly shielded for being operated in environments with high EMP levels.
The holder is designed to allow the positioning of two grids mounted parallel to each other and to the diamond. The separation between the two grids is of 40 mm as well as the separation between the second grid and the diamond. The first grid can be biased and isolated from the rest of the structure through a thermoplastic support. The second internal grid, aligned with the first one, is directly connected to the ground of the structure.
As discussed for the Faraday cups in Chapter 2, these two grids provide a static electric field which is useful to separate the electron component from the ionic one.

3.3.1 Detector characterization

Similarly to the previous case, the polycrystalline diamond was characterized by exposition to the 5.486 MeV α particles emitted by the ^{241}Am radioactive decay. The time-resolved signal is reported in Figure 3.10.a.
As expected, the FWHM of the signal is sensibly larger than that of the single crystal diamonds highlighting a slower temporal response.
The estimated charge collection efficiency is also sensibly lower with respect to the single crystal diamonds, coherently with what expected. It indeed drops to $\sim 30\%$. Both these parameters are resumed in Table 3.4.

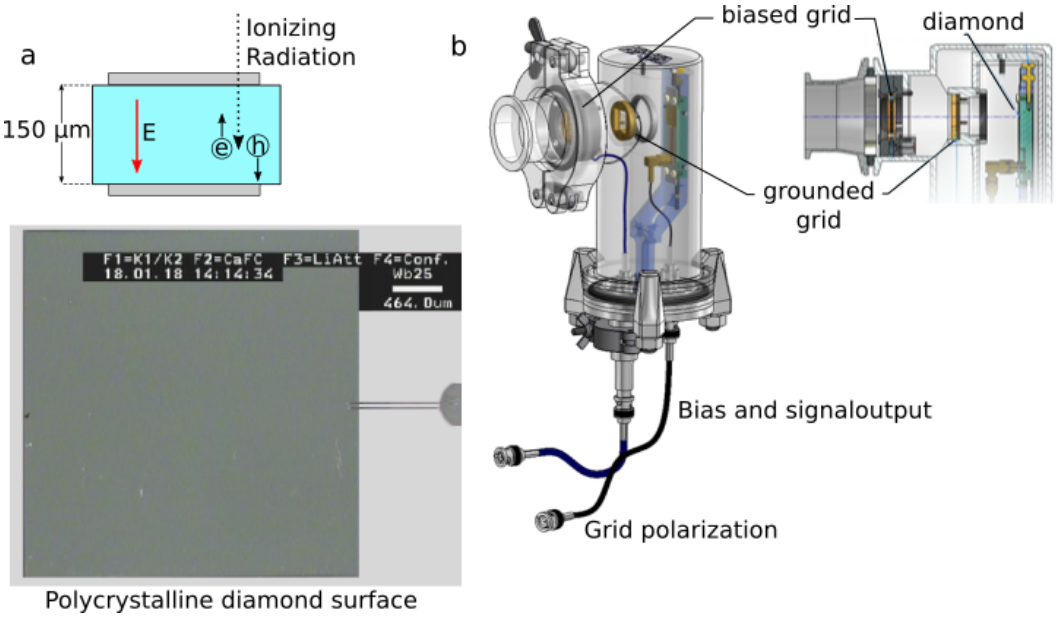

Figure 3.9. (a) Electrodes layout employed in the polycrystalline diamond detector and an image of its surface before being mounted in the ad-hoc holder shown in (b) which was optimized for working in environments affected by high EMP noise. In the scheme the position of the diamond and of the two grids that can be used for separating the electronic component from the ionic one are highlighted.

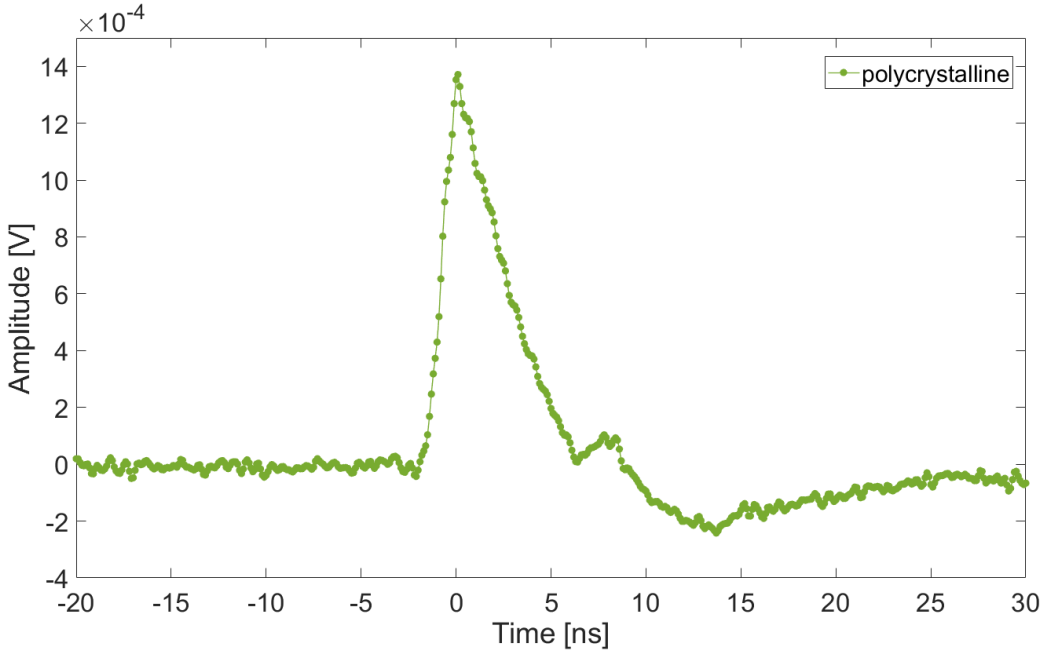

Figure 3.10. Time resolved signal for the polycrystalline diamond detector.

The low temporal resolution strongly affects the energy measurement in the TOF

Table 3.4. Temporal response and CCE measured for the polycrystalline diamond detector

	Bias (V)	FWHM (ns)	Q_α (C)	CCE (%)
Polycrystalline	+300	(3.4 ± 0.1)	(2.06 ± 0.06) $\times 10^{-14}$	(31 ± 1)

scheme. This can be partially balanced by employing a longer drift line. This solution is possible thanks to the wider surface area of the detector which allows to collect a larger amount of particles generating the signal. On the other hand, the low charge collection efficiency will cause a sensible decrement in the amplitude of the signal generated by a single particle impinging onto the detector lowering its sensitivity. All these effects have to be properly taken into account when aiming at an accurate proton spectrum reconstruction both during the signal collection and in data analysis.

3.4 Highlights and comments

The performed characterization of the three detectors highlights the peculiarity of each of them.
The two single crystal diamonds present a fast temporal response, the one equipped with sandwich contacts has also a remarkably high charge collection efficiency almost constant throughout its whole thickness. On the other hand, a thickness-dependent CCE has been observed for the interdigital electrode configuration which for protons of 2 MeV drops to $\sim 30\%$, as shown in Figure 3.7.
If the differences in the behavior of these two detectors are properly taken into account, we find that both of them are suitable to be used in detecting protons up to 3 MeV, fully stopped within the 50 μm thickness, providing a high energy resolution, as demonstrated in Chapter 5.3. Moreover the compactness of these devices can make them particularly suitable to be simultaneously employed in a small aperture angle as will be demonstrated in Section 5.4, where they were used to monitor the proton emission at different angles within a cone of 20°.
The polycrystalline diamond detector, as expected, has a lower, but still fast, temporal resolution as well as a lower CCE. Nevertheless, the large area covered by its surface represents an important advantage especially if a low flux of impinging particles is expected as it is the case for alpha particle detection in $p^{11}B$ fusion experiments[96].

It is now important to add one final notice. During the description of the methodology used for the detectors characterization, it was mentioned the importance of working in the velocity saturation regime. The latter is reached for a specific value of the applied electric field. Hence, in other words, the voltage applied to the electrodes of the detectors has to be high enough to work with a constant drift velocity of the charge carriers. The diamond characterization was thus carried out by working in this regime. Nevertheless, the charge density generated in the detector when alpha-particles from the radioactive source are stopped in it is very far from the one generated by a nanosecond, high charge proton bunch signal. Indeed, when the diamond detectors are applied for characterizing laser-accelerated protons, they

are subjected to high fluxes of particles and thus to ultrahigh current densities. These can induce a charge depletion in the bulk of the detector leading to a variation in the effective potential. If this happens, the drift velocities of the charge carriers could be modified and the actual temporal response of the detector could vary from the one retrieved in this chapter.
To prevent this phenomenon, during the measurement discussed hereinafter, the diamond detectors are linked to a custom BIAS-TEE (MIL-BT 010-6000) which includes a capacitor of ~ 50 nF. The capacitor is linked in series with the one formed by the electrodes of the detector and in parallel with the capacity of the cable connecting the bias tee to the detector. The overall large capacity leads to a large stored charge within the circuitry, insuring a negligible effect on possible potential variations due to the charge depletion caused by even the most intense ion bunches to be expected in common and near-future regimes of laser-matter interactions.

Chapter 4

Advanced methodologies for TOF measurements

In Chapter 2 the main diagnostic systems currently adopted to characterize the laser-accelerated particles have been illustrated and briefly discussed. Among them, the time-of-flight technique was shown to offer interesting features, useful for an online detection arrangement. Later on, in Chapter 3, some advantages in using diamond detectors, over other semiconductor detectors, were discussed.
Nevertheless, in order to develop an on-line diagnostic system based on TOF technique, there are still some issues to tackle. In particular, it is necessary to design an acquisition system able to appreciate the whole dynamic range characterizing the TOF signals. Moreover, the diagnostic has to cope with environments characterized by a strong EMP presence. Therefore, both the chosen detectors and the acquisition system have to be properly shielded. In the following, these aspects are finally addressed and the procedure to retrieve a calibrated proton spectrum is presented. First, in Section 4.1, a detection system able to enhance the dynamic range of the measurement is described. Then, in Section 4.2, the topic of EMPs is discussed and a procedure in setting-up the TOF line to reduce the electromagnetic noise impact on the measurement is proposed. This is followed by Section 4.3, which is dedicated to a procedure that has to be applied to take into account the frequency-dependent attenuation of the transmission line. Eventually, in Section 4.4 a detailed procedure to reconstruct the proton spectrum from the time-of-flight measurement is discussed. The procedure here presented can be applied to any kind of detector but, as already mentioned, during this doctoral thesis, the technique was applied only to the case of CVD diamond detectors.

4.1 High dynamic-range detection

The TOF measurements are intrinsically characterized by large dynamic-range signals due to the simultaneous collection of data associated with accelerated particles and emitted radiation in the UV-soft X-ray range. In order to retrieve all the useful information from the TOF measurement, to accurately estimate the energy of the incoming particles and to finally compute their spectrum, it is necessary to distinguish the finest details without cutting the most intense portion of the signal.

A typical signal obtained by a TOF measurement has been shown in Figure 2.7. It was obtained by irradiating a 500 μm thick aluminum target with the ABC laser (E $\simeq$ 50 J, $\tau_L \simeq$ 3 ns, $I_L \simeq 10^{15}$ W cm $^{-2}$). As already explained, it mainly consists of two parts: the photopeak and the particle contribution.
In order to obtain complementary information from the two parts of the detected spectrum, the signal collected by the detector can be divided in two nominally-equal parts by a calibrated splitter at 50%. The two portions of the signal will both have the same shape but half of the original amplitude. They can be acquired by two channels of a high-resolution and high-sensitivity scope set with different amplitude scales. In our setup, shown in Figure 4.1.a and b, the diamond detector is linked to the splitter through a cable connected with a custom large-capacity, high-frequency Millimetrica Bias-Tee (MIL-BT 010-6000). This isolated the scope from the -150 V bias voltage of the diamond, without losing significant information over the frequency range (300 kHz – 6 GHz) for which the Bias Tee was designed[159]. This frequency range is suitable for signals coming from the employed diamond detectors. Indeed, as it is possible to infer performing the Fourier transform of the time domain signals generated by the exposition to alpha particles and shown in the previous chapter, they are characterized by a 3 dB frequency bandwidth well contained in this range: the single crystal diamond in the interdigital configuration has a $f_{\mathrm{BW}_{3dB}} \simeq$ 210 MHz, the one in sandwich configuration $f_{\mathrm{BW}_{3dB}} \simeq$ 153 MHz and the polycrystalline $f_{\mathrm{BW}_{3dB}} \simeq$ 50 MHz. Then, the signal goes from the bias-tee to the splitter and eventually to the two channels of the scope. As shown in Figure 4.1 between the bias tee and the splitter it is also possible to include an attenuator to reduce the amplitude of the signal. This can be necessary in order to avoid the scope damage when signals with an amplitude greater than 5 V are expected.

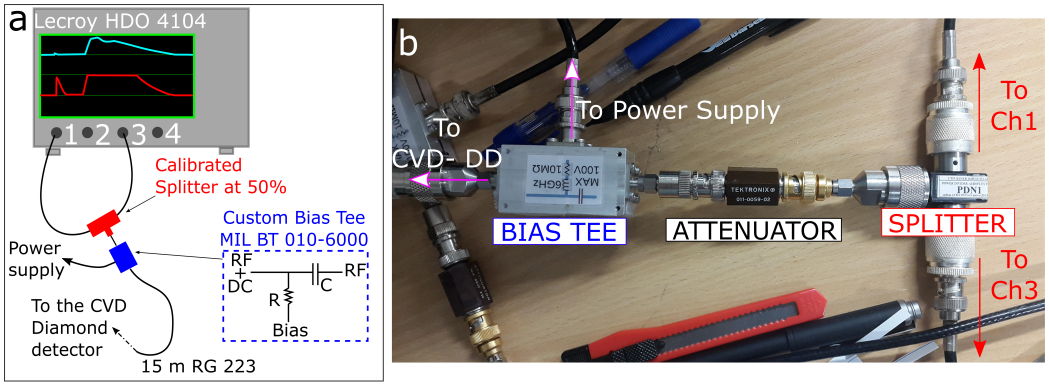

Figure 4.1. (a) The acquisition system adopted to enhance the dynamic range of the measurements, (b) A picture of the bias-tee, attenuator and splitter chain.

The described acquisition system allowed to collect the signal reported in Figure 4.2. This signal was due to the irradiated 10 μm aluminum target with the FLAME laser, having 30 fs temporal duration, 2.5 J energy for an intensity on target of 1.7×10^{19} W cm^{-2}.

Here it is evident that channel one (Ch1 in the figure) provides information about the

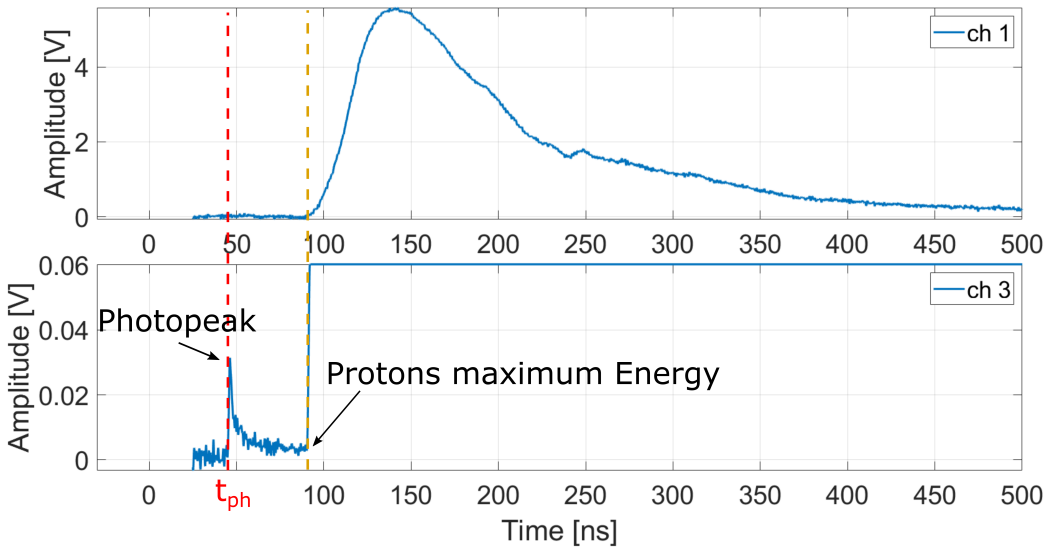

Figure 4.2. the signal obtained with the splitting technique and all the mentioned cautions to counteract the effects of the EMP pollution.

main signal generated inside the diamond but, because of the finite dynamic range of the scope, there is poor resolution on the smaller details which, instead, can be obtained from channel three (Ch3 in the figure) which was set to a finer scale. Since the two channels of the same oscilloscope are accurately synchronized, also thanks to the equal type and length of the cables going from the splitter to the scope, the temporal position of the photopeak can be retrieved from Ch3 and used as absolute reference for data shown in Ch1 which does not provide clear information about the photopeak temporal position. The consistency of this comparison is confirmed by the coincident temporal position of the proton maximum energy given by the initial point of the main signal (yellow dotted line in Figure 4.2).
It is possible to evaluate the maximum improvement in the achievable dynamic range by applying this methodology. In particular, for the reported measurement it was used the high dynamic LECROY HDO 4104 scope, having bandwidth of 1 GHz, sample rate of 10 GS/s per channel and a resolution of 12-bit with an Effective Number of Bits -ENOB- of 8.4 bit. Thus, the intrinsic dynamic range of the scope can be computed applying the relation DR [dB] $= 20log(\frac{V_{\max}}{V_{\min}})$ where $V_{\max}$ stands for the maximum voltage value measurable by the scope and $V_{\min}$ is the minimum value measurable employing the same scale used to measure $V_{\max}$. The value $V_{\min}$ can be estimated by the ENOB. being 8.4 bits. The minimum value measurable with the 1 V/div scale is given by the ratio 5 V over $2^{8.4}$ which gives 14 mV leading to a scope intrinsic dynamic range of ~ 51 dB.
The maximum increment in the dynamic range is achieved when the two synchronized channels are operated with very different full-scale values. In the Lecroy HDO 4104 scope this means to have channel one set with a full-scale of 5 V and channel three with a full scale of 5 mV. In this way the effective range of values which is possible to measure is defined by the range covered by the two channels combined together. The maximum measurable value is still 5 V, whereas the minimum is determined by the

channel operated with 1 mV/div scale. Considering just the ENOB, the minimum representable value is therefore given by $(1 \times 10^{-3})/2^{8.4} = 2.9\mu$V. Nevertheless, the vertical noise floor for the 1 mV/div scale in the HDO 4104 scope[160] is of 145 μV, thus the latter results to be the real lower limit for the measurable voltage. Hence, with the introduced methodology, the maximum achievable dynamic range is: DR [dB] $= 20log(\frac{5\times10^3\text{mV}}{1.45\text{mV}}) \simeq 70$ dB. Despite the intrinsic dynamic range of this low noise oscilloscope is already high, with this technique it was possible to further improve it by a factor $10^{1.3} \sim 20$ dB.

4.2 EMP management and reduction

As discussed in Chapter 1, Section 1.3, it is well known that in high power laser-matter interactions, the effect of the EMPs on diagnostics with electronic components can be remarkable[25,65,67,161,162]. The EMP production and characteristics generally depend on the specific type of laser matter interaction. They are usually characterized by a broadband frequency spectrum and by an associated electric field which scales with the laser energy and intensity on focus, easily reaching the order of MV/m intensity.[26]
Several precautions must thus be adopted to obtain signals with high signal-to-noise ratio from an electronic device in environments characterized by high electromagnetic pulse pollution. In particular, two types of EMP field couplings need to be avoided: that with the detector and that with the overall acquisition system.

EMP coupling with the detector

The first thing that can be done in order to minimize the detrimental effects caused by the EMP direct coupling with the detector is to develop a proper shielding of the latter. To this purpose, the diamond detector is mounted on a compact cylindrical metallic enclosure with a minimal circular aperture on the front, which is necessary to allow to the particles to reach the detector. The walls of the hollow cylinder are made in aluminum and have a thickness of 2 mm. These shield the inner part of the holder effectively by exploiting the skin effect[163]. The amplitude of the electromagnetic wave penetrating into the conductive walls exponentially decreases along with the penetration depth z according to the relation $E(z) \propto E_0 e^{-\frac{z}{\delta}}$. The parameter δ is the so-called skin depth[163] that can be conveniently expressed as:

$$\delta = \sqrt{\frac{\rho}{\pi f \mu_r \mu_0}} \tag{4.1}$$

where ρ and μ_r are the material resistivity and permeability respectively. At $z = \delta$ the value of the electromagnetic wave amplitude is reduced of a factor 1/e with respect to the value on the surface. Thus, a thickness of few multiples of the skin depth is sufficient to strongly attenuate, or even suppress, the electromagnetic wave propagating towards the inner part of the conductor. As it is clear from the relation (4.1), the skin depth is a function of the wave frequency. In particular, low frequency waves are able to penetrate deeper in the material with respect to those having higher frequency. In Figure 4.3 the skin depth as a function of the

electromagnetic wave frequency in the specific case of aluminum is shown. In particular, the point where the skin depth equals the thickness of the walls is highlighted.

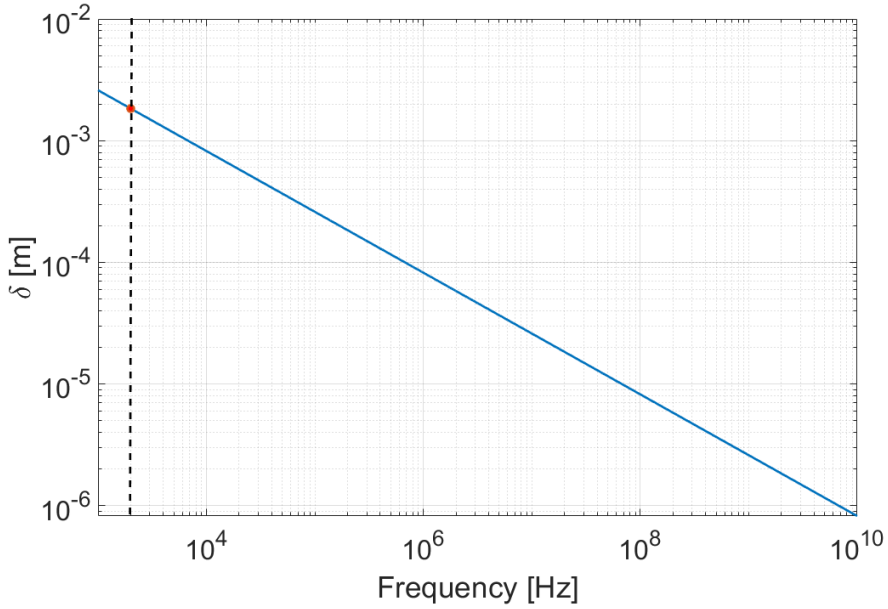

Figure 4.3. The skin depth as a function of frequency for aluminum. Highlighted in red is the frequency for which the skin depth equals the 2 mm thickness of the holder walls.

Thus, considering the penetration depth of electromagnetic waves in aluminum, the described enclosure can effectively attenuate electromagnetic waves with frequencies down to $\sim$ 2 kHz.

As already mentioned, the cylindrical enclosure presents a small hole on the front surface to allow the particles to reach the detector. In principle this hole can sensibly reduce the shielding effectiveness of the surrounding enclosure. Nevertheless, as shown in the sketch of Figure 4.4.a, the hole has a diameter of 4 mm. The small size of the aperture strongly limits the frequencies of the electromagnetic waves able to effectively propagate through it. Indeed, only those electromagnetic waves characterized by a wavelength smaller than the aperture are going to be able to freely pass through the hole and eventually interact with the detector electronics. For wavelengths comparable to the hole some attenuation is given, though. Thus, the presence of the hole does not remarkably affect the shielding action exerted by the aluminum enclosure for frequencies lower than a few GHz.
A picture of the holder used to shield the single crystal diamonds is shown in Figure 4.4b.

In addition to the shielding enclosure, the EMP coupling with the device can be minimized by limiting the frequencies able to propagates towards it exploiting the fundamentals of wave-guide theory[164]. In particular, this principles can be applied to the TOF line extension. It is indeed a common practice to use external pipes to extend the total length of the line of flight in vacuum as shown in Figure 4.5.

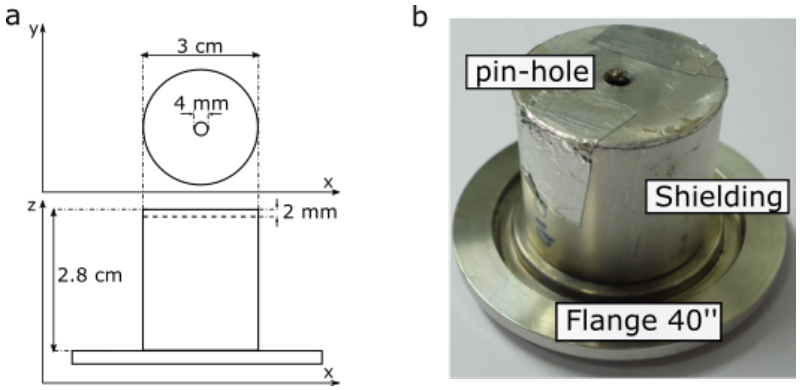

Figure 4.4. (a) Sketch of the cylindrical shielded holder used to limit the direct coupling of EMPs with the detector, (b) The shielded holder in which the CVD diamond detector is mounted provided by Tor Vergata University taking care of the diamond detector design and manufacturing.

If the final connection with the detector is made with a pipe of internal radius R_{wg} and length L_{pipe}, this acts as a cylindrical waveguide providing a cutoff frequency under which no electromagnetic wave can ideally further propagate.

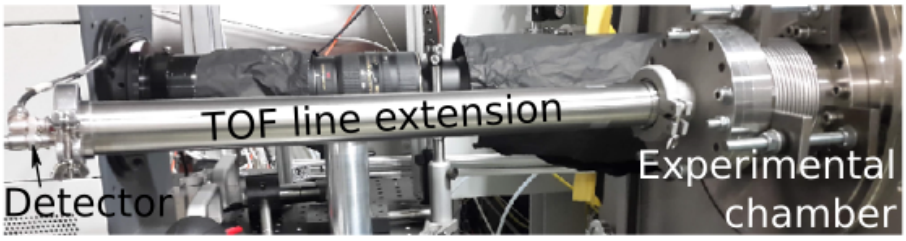

Figure 4.5. An example of a TOF line extension used during the experimental campaign performed at GSI research center with the PHELIX laser.

For a given mode this cut off-frequency can be written as[164]:

$$\begin{cases} f_{cutoff} = \frac{c}{2\pi}\frac{\dot{\chi}_{m,n}}{R_{wg}} & \text{for a TE mode} \\ \\ f_{cutoff} = \frac{c}{2\pi}\frac{\chi_{m,n}}{R_{wg}} & \text{for a TM mode} \end{cases} \tag{4.2}$$

where $\chi_{m,n}$ is the n-th rooth of the m-th Bessel function and $\dot{\chi}_{m,n}$ is the n-th root of its derivative. The main roots are given for reference in Table 4.1.
In particular, for a cylindrical pipe of 20 mm radius, which corresponds to a typically used TOF extension line, the cutoff frequency for the first waveguide mode TE_{11}, i.e. the lowest frequency mode able to propagate, is: $f_{cutoff} = c\,\dot{\chi}_{1,1}/\left(2\pi R_{wg}\right) \simeq 4.39$ GHz. In addition, the field intensity associated with a given mode decreases along the waveguide longitudinal direction z with dependence $e^{-\alpha_{m,n}z}$ where $\alpha_{m,n}$ is an attenuation coefficient depending on the waveguide geometrical parameters,

Table 4.1. Values of the n-th root of the m-th Bessel function and of its first derivative.

m	n	$\chi_{m,n}$	$\dot{\chi}_{m,n}$
0	1	2.405	3.832
0	2	5.520	7.016
0	3	8.654	10.173
1	1	3.832	1.841
1	2	7.016	5.331
2	1	5.136	3.054
2	2	8.417	6.706
3	1	6.380	4.201

conductivity (σ) and skin depth δ at the cut off frequency[164]. The coefficient $\alpha_{m,n}$ for a given mode can be determined from the relation[163,164]:

$$\alpha_{m,n}(f) = \sqrt{\frac{\epsilon}{\mu}} \frac{1}{R_{wg}\sigma\delta} \sqrt{\frac{f}{f_{cutoff}}} \frac{1}{\sqrt{1 - \frac{f_{cutoff}^2}{f^2}}} \left[\xi_{m,n} + \eta_{m,n} \left(\frac{f_{cutoff}}{f} \right)^2 \right] \tag{4.3}$$

where ϵ and μ are the electric permittivity and magnetic permeability of the medium filling the waveguide. The dimensionless parameters $\xi_{m,n}$ and $\eta_{m,n}$ are of the order of unity and depend on the considered mode[163]. In particular TM modes have $\eta_{m,n} = 0$ and $\xi_{m,n} = 1$ whereas for TE modes $\eta_{m,n} = 1$ and $\xi_{m,n} = 1/(\dot{\chi}_{m,n}^2 - m^2)$. Hence, with an accurate tailoring of the main characterizing parameters, such as the drift tube length and its diameter, a very good rejection to EMP fields traveling in the vacuum chamber can be achieved. The attenuation coefficient as a function of frequency for the TE_{11} mode provided by a pipe made in stainless steel with internal radius $R_{wg} = 20$ mm is reported in Figure 4.6.
Following the same principle, the small radius of the cylindrical aperture on the shielding case of the detector, can be schematized as a small waveguide which provides a cut-off frequency $\simeq 40$ GHz. Nevertheless its reduced length of 2 mm offers a rather low attenuation for frequencies closer to the cutoff.

EMP coupling with the acquisition system

In order to reduce the EMP coupling with the acquisition system, the best option would be to transport the signal from the detector to the scope by means of optical fibers. Nevertheless, their employment would require to convert the electrical signal produced by the detector in an optical one able to be transmitted through the optical fiber. This can be done by installing an electro-optical transducer near the detector site. However, this needs of a careful shielding from EMP and introduces severe limitations on the maximum current that can be processed. Since the output currents of the detector are expected to reach values up to several Amperes, the optical fibers do not appear to be a simple and viable solution.
The best compromise between the need of high current transmission and the avoiding the EMP coupling with the acquisition system, is to perform the main transmission

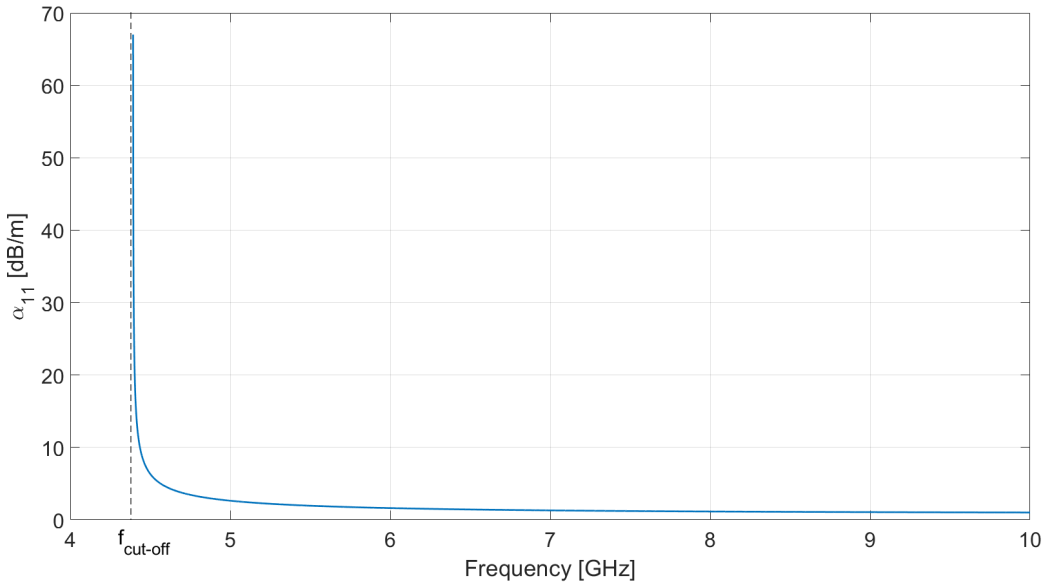

Figure 4.6. The attenuation coefficient for the TE_{11} mode propagating in vacuum in a stainless steel pipe with $R_{wg} = 20$ mm as a function of frequency.

link, used to transport the signal from the detector to the scope, with long double-shielded coaxial cables having low attenuation. These, according to their specific shielding properties for the involved frequency ranges, can suitably suppress the direct transmission of the EMP fields traveling in air to the inner coaxial conductor of the cable. Moreover these long cables can also contribute to the EMP rejection in several ways.

1. They behave as effective low-pass filters[65,165], giving high attenuation to possible contributions at high frequencies. On one side this improves the filtering of the high-frequency components of possible EMPs coupled to the detector. But on the other side it might introduce limitations to the temporal response of the detector setup.

2. The propagation of the EMP fields outside the experimental chamber can be classically described by the $1/r$ law. The use of long cables allows the positioning of the scopes far from the experimental chamber, and this decreases the possible direct coupling of EMP fields with the scopes themselves.

3. EMPs have a typical exponentially-decreasing time profile and become usually comparable to the background noise after few hundreds of nanoseconds. Since signals traveling in cables have lower velocity than those traveling in air, the cables can also be used to introduce a temporal delay of several tens or hundreds of nanoseconds between the high EMP contribution affecting the scopes and the detected signal[65].

Despite the employment of long double-shielded cables is a valuable instrument to reduce the detrimental effect of the EMPs on the signal acquisition, their length has to be wisely chosen. Indeed, if too long cables are used, they can sensibly reduce

the amplitude of the signal traveling through them and, most importantly, since they present a frequency-dependent attenuation, this can result in a variation of the actual slope of some portion of the signal. In particular, since they are characterized by an higher attenuation for the high-frequency components of the signal, the employment of very long cables can lead to the smoothing of the fast rising edges.
With proper cautions, the employment of long cables is thus an effective method to tackle the effects of the EMPs propagating in air and eventually reaching the scope. Nevertheless, the EMP field can induce a current flowing on the outer conductor of the cables. These currents, reaching the oscilloscope, will allow the associated EMP noise to affect the signal storage in the scope. In order to avoid this effect, it is possible to surround the cable with a set of different ferrite toroids[65] having various bandwidths. These provide damping of the current flowing on the outer conductor of the cables avoiding them to reach the scope.
Eventually, the choice of a proper scope can also affect the effectiveness in reducing the EMP noise affecting the signal[26]. A broadband scope will be sensible to electromagnetic waves on a wider frequency range. Reducing the bandwidth down to the minimum value necessary to properly acquire the TOF signal, can further improve the effectiveness in lowering the EMP noise due to the coupling with the acquiring system.
In the previous sections it has already been shown that the TOF signals are characterized by fast rising edges, and the photopeak usually has a steep one. This will determine the maximum frequency present in the signal to measure. To be able to properly reconstruct this front, it is necessary to sample it with at least three points. Hence, supposing to have a sampling rate of 10 GS/s, the minimum rising time that is possible to reconstruct is $\tau_{\text{rise}} = 0.3$ ns, which is a reasonable value for typical TOF measurements. This rising time can be related to the bandwidth (BW) of the scope through the rule-of-thumb relation[166]: $\text{BW}\tau_{\text{rise}} = 0.35$ leading to a minimum bandwidth of $\simeq 1$ GHz.

To show the effectiveness of these methods for EMP management, in Figure 4.7 a comparison among two signals is provided.

Both of them were collected during an experimental campaign performed at FLAME laser facility irradiating a 10 μm aluminum target with a 30 fs pulse having $E_L \simeq 3$ J and $I_L \simeq 2 \times 10^{19}$ W cm^{-2}. The signal reported in Figure 4.7.a has been collected preventing the EMP direct coupling with the detector by means of the optimized holder, shown in Figure 4.4, and cylindrical extension line both acting as waveguides. On the other hand, no caution concerning the acquisition system was taken. The scope was connected to the diamond by a short cable ($\simeq$4 m), without ferrite toroids and using the 5 GHz LECROY 8500 A scope to register the signal (so with bandwidth much higher than the 1 GHz value given before). The detrimental effects of the EMP pollution are evident. The signal is completely hidden by the oscillations due to the electromagnetic noise and it is not possible to perform any analysis to retrieve the particles energies.
This signal has to be compared with the one reported in Figure 4.7.b which was collected in nominally identical experimental condition but with a system optimized to cope with EMPs. The experimental set-up was modified swapping the short cable

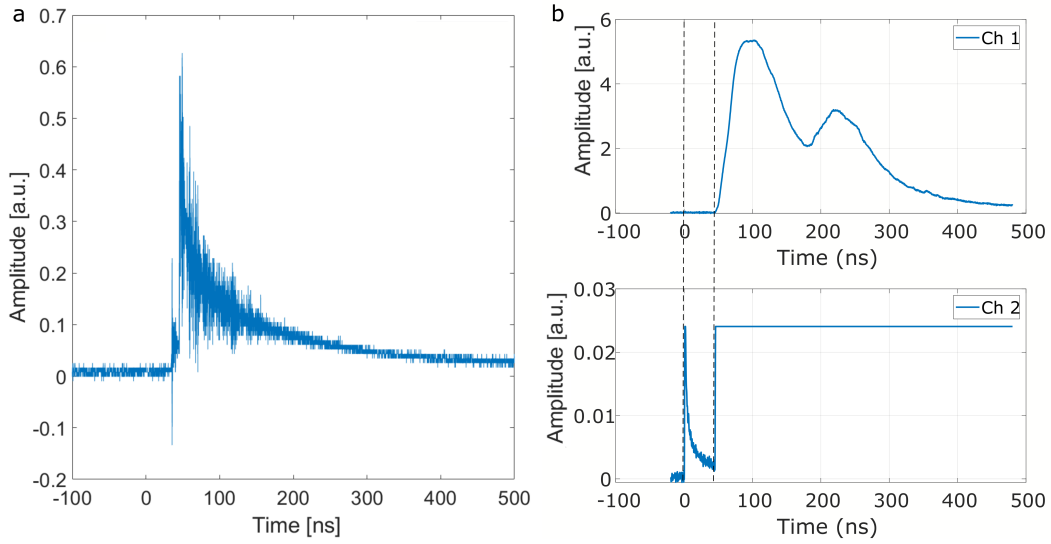

Figure 4.7. (a) The signal collected with a detection system not optimized to work in environments polluted by a strong EMP presence. (b) The signal acquired in nominally the same experimental conditions as the one reported in (a) but with the acquisition system optimized for EMP rejection.

with a 15 m long RG 223 double-shielded coaxial cable. This allowed to move the scope to a larger distance from the experimental chamber. As previously discussed, this provided an effective reduction in the direct coupling with the scope and produced a tens-of-nanoseconds delay between the EMP noise and TOF signal. The long cable was also surrounded by a suitable set of ferrite toroids (with bandwidths 0.5-5 MHz, 1 MHz - 1 GHz, 2-30 MHz, 20-200 MHz), representing a high impedance for the surface current flowing on the external conductor of the cable, stopping it well before reaching the scope. Moreover, the use of 15 meters long cable filtered the high frequency part of the signal, as also discussed in the next section. Furthermore, the low-noise 1 GHz LECROY HDO 4104 scope was now used. Its bandwidth is much lower than LECROY 8500 A used for collecting the signal in Figure 4.7.a. These choices contribute to a further decrement in the direct coupling issue while granting a good performance for the measurement. It is, indeed, important to notice that the signal shown in Figure 4.7.b is obtained without any numerical filtering operation and it represents the raw data collected during the measurement.

4.3 Cable de-embedding procedure

The employment of the long transmission line to bring the signal from the detector to the scope can be very helpful to filter the high part of the EMP spectrum out of the measurement, and to move the scope far from the interaction chamber, but can have a non negligible effect on the signal amplitude. The coaxial cables used to avoid EMP coupling to the scope are characterized by a frequency-dependent attenuation. Thus a suitable de-embedding procedure is required to recover the signal collected by the detector from the one recorded on the oscilloscope. The process is schematized in Figure 4.8. The signal stored in the scope is attenuated by

the transmission line. Thus, to recover the signal originated at the detector site, it is necessary to take into account the attenuation due to the transmission line. Since the latter has a frequency-dependent behavior, it is not possible to directly link the signal collected by the scope to the original one. To properly trace back the signal, is indeed necessary to work in the frequency domain, where the attenuation of the transmission line can be described by the transmission scattering parameter $S_{21}(f)$.

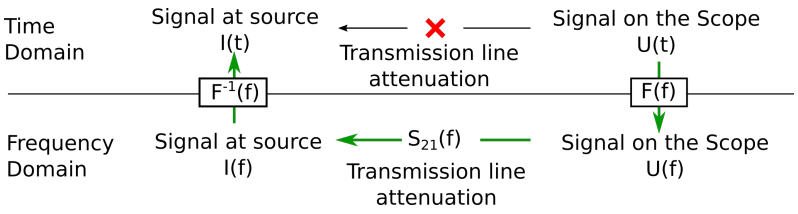

Figure 4.8. The signal reaching the scope is attenuated by the transmission line that has a frequency dependent attenuation. This contribution can be taken into account in the frequency domain by the transmission scattering parameter $S_{21}(f)$.

The whole transmission line is constituted not only by the cables but also by the Bias-Tee, the calibrated splitter for the high dynamic range detection and the short cable going from the latter to the scope, as shown in Figure 4.1.
The transmission line response in the frequency domain can be determined by measuring its transmission scattering parameter $S_{21}(f)$ with a Network Analyzer. In Figure 4.9 the one measured by means of the AGILENT N5230A Network Vectorial Analyzer for the whole series constituted by the 15 meters RG 223 cable, the Bias-Tee, the splitter and the short cable is reported.

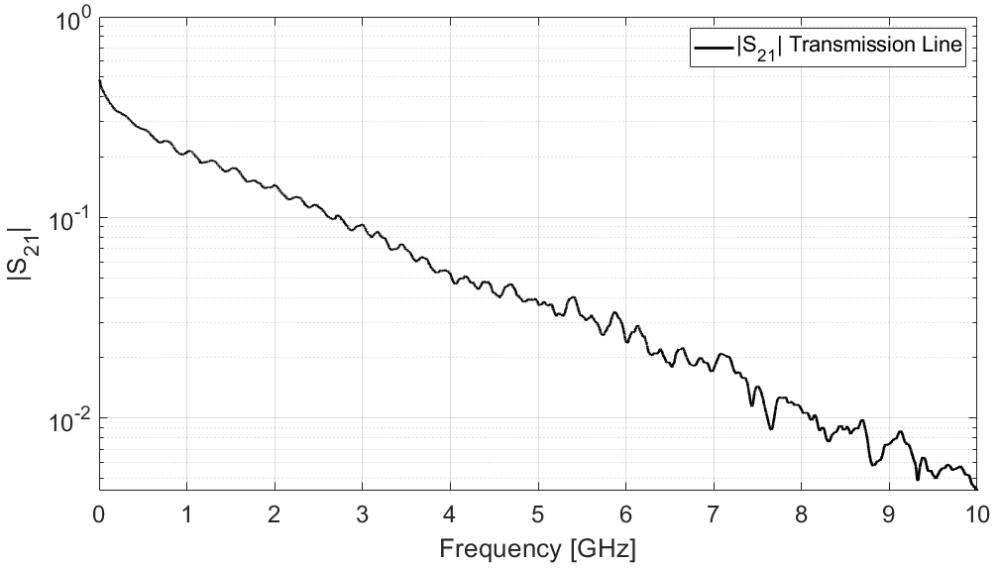

Figure 4.9. The module of the S_{21} scattering parameter measured for the whole transmission link used for the collection of the TOF signals.

The measurement of the scattering parameter gives a complex number. The module provides information on the amplitude loss whereas the phase gives information on temporal delay. In our case, since the phase increases linearly with frequency, providing constant temporal delays for each frequency, we can consider only the module.
Once the $S_{21}(f)$ is known, the de-embedded signal S_D can be computed by the following relation[65]:

$$S_D(t) = \mathcal{F}^{-1}\left[\frac{\mathcal{F}(V(t))}{S_{21}(f)}\right] \tag{4.4}$$

where V(t) is the voltage signal stored on the scope, $\mathcal{F}$ and $\mathcal{F}^{-1}$ are the Fourier Transform and the inverse Fourier Transform operators, respectively.
However, the previous procedure is rather delicate and should not be applied in a straightforward way; much care is instead needed in order to avoid numerical amplification of the noise. Indeed, for some frequencies the amplitude of the noise can overcome the one of the actual signal. To apply equation (4.4) only to the meaningful part of the acquired signal, a preliminary step is therefore needed. The Fourier transform of the signal and that of the background noise has to be computed and compared to determine the bandwidth where a suitable signal-to-noise ratio is achieved. Taking as reference the signal shown in Figure 4.10, obtained irradiating a 10 μm aluminum target with the FLAME laser (2.5 J energy, 30 fs temporal duration, 1.7 $\times 10^{19}$ W cm^{-2} intensity), with the assumption of white-noise condition, the information about the background noise can be retrieved from the portion of the signal collected in the time interval before the photopeak detection instant, when the laser-matter interaction is not occurred, yet.

Then, the frequency where the amplitude of the Fourier Transform of the noise is equal to the amplitude of the Fourier Transform of the signal can be selected as threshold frequency f_c (highlighted in Figure 4.11) and used to identify the frequency range in which the de-embedding procedure can be suitably applied. Namely for all those frequencies lower than the threshold one.

In Figure 4.12 the final de-embedded signal S_D is computed for the shot shown in Figure 4.10 and compared with the original raw signal V(t). It is clear that, in this case, the contribution of the transmission line cannot be ignored.

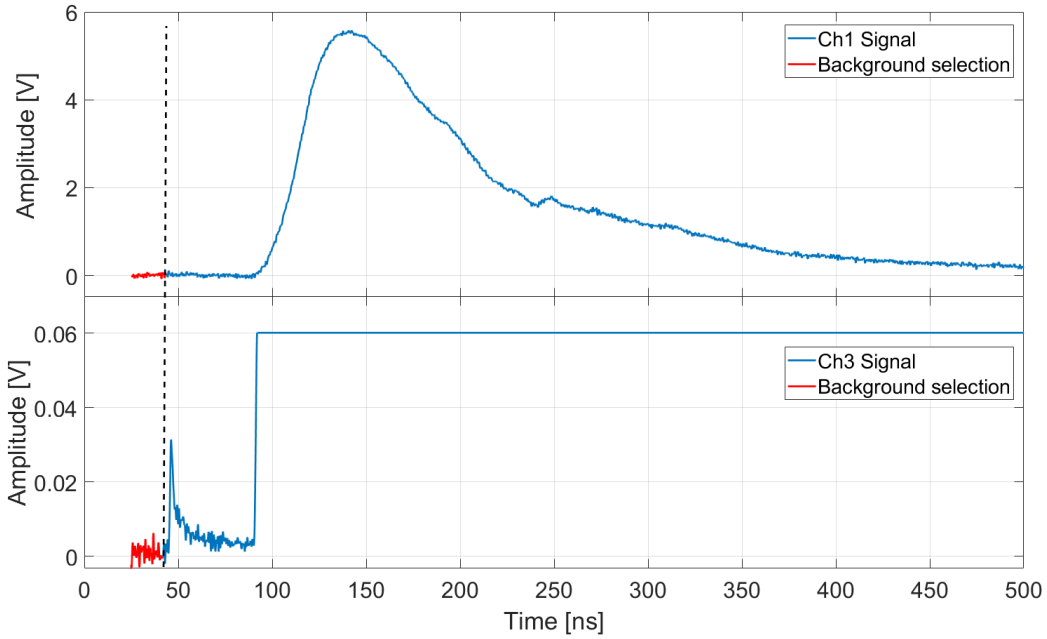

Figure 4.10. A signal collected with the acquisition system described in Section 4.1. The portion of signal from which it is possible to retrieve the information on the background noise is highlighted in red.

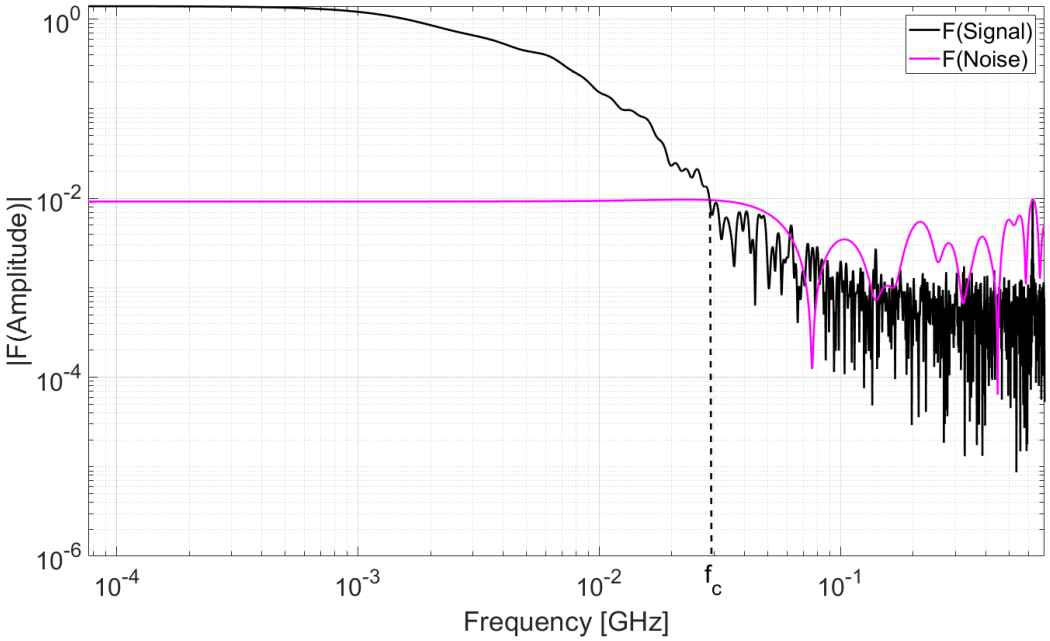

Figure 4.11. Comparison, in the frequency domain, of signal and noise with the determination of the f_c frequency.

Eventually, it is important to stress that the choice of the frequency f_c cannot be too restrictive. Indeed, in case a too low frequency is determined, the consecutive loss of information can lead to a poor signal reconstruction. On the other hand, if

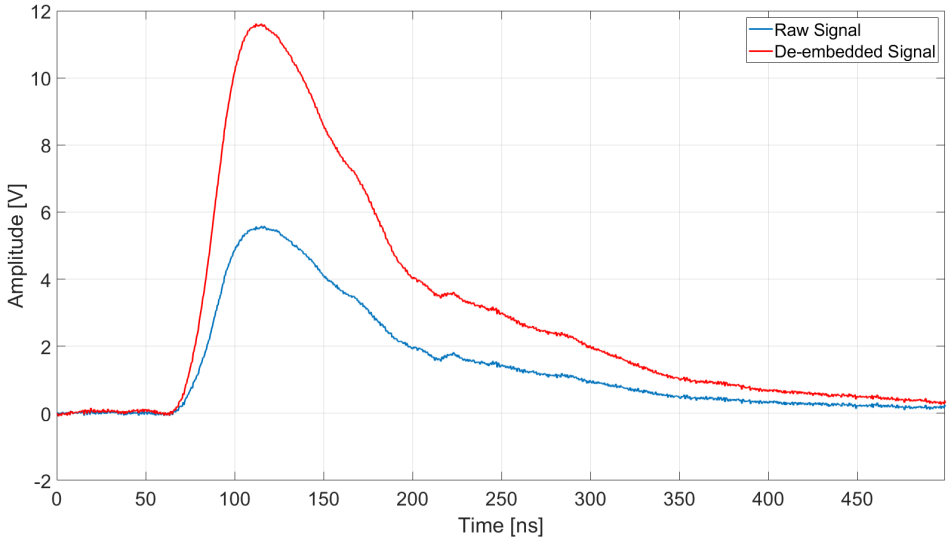

Figure 4.12. Comparison of the signal before (blue line) and after (red line) the de-embedding procedure.

all the frequencies are included in the computation, there could be some ranges in which the noise is going to be amplified significantly. The best compromise between the two conditions has thus to be pursued.
As an example, in Figure 4.13 the reconstructed signal obtained when a very low value of f_c was chosen is reported. It is possible to see how the lack of information negatively affects the final result.

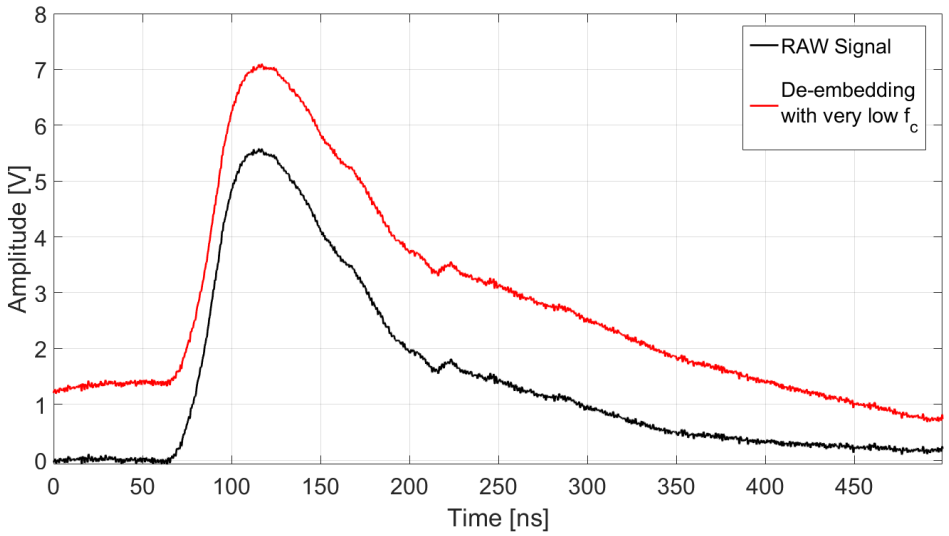

Figure 4.13. The signal already shown in Figure 4.12 has been now reconstructed by choosing on purpose a too low frequency, the reconstruction of the signal is negatively affected by the lack of information.

4.4 Analytical spectrum computation

Once a signal free from the EMP noise is obtained and the de-embedding procedure applied, it is possible to retrieve the spectrum of the particles generating the signal. This section is dedicated to a detailed analysis of this procedure.

Estimation of the particle energy

It has already been shown that the energy of the incoming particle can be retrieved by exploiting the relativistic energy definition together with the relations (2.8) and (2.9):

$$E_i = m_i \left[\left(1 - \frac{{d_{TOF}}^2}{c^2 \left(t_{TOF}\right)^2} \right)^{-1/2} - 1 \right] c^2 \tag{4.5}$$

where c is the speed of light, m_i is the particle mass, d_{TOF} the TOF line length and t_{TOF} is the time needed by the particle to cross the distance d_{TOF}. Thus, the tolerance on the energy measurement is affected by the finite temporal resolution Δt of the whole diagnostic system. The latter is influenced by the temporal resolution of the detector itself as well as by the front end electronics and the methodology used to retrieve the data. Nevertheless, the limiting factor is usually the detector temporal response. Starting from the relativistic expression of the kinetic energy, it is possible to evaluate the relative error as a function of the temporal resolution of the detector.
For a generic time interval ($t^s_{i,n}$,$t^f_{i,n}$), indicated with the n index, with $t^s_{i,n}$ and $t^f_{i,n}$ the initial and final extremes, the interval duration is $\Delta t_n = t^f_{i,n} - t^s_{i,n}$, with $E^f_{i,n}$ and $E^s_{i,n}$ the associated ion energies. The tolerance on the energy estimation will be given by:

$$\Delta E_{i,n} = \frac{\partial E_i}{\partial \gamma} \Delta \gamma_i = m_i c^2 \frac{\partial \gamma_i}{\partial t} \Delta t_n \tag{4.6}$$

where

$$\frac{\partial \gamma_i}{\partial t} = -\frac{d^2_{TOF}}{c^2} \frac{1}{\bar{t}^3_{i,n}} \left(1 - \frac{d^2_{TOF}}{c^2} \frac{1}{\bar{t}^2_{i,n}} \right)^{-\frac{3}{2}} \tag{4.7}$$

and $\bar{t}_{i,n} = \sqrt{t^f_{i,n} t^s_{i,n}}$ is the average ion arrival time in the n^{th} interval. Here we are not considering the error on the measurement of the distance d_{TOF} whose contribution is usually negligible due to length of the TOF lines. The tolerance $\Delta E_{i,n}$ can thus be written as:

$$\Delta E_{i,n} = -m_i \frac{d^2_{TOF}}{\bar{t}^3_{i,n}} \left(1 - \frac{d^2_{TOF}}{c^2} \frac{1}{\bar{t}^2_{i,n}} \right)^{-\frac{3}{2}} \Delta t_n \tag{4.8}$$

It is now convenient to express $\bar{t}_{i,n}$ as a function of the energy:

$$\frac{1}{\bar{t}_{i,n}} = \frac{c}{d_{TOF}} \left[1 - \left(\frac{\bar{E}_{i,n}}{m_i c^2} + 1 \right)^{-2} \right]^{\frac{1}{2}} \tag{4.9}$$

where $\bar{E}_{i,n} = \sqrt{E^f_{i,n} E^s_{i,n}}$ is the average ion energy in the n^{th} interval. Substituting the latter into equation (4.8) gives the following relation for the relative error on

the energy:

$$\frac{\Delta E_{i,n}}{\bar{E}_{i,n}} = -\frac{m_i c^2}{\bar{E}_{i,n}} \left(\frac{c\Delta t_n}{d_{TOF}}\right) \left[\left(\frac{\bar{E}_{i,n}}{m_i c^2} + 1\right)^2 - 1\right]^{3/2} \tag{4.10}$$

The negative sign is due to the fact that energy is a monotonically decreasing function of time.
In case of non-relativistic particles $\bar{E}_{i,n} \ll m_i c^2$, and the previous relation can be simplified obtaining:

$$\frac{\Delta E_{i,n}}{\bar{E}_{i,n}} = -2\sqrt{2}\frac{\Delta \mathrm{t_n}}{d_{TOF}}\sqrt{\frac{\bar{E}_{i,n}}{m_i}} = -2\frac{\Delta t_n}{\bar{t}_{i,n}} \tag{4.11}$$

As discussed in the previous chapters, laser-accelerated protons can reach energies of several tens of MeV, with typical spectra decreasing with energy. So, both high sensitivity and high resolution are required for a suitable description of the most energetic ions. Nevertheless, as it appears from equation (4.11), with TOF technique energy resolution and sensitivity have somehow opposite requirements. Indeed, improved energy resolution can be obtained in two ways: employing fast detectors, thus working with low Δt_n values, or placing the detector at larger distances from the target, so to increase d_{TOF} or equivalently the temporal delay $\bar{t}_{i,n}$ between the ion emission and its detection. However, the latter reduces the overall sensitivity by decreasing the solid angle of detection and thus the number of particles intercepted by the detector. Hence a compromise between the two is usually adopted with time-of-flight drift lines kept as long as the sensitivity of the detector allows to detect the signal with suitable intensity.

Particle number estimation

According to the type of detector employed for the TOF measurement, the number of particles can be obtained from the amplitude of the collected signal as shown in Chapter 2, Section 2.5. From now on it is useful to take as reference the case of semiconductor detectors which applies to our experiments.
First of all, an ideal device is considered, where all the charge generated inside the semiconductor detector is going to be collected by the electrodes. In this case, under the hypothesis that the particle is completely stopped in the detector and thus releases in it all its energy, the general relation that links the number of impinging particles N_i to the generated charge Q_i is:

$$N_i = \frac{Q_i \epsilon_g}{E_i q_e} \tag{4.12}$$

This relation by itself can lead to obtain an expression for the dN_i/dE_i spectrum even with a limited knowledge of the employed detector characteristics. Indeed performing suitable energy derivation of (4.12) it is possible to obtain[133]:

$$\frac{dN_i}{dE_i} = -\frac{\epsilon_g I(t)}{q_e E_i^2}\left(\frac{1}{2}t + \delta t\right) \tag{4.13}$$

where δ_t is the temporal resolution of the overall detection system and $I(t) = V(t)/R$ with $V(t)$ the measured signal amplitude and R the impedance of the acquiring system. This simple method allows to get the particle spectra with some accuracy, without specific detailed knowledge of the detector, requiring only its time resolution and the ϵ_g of the used semiconductor.
Nevertheless, in a real detector, the collected charge does not necessarily coincide with the one generated inside the device by the incoming radiation. This is due to different factors related to the specific characteristic of the detector in use that can lead to charge recombination or trapping in lattice defects, as discussed in more detail in Chapter 3. This effect is described with the charge collection efficiency (CCE) that weights the effectiveness in collecting the generated charges as a function of the energy of the incoming particles. Therefore, to obtain a reliable estimation of the real number of impinging ions it is necessary to include the effects of the charge collection efficiency in equation (4.12) which becomes:

$$N_i = \frac{Q_i \epsilon_g}{\mathrm{CCE}(E_i) E_i q_e} = \frac{Q_i \epsilon_g}{\varphi_i(E_i) q_e} \tag{4.14}$$

where the function $\varphi_i(E_i)$, defined as $\varphi_i(E_i) = \mathrm{CCE}(E_i)E_i$, has been introduced for compactness.
As shown in Chapter 3, the parameter $\mathrm{CCE}(E_i)$ can be measured by characterizing the response of the detector in use by exposition to particles of defined flux and energy. Since the CCE is defined through a discrete set of points, instead of performing the energy derivation to obtain an analytic expression for the dN_i/dE_i spectrum, it results more convenient to define equation 4.14 for each time interval associated with the temporal resolution of the detection system in use. In a generic n^{th} time interval, the value of the associated average charge due to the impinging particles can be computed as[132]:

$$\bar{Q}_{i,n} = \frac{1}{R} \int_{t^s_{i,n}}^{t^f_{i,n}} S_D(t) dt \tag{4.15}$$

where $S_D(t)$ is the de-embedded signal amplitude.
For each time interval, the equation (4.14) can be written as:

$$\bar{N}_{i,n} = \frac{\bar{Q}_{i,n}\ \epsilon_g}{\bar{\varphi}_{i,n}\ q_e}; \tag{4.16}$$

where $\bar{N}_i$ is the average number of particles and $\bar{\varphi}_{i,n}(E_{i,n})$ is the average value of the function $\varphi_i(E_i)$ in the nth interval. From the equation (4.16) the number of particles generating the signal can be obtained for each time interval.
The relative error on the number of incoming ions, which at this stage is only due to the finite temporal resolution of the employed detector, can thus be written as:

$$\frac{\Delta N_{i,n}}{\bar{N}_{i,n}} = \frac{N_{i,n}\left(E^f_{i,n}\right) - N_{i,n}\left(E^s_{i,n}\right)}{\bar{N}_{i,n}} = \bar{\varphi}_{i,n}\left[\frac{1}{\varphi_{i,n}\left(E^f_{i,n}\right)} - \frac{1}{\varphi_{i,n}\left(E^s_{i,n}\right)}\right] \tag{4.17}$$

The spectrum in Figure 4.14 was obtained applying this method to the signal reported in Figure 4.12 under the hypothesis that the signal was produced only by

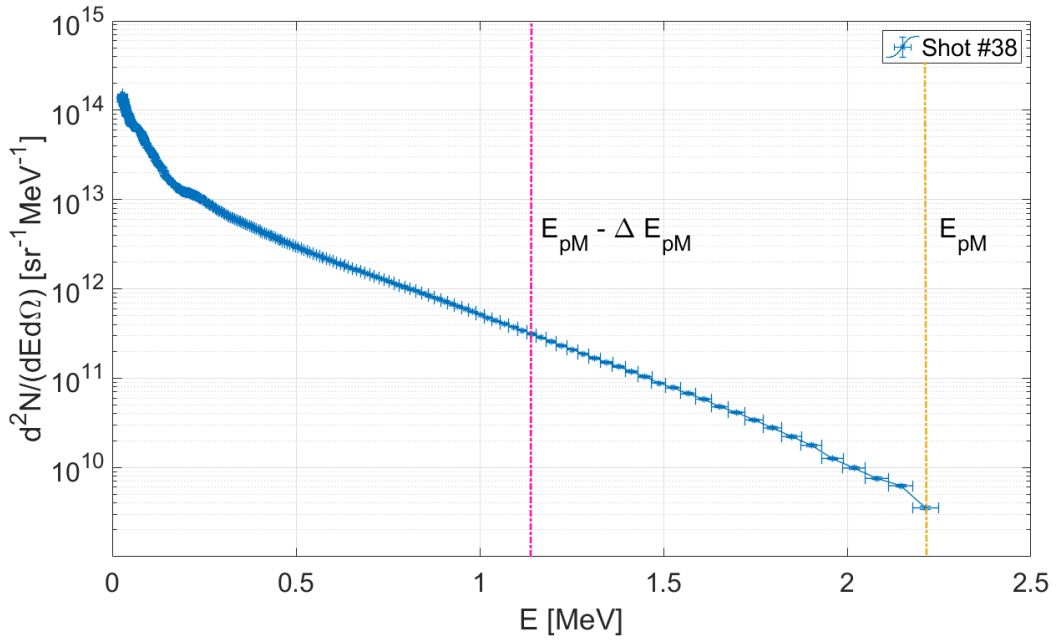

Figure 4.14. Spectrum obtained under the hypothesis that only protons contribute to the signal. The vertical yellow line indicates the maximum proton energy ($E_{p,M}$) and the magenta line corresponds to the energy where the ion contribution to the spectrum ends ($E_{p,M} - \Delta E_{p,M}$), in the most conservative hypothesis

proton detection.

It is indeed important to underline that the performed evaluation holds under the assumption that only one kind of particle is entering in the detector. This is due to the mechanism in which the signal is generated in semiconductor detectors, discussed in more detail in Chapter 3. In order to retrieve the number of particles interacting with the detector, it is necessary that only one type of ion is contributing to the signal generation or alternatively that the contribution of the different ion species is known in detail, for example by a Thomson spectrometer. Otherwise it will not be possible to relate the amount of generated charges with the number of impinging ions. Indeed, it is well known that multiple ionic populations are accelerated during the TNSA process[13]. Among them, as discussed in Chapter 1, protons are those with a lower mass and thus will be the first to be detected. But then, at later times, both protons and other ionic populations will simultaneously contribute to the TOF signal. Therefore, the a-priori assumption of single-ion-type detection, leads to an overestimation of the total number of particles of that species which are actually contributing to the signal. In particular, in the spectrum reported in Figure 4.14 the hypothesis that the whole signal is only due to protons will cause that the estimated number of protons is actually higher than the real one.
This can be also highlighted by performing a rather rough estimation for the generated proton density $N_{p,tot}$, the associated energy density $E_{p,tot}$ and the ratio between the overall proton energy and the laser energy $R_{L\to p}$. The evaluation of the latter is done under the assumption of emission limited to a unit of solid angle, and uniform

within it. Of course, this has limited accuracy, and a more realistic determination of these quantities would require the simultaneous use of several detectors at different angles, capable to characterize the angular variation of the emitted ion spectra. Nevertheless, it is possible to use these estimations as a very first evaluation to understand the order of magnitudes of the computed quantities. According to these premises, the following parameters were extracted: $N_{p,tot} = 9.9 \times 10^{12}\ sr^{-1}$, $E_{p,tot} = 0.3\ J\ sr^{-1}$ and $R_{L-p} = 12\%$. As expected, these values are far above those known in the literature[71,167].

It is therefore necessary to understand how it is possible to isolate the contribution of one single type of ions in order to be able to properly apply the described methodology. In the following, a simple argument is applied to evaluate when the hypothesis of single ion type detection holds and what can be done to extend the region of its validity.

4.4.1 Particle superimposition in time

The discussion presented in the previous section holds assuming that only one type of ions is impinging onto the detector or that the various contributions are known in detail. Indeed, in laser-matter interaction experiments, different ion species are classically accelerated and arrive at the detector usually superimposed in time. Indeed, in a classical TNSA scheme, ions are accelerated because of the electrostatic potential developed in the charged sheath formed within the target thanks to the electron emission[3,13], as shown in more detail in Chapter 1, Section 1.1.2. Because of this potential, ions are accelerated with a typical spectrum represented by a decreasing exponential function. A broad energy distribution is given by the acceleration of particles from different target depths and by the non homogeneous electronic distribution in the sheath[13,58]. As a general discussion, for a test ion accelerated by the Φ potential difference in the sheath, having A_i mass number, z_i charge state and Z_i atomic number, it is possible to write that the maximum achievable energy is $E_i = z_i q_e \Phi$. For ion energies up to several tens of MeVs, non-relativistic formulas can be used, and thus the ion time-of-flight at the diamond detector will be:

$$t_i = d_{TOF}\sqrt{\frac{A_i m_p}{2 z_i q_e \Phi}} = t_p\sqrt{\frac{A_i}{z_i}} \tag{4.18}$$

where m_p is the proton mass and t_p the time of arrival to the same detector of a proton accelerated by the same potential difference. Since for any ion, except for protons, it is $A_i > z_i$, then it will always be $t_i > t_p$. Thus, protons will reach the detector much before than other ions accelerated in the same shot. Moreover, there will be a time window where only protons can reach the detector. If we indicate with t_{pM} and t_{iM} the times of arrival to the detector of the proton with the maximum energy and of the corresponding ion with the maximum energy, generated respectively by the same acceleration process, the mentioned time window will be $(t_{pM},\, t_{iM}) = (t_{pM},\, t_{pM} + \Delta t_p)$. In the case of fully-stripped ions (i.e. $z_i = Z_i$), it is

possible to write:

$$\Delta t_p = t_{pM}\left(\sqrt{\frac{A_i}{Z_i}} - 1\right) \tag{4.19}$$

It is well known that for any element (with the exception of protons), it is $A_i \geq 2Z_i$, being the equality true for light elements (C, N, O, ...) classically accelerated in intense laser-matter experiments. So, it is:

$$\Delta t_p \geq t_{pM}(\sqrt{2} - 1) \tag{4.20}$$

It is possible to determine the same condition in the energy domain. So, the proton energy range associated with the extremes of the time interval (t_{pM}, t_{iM}) can be written as $(E_{pM} - \Delta E_p, E_{pM})$, where:

$$\Delta E_p = E_{pM}\left(1 - \frac{Z_i}{A_i}\right) \tag{4.21}$$

And, for fully-stripped ions, $A_i \geq 2Z_i$:

$$\Delta E_p \geq \frac{E_{pM}}{2} \tag{4.22}$$

So, for a given experiment of TNSA acceleration mechanism, or in general for any laser-matter process where ions are accelerated because of a potential difference, we can consider as a general criterion that if in a TOF scheme we are able to detect protons with maximum energy E_{pM}, then in at least the proton energy range $(E_{pM}/2; E_{pM})$ there will be no contribution coming from the superimposition of other ions. It is worth considering that this estimation has been achieved under the rather conservative hypothesis of fully stripped light ions, which is a very limiting case, since in typical experiments $z_i < Z_i$ for the largest part of the ions and, of course, in case of non fully stripped ions the interval is even increased.
Applying this argument to the spectrum reported in Figure 4.14, limiting the computation of the parameters $N_{p,tot}$, $E_{p,tot}$ and R_{L-p} only to the portion of the spectrum where we are expecting to have only proton contribution: $(E_{pM} - \Delta E_p, E_{pM})$ = (1.077 MeV, 2.154 MeV), we obtain: 5.9×10^{10} sr^{-1}, 0.01 J sr^{-1} and 0.4% respectively. These values are sensibly lower than those obtained in the evaluation performed in the previous section and they are also in much better agreement with those reported in literature for similar experimental conditions[71,167].

4.4.2 Filter application

It has been shown that, when interested in measuring protons, the contribution of UV radiation and of heavier ions to the TOF signal can hinder the spectrum reconstruction. The detection of UV radiation can cause the presence of a long descending photopeak tail which can hide the presence of the most energetic protons. Heavier ions, as widely discussed in the previous section, lead to a superimposition of different ionic populations which make difficult to retrieve the proton spectrum in the whole energy range, especially at low energies. To overcome these issues, thin sheets are usually employed as filters to cut both these contributions from the detected signal[135], with a little loss of information on protons. We define $E_{i,cutoff}$

the maximum energy of ions of a given species fully stopped by a certain filter. Its value can be determined performing simulations with the Montecarlo SRIM code[153]. In Table 4.2 the cutoff energies are listed for the main ion species, commonly present as pollutant in the vacuum chamber, for a set of different aluminum filter thicknesses.

Table 4.2. Cutoff energies obtained with the Montecarlo simulation code SRIM for an aluminum filter of different thicknesses. The values were computed for the main ion species usually accelerated during laser-matter interaction.

Ion	Al filter Thickness (μm)	$E_{i,cutoff}$ (MeV)
H	10	0.75
C	10	11.45
N	10	13.7
O	10	15.84
H	30	1.6
C	30	31.5
N	30	39.5
O	30	46.5
H	50	2.2
C	50	46.5
N	50	58.5
O	50	69.5

The effectiveness in using the filter is evident already from the time domain signals. As an example, in Figure 4.15, it is reported the signal collected during a shot performed in similar experimental condition as those in which the signals in Figure 4.2 and 4.7.b were acquired. The only difference is that, during this shot, a 10 μm aluminum filter was applied in front of the diamond detector.

In the Figure two temporal intervals have been highlighted with white and light blue colours. In the white region on the left, particles reaching the detector do not remarkably feel the effect of the filter, which is indeed affecting those arriving at later times, i.e. in the light blue region. In particular, at $t \simeq 100$ ns it is possible to spot the presence of a change of slope and for t > 100 ns the signal presents only a long smooth tail. This tail is given by two contributions. The first, and more important, contribution is due to the bremsstrahlung radiation generated by the particles interacting with the filter. The second is the contribution of the particles with energies very close to the cutoff, they are still able to pass through the filter but the latter strongly reduces their velocity and also their number leading them to reach the detector at later times. This second contribution has a minor effect that is negligible when the filter is placed at very close proximity of the detector surface. Indeed, in this case the variation in the particle time of flight due to the crossing of 10 μm filter is negligible. On the other hand, this contribution can play a role when the filter is placed rather far from the detector, since the particles with energies near the filter cutoff, slowed down by the filter, take longer to travel the final path to the detector.

The employment of a filter giving a threshold energy under which no ions other than protons can be detected, helps to down-extend the energy range where the

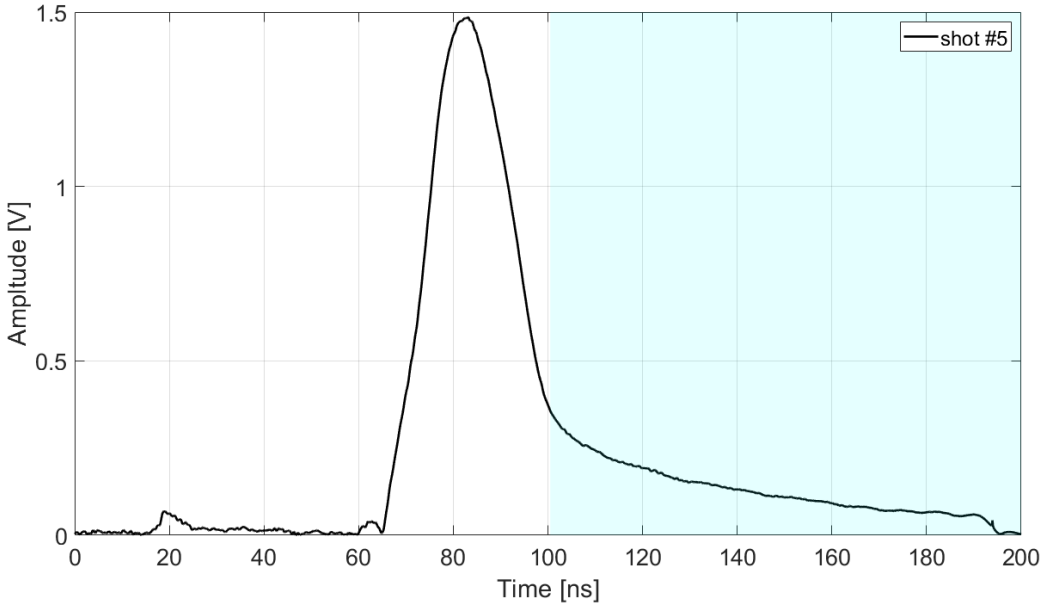

Figure 4.15. Signal obtained for a shot performed with the 10 μm aluminum filter covering the diamond detector.

estimation of proton number is still reliable with respect to what obtained in the previous section.
It is indeed important to take into account that the filter affects also the particles passing through it by causing a reduction of their energy. This effect is expressed by the attenuation factor that is obtained by the relation $k_{att}(E_{in}) = E_{out}/E_{in}$ where E_{in} is the energy of the particle impinging on the filter and E_{out} is the energy of the particle exiting the filter. In Figure 4.16 the coefficient of energy attenuation for protons able to pass through the filter is computed for the nominal 10 μm thickness and for the minimum and maximum values of thickness according to the filter tolerance. In case of the aluminum foil here used and purchased from the Good Fellow company[168] the tolerance is 15%, thus the minimum thickness is considered here to be 8.5 μm and the maximum 11.5 μm.
As expected, its effect is more significant for energies close to the threshold energy, where it cannot be neglected if aiming for an accurate reconstruction of the spectrum. Therefore, in case a filter is used between the target and the semiconductor detector, it is necessary to correct the number of particles estimated from equation (4.14) as it follows:

$$N_i = \frac{Q_i \epsilon_g}{k_{att}(E_i)\varphi_i(k_{att}E_i)q_e} \tag{4.23}$$

Following this caution it is then possible to compute the spectrum obtained from the signal reported in Figure 4.15. The spectrum evaluation was performed by considering both the nominal thickness of the aluminum foil, i.e. 10μm, and the lower and higher thickness limit given by the 15% tolerance on the foil thickness measurement. In Figure 4.17(a-c) the resulting spectra are reported.
The increase of the tolerance on the amplitude is due to the associated tolerance in the attenuation of the aluminium filter given in Figure 4.16 and, as expected, is

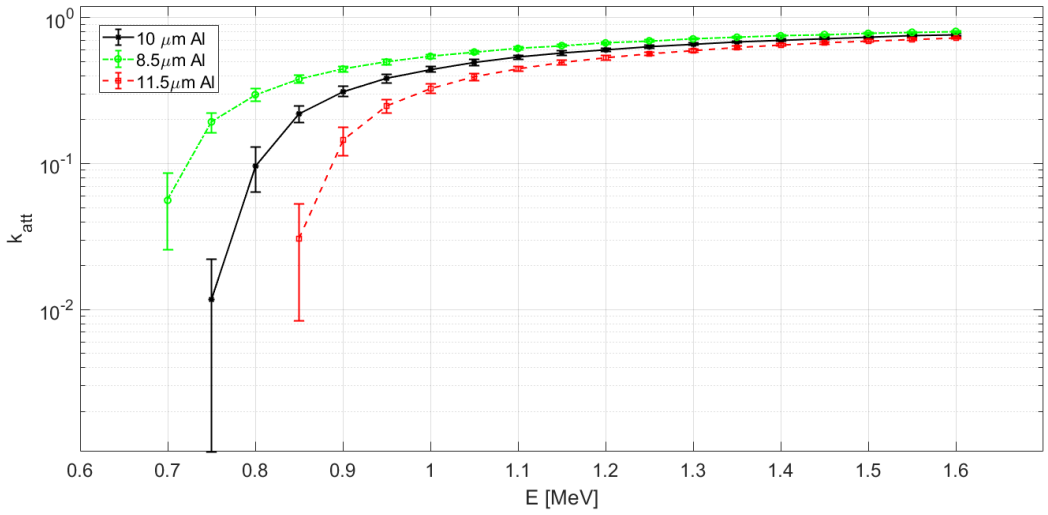

Figure 4.16. The attenuation coefficient computed by SRIM code for protons impinging on a 10 μm aluminum filter. The two additional curves show the attenuation factors for the thickest (11.5 μm) and the thinner (8.5 μm) limits given by the thickness tolerance of the aluminum foil purchased from from the Good Fellow company.

more relevant for low energy particles. With respect to the spectrum reported in Figure4.14, which was performed in similar condition and indeed presents roughly the same maximum proton energy, it is possible to see that the use of the filter allowed to down-extend the proton energy range, at expenses of the larger tolerances introduced in the lower part of the consequent spectrum. Moreover, approaching the lower energies, the three spectra present an abrupt change in their slopes. This is most likely due to a numerical effect when taking into consideration the attenuation coefficient of the filter near the cutoff energy.

An additional effect has to be taken into account. In a classical TOF scheme, the particle energy is easily linked to a specific time instant from the equation of uniform rectilinear motion. When a filter is used, the overall path is schematically split in two consecutive sections, where the same particle has different velocities. The first one, having length D, goes from the target to the filter and the second one, of length δ, from the filter to the detector as schematically shown in Figure 4.18.

In general, the overall arrival time $t_{p,n}$ of a proton to the detector can thus be written as:

$$t_{p,n} = t_{pD,n} + t_{p\delta,n} = D\sqrt{\frac{m_p}{2E_{p,n}}} + \delta\sqrt{\frac{m_p}{2k_{att}\left(E_{p,n}\right)E_{p,n}}} = \\ = \sqrt{\frac{m_p}{2E_{p,n}}}\left(D + \frac{\delta}{\sqrt{k_{att}\left(E_{p,n}\right)}}\right) \tag{4.24}$$

This relation links the particle arrival time and energy in the case a filter is used. Obviously, this kind of correction is relevant only when the filter, for geometrical constraints, cannot be applied near the detector surface, or if the line of sight of the

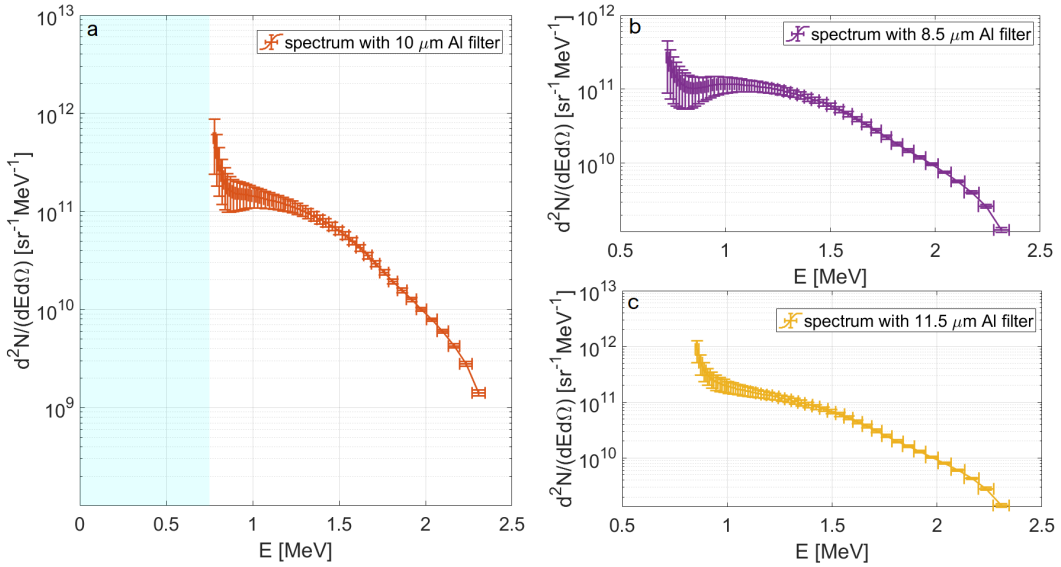

Figure 4.17. Proton spectrum obtained from the signal shown in Figure 4.15 by taking into account the effect of the aluminum filter of thickness (a) 10 μm (b) 8.5 μm and (c) 11.5 μm.

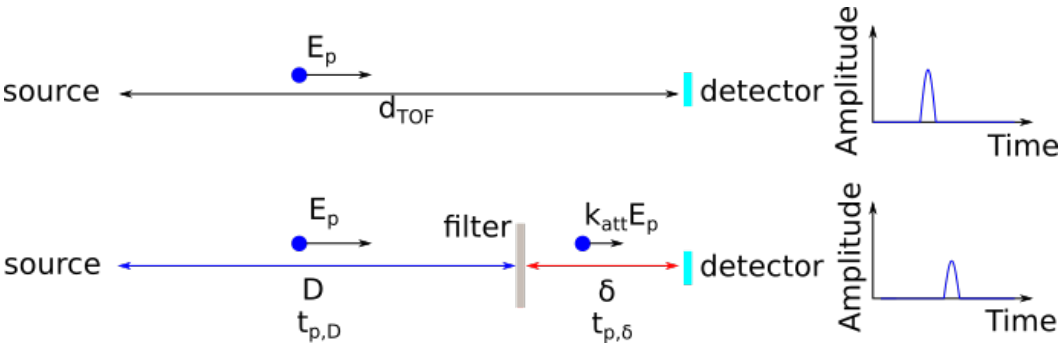

Figure 4.18. When a filter is applied in front of the detector, the TOF line is schematically splitted into two sections. The particle will cross the space between the filter and the detector with a velocity reduced due to the energy attenuation exerted by the presence of the filter.

detector is not completely free but obstructed by some kind of passive detector such as, for instance, an Imaging Plate.

Since k_{att} is a monotonic function of the energy, as observed in Figure 4.16 this relation can be inverted numerically to find the associate $E_{p,n}$. It is clear that the second term will be of interest only for particles with energy close to the filter cutoff, whereas it will be negligible for higher energies.

As a rule of thumb, we can consider that the effect of the drift space located after the filter starts to be relevant when the time needed by a particle to travel through this is one tenth of the time needed to travel the main drift space D. To evaluate for which proton energy this happens it is convenient to express the filter attenuation

factor as a function of the parameter $G = t_{p\delta,n}/t_{pD,n}$:

$$k_{att}\left(E_{p,n}\right) = \left(\frac{\delta}{D\ G}\right)^2. \tag{4.25}$$

This equation states that a given value of G will be reached for particles having a specific energy attenuation. Hence, for a given D and δ it is possible to foresee if the effect of the line of flight splitting has to be considered or can be neglected. For instance, during the acquisition of the signals reported in this chapter we had $\delta = 0.2$ cm and $D = 105$ cm. Imposing to have a value of $G = 0.1$ it was found that the correction would be needed for $k_{att} = 3.64 \times 10^{-4}$. This value of the attenuation factor, as shown in Figure 4.16, is obtained for protons with energies near the filter cutoff or lower than that.

The discussion shown in this chapter allows to obtain a TOF signal free from EMP noise and with a high dynamic range. It has also been shown how to retrieve an accurate proton spectrum from these signals and, in the previous chapter, a detailed characterization of diamond detectors was provided. In the next chapter, the measurement procedure, together with the spectrum computation, is going to be applied to different laser-matter interaction regimes whose detailed information, together with the results, are discussed.

Chapter 5

Application of the advanced TOF technique to different laser-matter interaction conditions

The diagnostic technique described in Chapter 4 has proven to be characterized by high versatility. This is highlighted in the following, where the main experimental campaigns in which this advanced TOF technique has been applied are presented and discussed. Each campaign was characterized by different laser-matter interaction conditions covering both short and long laser pulses with energies from hundreds of milli-Joules up to hundreds of Joules. The employment of the technique in such large variety of different interaction conditions allowed to investigate a wide range of aspects and also to test the effectiveness of the diagnostic methodology in response to the various possible requirements coming from different fields.

The purpose of this chapter is thus to show the peculiarities of the discussed diagnostic method in different experimental contexts. Section 5.1 is dedicated to the analysis of the data collected in experiments performed at the ABC laser located at ENEA - Centro Ricerche Frascati (Italy). The investigated regime is the one typical of inertial confinement fusion environments, where hydrodynamics plays a major role. In this frame the energy of supra-thermal ions is of the order of tens of keV and with a limited flux. Moreover, the high energy of the laser produces significant levels of EMPs. This experiment allowed to test the sensibility of the developed diagnostic system as well as its resistance to EMPs, providing high signal-to-noise ratio.
An experimental campaign was carried out in a facility delivering on targets hundreds of mJ in tens of fs, aiming for proton acceleration by TNSA scheme. It was performed at the ECLIPSE laser facility (France) and it is described in Section 5.2. This highlighted the capability of the discussed diagnostic to work at a repetition rate of 1 Hz.
In Section 5.3 and 5.4 the typical TNSA regimes are further investigated. The data obtained from two different experimental campaigns performed on similar laser facilities will be analyzed. The first was performed exploiting the FLAME laser

located at INFN-LNF research center (Italy). The campaign was dedicated both to the optimization of the TOF technique and to the investigation of the existing correlation between electron and proton acceleration. The campaign performed at the ALLS beamline, at INRS-EMT located in Varennes (Quebec, Canada) was dedicated to the beamline optimization together with the fine tuning of the diagnostic systems, for experiments of laser-driven PIXE. The simultaneous detection of the accelerated protons both with the TOF system and a calibrated Thomson spectrometer, positioned at similar angles, provided further validation of the TOF method here discussed.
The experimental campaign described in Section 5.5 was instead performed at the Lund Laser Center (Sweden) and it highlights the advantage to have an handy diagnostic that can be easily positioned at multiple angles to monitor the interaction and the characteristics of the emitted accelerated particles, such as their energy and number.
The real test bench for EMP resistance and signal saturation was the use of such diagnostics in the experiment carried out at GSI (Darmstad) exploiting the PHELIX laser delivering ~ 100 J on targets in hundreds of femtoseconds. The results obtained with the TOF detectors during this experiment are discussed in Section 5.6.

5.1 Experiments with the ABC laser at ICF regimes

The ABC Laser Facility[169], located at ENEA centro ricerche Frascati, is a solid state laser belonging to the class of neodymium doped lasers. The trivalent Nd^{3+} ions constitute the active dopant inside a host glass phosphate medium. The first harmonic of this four-level laser system has a wavelength $\lambda_0 = 1054$ nm. The duration of the pulse ranges from 3 to 5 ns with a rising time of 0.5 ns, for a maximum intensity on target of 1.5×10^{15} W cm^{-2}.
The interaction of the ABC laser with a solid target will thus generate a plasma with a long scale-length density profile that will interact with the same laser pulse, leading to the phenomena described in Chapter 1, Section 1.1.1. In particular, supra-thermal ion populations are going to be produced mainly via the electric field generated by the electron displacement due to the excitation of parametric instabilities, mainly here the Two Plasmon Decay[46]. A signature of the occurrence of the latter is the detection of the three-half harmonic emission. This is produced by the non linear coupling of one of the excited plasma waves, having $\omega \simeq \omega_L/2$, with the incident laser electromagnetic wave.
In Figure 5.1 three optical spectra acquired with the Ocean Optics HR4000 CG-UV-NIR spectrometer during three different shots are reported. The ABC laser was operated with $E_L \simeq 45$ J, $\tau_L = 3$ ns and a focal spot on target $f = 100$ μm for an intensity $I_L \simeq 2 \times 10^{14}$ W cm^{-2}. The three spectra were obtained by shooting on thick solid polystyrene targets (1100 μm for shot # 5209 and 1120 μm for shot #5170) and thick aluminum target (1920 μm in shot # 5285). All the three spectra show the laser emission ($\lambda = 1054$ nm) the second harmonic emission ($\lambda_{\frac{1}{2}} = 527$ nm) and the three half-harmonic emission ($\lambda_{\frac{2}{3}} = 703$ nm), signature of the Two Plasmon Decay instability[46]. Therefore, a supra-thermal component in the accelerated ions

is expected as a consequence of the electron heating due to the plasma wave excitation.

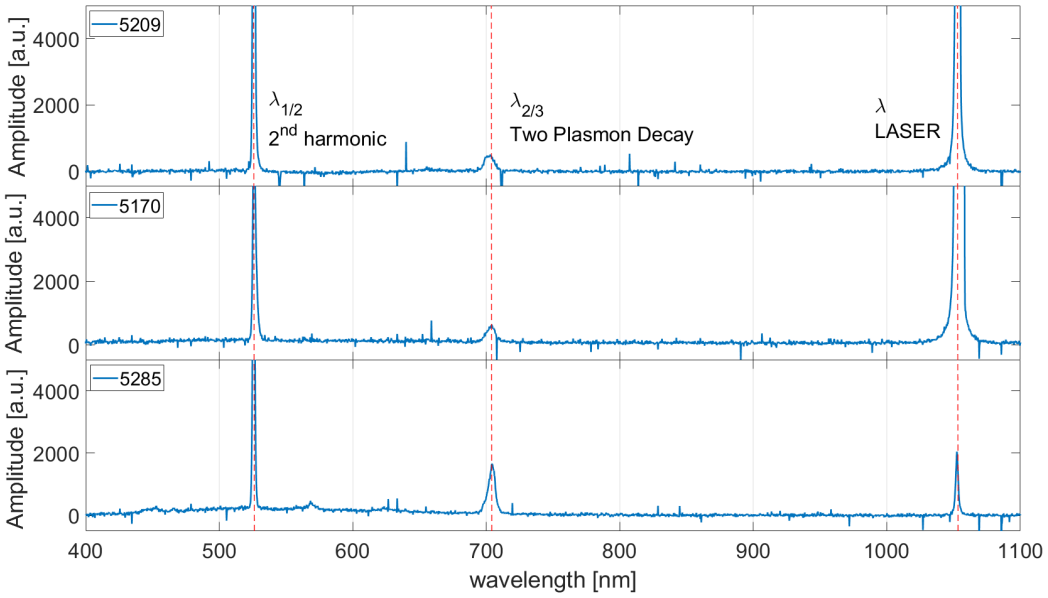

Figure 5.1. The spectra obtained with the Ocean Optics HR4000 CG-UV-NIR spectrometer during three different shots. The presence of the second harmonic emission ($\lambda_{\frac{1}{2}} = 527$ nm) and the three half harmonic emission at $\lambda_{\frac{2}{3}} = 703$ nm, which indicates the occurrence of the Two Plasmon Decay instability, are highlighted.

This aspect was verified by installing several ion diagnostics, as shown in Figure 5.2. Multiple TOF lines equipped both with Faraday cups and diamond detectors in interdigital configuration were set up all around the experimental chamber. The choice to use the interdigital electrode configuration arises from the range of energies that are expected in this regime. The excitation of parametric instabilities and the subsequent electric field generation produced here ions having energies ranging from few tens of keV up to $\sim$ 100 keV. These are going to be stopped near the surface of the diamond wafer, where the applied electric field is more intense for an optimal detector performance for the low energy ions.
The TOF line equipped with diamond detector had a drift length of $d_{TOF,DD} = 1.13$ m, whereas those equipped with the Faraday cups had a length of $d_{TOF,FC} = 0.551$ m. The maximum distance at which the latter can be placed is limited by their sensitivity. Indeed, it would have been useful to place them further away to limit the EMP coupling with the detector but the amplitude of the signal would have been sensibly reduced hindering the ion detection.
This difference in the sensitivity of the two kinds of detectors is strictly related to the principle on which they rely to generate an electric signal. As discussed in Chapter 3, diamond detector response is proportional to the amount of energy deposited inside its active layer, thus one proton with higher energy will produce a signal with amplitude higher than one proton with lower energy. On the other hand, Faraday cups respond according to the charge of the detected particle, regardless its energy. Thus, a large amount of low energy protons will produce a signal with amplitude

larger than few energetic protons.
Faraday cups and diamond detectors are therefore expected to provide complementary information. In this regime, few ions with energy of tens of keV are going to be produced and they can be effectively detected by the diamonds whose signal is proportional to the energy released in their active layer. On the other hand, the low energy component of the produced ions, can be detected also by the Faraday cups.

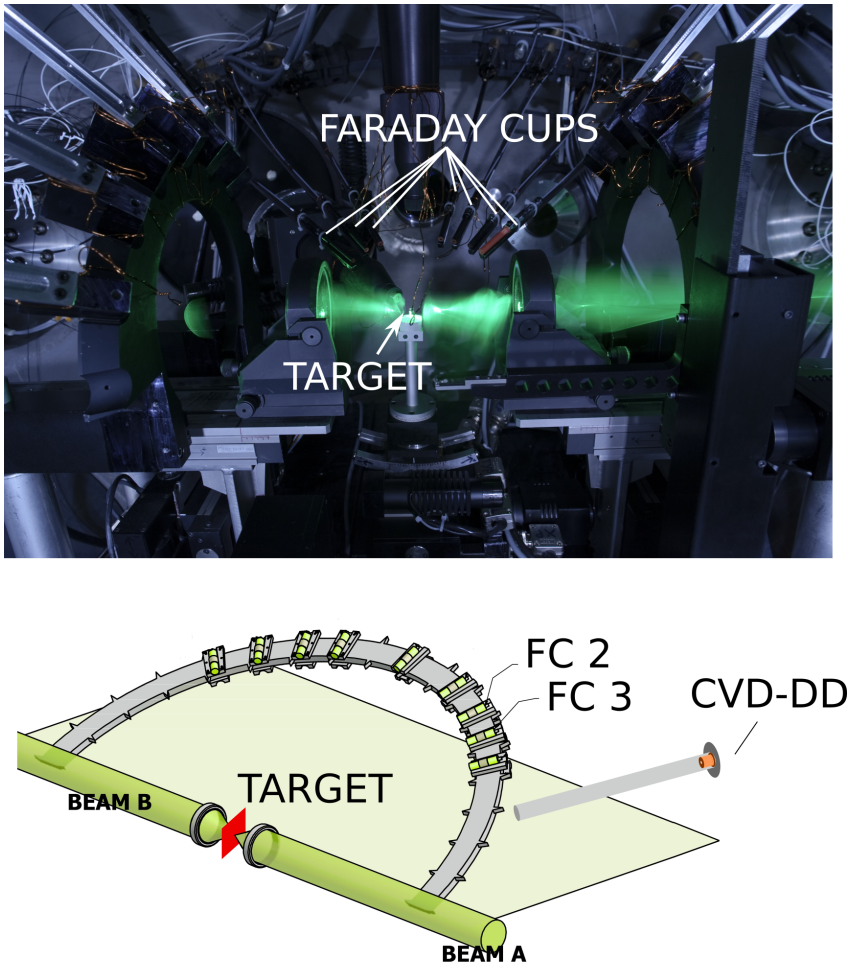

Figure 5.2. The experimental chamber layout. In the picture it is possible to see all the TOF lines equipped with the Faraday cups, whose positions are depicted in the scheme on the bottom together with the TOF line equipped with the diamond detector. During the shots here analyzed the target was irradiated only with one laser beam, labeled "BEAM A" in the scheme.

The Faraday cups employed in this experiment were connected to the 4 channels of a Tektronix TDS684B scope (1 GHz bandwidth, 5 GS/s sample rate) through $\sim$ 30 meters long cables. In order to fruitfully employ the Faraday cups in a TOF scheme, their signal was combined with one coming from a photodiode placed in the laser-path before the experimental chamber. This provided a temporal benchmark from which the laser-matter interaction instant was easily retrieved enabling the estimation of the energies of the collected particles.
In Figure 5.3.a the time domain signals coming from the Faraday cups placed at $53.38°$ and $48,91°$ (FC2 and FC3 respectively) are shown together with the one obtained from the diamond detector placed at $65°$.

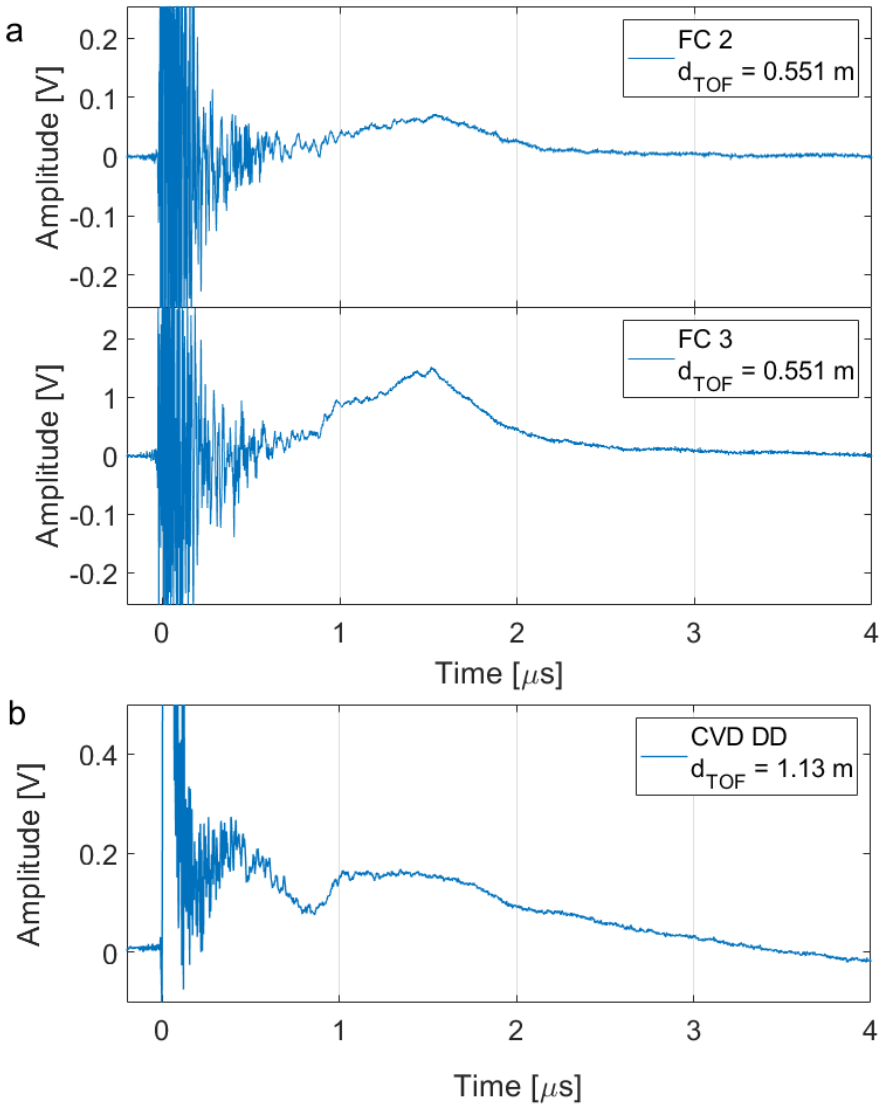

Figure 5.3. (a) The raw signals collected by the two Faraday cups highlighted in Figure 5.2 during the shot # 5285. (b) The raw signal collected by the diamond detector during the same shot.

In both the Faraday cups the ion signal is preceded by the EMP noise. The electric field associated with the electromagnetic pulse pollution as well as their spectral bandwidth have been measured in several experiments performed at the ABC laser facility[67,170]. Under these regimes, for conditions similar to those of the interaction here analyzed, a peak electric field of ~ 260 kV/m was measured at ~ 10 cm from the target.
Two main spectral components were highlighted by means of an electro-optical probe and a super-wide-band antenna: a long lasting component (~ 1 μs) for frequencies below 50 MHz and one component lasting only for the first 300 ns of the measured signal at higher frequencies ~ 130 MHz[170].
Once the noise due to the EMP is extinguished, in the first of the two Faraday cup signals it is possible to recognize the contribution of one main ion population whereas in the signal provided by the second Faraday cup, two different contributions can be identified.
Since we are interested in protons of maximum energy of ~ 100 keV, the diamond detector was operated without any filter foil.
The diagnostic setup was done as previously described in Chapter 4, Section 4.1, by employing the custom bias tee and the calibrated splitter at 50 %. The collected signal was sent to the LeCroy 735Zi scope (3.5 GHz bandwidth and 20 Gs/s sample rate) by means of ~ 5 meters long AIRCEL double shielded cables. From the acquired signal shown in Figure 5.3.b, it is possible to spot the contribution of different ion populations following the photopeak. The very first one is partially hidden by EMP noise, then the first to be clearly detected starts around 500 ns, and this is followed at about 1 μs by a wider bump generated by the detection of a second population. Eventually at 2 μs the contribution of a lower energy ion population is detected resulting in a change in the slope of the descending tail.

In Figure 5.4 the time domain signals coming both from the diamond detector and from the two Faraday cups have been converted in terms of energy per atomic mass unit (a.m.u.) and plotted one over the other for a prompt comparison. It is interesting to note that the information on ions with energies higher than a few keV is lost in the signals provided by the two Faraday cups. The diamond detector, on the other hand, for this energy presents a contribution due to the detection of a first population of supra-thermal ions whose maximum energy is ~ 10 keV. Then another contribution is detected and, even if partially hidden by the noise due to the electromagnetic pulses, the ion contribution is clearly distinguishable up to several tens of keV.

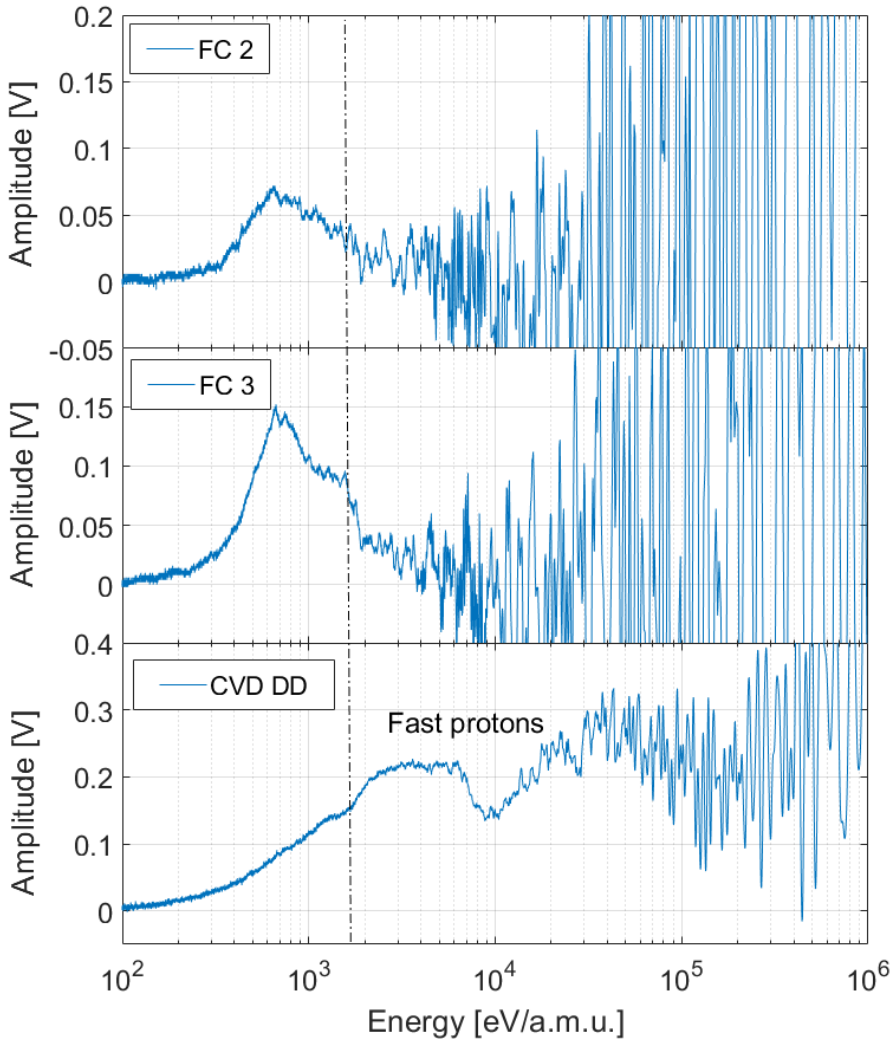

Figure 5.4. From top to bottom: the signals provided by the two Faraday cups and from the diamond detector expressed as a function of energy/amu. For a prompt comparison the dashed vertical line highlights the change in the slope of the signal of the diamond detector which roughly identify the maximum ion energy detected by the Faraday cups.

Following the procedure described in the previous chapter, the spectrum has been retrieved from the TOF signal acquired by the diamond detector and it is shown in Figure 5.5. This has been obtained in the hypothesis of pure proton contribution which, for the lower energy portion of the spectrum, can lead to an overestimation of the actual particle number. In particular, exploiting the argumentation presented in Chapter 4, Section 4.4.1, it is possible to assume that the spectrum in the energy range (14, 28) keV is generated by a pure proton contribution whereas for energies lower than 14 keV heavier ions can be detected.

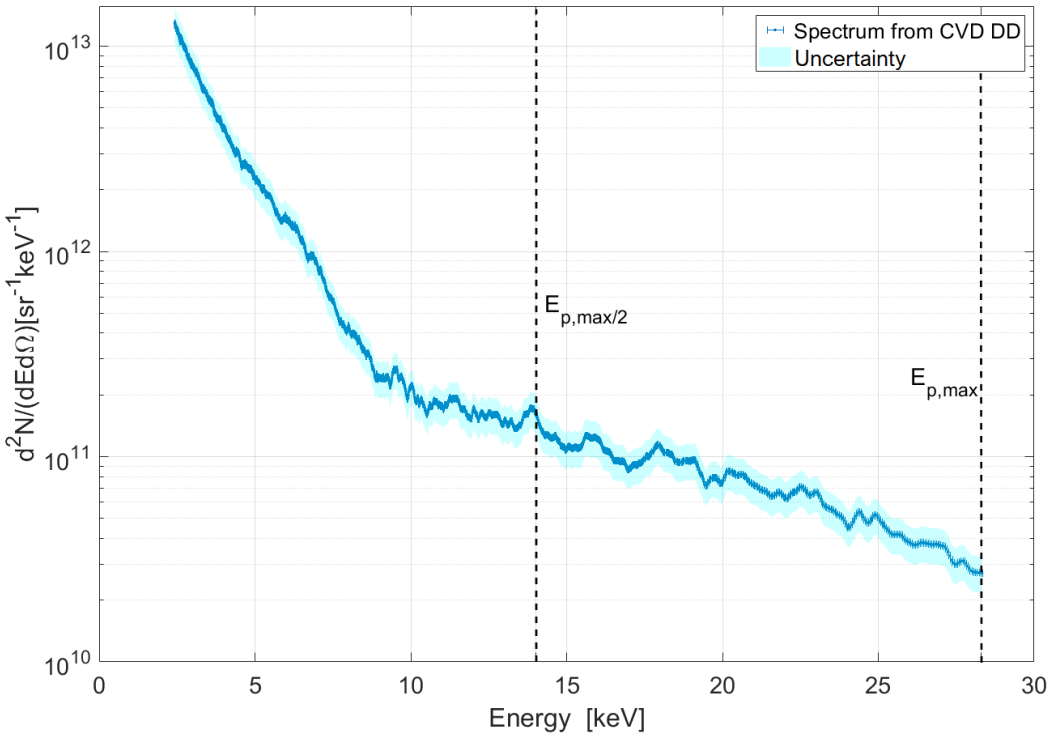

Figure 5.5. The spectrum obtained under the hypothesis of pure proton contribution from the signal collected with the diamond detector and reported in Figure 5.4. The two dashed lines enclose the energy range in which a pure proton contribution is expected.

Highlights of the experimental campaign

The measurements performed at the ABC laser facility allowed to investigate two aspects of the developed diagnostic. In first place a relatively high resistance to the produced EMPs was demonstrated.
Moreover it was possible to have a direct comparison between a TOF line equipped with a diamond detector and optimized to work in environments polluted by a high level of electromagnetic noise and two TOF lines equipped with Faraday cups. This comparison was indeed very interesting since it highlighted the intrinsic differences between the two kind of detectors. The signal generation mechanism of Faraday cups relies only on the amount of collected charges regardless the energy of the incoming particles, for this reason they result particularly suitable to measure bunches of ions having low energies but a high particle density. On the other hand, this energy range is the one in which diamond detectors, whose signal amplitude is proportional to the amount of energy deposited in its active layer by the incoming particle, are less performing. This fact explains why, in Figure 5.4, at around 1 keV, Faraday cup signals show a maximum whereas the signal generated by the diamond detector barely shows a variation in the slope.

5.2 Experiments with ECLIPSE laser at high repetition rate

The ECLIPSE laser is hosted at the Center for Intense Lasers and Applications (CELIA) located in Bordeaux. ECLIPSE is based on Ti:Sapphire technology ($\lambda = 810$ nm) and it delivers up to 150 mJ in 35 fs running at 10 Hz.
The experimental campaign held at this laser facility was devoted to the characterization of a laser-accelerated proton beam suitable for employment in proton-boron fusion scheme[96]. As discussed in more detail in Chapter 1, Section 1.4.4, the $p^{11}B$ cross section presents one main resonance that can be exploited to trigger the fusion reaction. The most favorable condition is found for protons providing a center of mass energy of 614 keV. However, to facilitate the detection of fusion products[96], it is more convenient to work with lower proton energies, down to the second resonance at 148 keV, in this way TNSA protons will produce the reaction in the superficial layer of the solid boron target. The lower reaction rate can be compensated with the high repetition rate of the laser providing many subsequent shots with a good reproducibility.
The ECLIPSE laser was used to irradiate 6 μm aluminum targets with an energy of 120 mJ for an intensity of 2×10^{18} W cm^{-2}, with an energy stability of 15% RMS shot to shot. The temporal contrast was of 4×10^{-9} at 12 ns and 10^{-5} at ASE level. The laser was operated at a repetition rate of 1 Hz to allow for target mechanical displacement.
As shown in Figure 5.6, a TOF line equipped with a single crystal diamond detector in the interdigital configuration was used to have an on-line characterization of the accelerated proton beam.

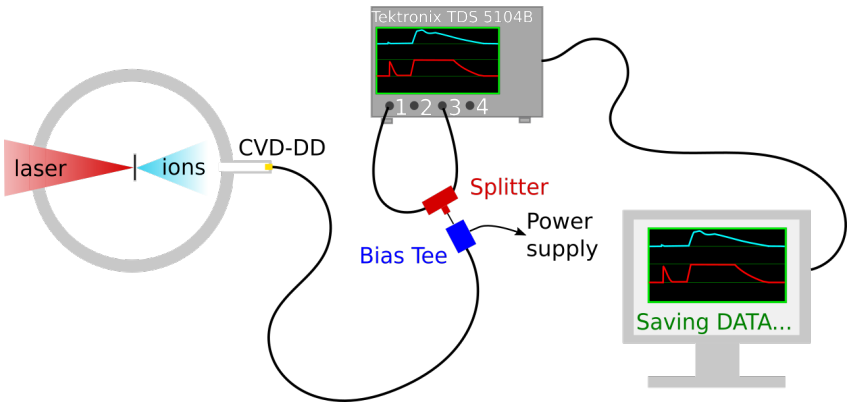

Figure 5.6. Experimental layout during the campaign held at ECLIPSE.

The detector was placed 72 cm downstream the target and it was biased with −150 V. The diamond was connected to a Tektronix TDS 5104B oscilloscope (1 GHz bandwidth, 5 GS/s sample rate) which was placed near the experimental chamber. Indeed, due to the relatively small energy of the laser beam, the level of produced EMP was low enough to allow to keep the scope at just few meters from the chamber, and quite short cables ($\simeq$ 5 meters long) were employed. The acquired signals were

then sent to a computer which was automatically downloading and storing the data after every shot, enabling a real-time characterization of the accelerated ion beam. This system allowed to acquire 148 consecutive and comparable shots enabling a repeatability study over a large statistics.
In Figure 5.7.a a mean TOF signal, computed by averaging those signals collected during the various shots, is shown.

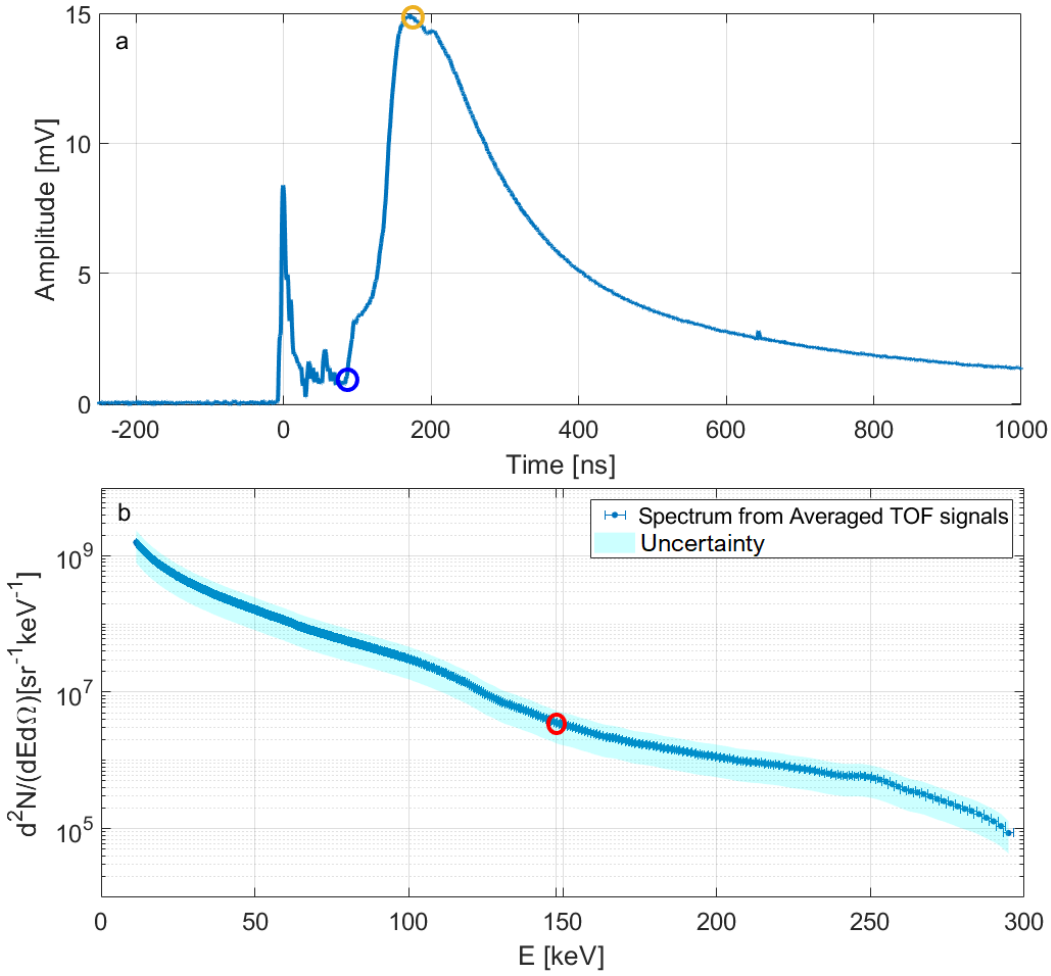

Figure 5.7. (a) TOF signal obtained by averaging all the 148 collected shots. The blue and orange dots highlight the portion of the signal taken into account by the statistical analysis shown in Figure 5.8. (b) The averaged TOF signal was used to compute a calibrated proton spectrum, following the procedure described in Chapter 4.

The contribution of two different populations can be highlighted. Indeed it is possible to see a change in the slope of the ion peak around 150 ns. This can be interpreted as a first energetic bunch of protons hitting the detector followed by a slower ion (or proton) population. The blue circle highlights the minimum TOF delay, i.e. the maximum detected proton energy, whereas the orange circle is used to spot the maximum signal value in the time domain.
In Figure 5.7.b the spectrum obtained from this averaged signal is shown. Due to

the small amplitude of the collected signals and their low energy, no filter was used. This means that the low energy spectral region can be affected by the presence of heavier ions. Following the argument presented in Chapter,4, Section 4.4.1, it is possible to assume a pure proton contribution only in the energy range (147, 294) keV. Nevertheless pure proton contribution at still lower energy is here very likely. On the other hand, to avoid any contribution from slow electrons hitting the detector, a grid biased at -500 V was used to deflect them before reaching the detector surface.

From the analysis of the collected data, the presence of two main proton populations was highlighted. In Figure 5.8 the distribution of the maximum proton energy and the one corresponding to the maximum particle yield is shown. Both are well described by a Gaussian fitting, having mean and standard deviation (μ, σ) of (288, 55) keV and (93, 30) keV respectively[132].

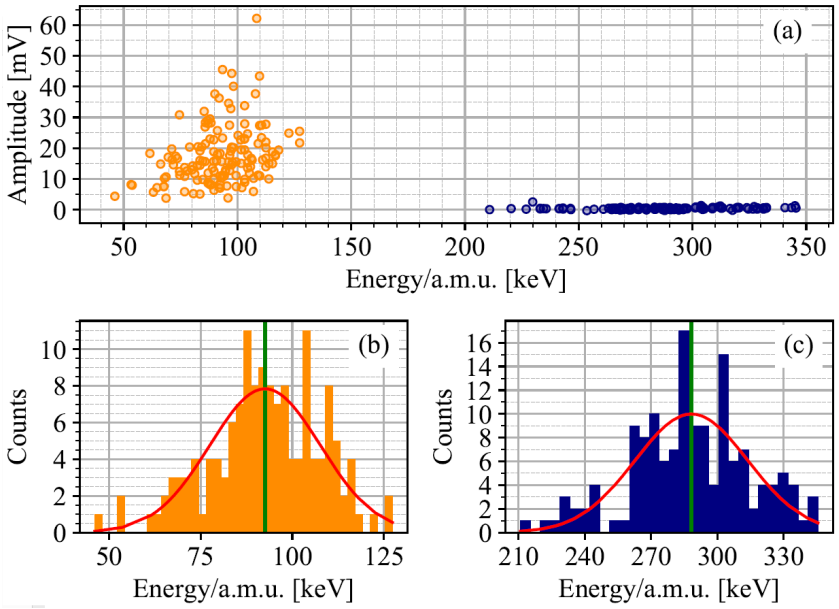

Figure 5.8. The results of the statistical analysis of the shots collected in the campaign. (a) For each shot the maximum detected ion energy (blue dots) and the one corresponding to the maximum ion yield are indicated; (b, c) histograms of the values in (a). The green line indicates the mean value, the red line is the Gaussian fitting. From *Cipriani et al.*[132]

Highlights of the experimental campaign

One of the main result achieved during this campaign is the demonstration of the capability of the developed diagnostic system to run at high repetition rate providing a real-time characterization of the accelerated ion beam.
This feature is of the utmost importance to enable the employment of laser-plasma accelerated ion beams in several applications. Indeed, one of the possible drawbacks of laser-plasma sources is the lower degree of repeatability with respect to conventional

accelerators. This is due to the nature of the acceleration process itself which depends on plenty of variables ranging from the laser beam quality to the characteristic of the irradiated target. The possibility to have a diagnostic able to monitor the interaction in real-time, shot after shot, is therefore a remarkable and essential advantage.

5.3 Experiments with the FLAME laser: TNSA regime

The Frascati Laser for Acceleration and Multidisciplinary Experiments (FLAME)[171] is based on Ti:Sapphire technology exploiting the Chirped Pulse Amplification (CPA)[10] scheme. An ultra-short pulse, provided by an oscillator, undergoes to temporal stretching so to be safely amplified by means of solid materials without damaging them. After amplification, the pulse is compressed back to a value as close as possible to the initial one. In this way a high intensity ultra-short pulse can be obtained. FLAME laser is designed to deliver up to 3 J energy in a pulse of 25 fs reaching a peak power of 200 TW. The employment of a compact multi-pass amplifier (Booster) allows to have a Amplified Spontaneous Emission (ASE) pre-pulse contrast lower than 10^{-9}.
During the experiment, carried out in collaboration with the INFN-LNF group headed by M. Ferrario and A. Ziegler, a 10 μm aluminum foil was mounted in a multi-target holder that allowed to have several consecutive shots without opening the experimental chamber. Two main diagnostics were employed to monitor the products of the laser-matter interaction. Ultra fast electrons, able to escape from the target, were characterized with the Electro Optic Sampling (EOS) technique performed by means of an electro optical ZnTe crystal[172,173]. Accelerated protons were measured by means of mono-crystalline diamond detector mounted at the end of a TOF line. This configuration allowed to have simultaneous information on protons and electrons to investigate possible correlation among the two populations[174].
As shown in Figure 5.9, the EOS crystal was placed 2 mm far from the target and above it, so to not intercept the proton emission on the target normal axis. Moreover, since the crystal was placed at a distance from the target larger than the Debye length (~ 1 μm for the discussed experimental conditions), only the electrons having energies sufficient to overcome the potential barrier generated at the rear side of the target were able to reach the crystal location[173]. The electric field of the electron beam then induces a local birefringence in the crystal that can be detected by a laser probe beam, whose polarization is modulated according to the electron bunch temporal profile. This allowed to map the longitudinal spatial distribution of electrons, encoded in the transverse profile of the probe laser, as well as the longitudinal charge distribution. The geometry of the set up, combined with the probe laser size, allowed to monitor a temporal window of 8 ps with a resolution of 100 fs[173].

The TOF line equipped with mono-crystalline diamond detector (CVD DD in Figure 5.9) was placed at the rear side of the target at 0° with respect to the target normal axis, for a total drift length $d_{TOF} = 105$ cm. In the experiment, both sandwich and interdigital electrode configuration diamond were, in turn, used.

During this experimental campaign, the technique was optimized to work in environments strongly affected by EMP pollution. To this purpose an EMP diagnostic

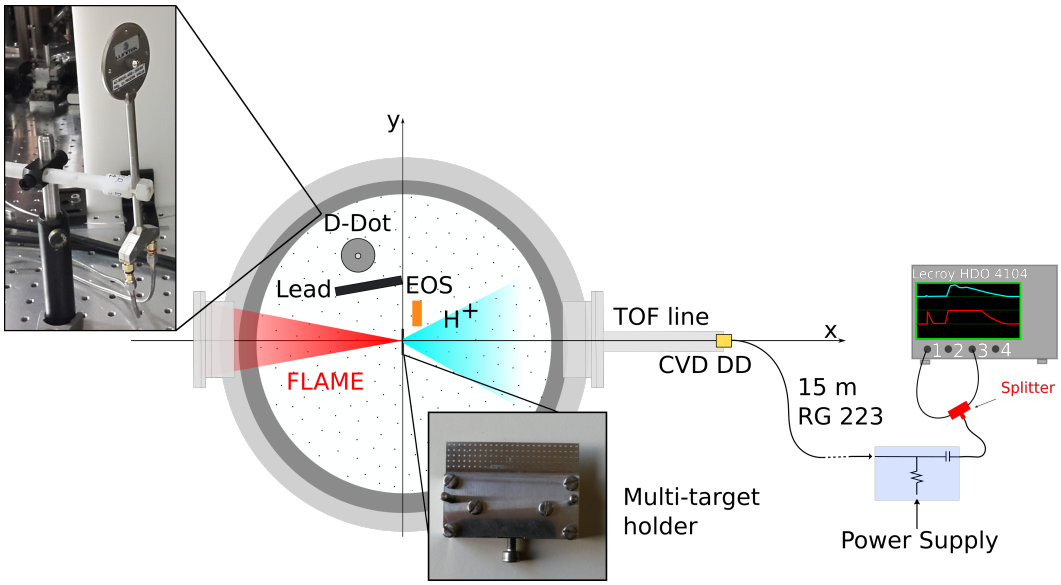

Figure 5.9. The experimental chamber layout, at the end of the KF40 pipe with the shielded holder containing the diamond detector. This was in turn switched between the IEC diamond and the SC diamond without modifying the surrounding set-up.

was also set up to monitor the electromagnetic field in the experimental chamber. This diagnostic was a customized version of the AD-80D(R) D-Dot differential electric field sensor (shown in Figure 5.9). It was positioned at 31 cm from the target and had 15 cm height from the chamber floor and -3 cm shift in the x direction with respect to the target position.
A typical EMP signal measured during the present experimental campaign is shown in Figure 5.10.a. From a shot with laser energy $E_L = 2.5$ J and intensity on target of $I_L = 1.7 \times 10^{19}$ W cm^{-2}. The sensing direction of the probe was radially oriented to the target, and a 5 cm thick lead block was used to shield the D-Dot from ionizing radiation generated by the interaction. The BIB-100G balun (250 kHz–10 GHz bandwidth) was connected to its terminals with two semi-rigid cables. The balun output was connected through a long double-shielded cable to the Tektronix DPO72004B (16 GHz, 50 GS/s) fast oscilloscope which was used to store the acquired data. In Figure 5.10.b the frequency spectrum of the detected signal, obtained by suitable Fourier Transform, is also given. It is evident that the produced EMP had a very wide band.
From the acquired measurement it was possible to get an estimation of the associated maximum peak-to-peak electric field[26] ~ 25 kV/m at that position, that is coherent with what expected for these experimental conditions[26].

As discussed in Chapter 4, Section 4.2, such high level of EMP fields are expected to produce diamond signals strongly affected, and sometimes they were even hidden, by the EMP oscillations. This was the case also here, at the beginning of the campaign. Nevertheless, thanks to the optimization of the acquisition system that avoided the electromagnetic field coupling with both the detector and the scope, it was possible to have clean TOF signals, from which spectrum reconstruction was

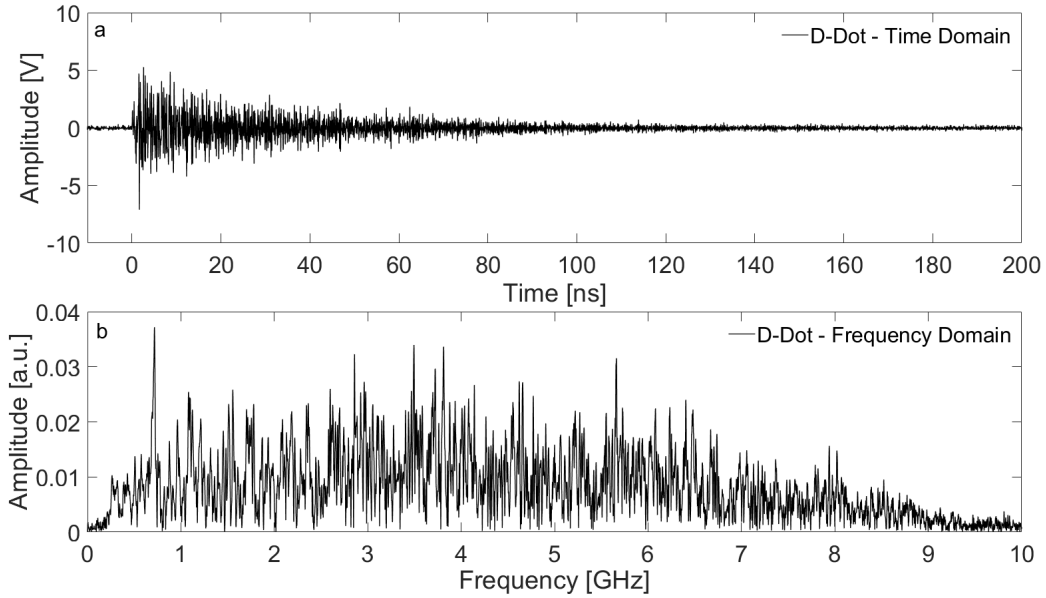

Figure 5.10. (a) The signal acquired by the D-Dot probe in the time domain; (b) the spectrum retrieved from the reported signal performing suitable Fourier transform. From *Salvadori et al.*[154]

possible[175].
As an example of the detrimental effects that the EMP coupling with the acquisition system can generate, two signals acquired during the first shots taken with the FLAME laser are shown in Figure 5.11. The detrimental effects of the EMPs are evident. The measurement of the time-of-flights of ion is completely hidden by the strong presence of EMPs and it is thus impossible to retrieve the particle spectrum. The improvement in the signal-to-noise ratio that was achieved by adopting the developed procedure is remarkable and can be appreciated in Figure 5.12 for similar experimental condition.
This signal was collected under conditions similar to those under which the signals shown in Figure 5.11 were measured. The difference was the employment of a scope with a lower bandwidth to which the diamond detector was linked by means of longer double-shielded cables. As discussed in Chapter 4, Section 4.2, this allowed to move the scope to larger distance from the experimental chamber so to reduce the direct EMP coupling with the scope. It also provided tens of nanoseconds delay between the EMP noise and TOF signal, giving a further effective EMP decrement on the measurements.

In the following sections the main results of the campaign are reviewed. In Section 5.3.1 the simultaneous characterization of protons and electrons is presented. Then, particular emphasis is given to the analysis of the proton measurements obtained with the TOF line. In Section 5.3.2 the importance to take into account the actual response of the detector in use is highlighted and, in Section 5.3.3, the performances of the two different electrode layouts of the single crystal diamond detectors are discussed.

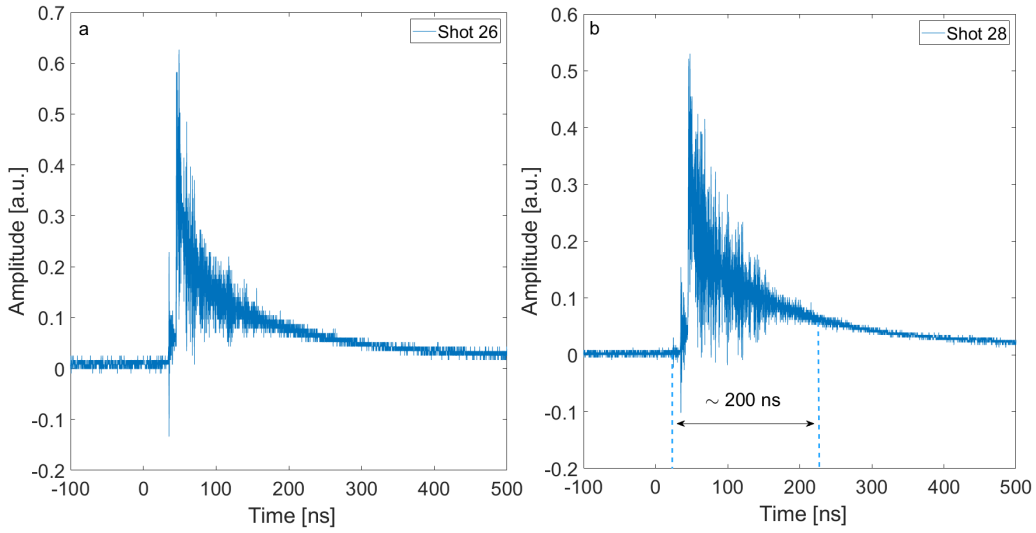

Figure 5.11. (a) a-b) The signals acquired from channel 1 of the scope during two different shots, performed in similar experimental conditions, where the detrimental effects of EMPs are apparent. In (b) the whole temporal extension of the EMP modulating signal is highlighted and estimated to be ≃200 ns.. From *Salvadori et al.*[175]

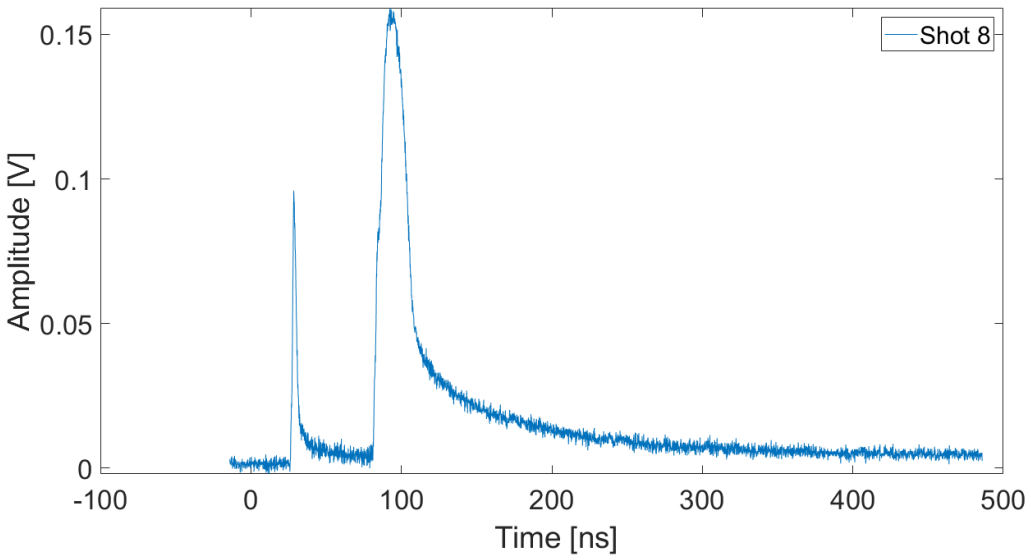

Figure 5.12. A signal acquired is similar condition to those shown in Figure 5.11 but employing a 15 m coaxial double-shielded cable and a scope with a lower bandwidth placed at much larger distance from the chamber.

5.3.1 Electrons and protons simultaneous characterization

The simultaneous employment of the EOS crystal and the TOF line allowed to obtain complementary information on accelerated electrons and protons[174,176,177]. Since the total charge and the energy distribution of the escaping electrons are linked to the hot electron temperature and thus to the accelerated ion energy, the capability of measuring their characteristics and correlating them with the accelerated proton

bunch parameters represents an useful instrument to obtain quantitative details of the acceleration process itself. The topic attracted thus the interest of different research groups[178–181] who reported on the existing correlation between the measured hot electron energy spectrum and the accelerated proton spectrum.
In the experiment carried out at FLAME laser facility, the EOS crystal provided information on the total charge and on the temporal length of the ultrafast electron bunch, i.e. the small fraction of hot electrons having enough energy to overcome the barrier potential generated by charge separation at the rear side of the target and thus are able to reach the location of the EOS crystal[173,174].
The TOF line equipped with the diamond detector allowed to have information on the maximum energy and the total number of accelerated protons. The behavior of both electrons and protons was thus investigated varying the laser parameters[174,176].
During the experiment, the temporal length of the laser was changed from 30 to 300 fs and the focal spot size from 30 to 120 μm ($1/e^2$ diameter) keeping the laser energy on target constant at 2 J.
In Figure 5.13 and 5.14 the main results are shown. For each set of parameters, several shots were taken. The experimental values are thus reported with their own statistical error. In Figure 5.13.a and b, it is possible to see that for both temporal duration and laser spot size scaling, the proton measured energy can be fitted with a power law[176]:

$$F(x) = \alpha x^{\beta} \tag{5.1}$$

being α and β free fitting parameters. The proton beam maximum energy as a function of the temporal duration of the laser pulse seems to be almost constant and can be described by the relation[176]:

$$E_{p,M} = (3.5 \pm 0.4)\tau_L^{-0.09} \tag{5.2}$$

where $E_{p,M}$ is in MeV and τ_L is in fs.

The ultrafast electrons detected by the EOS were characterized in terms of total charge and temporal duration. The information regarding their total charge is shown in Figure 5.13.a,b together with the already discussed results obtained for the proton maximum energy. The information regarding the temporal duration is instead shown in Figure 5.14.a,b. In the latter the results obtained for the proton maximum energy are reported for a prompt comparison.
The ultrafast electrons present an exponentially decreasing charge together with a linearly increasing temporal duration of the bunch as shown in Figure 5.13.a and in Figure 5.14.a, respectively. Concerning the dependence on the focal spot dimension, things are quite different: the protons maximum energy, as well as the number of energetic electrons, exponentially decreases with the widening of the focal spot on target as it is possible to see in Figure 5.13.b and in Figure 5.14.b. The dependence of the maximum proton energy on the focal spot size can be written as[176]:

$$E_{p,M} = (4.8 \pm 0.2)r_L^{-0.25} \tag{5.3}$$

where $E_{p,M}$ is in MeV and r_L is in μm Given the dependence of the laser intensity on both the laser temporal duration and focal spot dimension ($I_L = E_L/(\pi r_L^2 \tau_L)$), from the previous two equations it is possible to infer the relation between $E_{p,M}$ and

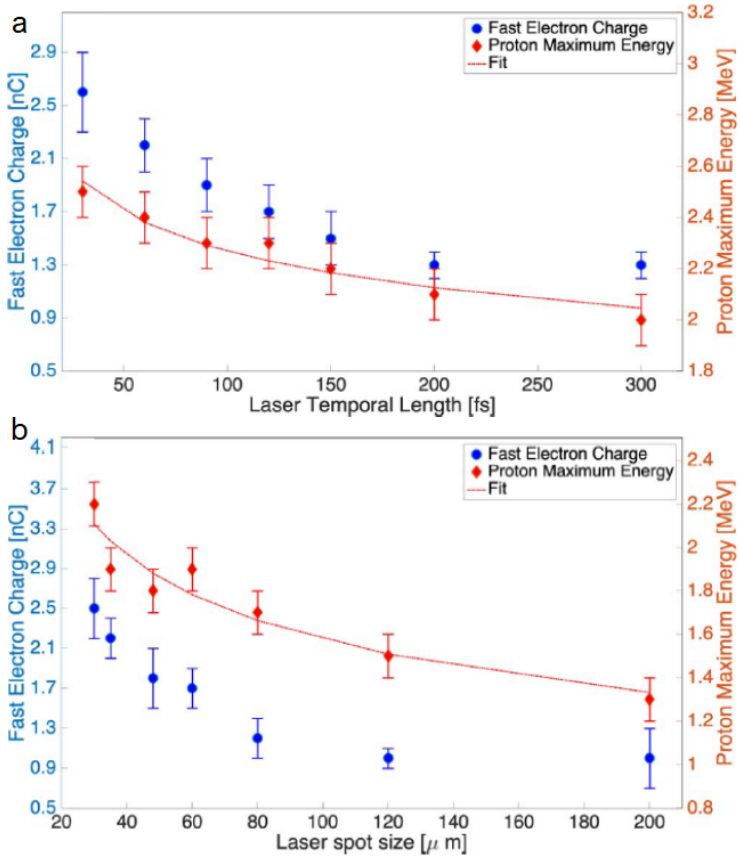

Figure 5.13. The measured charge of the fast electron bunch (blue dots) and the proton maximum energy (red dots) as a function of (a) laser temporal length and (b) laser spot size. From *Bisesto et al.*[174].

the laser intensity:

$$E_{p,M} \propto I_L^{0.1}. \tag{5.4}$$

This relation holds for a constant laser energy on target of 2 J, temporal duration spanning from 30 to 300 fs and a focal spot in the range 30-120 μm, corresponding to an intensity on target $I_L = 0.1 - 2 \times 10^{19}$ W cm^{-2}.

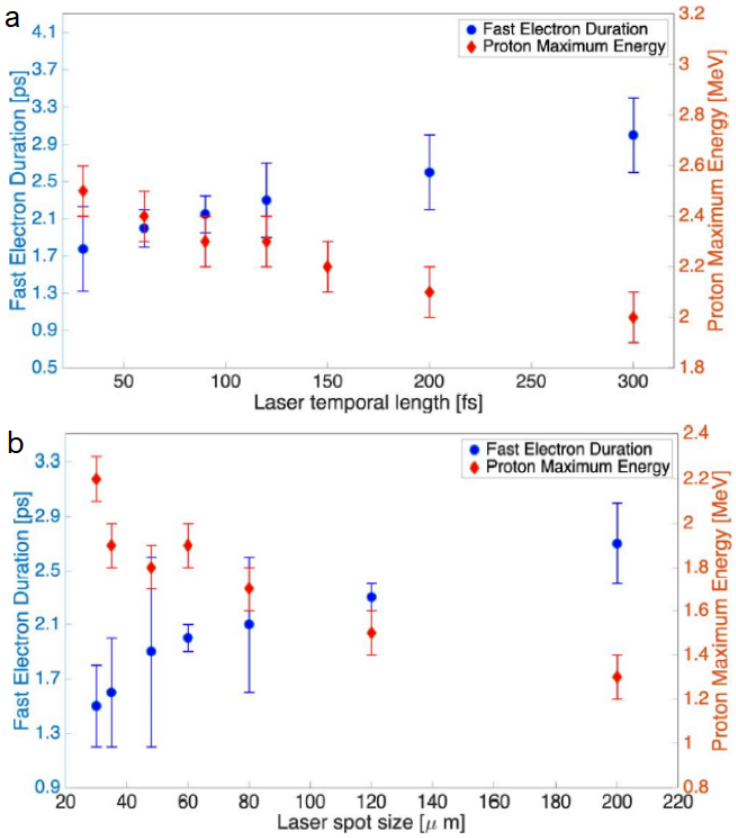

Figure 5.14. The measured temporal duration of the fast electron bunch (blue dots) and the proton maximum energy (red dots) as a function of (a) laser temporal length and (b) laser spot size. From *Bisesto et al.*[174].

5.3.2 Influence of the detector characteristics on the spectrum reconstruction

The main purpose of this section is to evaluate the influence of the detector characteristics when estimating the proton spectrum. The measurements were performed by employing the diamond detector in interdigital configuration, whose characterization has been presented in Chapter 3, Section 3.2.
The detector was used without any filter and it was connected to two channels of the scope operated with different scales, to increase the dynamic range of the diagnostic system, as discussed in Chapter 4, Section 4.1.
The shots were performed by irradiating a 10 μm aluminum target with the FLAME laser operated with energy of 3 J and 30 fs temporal duration for an intensity on target reaching $\sim 2 \times 10^{19}$ W cm^{-2}. The obtained time domain signal is shown in Figure 5.15.

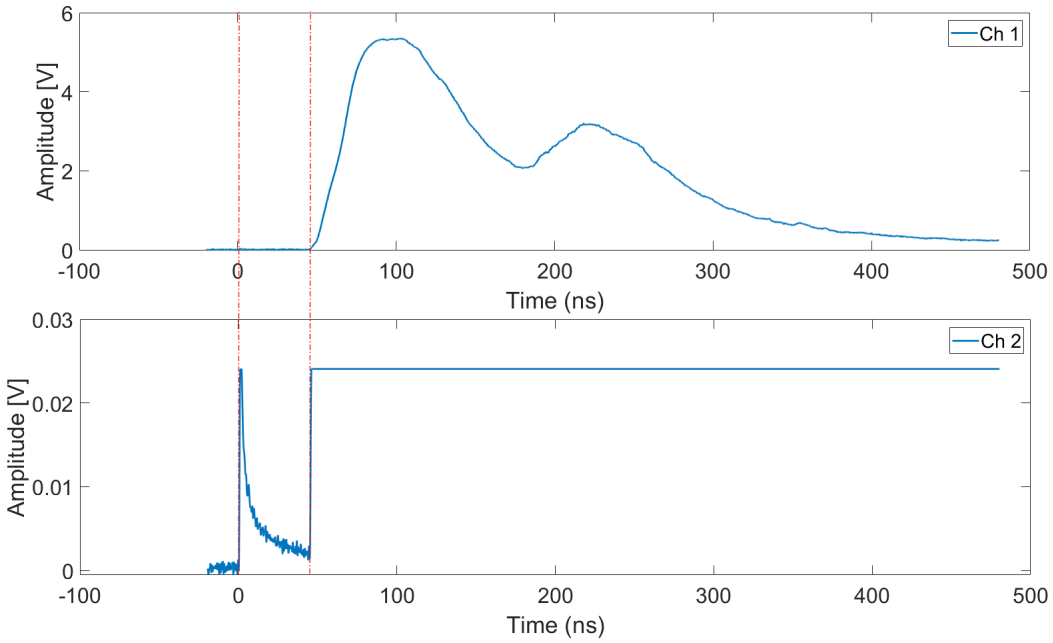

Figure 5.15. The time domain signal acquired with the diamond detector in interdigital configuration without any filter. The two dashed lines highlight the synchrony between the two channels of the scope used for the signal acquisition. From *Salvadori et al.*[175].

To retrieve the spectrum, a de-embedding procedure was applied to consider the effects of the used long cable, that acts like a low-pass filter, attenuating the high frequency signal, as described in Chapter 4. Then, two methods were used to compute the proton spectrum from a signal acquired with a TOF line equipped with an interdigital diamond detector.
The first method, which exploits equation (4.13), does not take into account the response of the specific detector in use for different energies and was used in previous works[133]. The second, on the other hand, relies on the accurate detector calibration to retrieve the actual behavior of the diamond in use, as described in Chapter 4. In particular, equation (4.14) was applied for each temporal interval defined by the temporal resolution of the used detector, which is $\simeq$ 500 ps (see Chapter 3), and then divided by the associated energy.
The spectra obtained applying these two methods are shown in Figure 5.16. Both the techniques agree on the main features of the spectrum; nevertheless it is possible to note that the spectrum estimated by applying equation (4.13) systematically underestimates the number of detected particles for energies higher than $\simeq$ 700 keV, because it assumes a uniform Charge Collection Efficiency CCE = 1 over the whole detector thickness.
The observed discrepancy grows with increasing energy because, in this detector, for particles with higher energy, and thus larger range, the charge collection efficiency is lower. Indeed, the difference in the behavior is ascribable to the interplay of two factors, both considered in equation (4.14) with the CCE (E_p) term:

1. The amount of charge that is collected at the detector electrodes is lower than

that generated by an incoming particle along its path in the semiconductor, since some charges are recombined while traveling to the electrodes.

2. The drop of the collection efficiency at increasing depth which, in this electrode set up, is caused by the larger distance from the electrodes as discussed in Chapter 3, Section 3.2.

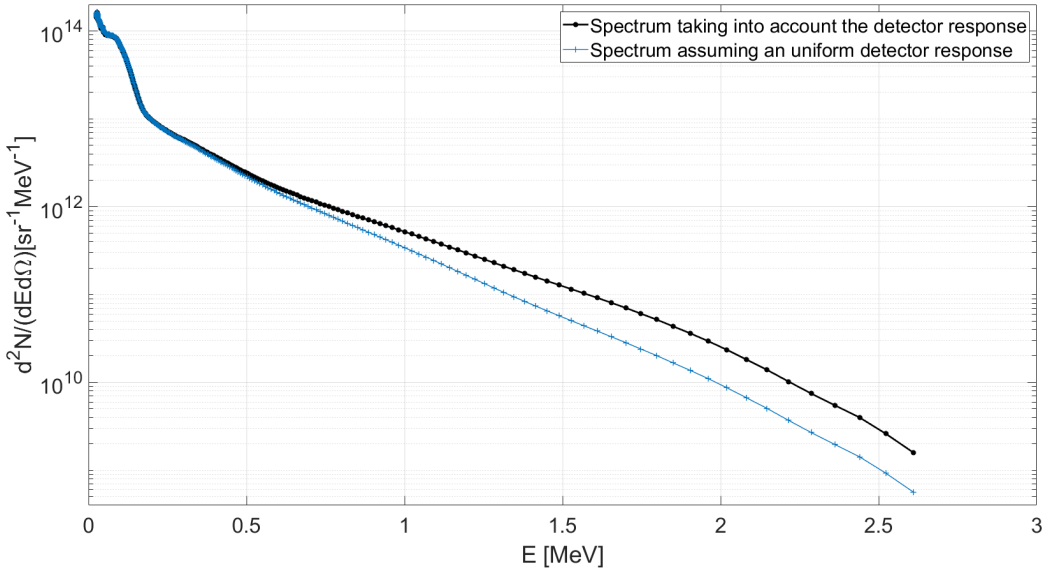

Figure 5.16. Proton spectrum obtained following the two described methods. Both the curves present the same main features, but the one computed assuming an uniform detector response systematically underestimates the proton number for energies above $\simeq$ 700 keV since it does not consider the actual CCE of the detector. From *Salvadori et al.*[175].

5.3.3 Comparison among two different electrode layouts

In Chapter 3 a detailed characterization of two different electrode layouts for a monocrystalline diamond detector has been performed: the interdigital electrode configuration (IEC) and the sandwich configuration (SC).
During this experiment they were tested in similar experimental conditions to evaluate their performances in terms of proton detection and to compare the obtained results when their actual response is carefully taken into account.
They were in turn placed at the end of the TOF line and collected data for several consecutive shots. In order to avoid any possible spurious effect, they were both employed without any filter covering the active surface.
In Figure 5.17 the signals collected by the two diamond detectors during similar shots (five for each detector) are reported. For all the analyzed shots the energy on target was of 2.6 ± 0.05 J and the temporal duration $\tau = 30$ fs, for a mean intensity on target of $\sim 1.8 \times 10^{19}$ W cm^{-2}.

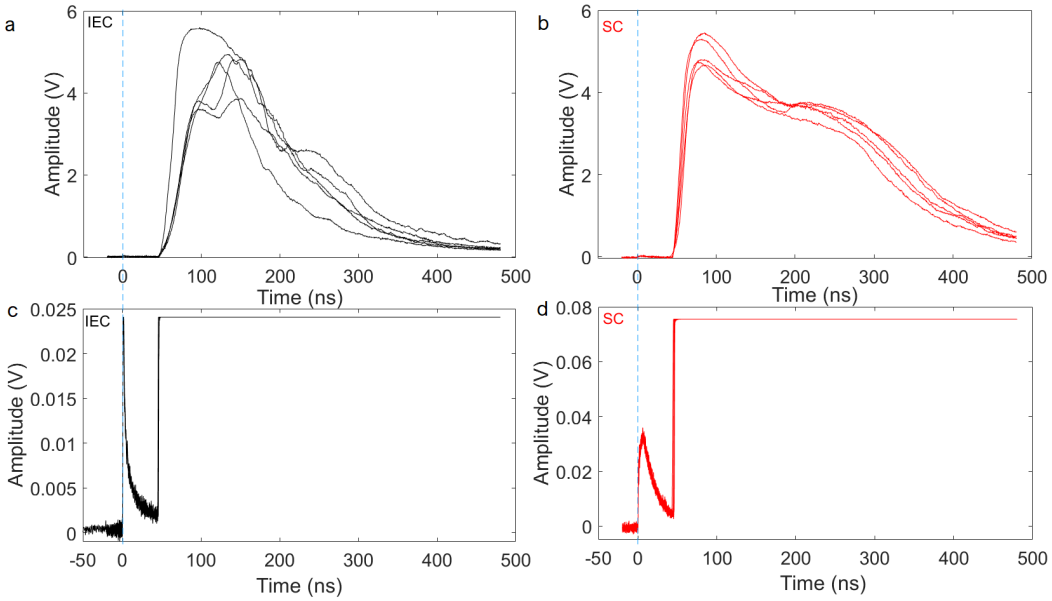

Figure 5.17. The collected signals during different similar shots from the (a) IEC detector and (b) the SC detector. In (c) and (d) the signals collected with the channel operated with a finer scale from the IEC and the SC detector respectively are shown.

The signals collected by the two detectors systematically present some differences. The photopeak in the signal collected by the SC diamond detector presents a wider FWHM as well as a larger amplitude with respect to the one provided by the IEC detector. This can be explained by the greater sensitivity to the emitted X-ray radiation and to slow electrons of the SC detector. On the other hand, the signals obtained with the IEC detector are characterized by the presence of different peaks due to the detection of heavie ions population. These peaks result in a smooth modulation of the signal in the SC detector. This difference in the behavior of the two detectors arises from their different charge collection efficiency. Indeed, ad discussed in detail in Chapter 3, Section 3.2 the IEC diamond is characterized by a charge collection efficiency which has its maximum near the detector surface and then it starts to decrease for increasing depths. This is due to the fact that the electric field is more intense near the surface where the electrodes are placed. As highlighted in Chapter 3, both the detectors presented comparable temporal responses ($\simeq$ 500 ps) when irradiated with α particle of 5.486 MeV. Nevertheless, the latter were stopped at a depth of $\sim$ 15 μm, where electric field of the IEC detector has already started to decrease. Thus it is possible to assume that for ions stopped at depths $<$ 15 μm the effective temporal response of the IEC detector is sensibly higher than the one of the SC detector which on the contrary presents an almost uniform electric field along all its thickness.
This slower temporal response leads, for low-energy ions, to an integration of the signal over a larger temporal step, smoothing the different peaks. One more difference that is more evident in Figure 5.18, where one signal coming from the IEC detector is overlapped to one provided from the SC for a better comparison, consists in the slope of the rising edge of the signal produced by protons detection, which is greater for

the SC detector. This is ascribable to its higher collection efficiency for protons with high energies. Indeed, the two detectors provide the same minimum detected arrival time which corresponds to a maximum proton energy of $\simeq 2.5$ MeV. A proton of this energy, according to the simulation made with the SRIM code[153], is completely stopped inside the diamond at a depth of $\simeq 36$ μm where most of its energy is lost. But at that depth the efficiency of the IEC detector has already dropped, thus providing a smaller signal than the SC detector for the same amount of generated charge.

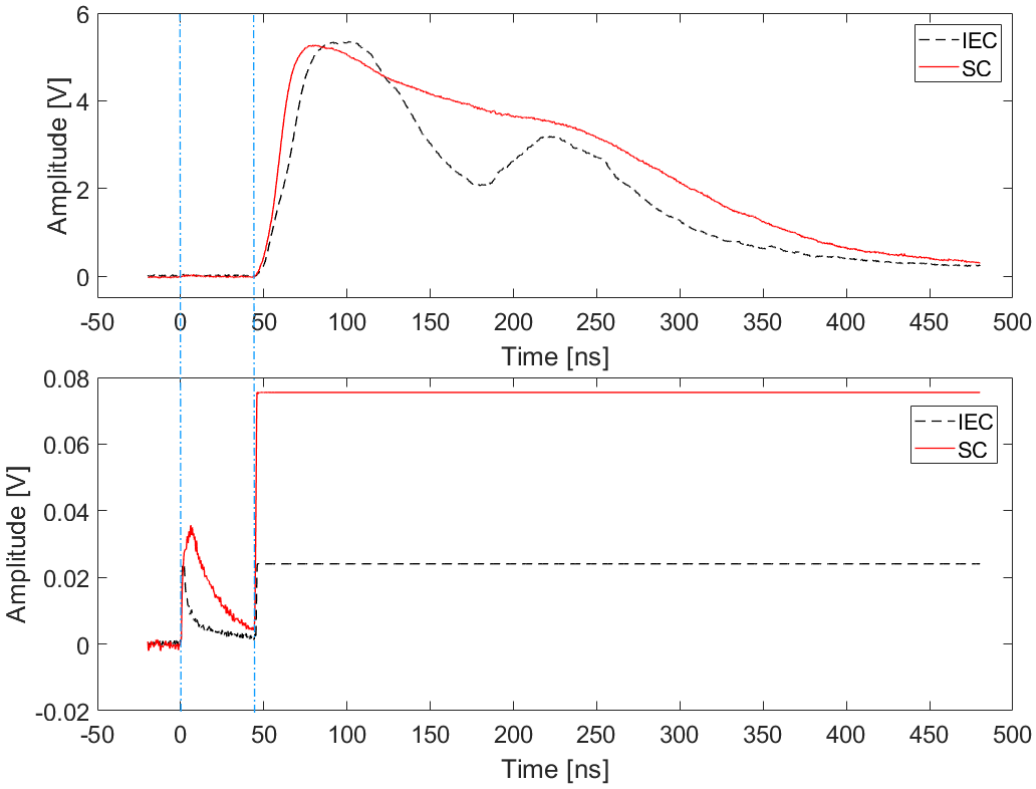

Figure 5.18. Signals collected by the SC diamond detector (red solid line) and by the IEC diamond detector (black dashed line).

The spectra obtained for the two cases are shown in Figure 5.19.

Both the spectra have been computed taking into account the detectors calibration, in particular for the SC detector a constant charge collection efficiency has been used, whereas for the IEC detector, CCE(E_p) has been computed for each energy bin exploiting the relationship (3.2). Indeed, in this experiment, all the detected protons had energies low enough to get them completely stopped inside the detector active volume, hence for the SC detector it is reasonable to impose CCE(E_p) $\simeq 1$. On the other hand, the CCE(E_p) of the IEC detector changes according to the depth reached by the impinging protons inside it.

The solid angles $d\Omega = \frac{A}{d_{TOF}^2}$ were calculated taking into account the sensitive area A of the detectors, previously estimated in Chapter 3, Section 3.2.1. To retrieve

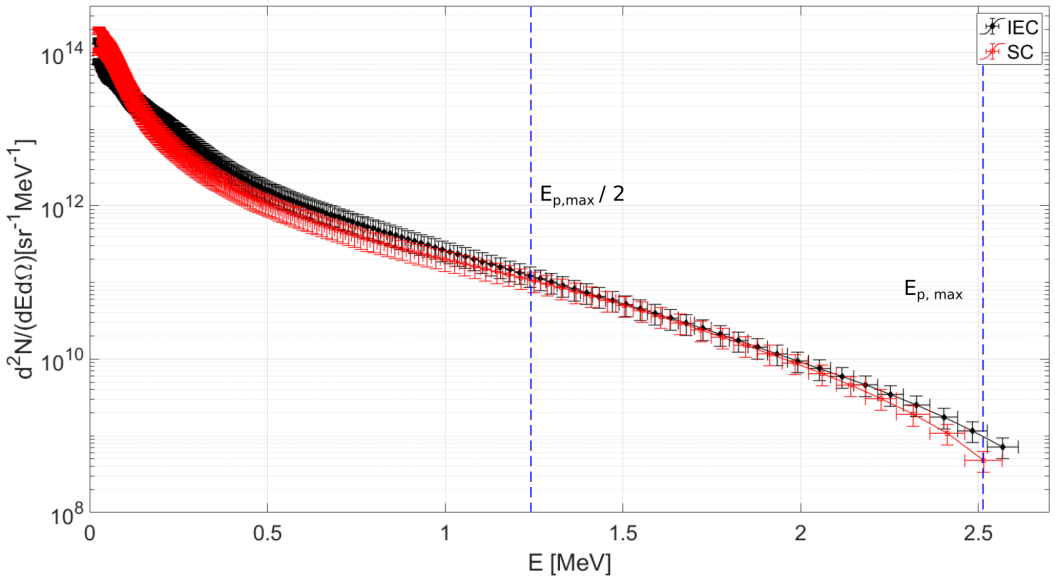

Figure 5.19. Spectra obtained from data collected by the SC diamond detector (red line with square marker) and by the IEC diamond detector (black line with full dots). The blue dashed lines delimit the range in which the spectra are due to a pure proton contribution.

the spectrum, we made the simple assumption that only protons were detected. This is useful for the considerations here discussed, but it is important to remark that different ion species are accelerated during the interaction and they contribute to the acquired signal.
Nevertheless, assuming that particles were accelerated just by a pure TNSA mechanism in classical conditions, it is possible to identify different regions in the spectra as discussed in section 4.4.1. Hence, given the proton maximum energy $E_{p,MAX}$, in the energy range ($E_{p.MAX}/2$; $E_{p.MAX}$), only protons can contribute to the signal, whilst for lower energies it is likely to have the contribution also from heavier ions such as carbon, oxygen, nitrogen and aluminum. The two reported proton energy spectra are almost identical in the range $1.2 - 2.5$ MeV proton energy. This result also highlights the reproducibility of the experiment thanks to the low shot-to-shot fluctuations that were achieved. Moreover, despite all the mentioned differences among the IEC and SC detectors, the accurate knowledge of their characteristics allowed to properly weight and convert the raw acquired signals, which at a first glance were quite different, into a consistent proton number for each energy interval. In the proton energy range lower than 1 MeV, slight differences can be observed between the two curves. This is probably due to the heavier ion contributions considering the different efficiency of the two detectors to them.

Highlights of the experimental campaign

The experimental campaign hosted at FLAME laser facility has been an integral part of the development process of the presented TOF diagnostic technique. The needs of the experiment was the real time characterization of particles with energies

up to few MeV/a.m.u. with remarkable levels of EMPs.
This environment offered the chance to test and refine the optimization made during the experiments performed at ABC and ECLIPSE and it was also possible to exploit the high energy and high repetition rate of this laser system (a shot every few minute versus a shot every hour) to collect a statistics over several shots so to characterize the behavior of the employed diamond detectors in a real case scenario, to compare different layouts and to get accurate spectra.

5.4 Experiments with the ALLS laser: TOF as a handy online monitoring system

The ALLS laser system[182] exploits an amplification scheme similar to the FLAME laser but it benefits of a double CPA system. It is also based on the Ti:sapphire active medium and is able to deliver up to 5 J in 20 fs. The beam can be focused down to ~ 4 μm allowing an intensity on target of 5×10^{20} W cm^{-2}. The laser beamline benefits of a cross-wave polarizer (XPW) as part of a beam cleaning technique before injecting in the second CPA, which leads to an ASE pre-pulse contrast of 10^{-10} at -100 ps before the main pulse, along with a steep power rise with contrast of 10^{-6} at -3 ps.
Two main experimental campaigns were carried out exploiting the ALLS laser system. The first was devoted to the proton beam line optimization and it served as preparation for being used as laser-driven proton source for evaluating the effectiveness in Ion Beam Analysis (IBA) applications.
The results of these two campaigns are reported below. In Section 5.4.1 the cross calibration performed during the preparatory phase is described in detail and, in Section 5.4.2 the experimental results on the laser-driven Particle Induced X-ray Emission (PIXE) are briefly discussed.

5.4.1 Time of Flight and Thomson spectrometer cross calibration

During the preliminary experiments the ALLS laser was used to irradiate targets of different materials (aluminium, copper and gold) and thicknesses (ranging from 1 μm up to 5 μm). The laser energy on target was $E_L = 2$ J, providing an intensity on target of $I_L = 1.3 \times 10^{20}$ W cm^{-2}.
As shown in Figure 5.20.a and b, to monitor the proton emission, two TOF lines, both equipped with single crystal diamond detectors covered with a 10 μm aluminum filter, were mounted at $+6°$ and $-9°$ with respect to the target normal axis at a distance $d_{TOF,+6°} \simeq 102$ cm and $d_{TOF,-9°} \simeq 120$ cm from the target respectively.
The employed diamonds presented two different electrode layout; one was in the interdigital configuration and the other in the sandwich configuration. Since the two have different sensitivities for different energy ranges, in order to reduce any systematic error in the energy measurements, they were in turn switched between the two TOF lines to check the consistence of their measurements.

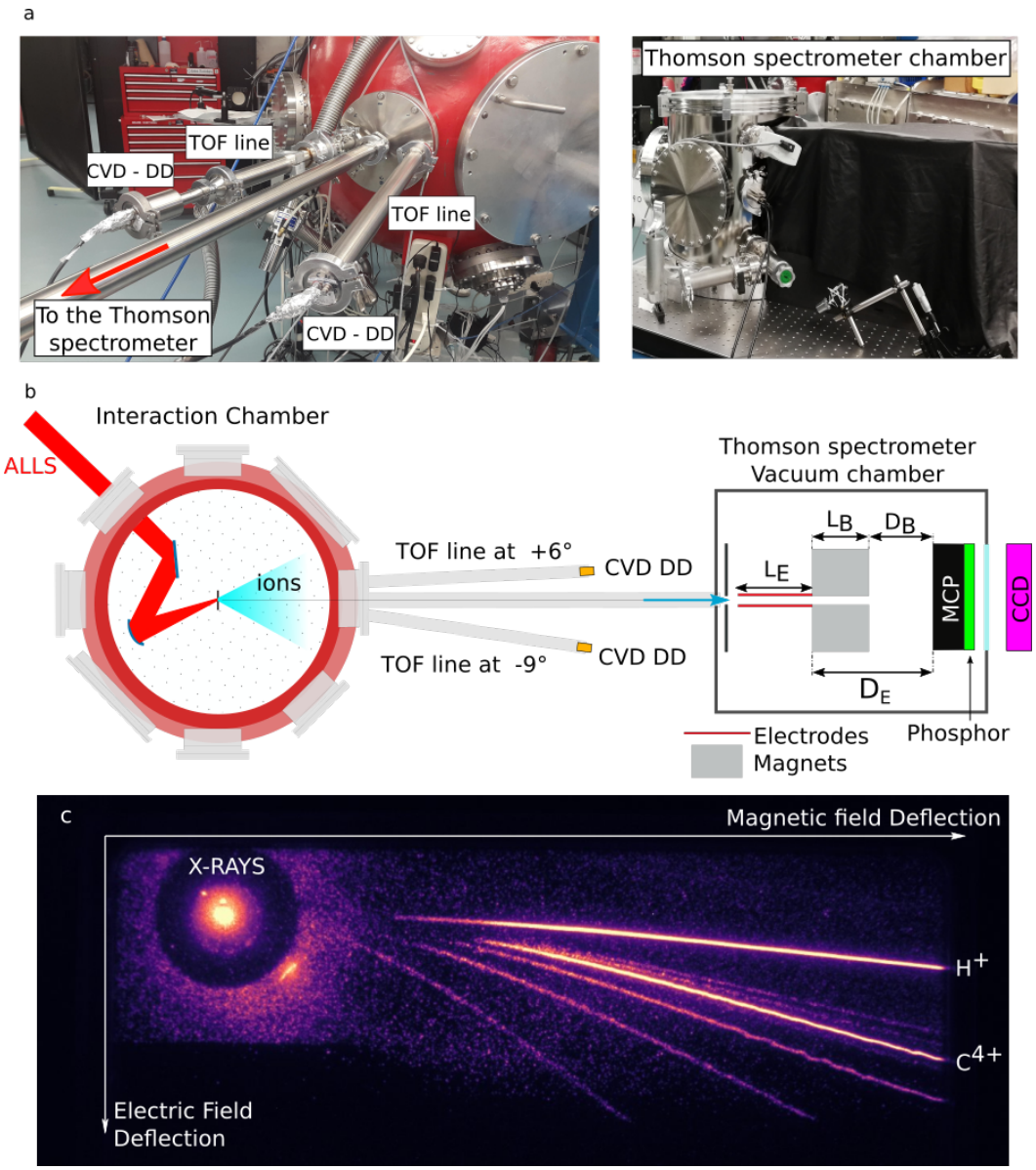

Figure 5.20. (a) The experimental chamber set-up during the preliminary phase. Two TOF line were set up at $-9°$ and $6°$ degrees and equipped with single crystal CVD diamond detectors. A thomson Spectrometer was placed on the target normal axis. (b) A raw signal collected from the Thomson spectrometer during a typical shot.

The signal collected by the diamond detectors was sent to a Tektronix DPO 7104 scope (1 GHz bandwidth and 5 GS/s sampling rate) through 15 m long calibrated double-shielded RG 223 cables. The transmission line was characterized by measuring its total S_{21} scattering parameter using the Agilent E8364B Network Analyzer. Simultaneously, a Thomson spectrometer coupled with a MCP - phosphor assembly was installed on the target normal axis. The MCP detector was in Chevron configuration and provided very high gain ($10^6 - 10^7$) suitable for particle counting. It was coupled with the the P43 phosphor which has a high light yield and a decay time of

3.2 ms. In Figure 5.20.b a scheme of the spectrometer is shown and in Figure 5.20c a signal acquired with this Thomson spectrometer, during a typical shot is reported. The described set up allowed to have information on the angular distribution of the accelerated proton beam and to cross-calibrate the two diagnostic systems.
The MCP-phosphor assembly has been calibrated in intensity on the 2×6 MV Tandem linear accelerator from Université de Montréal, to retrieve the particle scaling factor that is needed to determine the particle number observed in the MCP-Thomson spectrometer for protons and carbon ions[183].
A cross-calibration between the two different diagnostics was then performed in a real setting scenario:

1. **TOF energy estimation as benchmark for TS calibration** The accurate characterization of the diamond detector ensures a reliable estimation of the maximum proton energy. This was used to adjust two fundamental parameters for the Thomson spectrometer employment, namely the field integrals I_E and I_B.

2. **Comparison of TOF and TS measurements at similar angles** The Intensity calibration performed on the MCP-phosphor assembly allowed to have a reliable estimation of the number of protons detected by the Thomson spectrometer during the experiment. This was used to verify the effectiveness of the methodology adopted to retrieve the proton spectra from TOF measurement.

1.TOF energy estimation as benchmark for TS calibration

Since the TOF technique coupled with diamond detectors ensures an accurate measurement of the maximum proton energy, this technique was used to calibrate the relevant parameters of the Thomson spectrometer required for the kinetic energy retrieval (i.e. the field integrals I_E and I_B introduced in Chpater 2).
On the other hand, the calibration of the proton numbers obtained on the Tandem accelerator was used to validate the calibration of the diamond detectors (given in Chapter 3).
The non-relativistic, non-paraxial dispersion equations for the solution of charged-particle kinematics traversing static electric and magnetic fields were used to compute the theoretical trajectory of ions passing thorugh the Thomson spectrometer. These are given by[183]:

$$x(E_k, I_B) = \frac{\sqrt{2E_k m L_B}}{qI_B}\left\{\cos\left[\arcsin\left(\frac{qI_B}{\sqrt{2E_k m}}\right)\right] - 1\right\} - D_B \tan\left[\arcsin\left(\frac{qI_B}{\sqrt{2E_k m}}\right)\right] \tag{5.5}$$

$$y(E_k, I_E) = \frac{qI_E}{2E_k}\left(\frac{L_E}{2} + D_E\right) \tag{5.6}$$

where q, m and E_k are particle parameters, being its charge, mass and kinetic energy respectively. Whereas the parameters depending on the Thomson spectrometer

characteristics are I_B, I_E, L_B, L_E,D_B and D_E. The quantities I_B and I_E are the magnetic and electric field integrals, L_B and L_E are the magnetic and electric field length, D_B and D_E the magnetic and electric field drift length.
The fields integral, already defined in Chapter 2, for the specific design of the Thomson spectrometer here discussed, can be written as:

$$\begin{cases} I_B = \int_0^{L_B} B(z)dz = \bar{B}L_B \\ I_E = \int_0^{L_E} E(z)dz = \bar{E}L_E \end{cases} \tag{5.7}$$

Therefore, the cross calibration was performed adopting the following methodology[183]:

i The magnetic field $B(z)$ was measured with a calibrated Gaussmeter. The length of the magnets L_B was used as a first approximation to determine the magnetic field integral I_B.

ii Both the voltage across the electrodes ΔV and the electrode separation distance d, including their length L_E, were measured and used as a first approximation to determine the electric field integral I_E.

iii The diamond detector with the electrodes in sandwich configuration was temporarily moved on the 0° axis. Over a statistically significant amount of laser shots, the TOF detector was used to measure the maximum proton energy.

iv After placing back the TOF detector and the Thomson spectrometer to their initial positions, the parameter I_B was adjusted until a good match between the two maximum energies obtained on the 0° axis by the TOF and Thomson spectrometer was achieved. The maximum proton energy ratios at different angles (i.e. energy at +6° vs 0°) should be in agreement with typical TNSA-based proton beam values found in literature[18,184].

v For a given ion species (protons for instance), I_E is incremented until best match is achieved with the experimental positions on the detector and the theoretical curves given in (5.5) and (5.6) .

vi As a final verification, the theoretical curves can be generated for other ion species (carbon ions for instance), and should match with experimental positions on the detector. This should confirm the correct parameters I_B and I_E.

The performed characterization of the employed diagnostic allows using detectors located away from the 0° axis to retrieve indirectly the characteristics of the beam on the central axis, in particular for what concern the value of the maximum proton energy. Indeed, during the cross-calibration procedure, it was possible to verify the relation existing among the maximum proton energy achieved on the target normal axis and the one both at +6° and -9° for the specific laser parameters and target material and thickness. Therefore from the measurement performed by means of one of the two TOF line it is possible to infer the characteristics of the proton beamline on the TNSA axis.

This feature was exploited when the beamline was used as laser-driven proton source for Particle Induced X-ray Emission application, as discussed in more details in Section 5.4.2.

2. Comparison of TOF and TS measurements at similar angles

Figure 5.21.a shows the comparison between the maximum proton energy estimated by the Thomson spectrometer and the two TOF lines, for different shots performed in similar conditions (i.e. using the same laser pulse energy and 5 μm copper foil targets). The mean value of the maximum energy of the selected shots is (6.6 ± 0.9) MeV for the Thomson spectrometer at 0°, (5.9 ± 0.8) MeV for the TOF at 6° and (4.9 ± 0.7) MeV for the TOF at −9°.

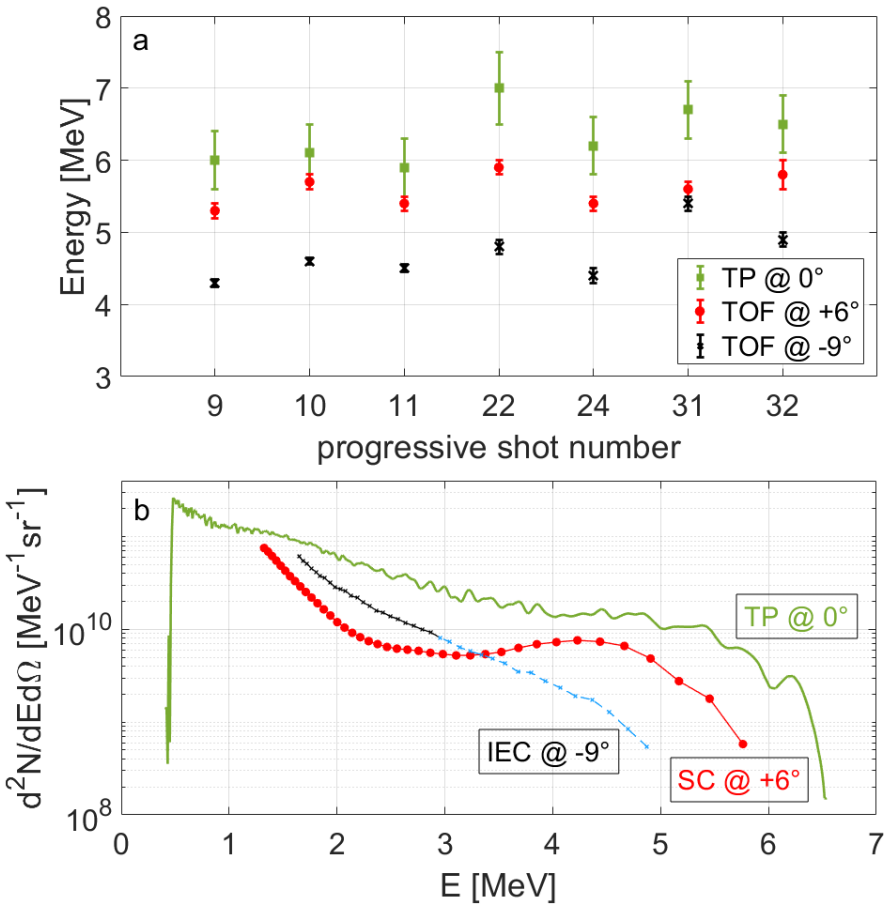

Figure 5.21. (a) Maximum proton energies at different angles obtained by the three used diagnostics: The two TOF lines placed at −9° and 6°, as well as the Thomson spectrometer (TP) placed at 0°. All the data are obtained with shots performed on 5 μm copper targets. Measurements were performed over 8 shots during which all diagnostics were operational. (b) Comparison among the spectra obtained by the aforementioned diagnostics for a typical shot, labeled as 32 in (a).

It is possible to observe a good agreement between all the three diagnostics which respond similarly for each shot. Small shot-to-shot fluctuations were observed with a standard deviation on the maximum energy of 14% for the three diagnostics, indicating a good repeatability.
In Figure 5.21.b, the proton spectrum obtained with the Thomson spectrometer is shown for a typical shot together with the spectra provided by both TOF lines.
These two spectra were retrieved from the time domain signal following the procedure discussed in Chapter 4 with some additional cautions. First of all the lower energy extreme of the interval for the reconstructed proton spectra is determined by the growing uncertainty due to the presence of the 10 μm aluminum filter, that produces high uncertainty for energies close to its proton energy cut-off ($\sim$ 750 keV).
Moreover, concerning the number of estimated particles, two different energy ranges have to be taken into account. Up to 3 MeV, the behavior of the two diamond detectors is well characterized by the calibration discussed in Chapter 3. Indeed, protons are completely stopped inside the active thickness of the detector, depositing their whole kinetic energy.
Beyond this limit, a correction factor has to be introduced to properly estimate the proton numbers. The uniform response $\mathrm{CCE}_{i,SC}$ of the diamond detector with electrodes in the sandwich configuration (i.e. 6°) allows to easily take this into account. For protons of impinging energy ranging from 1 up to 20 MeV, SRIM code was used to compute the energy effectively deposited inside the diamond detector. Then the ratio $R(E)$ between the deposited energy and the impinging proton energy was computed. This was used as multiplication factor for the energy in eq. (4.14) which becomes:

$$N_i = \frac{Q_i \epsilon_g}{\mathrm{CCE}_{i,SC} E_i R(E_i) q_e} \tag{5.8}$$

On the other hand, the energy-dependent charge-collection-efficiency of the interdigital configuration (i.e. $-9°$) does not allow to follow the same procedure. In this case a calibration with high-energy protons at a conventional accelerator is necessary to have a reliable estimation of the proton number and is planned in the near future. Consequently, the spectrum estimated by the TOF placed at 9° is expected to be underestimated for energies higher than 3 MeV (dashed blue line in Figure 5.21.b), whereas a reliable behavior is ensured for proton energies below 3 MeV.
Since the two TOF lines are placed at $+6°$ and$-9°$ whereas the Thomson spectrometer is on the target normal direction, the number of detected high-energy protons, as well as the maximum energy detected by the TOF, is lower. Nevertheless both the diagnostics provide similar proton spectra which follow roughly the same trend.
The main difference between the three spectra relies on the smooth peak at energies higher than 3 MeV which is visible in the spectrum retrieved from the sandwich diamond signal. This is most likely ascribable to the presence of a high energy proton population which indeed can be highlighted also in the respective time domain signal, reported in Figure 5.22. .

The time-domain signal reported in Figure 5.22 allows to introduce another issue that has to be properly taken into account when an accurate evaluation of the

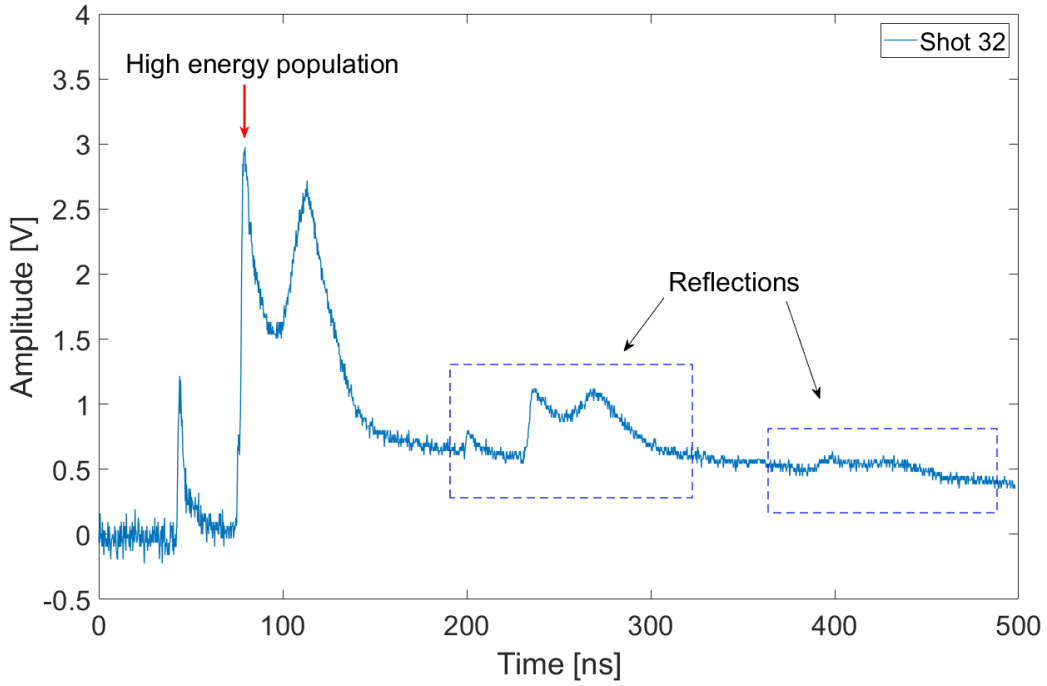

Figure 5.22. The raw time-domain signal collected by the SC diamond detector for the spectrum reported in Fig. 5.21. The presence of a high energy proton contribution is highlighted.

impinging number of particle is needed.
It is possible to see that the signal generated by the particle distribution in the time-domain, from $\sim$ 70 ns to $\sim$ 150 ns, is clearly duplicated at later times with lower amplitude. The first replica is at $\sim$ 195 ns and the second one at $\sim$ 390 ns. These were demonstrated to be reflections of the main signal due to an impedance mismatch. Only a portion of the signal will reach the scope, whereas the remaining part will be reflected towards the diamond and then reflected back towards the scope by the diamond, which is intrinsically an open circuit when not activated by ionizing radiation.
The portion of signal which is reflected back will be detected at later times after traveling the whole transmission line for a second time (a scheme is shown in Figure 5.23).

All the contributions can be properly taken into account thanks to the calibration performed on the transmission line and the additional attenuation coefficient α, due to the presence of reflections, can be estimated as

$$\begin{cases} \alpha a_{att} a_{cable} S_0 = S_1 \\ \alpha a_{att} (1-\alpha) a_{cable}^3 S_0 = S_2 \end{cases} \tag{5.9}$$

where a_{att} is the contribution of the used attenuator and a_{cable} is the attenuation due to the cable. The latter can be retrieved by comparing the amplitude of the acquired signal before and after the de-embedding procedure. S_1 and S_2 are the amplitudes of the main signal and of the first replica, respectively, and S_0 is the unknown

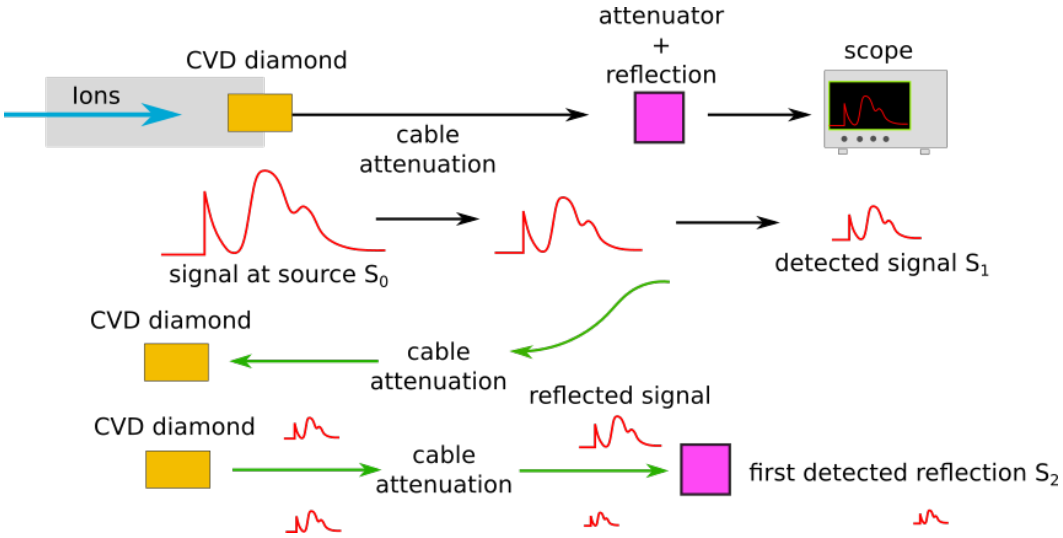

Figure 5.23. The signal generated at the detector site traverses the whole transmission line and is attenuated by the cable as discussed in the previous chapter. When the signal has to cross the attenuator used to lower the signal amplitude, only a portion is able to cross it, whereas the other one is reflected back. This portion of the signal travels through the transmission line for two more times before being detected from the scope generating the first replica of the signal.

amplitude of signal coming from the detector and produced by the radiation. Solving (5.9) for α, the following relation can be obtained:

$$\alpha = 1 - \frac{S_2}{S_1}\frac{1}{a_{cable}^2} \tag{5.10}$$

To retrieve the actual amplitude of these signals obtained when the reflections are present, the measured amplitude have to be multiplied by a factor $1/\alpha$ which, in the case of the signal reported in 5.24.a, results to be 1/4.
In Figure 5.24.b the TOF spectrum in blue is computed without the reflection contribution, whereas that over it (red with dot markers) is with the α coefficient included.

The performed beamline cross-characterization by means of a Thomson spectrometer along with the two TOF lines, allowed us to verify the proton beam alignment on a shot-to-shot basis and to characterize the beam divergence by comparing the maximum proton energy and the yield obtained at the three investigated angles (0°, +6°,-9°).
Moreover, this allows knowing the proton beam characteristics on shots where the 0° axis of the Thomson spectrometer is blocked by a secondary target, but not the axes of the TOF lines. This is the case discussed in the next section where the setup used to investigate the laser-driven particle-induced X-ray emission (PIXE) and X-ray fluorescence (XRF) is presented.
The discussion of the main results of the experimental campaign goes beyond the purpose of this PhD thesis, and they are presented in detail in *Puyuelo's PhD thesis*[185]. Nevertheless, in the following, we analyze one particular aspect that allows us to

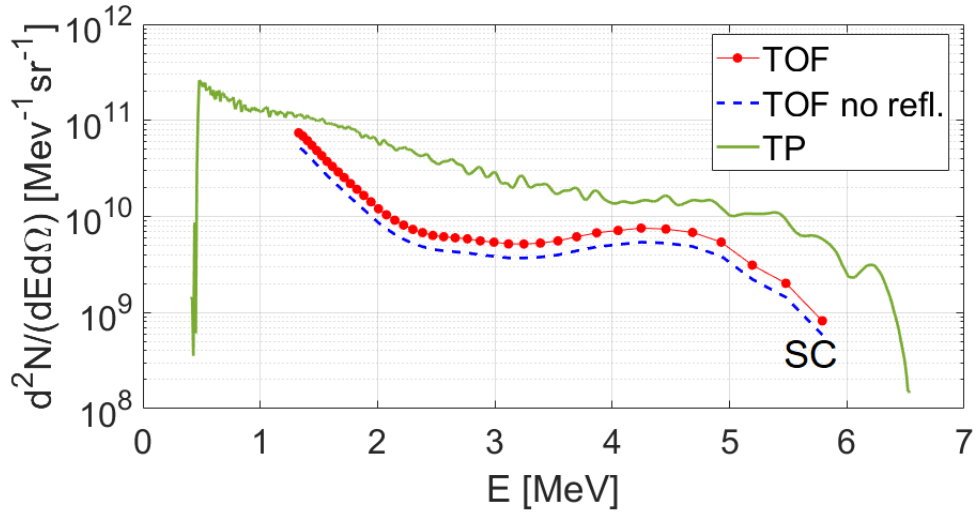

Figure 5.24. The spectrum with the correction due to the reflections contribution compared to the one without taking them into account.

emphasize the benefits of having a TOF line providing shot-to-shot characterization of the proton beam at 9° from which, thanks to the performed cross-calibration of the diagnostics, it is possible to retrieve in a first approximation the beamline behavior on the TNSA axis. The information on the proton spectra, retrieved by the analysis of the TOF measurements, allowed to understand if only one of the two processes (PIXE/XRF) was contributing to the X-ray spectra generation or if, instead, it was produced by a combination of both mechanisms.

5.4.2 Laser driven particle source for PIXE and XRF analysis

During the experimental campaign on PIXE and XRF the arrangement of the diagnostic was modified to include a small auxiliary vacuum chamber where the investigated samples were positioned to be irradiated. The TOF line at $-9°$ was equipped with a diamond detector in the interdigital configuration whereas the one at $+6°$ was removed to install a X-ray camera devoted to monitor the X-ray emission induced by laser-driven accelerated protons impinging on the sample to be analyzed. The X-ray camera used was a PI-LCX:1300 (1300 $\times$ 1340 pixel of 20 μm), during operation it was cooled with liquid nitrogen and placed at 8 cm from the exposed sample at 90° with respect to the target normal axis. The high quantum efficiency of the chosen X-ray camera allowed to retrieve the X-ray spectra by single photon counting in the range 2.2 - 20 keV. A scheme of the described set up is shown in Figure 5.25.

This setup allowed the sample to be inserted inside the auxiliary chamber before every shot using gate-valve isolation along with an independent pumping system. The positioning of the auxiliary chamber on the TNSA axis obstructs the line of sight of the Thomson spectrometer that was not used when the secondary target is in place. During these shots, the TOF line is devoted to the characterization of the accelerated protons. Nevertheless, thanks to the gate-valve isolation, it was possible

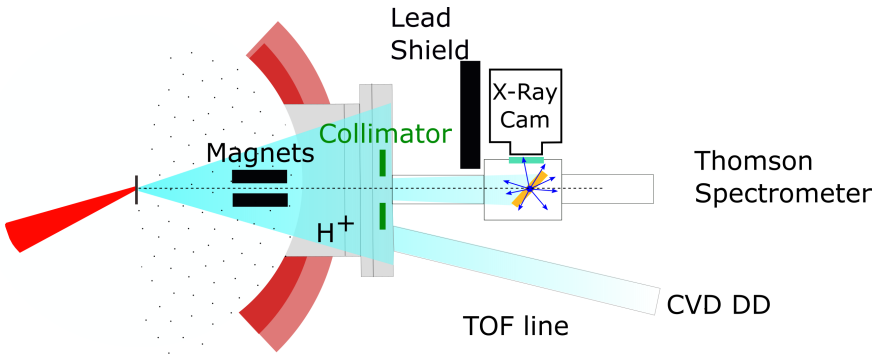

Figure 5.25. The experimental chamber set up during the PIXE measurements. A secondary auxiliary vacuum chamber was mounted on the line of sight of the Thomson spectrometer. One TOF line is operational during each shot at 9°. The X-ray camera is shielded by the radiation emitted during the laser-matter interaction by a thick lead brick.

to free the Thomson spectrometer line-of-sight in a few minutes.
With this configuration, it was possible to employ simultaneously the TOF and the Thomson spectrometer when measuring the proton spectra, as it was done for the cross-calibration procedure, and to relate the proton spectra, measured at 9° by the TOF line, with the one measured at 0° by the Thomson spectrometer. With this configuration, it was possible to infer the main characteristics of the proton beam impinging on the target shot-by-shot and in real-time, even if the sample was blocking the Thomson spectrometer. During the measurements, a 15 μm aluminum filter was placed in front of the diamond detector to cut the heavier ion contributions. Due to this filter, the minimum detectable proton energy by the TOF line was 1.8 MeV.
As already mentioned, two different mechanisms may contribute to the X-ray emission from the exposed sample. The X-ray Fluorescence (XRF)[186] and the Proton induced X-ray emission (PIXE)[90,91]. In both cases the emission of characteristic X-rays from the sample is due to the re-arrangement of the electrons in the orbitals as they release the energy acquired via the photoelectric effect from the impinging energetic photon (in XRF) or via Coulomb interaction from charged particles (in PIXE).
The X-rays emitted as a consequence of an electron transition to the K-shell are denoted as K X-rays. In particular, two line emissions are usually distinguished, the K_α and K_β. The first is generated when the electron filling the vacancy in the K-shell was from the L-shell, the second when the electron come from the M-shell. The number N_X of emitted photons produced by the transition of an electron to the K-shell can be written as:

$$N_X = N_a N_p(E_p)\sigma_K(E_p) \tag{5.11}$$

Thus, N_x can be estimated from the number of atoms for the unit surface of the sample N_a, the number of impinging particles N_p (or, for the XRF, the intensity of the photon beam), and the transition cross-section of the impinging particle energy, $\sigma_K(E_p)$ for the K transition.
In Figure 5.26.a the PIXE X-ray K_α cross section is plotted as a function of the

sample atomic number for different proton energies. In Figure 5.26.b, the case of the 4 MeV proton beam is compared with the cross sections induced by X-rays of different energies (XRF process).
The knowledge of the proton spectrum is thus a useful information to foresee the amount of emitted X-rays from a sample and for a full comprehension of the acquired X-ray spectra. Indeed, the total amount of emitted X-rays is going to be determined by a superimposition of the various transitions induced by the broad energy spectrum typical of laser-driven proton sources.

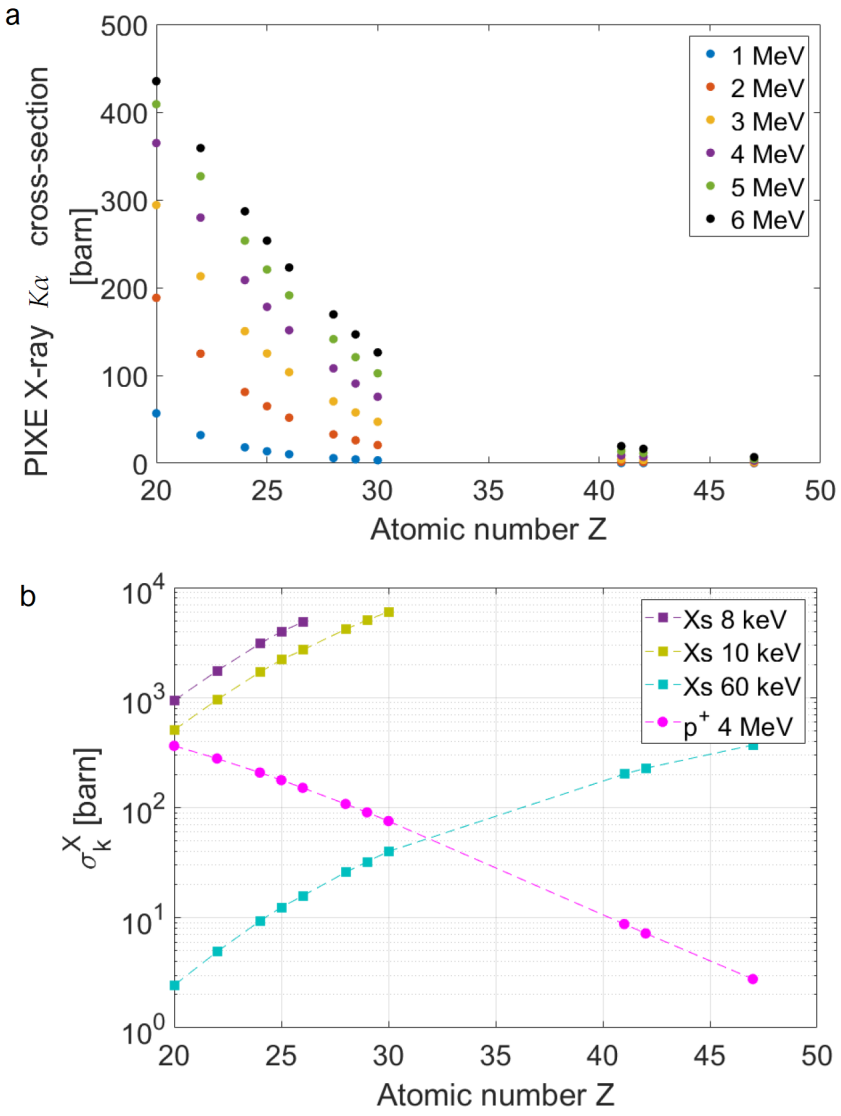

Figure 5.26. (a) PIXE X-ray K_α cross section with different proton energies as a function of the sample atomic number. (b) X-ray K_α cross-sections induced by photons of different energies and the one induced by 4 MeV protons. From *Puyuelo's PhD thesis*[185]

As an example we want to compare two X-ray spectra obtained from the same sample when different targets were employed for the laser-matter interaction. To

this purpose as secondary target a stainless steel sample was used. The latter was previously analyzed by means of Energy Dispersive X-ray (EDX) spectroscopy, obtaining the spectrum shown in Figure 5.27.a. The EDX spectroscopy technique was used in conjuction with a Scanning Electron Microscope (SEM) and relies on the detection of the X-rays emitted by the samples irradiated by the SEM electron beam. This analysis highlights the presence of four components: iron, chromium, calcium and nickel. The same sample, irradiated by two different laser-driven sources, provided the X-ray spectra shown in Figure 5.27.b and 5.27.c. The first was obtained using a 3 μm aluminum foil as laser-matter interaction target, whereas the second one was produced using a 5 μm copper foil.

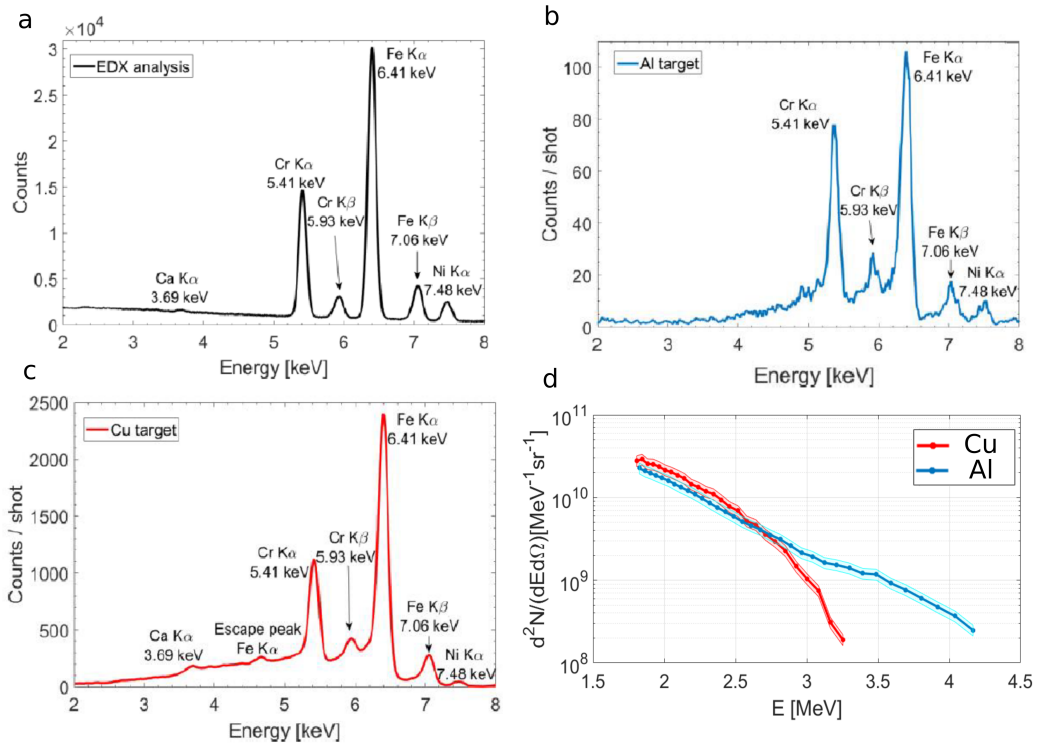

Figure 5.27. The characterization of a stainless steel sample obtained with (a) EDX analysis, (b) single shot laser-driven X-ray emission spectrum obtained employing as laser-matter interaction target an aluminum foil and (c) a copper target. (d) The proton spectra obtained from the TOF line for the shots providing the X-ray spectra reported in (b) and (c). The X-Ray spectra in a,b and c are taken from *Puyuelo's PhD thesis*[185].

Few differences among the three X-ray spectra can be spot. The presence of the same elements is shown in the three of them with the exception of the calcium which is identified only from the EDX analysis and the copper laser-driven source. This is ascribable to the greater spectral intensity obtained when using the copper target. This enhancement in the X-ray yield can be explained by two factors: a strong increment in the proton spectra when using a copper target, or by the contribution of XRF which is absent when irradiating aluminum. Indeed, the line-emission X-rays produced by the laser interaction with the aluminum target are not producing any

detectable XRF (since it falls outside the range 2.2-20 keV to which the used X-ray camera is sensible).
The first hypothesis can be easily verified by comparing the spectra obtained from the TOF line for the investigated shots. As shown in Figure 5.27.d, the two are almost identical for energies lower than ~ 2.7 MeV, but then, the proton spectrum obtained from the aluminum target, which was the thinner among the two, has a larger yield and extends to higher energies. Nevertheless, a first rough estimation of the total number of protons per unit solid angle gave similar values. For the shot performed on aluminum target we got 1.2×10^{10} sr^{-1} whereas for the one performed on copper we obtained 1.4×10^{10} sr^{-1}. As shown in equation (5.11), for a fixed proton energy, the number of emitted X photons depends linearly on the number of protons irradiating the sample surface. Hence, the difference in the proton spectra does not justify the 20-fold larger amplitude of the X-ray spectrum obtained when the copper target is used as source. The cause of the increment in the fluorescence yield has to be found in the XRF contribution.
This second hypothesis was verified by means of Geant4 simulations. The material sample was modeled by using the results from the EDX analysis. The simulation results were scaled by using the measured proton spectra and the number of primary atomic X-rays generated in the laser-matter interaction. In the case of aluminum target, only protons were used as irradiation source, hence only PIXE mechanism is considered. On the other hand, in the case of copper, also the X-ray contribution was introduced, so to consider both PIXE and XRF mechanisms interplay. The results of the simulations present a remarkable agreement with the experimental data, as shown in Figure 5.28 where the integrated measured counts in the K_α peaks of the three main elements shown in the spectra of Figure 5.27 (Cr, Fe and Ni) are compared with those resulting from the simulation.
This confirms that in the case of aluminum the dominant mechanism is the PIXE whereas in the case of copper the contribution coming from XRF cannot be neglected and plays a major role.

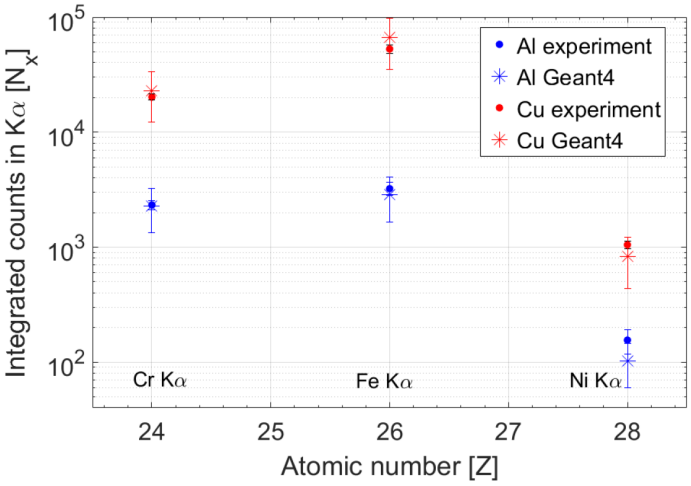

Figure 5.28. Measured integrated number of counts in the respective Cr, Fe, and Ni K_α peaks obtained from the spectra depicted in Figure 5.27b and c. These are compared to the Geant4 simulation results. From *Puyuelo's PhD thesis*[185].

Highlights of the experimental campaign

Two main goals were achieved during the experiments performed at the ALLS facility.

- The simultaneous employment of a Thomson spectrometer and the TOF line at similar angles allowed to perform a cross-calibration of the two diagnostic systems. Then a careful analysis of the data collected during several shots was performed to validate the methodology presented in Chapter 4 to retrieve the accelerated particle spectrum

- The employment of the developed TOF diagnostic for a real-time characterization of the accelerated proton beam used for Ion Beam Analysis application. This gives a nice demonstration of the feasibility in employing the optimized TOF line as an on-line monitoring system for laser-driven proton beams used for various applications.

5.5 Experiments with the LLC laser: on line detection at multiple angles

The Lund Laser Center hosts a 40 TW laser based on Ti:sapphire ($\lambda = 810$ nm) technology[187] exploiting the CPA scheme. The laser is designed to deliver up to 1.5 J energy in a pulse duration of $\tau_L = 35$ fs with a contrast of $0.5 - 1 \times 10^{-9}$ up to 50 ps before the main pulse. Moreover, the system benefits of a double plasma mirror (DPM) configuration, which is able to provide an ultra high pre-pulse contrast of 10^{-12} at 3 ps before the main pulse, at expenses of the maximum energy on target which is reduced of $\sim 40\%$.
The experimental campaign, carried out in collaboration with the Lund University group headed by C.G. Wahlström, was devoted to the evaluation of a possible enhancement in the TNSA process efficiency by means of structured targets. The basic idea behind the employment of such targets is to enhance the laser absorption mechanism, so to obtain higher laser-to-proton energy conversion efficiencies. This objective is pursued by exploiting the higher surface-to-volume ratio and the high porosity provided by this kind of targets which allows the laser to interact with a larger portion of the target materials[91].
To fully take advantage of these features, the laser needs to have a high contrast ratio, in order to avoid the nanostructures to be destroyed by the pre-pulse.
Several kinds of structures have been already investigated both theoretically[188–191] and experimentally[192–195] in the past. During this experimental campaign, two main types of structures were employed:

1. copper nanowires (NW) grown on thin gold foil, with nanowires having an average diameter of 200 nm and lengths ranging from 0.5 up to 10 μm[196] (see Figure 5.29.a,b);

2. a random distribution of zincum oxide nanofibers deposited on 10 μm aluminum foils. The thickness of the deposition ranged from 5 μm up to 10 μm (see Figure 5.29c).

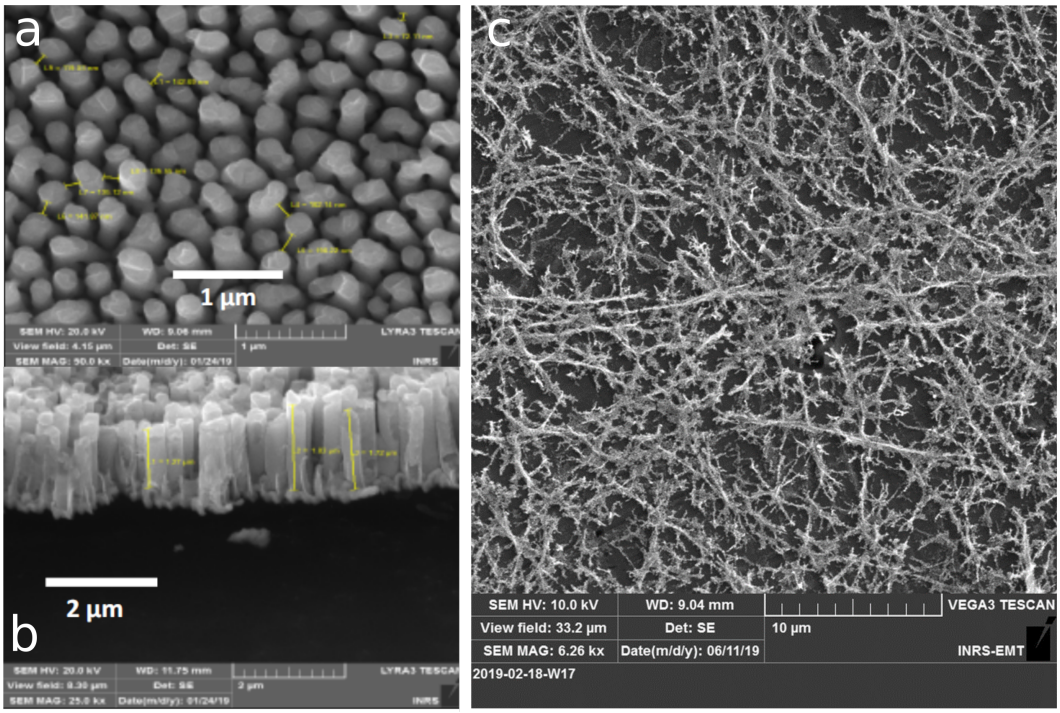

Figure 5.29. SEM images obtained for the two investigated types of nanostructured targets: (a) Top view of the nanowire structure. (b) Side view of the 2 μm long nanowires. (c) Top view of the randomly distributed ZnO nanofibers.

As shown in the scheme in Figure 5.30, these targets were mounted in a multi-target holder so to perform many consecutive shots without opening the experimental chamber.
Two main diagnostic systems were adopted to monitor the accelerated particle emission. One Thomson spectrometer, equipped with a micro-channel plate coupled with a phosphor screen, was mounted on the TNSA axis. This allowed to obtain information both on the protons emissions and on the other ion populations.
Multiple TOF lines, all equipped with diamond detectors, were set at different angles, namely at -22, 40, 60 and 180 degrees. They allowed to monitor the angular distribution of the emitted ions, providing complementary information to those obtained by the Thomson spectrometer. Since a low flux of energetic protons was expected, no filters were placed in front of the diamond detectors. This ensured to possibly detect protons having the maximum energy but, on the other hand, resulted in an overestimation of the particle number in the lowest energy portion of the spectrum, where the contribution of heavier ions cannot be neglected, as discussed in Chapter 4.

The diamonds were linked to the scope through 15 m long, double shielded coaxial cables. The signal of each detector was acquired with two different channels of the two dedicated scopes: a Tektronix DPO 7254 (2.5 GHz bandwidth, 10 GS/s sample rate) and a Lecroy 104MX (1 GHz bandwidth, 5 GS/s sample rate). The length of the line-of-flights was changed throughout the experimental campaign, according to the specific needs of each series of shots. Since the level of EMPs produced

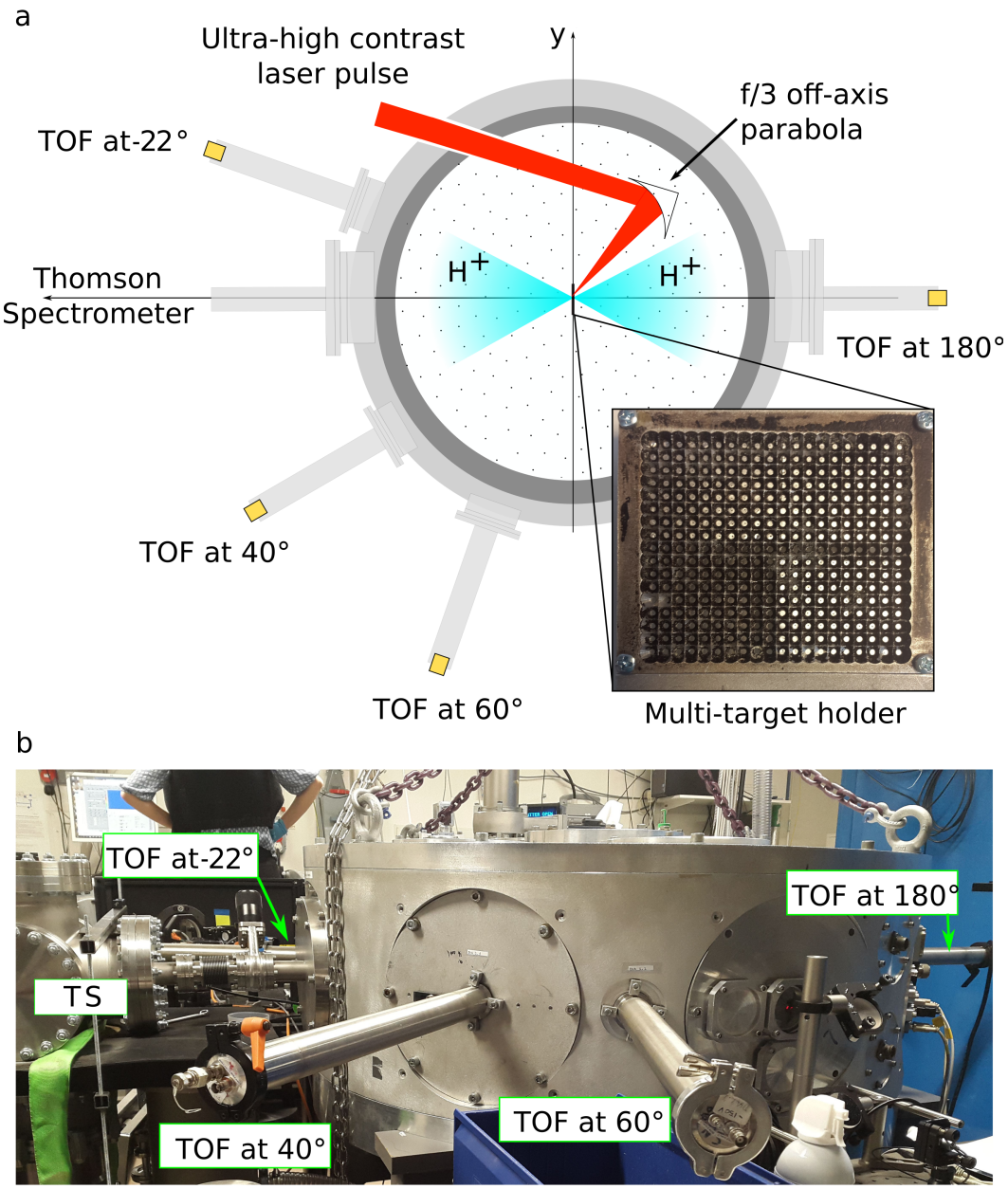

Figure 5.30. (a) A schematic layout of the experimental chamber. Four TOF lines equipped with diamond detectors were set up at different angles, to monitor the angular distribution of the ion emission. In addition to these, on the TNSA axis a Thomson spectrometer equipped with a MCP coupled to a phosphor screen was mounted. (b) A picture of the experimental chamber showing the different TOF line positions and the Thomson spectrometer location.

during this campaign was found not to be so dramatic, here it was even possible to place the detector right on the experimental chamber flange without any further need to exploit the waveguide action of the TOF line extension discussed in Chapter 4.

The presence of the TOF line at 180° was of particular help since it enabled the study of the backward acceleration phenomenon. The simultaneous measurements performed with the Thomson spectrometer allowed to evaluate the relation between the front side and the rear side ion acceleration. The other TOF lines provided some information on the angular distribution of the emitted particles. As expected from the TNSA mechanism, producing rather collimated ion bunches, for the majority of the shots only the TOF lines placed at 22° detected an ion signal whereas the two lines placed at 40° and 60° showed only the photopeak.

In the following, the results obtained by irradiating nanowire targets (NW) and ZnO nanofiber coated targets are briefly discussed. The information on the TNSA axis were retrieved by analyzing the data obtained by the Thomson spectrometer, whereas the one at -22° and 180° were computed from TOF measurements. For each target type several shots were performed and the spectra shown in Figure 5.31 and 5.32 were obtained by averaging over a set of comparable shots.

Nanowire targets

When compared to the spectra obtained by irradiating thin copper foils, the spectra produced by nanowire targets present some interesting properties.
In Figure 5.31.a the results obtained by analyzing the data collected by the Thomson spectrometer placed on the target normal axis are shown. The averaged spectra obtained by irradiating the nanostructured target characterized by a nanowires length of 0.5, 2 and 10 μm are compared with the spectra obtained by irradiating thin copper foils with thickness 0.5, 2 and 10 μm, respectively[196]. It is possible to see that, depending on the length of the nanowires, there is an enhancement both in the proton yield and in the proton maximum energy. The optimum seems to be reached with nanowires of 2 μm length where the averaged maximum energy reaches a value of $\sim$ 5.1 MeV, providing an increment with respect to plain copper foils of 1.9. Moreover, in terms of yield, the nanowires produce almost 2.4 times the protons obtained employing bare copper foils[196].
The TOF line placed at -22° highlights a wider divergence of the proton beam when nanowires are used. This is observed in particular for nanowires of 0.5 and 2 μm length, as shown in Figure 5.31.b. Here the data for the 10 μm case is not reported since it did not provide any detectable signal on the diamond detector.
Concerning the backward acceleration proton phenomenon, the measurement performed with the diamond detector and the related spectra shown in Figure 5.31.c highlighted a quite different behavior with the results obtained in the forward direction. This is probablyd due to the stron asymmetric design of the nanostructured targets.

It is important to stress the point that, since no filter was applied in front of the diamond detectors, it is possible to retrieve reliable information about the proton beam only for energies higher than the half of the maximum detected energy (see Chapter 4, Section 4.4). For instance the spectrum obtained for the 2 μm long nanowires reported in Figure 5.31.b gives information on pure proton contribution only in the energy range (1.7-3.4) MeV whereas for energies lower than 1.7 MeV the

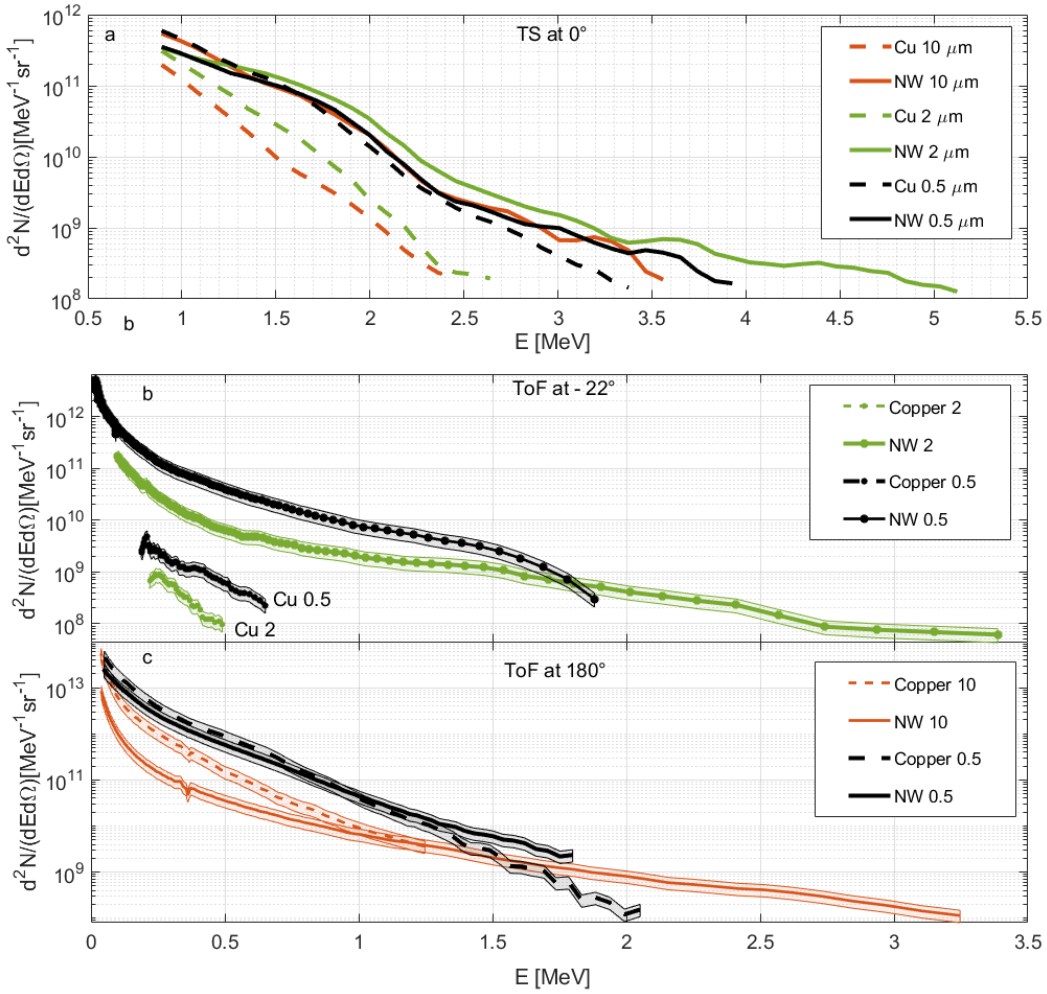

Figure 5.31. The proton spectra obtained for Nanowire targets and copper foils (a) on TNSA axis by means of Thomson spectrometer, (b) at -22° and (c) 180° by means of TOF measurement performed with diamond detectors. Since the latter were not covered with filters, in the lowest energy portion of the spectra, the strong contribution of heavy ions made our evaluation of the number of protons not reliable.

heavier ion contribution cannot be neglected. Nevertheless, the full spectrum is a very useful data for comparing results on the same diamond but from different targets.

ZnO nanofiber targets

In Figure 5.32.a, the spectra obtained on the TNSA axis when irradiating a plain aluminum foil are compared with those produced irradiating the same aluminum foil covered with a layer of ZnO nanofibers having different thicknesses. The thinnest nanofiber layer, i.e. 5 μm thick, does not seem to affect the acceleration process remarkably. A slight enhancement in the yield and in the maximum energy achieved is instead produced by the two thicker layers, i.e. 7.5 and 10 μm. Nevertheless, the enhancement is weak and almost within the uncertainty of the measurements. The

results obtained from the TOF line placed at -22°, shown in Figure 5.32.b, confirm the trend highlighted with the Thomson spectrometer.
More interesting results are highlighted for the backward acceleration phenomenon. Indeed, in Figure 5.32.c both the averaged maximum energy and the proton yield obtained by irradiating the aluminum foils covered with ZnO nanofibers, progressively grow with the thickness of the latter. For the 10 μm ZnO nanofibers the achieved maximum energy is 4.2 MeV, whereas the one provided by the irradiation of bare aluminum foil is 1.84 MeV, for an increment of a factor 2.2. One possible reason of this lack of symmetry can be the employment of a 10 μm aluminum substrate that partially hinders the electron motion, reducing the amplitude of the sheath field at the rear side.

As in the case of nanowires, the spectra at $-22°$ and $-180°$ were obtained by non-filtered diamonds. This means that the contribution of heavier ions cannot be neglected and it leads to an over-estimation of the particle number at low energies. In particular for energies lower than $E_{p,max}/2$.

Highlights of the experimental campaign

During this experimental campaign the role of the TOF line equipped with diamond detectors was to provide information on the angular distribution of the emitted ion beam.
This task was accomplished thanks to the limited dimension of the detection system which allowed to exploit every small spot having a free line of sight to the interaction point.

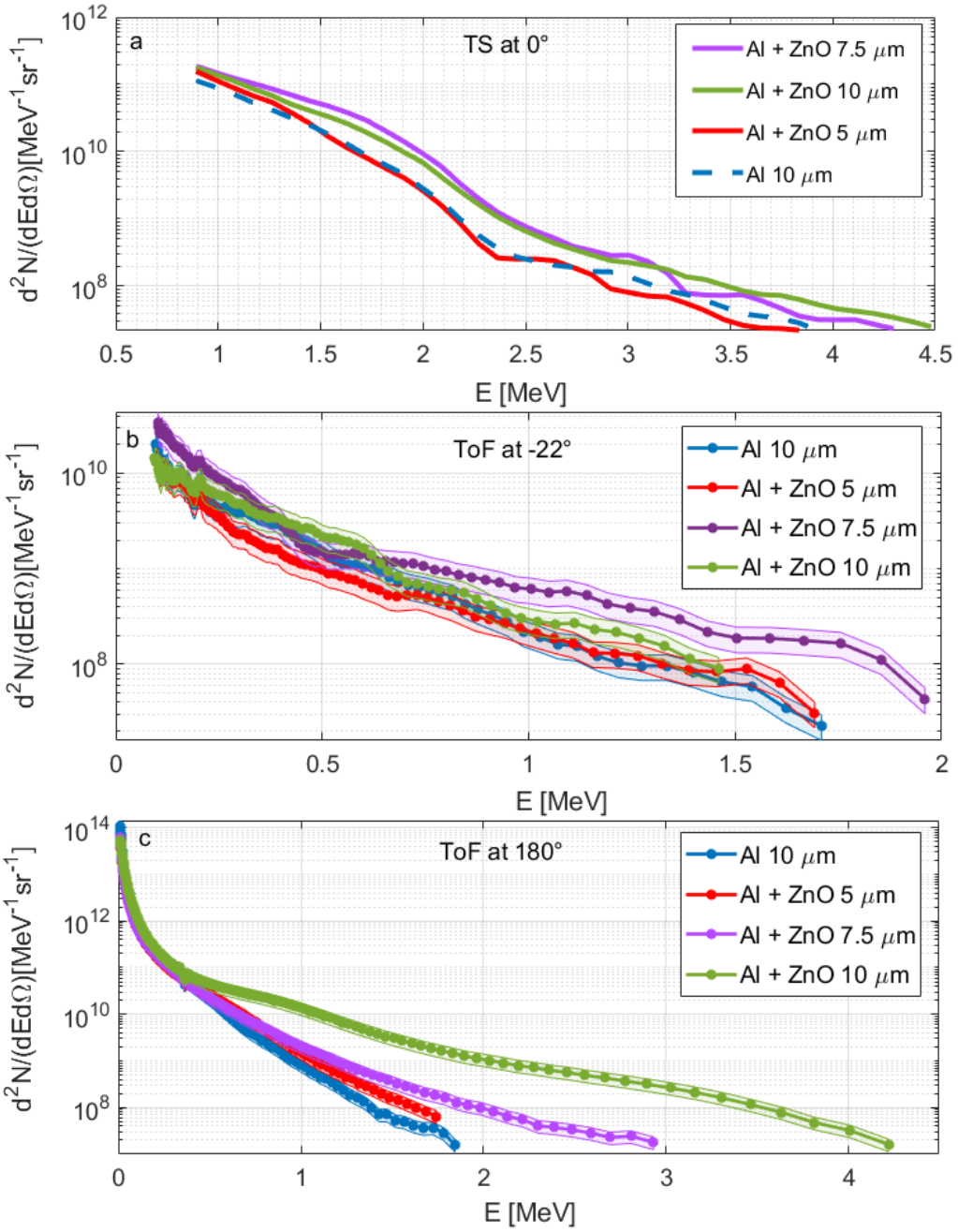

Figure 5.32. The spectra obtained for ZnO nanofibers and aluminum foil (d) on TNSA axis by means of Thomson spectrometer, (e) at 22° and (f) 180° by means of TOF measurement performed with diamond detectors. Since the latter were not covered with filters, in the lowest energy portion of the spectra, the strong contribution of heavy ions made our evaluation of the number of protons not reliable.

5.6 Experiments with the PHELIX laser: operation in highly EMP polluted environments at high energy and intensity regimes

The Petawatt High Energy Laser for Heavy Ion eXperiments (PHELIX) facility is a hybrid Ti:Sapphire/Nd:glass laser system offering a dual front end[197]. The short-pulse operation mode exploits the CPA technique, producing pulses of temporal duration down to 400 fs, delivering up to 120 J, reaching an intensity on target of $\sim 10^{20}$ W cm^{-2}. An ASE contrast of the order of 10^{-10} has been enabled by a recent upgrade, exploiting the direct amplification of the oscillator pulse in an ultra short optical parametric amplifier (uOPA) combined with a linear regenerative amplifier which together allow for continuous tuning of the temporal contrast[198,199]. The nanosecond front end, with the subsequent amplification chain based on flash-lamp-pumped Nd:glass rods, allows to obtain pulses with duration between 700 ps and 20 ns, delivering energies in the range of 0.3-1 kJ for a maximum intensity of 10^{16} W cm^{-2}. In Figure 5.33 the layout of the PHELIX laser facility is shown.

In our experimental campaign, carried out in collaboration with the GSI group

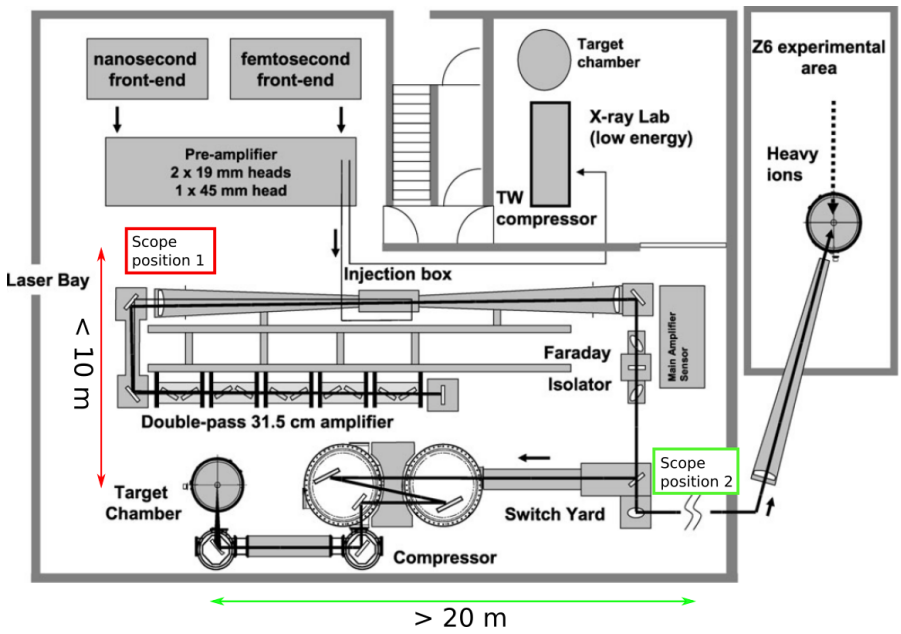

Figure 5.33. The PHELIX laser facility layout. During the experiment the scope used to acquire the TOF signal was moved from "position 1" (highlighted by the red box) to "position 2" (highlighted by the green box) since in the first setup the EMP caused an early triggering of the scope which made the signal acquisition impossible. The map of the laser bay is From *Bagnoud et al.*[197].

headed by O. Rosmej, the two laser pulses were combined together to study the effect of a controlled pre-plasma on laser-driven acceleration[200,201]. A hydrodynamically stable, long-scale-length near-critical-density plasma was generated by irradiating low density polymer foams[202] with a nanosecond pulse kept at an intensity of $\sim 5 \times 10^{13}$ W cm^{-2}. Then with a delay of $2 - 3$ ns a short pulse of 750 fs was used to irradiate

this plasma delivering up to ~ 100 J for an intensity of $\sim (1 - 2.5) \times 10^{19}$ W cm^{-2}. Several diagnostics were installed to monitor the interaction and to characterize the accelerated electrons and ions. The majority of them were off-line detection methods such as stack of passive detectors, nuclear activation technique, magnetostatic spectrometers and Thomson spectrometers equipped with Imaging Plates to avoid the interference of the strong electromagnetic pulses (EMP) produced during the interaction. Indeed, at this facility, the issues related to the strong EMP presence are known to be remarkable[26].
The EMP level was monitored by means of two custom D-Dot probe. During a typical shot, the maximum electric field associated with these electromagnetic pulses exceeded at least 60 kV/m in a wide spectral band covering the whole bandwidth of the scope used for the measurement (i.e. Lecroy 735 Zi, 3.5 GHz bandwidth), as shown in the signal reported in Figure 5.34. The reported spectra was acquired by a D-Dot probe placed behind a 10 cm thick teflon shield at ~ 120 cm from a 10 μm Titanium target, that was irradiated with a laser pulse energy $E_L \simeq 88$ J and a temporal duration of ~ 750 fs.

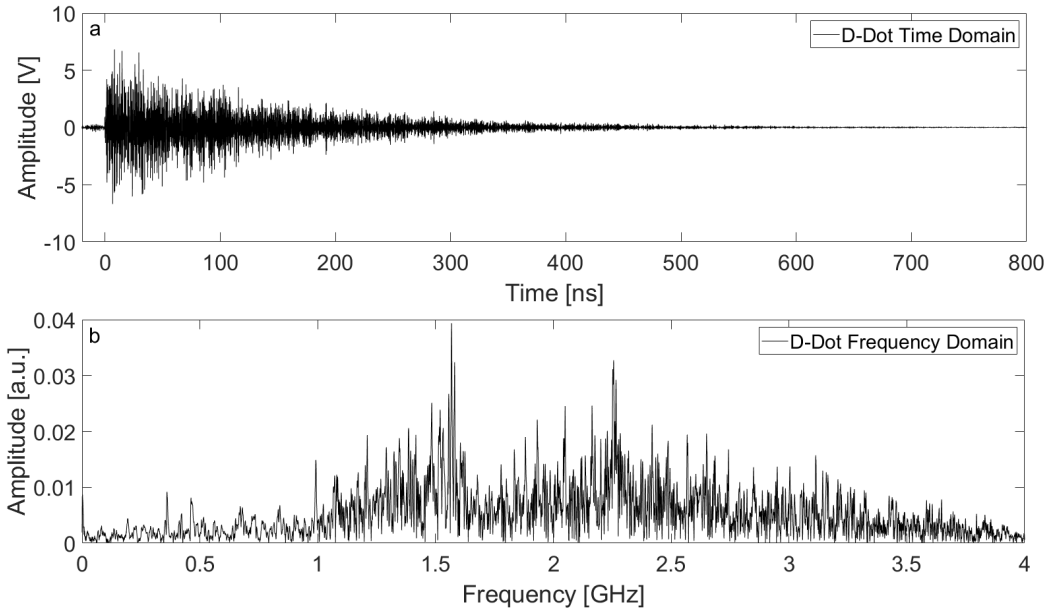

Figure 5.34. (a) The signal acquired by the D-Dot probe in the time domain; (b) the spectrum retrieved from the reported signal by suitable Fourier transform.

The issue of the presence of electromagnetic noise was thus quite severe. It is indeed worth to compare the level of EMP measured here with those observed during the experimental campaign carried out at the FLAME laser facility.
As just shown, during a typical shot performed with PHELIX laser, the electric field associated with the measured EMP exceeded 60 kV/m. On the other hand, as discussed in Section 5.3, the one associated with the EMP measured at FLAME was ~ 25 kV/m. The difference is already quite remarkable, but it is important to consider that in the first case the D-Dot probe was placed at 120 cm from the

target, whereas in the experiment performed at FLAME it was at just 31 cm from the interaction point. Therefore, assuming a simple $1/r$ spherical spreading loss of power, the equivalent field associated with the EMP measured at PHELIX at 31 cm from the target would be $\sim$4 times higher, and so estimated 250 KV/m at the same FLAME distance.
This experimental campaign offered thus the perfect chance to test the developed TOF methodology in a challenging environment for all the electronic devices placed nearby the experimental chamber. Indeed, in addition to the aforementioned diagnostics, multiple TOF lines were also installed and equipped with diamond detectors. Apart from the D-Dot probes that were monitoring the EMPs level, this diagnostic system was the only one that was able to deliver a real-time characterization of the interaction since all the other techniques were relying on passive detectors.
As shown in Figure 5.35, the TOF lines were placed at quite large angles with respect to the target normal axis, being the minimum detection angle of 37°.

Their set-up was done following all the cautions discussed throughout this thesis and optimized during the previous experimental campaigns. In particular during the one carried out at the FLAME laser facility in which, despite the sensibly weaker EMP fields measured, the TOF signal were strongly affected by the electromagnetic noise presence, as shown in Figure 4.7 and 5.11). The acquired expertise was essential in order to achieve in the present campaign a working diagnostic system after few adjustments. It was indeed necessary to carefully take into consideration both the EMP coupling with the detectors and the one with the acquisition system, as discussed in Chapter 4, Section 4.2.

Avoiding EMP coupling with the acquisition system

The scope used was the eight channels Lecroy HDO8108A having 1 GHz bandwidth and 2.5 GS/s sample rate. The bandwidth of the scope was kept at minimum so to allow for optimal measurement performances while avoiding coupling with the high frequency component of the EMPs.
The positioning of the scope acquired also high importance since, in a first attempt, its positioning near the laser pre-amplifier, at less than 10 m from the interaction chamber (Position 1 in Figure 5.33) made impossible to acquire the signal, due to the scope early triggering caused by the strong electromagnetic pulses coming from the first laser amplification stages. As shown in Figure 5.33, it was necessary to place it at about 20 m from the interaction chamber on the opposite side of the laser bay (labeled as position 2 in the Figure) in order to be able to obtain suitable TOF measurements. This position was far enough from both the laser pre-amplifier and the interaction chamber. The increment in the distance from possible EMP sources allowed to exploit the $1/r$ law describing the propagation of the EMP fields in free space.
Moreover, the link of the diamond detectors to the scope was performed employing long coaxial double-shielded cables surrounded by toroids of suitable composition. As already discussed, the employment of long cables provided further attenuation for the high frequency components and introduced temporal delay between the TOF

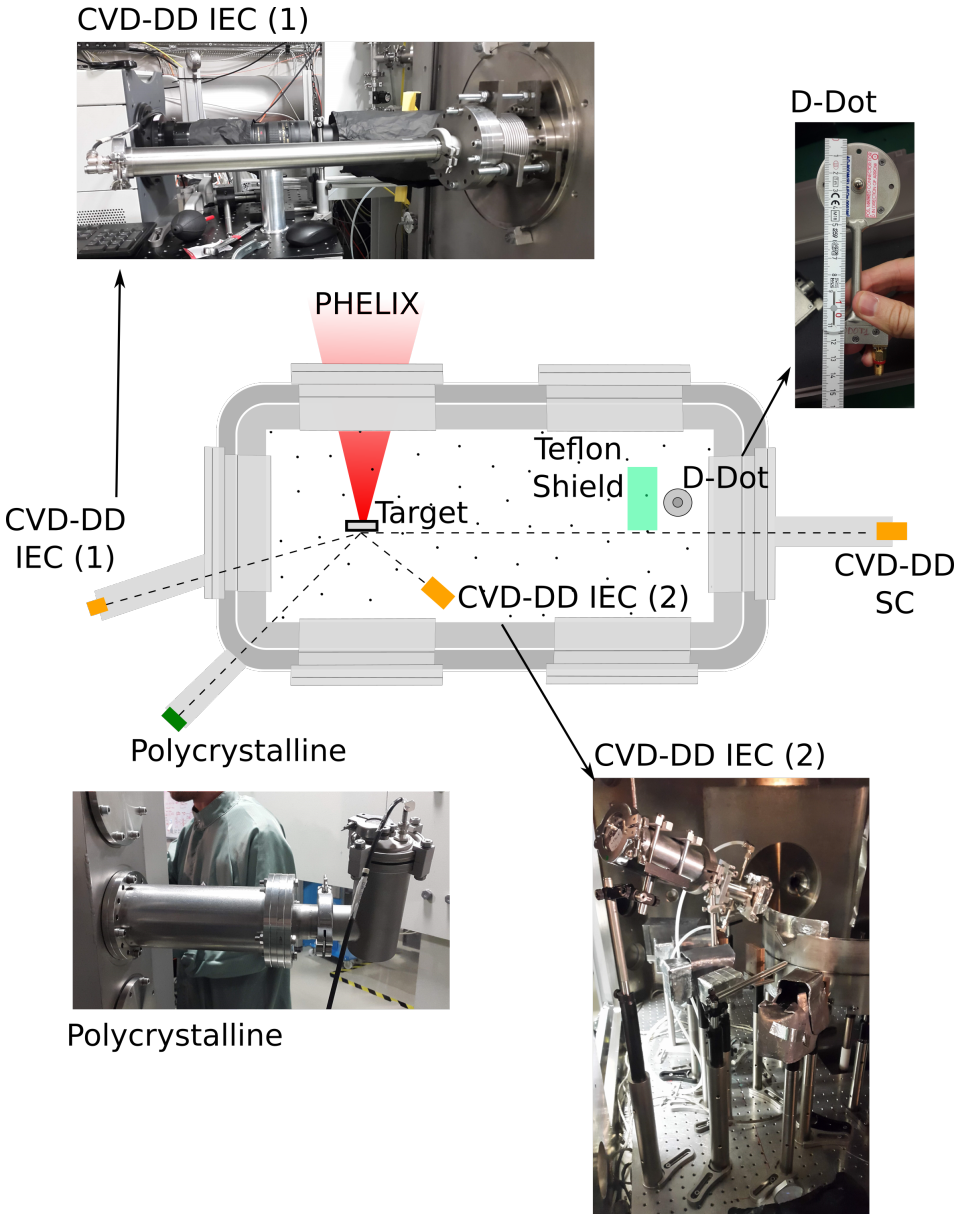

Figure 5.35. The experimental chamber layout. Four different TOF lines were simultaneously activated to monitor the proton emission from different angles. The EMP level was monitored by means of a D-Dot probe.

signals and the EMP contribution generated by the possible direct coupling with the scope (see Chapter 4, Section 4.2 for more details).

TOF measurements from single crystal and polycrystalline diamonds

Three TOF detectors were placed outside the experimental chamber and mounted at the end of pipes connected to the experimental chamber walls through KF-40 flanges. This set-up allowed to exploit the waveguide action of the pipes to reduce

the amount of EMPs reaching the detectors, as discussed in more details in Chapter 4, Section 4.2.
The detectors mounted were single crystal diamonds both in interdigital and sandwich configuration covered with 10 μm aluminum filter, and a large area polycrystalline diamond (detector shown in green in Figure 5.35) which was covered with 20 μm aluminum filter. As usual, the signal generated from each diamond was acquired by two channels of the mentioned scope to enhance the dynamic range of the measurement (Chapter 4, Section 4.1).
Due to their positioning at quite large angles with respect to the target normal, it was not always possible to obtain ion signals, in particular when shooting on bare thin foils. Nevertheless, the photopeak was always detected with a good signal-to-noise ratio, meaning that the cautions adopted to manage the EMPs were sufficient to get clean signals, even in presence of the aforementioned strong electromagnetic fields. As an example of the achieved high signal-to-noise ratio, in Figure 5.36.a the time domain signal acquired by one of the single-crystal diamond detector in the IEC configuration is reported. The shot was performed irradiating a 300 μm thick Foam with a laser energy $\simeq$ 86 J. The spectrum obtained from this signal is reported in Figure 5.36.b

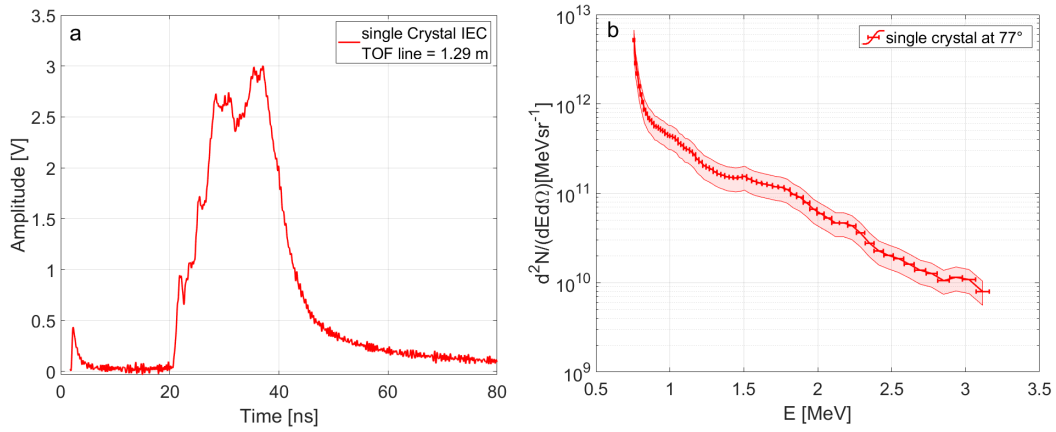

Figure 5.36. The time domain signals acquired by the mono-crystalline diamond detector placed at 77° with respect to the target normal. (b) The spectra obtained from the signal reported in (a).

The simultaneous employment of TOF lines equipped with the two different diamond crystalline structures, the polycrystalline and the single crystal one, allowed to have a direct comparison of the two detectors in a real-case scenario, in terms of energy resolution and sensitivity. The time domain signal acquired by the polycrystalline diamond in a shot performed on a 425 μm Foam target is reported in Figure 5.37.a. In Figure 5.37.b the spectrum obtained from the polycrystalline signal is shown together with the one estimated from the single-crystal diamond detector, placed at 77°, during the same shot.

It is possible to see that by employing the polycrystalline detector, the energy resolution of the spectrum is lower than in the case a single crystal diamond is used.

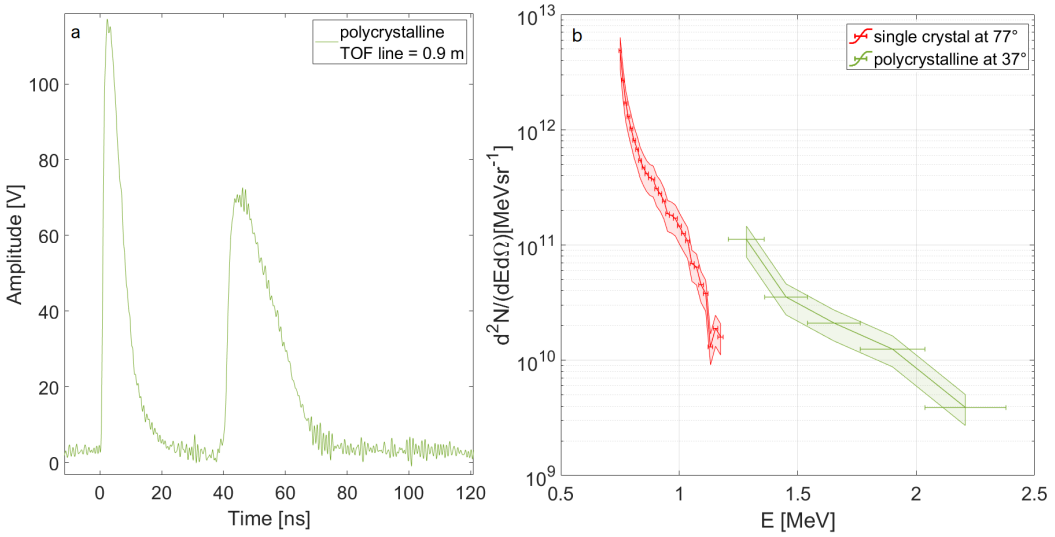

Figure 5.37. The time domain signals acquired by the polycrystalline diamond detector placed at 37° with respect to the target normal spectra obtained from the signal reported in (a) together with the one obtained from the TOF line placed at 77° and equipped with a single-crystal diamond detector.

This is due to its lower temporal resolution. This is coherent with what reported in Chapter 3 for sxposition to single alpha particle: the mono-crystalline structure in IEC configuration presents a FWHM of ~ 0.520 ns whereas, under the same conditions, the polycrystalline structure has a FWHM of ~ 3.5 ns.
Nevertheless, the larger detection area characterizing the polycrystalline diamond detector enabled to reach high signal to noise ratio. This was possible thanks to the accurate shielding made for EMP rejection of the detector itself. Indeed the large polycrystalline area allows to have a larger solid angle, enabling the measurements of low-flux particles but, on the other hand, it is more susceptible to direct coupling with EMPs. Therefore, the capability to collect the signal from the polycrystalline diamond with such high signal to noise ratio is a confirmation of the effectiveness of the developed methodology to improve the EMP resistance of the diagnostic.
Another advantage of the polycrystalline detector that well combines with the large area is its thickness of 150 μm much higher than the 50 μm of the single crystal diamonds. This means that the polycrystalline response is well characterized for all those particles having energies up to ~ 6 MeV, which are completely stopped inside the detector and thus release all their energy in it.
On the contrary, as shown in Section 5.4, in order to have a reliable reconstruction of the detected particle spectrum, the reduced thickness of the single crystal diamonds required the introduction of a correction factor for particles above 3 MeV, which release only a portion of their energy in the diamond.
Given the typical laser-accelerated proton spectrum, the number of protons decreases at higher energies. Therefore having a high sensitivity and a good response for energetic particles is a crucial point for a detector to guarantee a clean measurement of the most energetic portion of the spectrum. These two features are provided in the polycrystalline detector optimized for EMP rejection by its large area and

thickness at expenses of the energetic resolution.

Avoiding EMP coupling with the TOF detector: setup inside the experimental chamber

As shown in Figure 5.35 one of the single crystal diamonds was placed inside the experimental chamber. It was equipped with a 10 μm aluminum filter and presented the electrodes in the interdigital configuration.
The positioning of this detector required some additional caution to achieve a clean TOF measurement. Indeed, the intense electromagnetic field at which it was subjected initially hindered the acquisition of any TOF signal. In fact, when the detector was placed completely inside the chamber with only a short 40 mm diameter pipe as protection from the EMPs, as shown in the scheme in Figure 5.38.a, the acquired signal was entirely hidden by the electromagnetic noise. An example is reported in Figure 5.39.a.

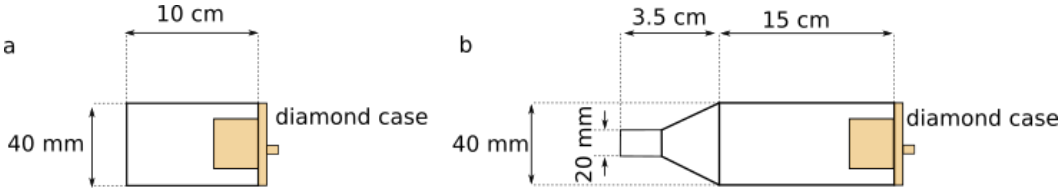

Figure 5.38. (a) The set-up for the IEC diamond detector placed inside the chamber; in a first attempt a short pipe with 40 mm diameter was used as EMP protection. This was not enough to avoid the EMP coupling to the detector, it was therefore upgraded employing a longer pipe coupled with a KF-40 to KF-20 transition for an overall length of 18.5 cm, as shown in (b)

As expected the EMP effect is indeed much more severe than the one shown in the FLAME experimental campaign. Indeed, in Figure 5.11, despite the strong electromagnetic noise did not allow to retrieve any useful information from the acquired signals, it was possible to recognize a fast rising front followed by a descending tail. On the contrary, in the signal shown in Figure 5.39.a the typical TOF signal appearance is completely washed out by the EMP contribution and it is not possible to recognize any typical feature characterizing the TOF signals.

The same diamond used to collect the signal in Figure 5.39.a, placed in the same position, was then equipped with a longer 40 mm pipe coupled to a KF-40 to KF-20 transition, as shown in Figure 5.38.b. The KF-20 transition was used to reduce the aperture of the waveguide. With this improved set-up the diamond was able to acquire the signal shown in Figure 5.39.b.
The two shots were performed on similar conditions. In both cases the laser was used to irradiate cellulose triacetate (TAC, $C_{12}H_{16}O_8$) foam target having 2 mg/cc density and almost identical thicknesses (300 μm in the first case and 325 μm in the second case). In both the shots, the laser was delivering a first long pulse followed by a second short one, with a delay of 2.5 ns[201]. The laser energy in the main pulse

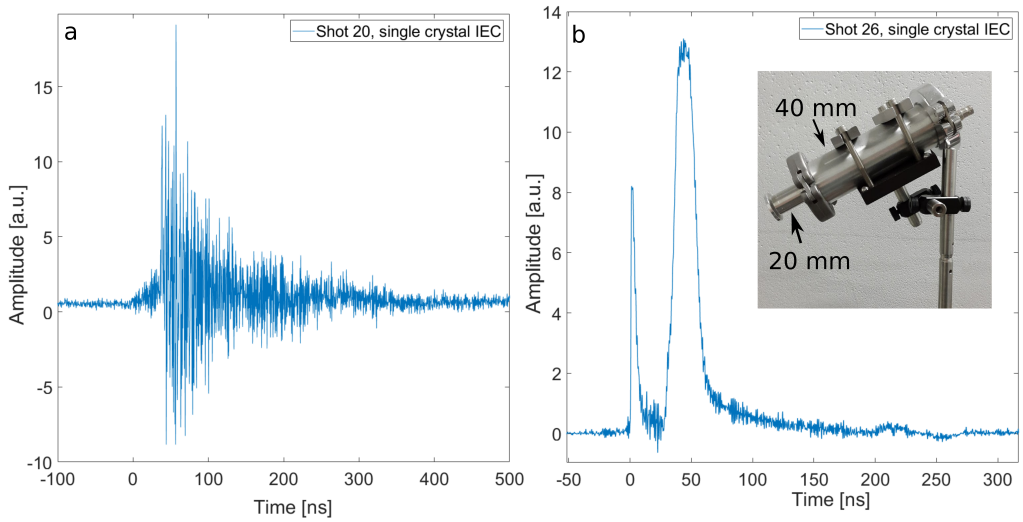

Figure 5.39. (a) A signal acquired by the single crystal diamond detector placed inside the experimental chamber exploiting only a short 40 mm pipe as protection from EMP noise. (b) The signal acquired by the same diamond detector, placed in the same position as in (a) but with a longer pipe coupled to a KF-40 to KF-20 transition to reduce the aperture of the small waveguide as shown in the inset.

was 93 J in the first shot and 90 J in the second.

The time domain signal shown in Figure 5.39.b has been obtained without any numerical filtering procedure. It is possible to see that a good signal-to-noise ratio was achieved exploiting the principles of waveguides cutoff as discussed in Chapter 4, Section 4.2. Indeed, the reduction of the waveguide aperture, besides providing a higher cutoff frequency, makes the attenuation of the electromagnetic waves propagating towards the detector more efficient. This, combined with the overall longer traveling path (given by the combination of the longer 40 mm pipe with the KF-40 to KF-20 transition) resulted in a very effective way to reduce the EMP coupling with the detector remarkably.
This is of high importance, because allows for positioning the detector closer to the target, still maintaining a reasonable distance and thus enerfy resolution, increasing the solid angle of detection and thus the sensitivity.

Highlights of the experimental campaign

The experimental campaign performed at the PHELIX laser facility represented an important stress-test for the developed diagnostic systems. Setting up the TOF lines was indeed challenging; every caution described in Chapter 4, Section 4.2 had to be carefully applied, in order to be able to collect clean signals.
The measurements carried out at this facility demonstrate that the optimized TOF line is suitable for future application in real-time detection and characterization of ions in environments that are expected to produce an extremely high level of electromagnetic noise.
Moreover, during this campaign it was possible to field up the large area polycrys-

talline diamond detector and compare its behavior to the single crystal performances. Firstly it was verified that the ad-hoc enclosure was actually able to avoid the EMP coupling with the large-area detector. Furthermore, its employment allowed to highlight some advantages provided by its thickness and large area when dealing with high-energy particles characterized by a lower flux. This is achieved at some expenses of its energetic resolution, but with enhanced sensitivity especially at higher energies.

5.7 Definition and features of a layered diamond structure

Throughout the development process of the optimized TOF diagnostic system as well as during the tests carried out at the different facilities, it was possible to carefully analyze the benefits and the shortcomings of the technique. This allowed to identify some possible points for a further improvement of the diagnostic performances. In particular, it has been shown that, in TOF technique, energy resolution and sensitivity have somehow opposite requirements. Indeed, as shown in the relation (4.11), the uncertainty on the energy estimation is directly proportional to the temporal resolution of the acquisition system and inversely to the length of the TOF line. Thus, improved energy resolution is commonly obtained by using fast detectors or placing them at larger distances. This last option, however, reduces the overall sensitivity by decreasing the solid angle of detection and thus the number of particles intercepted by the detector.
The response velocity of semiconductor detectors, on the other hand, is mainly limited by the thickness of the active sensitive region, associated with the time of charge collection to the electrodes. The typical single-crystal diamond detector response to a single 5.486 MeV α particle emitted by ^{241}Am decay can have FWHM up to 8 ns for a detector with 500 μm thickness, up to 1.1 ns for one with just 100 μm thickness[203] and up to 0.8 ns or below for one with 50 μm thickness[132,150,157]. So thinner detectors should be preferred for better energy resolution, but on the other hand energetic protons will pass through them more easily, leaving in the active layer only a small amount of their energy and leading to a reduced sensitivity of the detector to them. This issue was partially addressed here in Section 5.4.1 by introducing a correction factor. Indeed, for particles passing through the whole detector and producing signal still reasonably higher than the background, it is possible to estimate, by means of suitable numerical simulations[133], the initial particle energy from the small portion released in the detector, and thus estimate the associated number of detected particles. Nevertheless, if the signal produced in the detector is small with respect to the background noise, the information on the associated particles can be lost. As observed, the emitted proton spectrum in these type of laser-acceleration experiments decreases with energy, and thus this problem is even more significative for the most-energetic protons. For these reasons, whenever improved sensitivity for the most energetic ions is required, thicker detectors are used[133,193,203] but at expenses of the time resolution, and thus of the related energy resolution, accordingly.
The basic idea is to overcome this impasse by using a composite structure made of a

set of several detectors, which can be positioned as a stack, one after the other along the direction of the impinging ions emitted from the laser-matter interaction[154,204]. Filters of different materials and thicknesses can be also used in front of each detector to condition the incoming particle beams. As indicated in the scheme of Figure 5.40. In this work diamond detectors have been mainly discussed, but the methodology can be applied also to solid-state detectors made of other semiconductors, such as for instance SiC detectors. The thickness of each detector in the stack can be chosen to optimize the performances of the whole sensor. The total length would be given by the sum of all the detector thicknesses in the stack. In particular, the use of thin (i.e. 50-100 μm) modules may give high energy resolution and nice sensitivity to high-energy protons, at expenses of a larger number of modules in the stack. In addition, the use of thin diamond layers would allow for a high radiation hardness of the whole diamond detector[205].

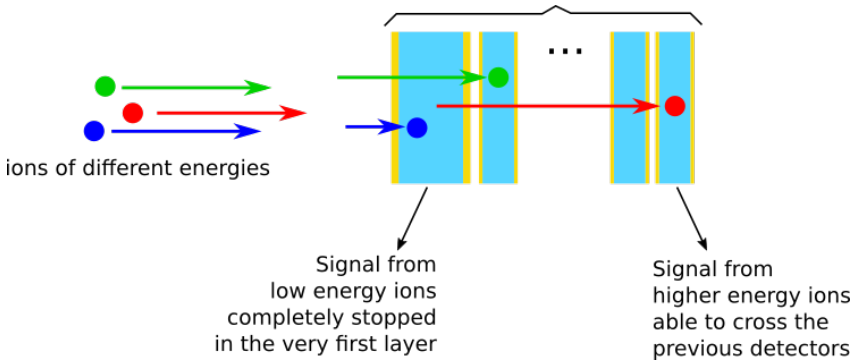

Figure 5.40. A scheme of the layered detector structure and the working principle. The ions having lower energies are going to be stopped in the very first layer of the stack whereas the more energetic will cross the very first layers depositing in them just a small portion of their total energy, thus giving a small contribution to the signal coming from that specific layer. These ions are going to be stopped in the consecutive layers where they will generate a detectable signal, with good temporal resolution.

The main advantage of this novel design would be the capability to detect both high and low energy particles with good sensitivity, without sacrificing the energy resolution. The sensitivity features of thick diamonds can be thus replaced with the layered multiple thin diamonds, insuring fast time response and high radiation hardness. It is worth to underline that the technology of diamond detectors is already mature for such complex structures. Devices based on multiple diamond detectors are reported in the literature for other applications[206,207] and one dedicated to TOF measurements is currently under manufacturing in collaboration also with the University of Tor Vergata[154,204].

Whenever these schemes will be applied to detect ions emitted by intense matter interactions with high energy and intensity laser pulses up to the femtosecond and attosecond time-scales, the main limitations to the method sensitivity will be thus given by the coupling of giant EMPs (up to several MV/m levels) to the related electronic devices. This is known to be a major issue especially for devices working at larger frequency bandwidths and will thus be more serious for the fast (i.e. thin) detectors.

Nevertheless, in this work it has been shown how the issue of EMP can be addressed by reducing the coupling both with the detector itself and the acquisition system. Therefore, using these advanced methodologies, fast diamond detectors can be successfully adopted as a main constituent of a layered structure made of a stack of them.

Chapter 6

Conclusion and perspectives

The research activity on laser-accelerated ions is rapidly growing and the employment of laser-driven proton sources appears to be soon feasible for a variety of applications from medical treatments to cultural heritage, just to mention a few examples.
In order to be used, the laser produced proton beamline has to be properly characterized. In this thesis the need for a diagnostic system able to work at high repetition rate in environments highly polluted by EMP fields has been discussed. Among the existing diagnostic techniques, reviewed in Chapter 2, Time-of-Flight detection offers several advantages and promising features to fulfill the aforementioned requirements. The main purpose of this thesis was the development and testing of an advanced on-line TOF diagnostic system and to enable its employment in environments characterized by the production of intense electromagnetic fields, i.e. high energy and intensity laser experiments. This task was fully achieved thanks to the methodologies described in Chapter 4. The acquisition system was optimized together with the set-up of the diagnostics in order to get a high signal-to-noise ratio on the whole dynamic range of the collected signals. The latter was obtained thanks to the high rejection to the EMP fields that was reached providing ad-hoc enclosures for the employed detectors and exploiting the TOF line extensions acting as waveguides. Moreover, long double shielded cables where used to transport the collected signal. These have two effects: they provide temporal separation between the noise due to the EMPs and the TOF signal and also act as low-pass filters. The tailored optimization of the analogical signal management enabled the retrieving of both the interaction-time and the particle information from the recorded data with high accuracy.
The TOF method was here used to get information on the pure proton contribution to the spectrum. To this purpose, the introduction of thin foils in the line of flight allowed to get rid of the heavier ion contribution which are also detected by diamond detectors, used to enhance the performance of the technique. This choice was discussed in Chapter 3 where the diamond detectors are compared to other semiconductors and accurately characterized. The detailed knowledge of the detector was then used in the procedure presented in Chapter 4 for getting the calibrated proton spectrum associated to the time-domain measurements.

The discussed technique has been mainly developed at ENEA Centro Ricerche

Frascati, exploiting the ABC laser facility, and some detectors were developed by the University of Tor Vergata. In ENEA it was possible to compare this TOF line with other non-optimized TOF lines coupled with Faraday cups. The capability to work at high repetition rate was proven during the experimental campaign at ECLIPSE, where several consecutive shots where taken at 1 Hz. Measurements and data retrieving were performed in real-time for every shot, without any need of opening the vacuum chamber.
Further study and progresses in the technique optimization were made in the experimental campaign held at INFN-LNF with the FLAME laser and at INRS with the ALLS laser. The campaign carried out with the FLAME laser offered the chance to collect a statistics over several shots, that allowed the characterization of the behaviour of different diamond detector layouts and the optimization of the technique about the development of the analogue conditioning of the signal and of the spectrum determination. During the experimental campaign performed at the ALLS laser facility, the simultaneous employment of a Thomson spectrometer placed at an angle close to the TOF line allowed to perform a cross calibration of the two diagnostics, validating both the TOF technique and the procedure to retrieve the related calibrated spectrum.
After these first campaigns, the system was applied both to monitor the proton beam during laser driven PIXE/XRF (at ALLS) and to characterize the angular distribution of an accelerated proton beam originated by irradiating structured targets (experimental campaign held at the Lund Laser Center).

The actually remarkable test of the developed advanced methodology was eventually the experimental campaign performed at PHELIX laser ($E_L \sim 100$ J, $\tau_L \sim 750fs$, $I_L \sim 10^{20}$ W cm^{-2}) to understand the possible application to facilities affected by even higher EMP pollution levels. Here several TOF lines equipped with diamond detectors were installed and succesfully provided signals characterized by high energy resolutions and signal-to-noise ratio.
A further experiment to test the implemented methodology and its resistance to EMP was prepared in March 2020 at the VULCAN -PW laser at the Rutherford Appleton Laboratory in Didcot. Unfortunately due to the COVID-19 pandemia, the campaign was stopped and moved to 2021 and it is thus not included in this work.

The capability of performing such on-line accurate measurements in environments with high EMP levels, even without the use of Faraday cages, is of crucial importance to monitor and effectively characterize the particles accelerated via laser-plasma interaction in high-repetition laser-matter experiments. This is a key point for high-intensity and high-energy laser facilities for both laser-plasma acceleration and inertial confinement fusion (PETAL, Vulcan Petawatt, Extreme Light Infrastructure (ELI)), where high levels of EMPs are classically produced[26]. Since the EMP fields are known to scale with the laser energy and intensity, the problem will be of increasing importance for future facilities which will be operating soon (Apollon 5 PW, ELI L4 10 PW, ...), where higher EMP levels are expected.

The multi-layered diamond structure, whose concept and design is presented in Chapter 5, Section 5.7, is expected to have remarkable features[154], enabling real-time

detection of ions with high signal-to-noise ratio, high sensitivity and high energy resolution over a wide range of ion energies.

These considerations confirm that the described methodology, together with the overall advanced associated detection system, is a promising candidate for the fast, accurate, high-resolution, high sensitivity, high radiation hardness and real-time detection of energetic ions in experiments of high energy and high intensity matter interaction with ultra-short laser pulses.

Bibliography

[1] T. H. Maiman. “Stimulated Optical Radiation in Ruby”. *Nature* 187,493 (1960).

[2] J. Hecht. “Short history of laser development”. *Optical Engineering* 49,1 (2010).

[3] A. Macchi, M. Borghesi, and M. Passoni. “Ion acceleration by superintense laser-plasma interaction”. *Reviews of modern physics* 85,751 (2016).

[4] R. Betti and O. A. Hurricane. “Inertial Confinement Fusion with lasers”. *Nature physics* 12,435 (2016).

[5] S. Atzeni and J. Meyer-Ter-Vehn. *The Physics of inertial fusion - Beam Plasma interaction, hydrodynamics, dense plasma physics*. Oxford: Clarendon Press, 2004.

[6] C. A. Haynam et al. “National Ignition Facility laser performance status”. *Applied Optics* 46,3276 (2007).

[7] V. Denis et al. “The Laser Megajoule Facility: laser performances and comparison with computational simulation”. In: *High Power Lasers for Fusion Research IV*. Ed. by Abdul A. S. Awwal. Vol. 10084. 52 – 60. International Society for Optics and Photonics. SPIE, 2017.

[8] E. M. Campbell and W. J. Hogan. “The National Ignition Facility - applications for inertial fusion energy and high-energy-density science”. *Plasma Physics and Controlled Fusion* 41,B39 (1999).

[9] E. Moses. “Multi-megajoule NIF: ushering in a new era in high energy density science”. In: *High-Power Laser Ablation VII*. Ed. by Claude R. Phipps. Vol. 7005. 125. International Society for Optics and Photonics. SPIE, 2008.

[10] D. Strickland and G. Mourou. “Compression of amplified chirped optical pulses”. *Optics Communications* 56,219 (1985).

[11] C. Danson et al. “Petawatt class lasers worldwide”. *High Power Laser Science and Engineering* 3,e3 (2015).

[12] C. Danson et al. “Petawatt and exawatt class lasers worldwide”. *High Power Laser Science and Engineering* 7,e54 (2019).

[13] H. Daido, M. Nishiuchi, and A. S. Pirozhkov. “Review of Laser-Driven Ion sources and Their Applications”. *Report on progress in Physics* 75,056401 (2012).

[14] D. Giulietti et al. “Laser-plasma energetic particle production for aneutronic nuclear fusion experiments”. *Nuclear Instruments and Methods in Physics Research Section B: Beam Interactions with Materials and Atoms* 402,373 (2017). Proceedings of the 7th International Conference Channeling 2016: Charged and Neutral Particles Channeling Phenomena.

[15] A. Picciotto et al. “Boron-Proton Nuclear-Fusion Enhancement Induced in Boron-Doped Silicon Targets by Low-Contrast Pulsed Laser”. *Physical Review X* 4,031030 (2014).

[16] D. Doria et al. “Biological effectiveness on live cells of laser driven protons at dose rates exceeding 109 Gy/s”. *AIP Advances* 2,011209 (2012).

[17] S. V. Bulanov et al. “Laser ion acceleration for hadron therapy”. *Physics-Uspekhi* 57,1149 (2014).

[18] P. R. Bolton et al. “Instrumentation for diagnostics and control of laser-accelerated proton (ion) beams”. *Physica Medica* 30,255 (2014).

[19] J. Miyahara. “Imaging plate”. In: *Computed Radiography*. Ed. by Yukio Tateno, Takeshi Iinuma, and Masao Takano. 7. Tokyo: Springer Japan, 1987.

[20] I. Radomir and A. D. Saeed. “Solid state nuclear track detectors”. In: *Handbook of Radioactivity Analysis (Second Edition)*. Ed. by Michael F. L’Annunziata. Second Edition. 179. San Diego: Academic Press, 2003.

[21] F. Nürnberg et al. “Radiochromic film imaging spectroscopy of laser-accelerated proton beams”. *Review of Scientific Instruments* 80,033301 (2009).

[22] Sir J.J. Thomson. “Rays of positive electricity”. *The London, Edinburgh, and Dublin Philosophical Magazine and Journal of Science* 20,752 (1910).

[23] A. E. Cameron and D. F. Eggers. “An Ion “Velocitron””. *Review of Scientific Instruments* 19,605 (1948).

[24] M. M. Wolff and W. E. Stephens. “A Pulsed Mass Spectrometer with Time Dispersion”. *Review of Scientific Instruments* 24,616 (1953).

[25] P. Bradford et al. “EMP control and characterization on high-power laser systems”. *High Power Laser Science and Engineering* 6,e21 (2018).

[26] F. Consoli et al. “Laser produced electromagnetic pulses: generation, detection and mitigation”. *High Power Laser Science and Engineering* 8,2095 (2020).

[27] D. Haffa et al. “I-BEAT: Ultrasonic method for online measurement of the energy distribution of a single ion bunch”. *Scientific Reports* 9,6714 (2019).

[28] V. I. Veksler. “The principle of coherent acceleration of charged particles”. *The Soviet Journal of Atomic energy* 2,525 (1957).

[29] W.I. Linlor. “Ion energies produced by laser giant pulse”. *Applied Physics Letters* 3,210 (1963).

[30] S. J. Gitomer et al. “Fast ions and hot electrons in the laser–plasma interaction”. *The Physics of Fluids* 29,2679 (1986).

[31] T. Ditmire et al. “High-energy ions produced in explosions of superheated atomic clusters”. *Nature* 386,54 (1997).

[32] G. S. Sarkisov et al. "Self-focusing, channel formation, and high-energy ion generation in interaction of an intense short laser pulse with a He jet". *Physical Review E* 59,7042 (1999).

[33] A. Maksimchuk et al. "Forward Ion Acceleration in Thin Films Driven by a High-Intensity Laser". *Physical Review Letters* 84,4108 (2000).

[34] E. L. Clark et al. "Energetic Heavy-Ion and Proton Generation from Ultraintense Laser-Plasma Interactions with Solids". *Physical Review Letter* 85,1654 (2000).

[35] R. A. Snavely et al. "Intense High-Energy Proton Beams from Petawatt-Laser Irradiation of Solids". *Phys. Rev. Lett.* 85,2945 (2000).

[36] S. P. Hatchett et al. "Electron, photon, and ion beams from the relativistic interaction of Petawatt laser pulses with solid targets". *Physics of Plasmas* 7,2076 (2000).

[37] S. C. Wilks et al. "Energetic proton generation in ultra-intense laser–solid interactions". *Physics of Plasmas* 8,542 (2001).

[38] C. J. Joachain. "High-intensity laser-atom interactions". *Europhysics Letters* 108,44001 (2014).

[39] P. Gibbon. *Short pulse laser interactions with matter : an introduction.* London: Imperial College press, 2005.

[40] N. A. Krall and A. V. Trivelpiece. *Principles of Plasma Physics.* Mc-Graw Hill, 1973.

[41] F. Chen. *Introduction to Plasma Physics and Controlled Fusion.* Switzerland: Springer, Cham, 2016.

[42] W. L. Kruer. *The physics of laser-plasma interactions.* Redwood city, California: Addison-Wesley, 1988.

[43] A. Macchi. *A Superintense Laser-Plasma Interaction Theory Primer.* Heidelberg New York London: Springer, 2013.

[44] D. Giulietti and L. Gizzi. "X-ray emission from laser-produced plasmas". *La rivista del nuovo cimento* 21,1 (1998).

[45] S. C. Wilks and W. L. Kruer. "Absorption of ultrashort, ultra-intense laser light by solids and overdense plasmas". *IEEE Journal of Quantum Electronics* 33,1954 (1997).

[46] M. N Rosenbluth. "Parametric Instabilities in Inhomogeneous Media". *Physical Review Letters* 29,565 (1972).

[47] P. J. Catto and R. M. More. "Sheath inverse bremsstrahlung in laser produced plasmas". *The Physics of Fluids* 20,704 (1977).

[48] F. Brunel. "Not-so-resonant, resonant absorption". *Physical Review Letters* 59,52 (1987).

[49] W. L. Kruer and K. Estabrook. "J×B heating by very intense laser light". *The Physics of Fluids* 28,430 (1985).

[50] V. T. Tikhonchuk. "Interaction of a beam of fast electrons with solids". *Physics of Plasmas* 9,1416 (2002).

[51] P. Sharma and R.K. Vatsa. "Chapter 16 - Nanoclusters Under Extreme Ionization Conditions". In: *Materials Under Extreme Conditions*. Ed. by A.K. Tyagi and S. Banerjee. 575. Amsterdam: Elsevier, 2017.

[52] T. Esirkepov et al. "Highly Efficient Relativistic-Ion Generation in the Laser-Piston Regime". *Physical Review Letters* 92,175003 (2004).

[53] A. J. C. Palmer et al. "Monoenergetic Proton Beams Accelerated by a radiation Pressure Driven Shock". *Physical Review Letters* 106,014801 (2011).

[54] Dan Haberberger et al. "Collisionless shocks in laser-produced plasma generate monoenergetic high-energy proton beams". *Nature Physics* 8,95 (2012).

[55] P. Bolton, K. Parosi, and J. Schreiber. *Applications of laser-Driven Particle Acceleration*. Boca Raton, Florida: CRC press, taylor & Francis group, 2018.

[56] A. Higginson et al. "Near-100 MeV protons via a laser-driven transparency-enhanced hybrid acceleration scheme". *Nature communications* 9,724 (2018).

[57] H. Schwoerer et al. "Laser-plasma acceleration of quasi-monoenergetic protons from microstructured targets". *Nature* 439,445 (2006).

[58] M. Roth and M. Schollmeier. "Ion Acceleration - Target Normal Sheath Acceleration". *CERN Yellow reports* 1 (2016).

[59] D. C. Carroll et al. "Active manipulation of the spatial energy distribution of laser-accelerated proton beams". *Physical Review E* 76,065401 (2007).

[60] H. Wiedemann. *Particle Accelerator Physics*. Verlag Berlin Heidelberg: Springer, 2007.

[61] M. Hegelich et al. "MeV Ion Jets from Short-Pulse-Laser Interaction with Thin Foils". *Physical Review Letters* 89,085002 (2002).

[62] B. M. Hegelich et al. "Spectral properties of laser-accelerated mid-Z MeVu ion beams". *Physics of Plasmas* 12,056314 (2005).

[63] J. F. Kolb, S. Kono, and K. H. Schoenbach. "Nanosecond pulsed electric field generators for the study of subcellular effects". *Bioelectromagnetics* 27,172 (2006).

[64] A. G. Pakhomov, D. Miklavcic, and M.S Markov. *Advanced Electroporation Techniques in Biology an Medicine*. Boca Raton: CRC Press, 2017.

[65] F. Consoli et al. "Generation of intense quasi-electrostatic fields due to deposition of particles accelerated by petawatt-range laser-matter interactions". *Scientific Reports* 9,8551 (2019).

[66] F. Consoli et al. "Sources and space-time distribution of the electromagnetic pulses in experiments on inertial confinement fusion and laser-plasma acceleration". *Philosophical Transactions of the Royal Society A: Mathematical, Physical and Engineering Sciences* 379,20200022 (2021).

[67] F. Consoli et al. "Measurement of the Radiofrequency-microwave Pulse Produced in Experiments of Laser-plasma Interaction in the ABC Laser Facility". *Physics Procedia* 62,11 (2015). 3rd International Conference Frontiers in Diagnostic Technologies, ICFDT3 2013, 25-27 November 2013, Laboratori Nazionali di Frascati, Italy.

[68] J. Krása et al. "Effect of expanding plasma on propagation of electromagnetic pulses by laser-plasma interaction". *Plasma Physics and Controlled Fusion* 62,025021 (2019).

[69] M. Guglielmi, R. Sorrentino, and G. Conciauro. *Advanced Modal Analysis: CAD Techniques for Waveguide Components and Filter*. John Wiley & Sons, Inc., 1999.

[70] B. Dromey et al. "Picosecond metrology of laser-driven proton bursts". *Nature Communications* 7,10642 (2016).

[71] L. Robson et al. "Scaling of proton acceleration driven by petawatt-laser–plasma interactions". *Nature Physics* 3,58 (2007).

[72] S. Kar et al. "Ballistic Focusing of Polyenergetic Protons Driven by Petawatt Laser Pulses". *Physical Review Letters* 106,225003 (2011).

[73] B. Qiao et al. "Dynamics of high-energy proton beam acceleration and focusing from hemisphere-cone targets by high-intensity lasers". *Physical Review E* 87,013108 (2013).

[74] C. McGuffey et al. "Focussing Protons from a Kilojoule Laser for Intense Beam Heating using Proximal Target Structures". *Scientific Reports* 10,9415 (2020).

[75] V. Malka et al. "Practicability of protontherapy using compact laser systems". *Medical Physics* 31,1587 (2004).

[76] M. Borghesi et al. "Macroscopic Evidence of Soliton Formation in Multiterawatt Laser-Plasma Interaction". *Physical Review Letters* 88,135002 (2002).

[77] M. Borghesi et al. "Electric field detection in laser-plasma interaction experiments via the proton imaging technique". *Physics of Plasmas* 9,2214 (2002).

[78] M. Barberio et al. "Laser-Accelerated Proton Beams as Diagnostic for Cultural Heritage". *Scientific Reports* 7,40415 (2017).

[79] K. W. D. Ledingham et al. "Towards laser Driven Hadron Cancer Radiotherapy: A Review of Progress". *Applied Science* 4,402 (2014).

[80] H. Y. Wang et al. "Autofocused, enhanced proton acceleration from nanometer-scale bulged foil". *Physics of Plasmas* 17,113111 (2010).

[81] J. H. Bin et al. "On the small divergence of laser driven ion beams from nanometer thick foils". *Physics of Plasmas* 20,073113 (2013).

[82] T. Toncian et al. "Ultrafast laser-driven microlens to focus and energy select mega-electronvolt protons". *Science* 21,410 (2006).

[83] M. Schollmeier et al. “Controlled transport and focusing of laser accelerated protons with miniature magnetic devices”. *Physical Review Letters* 101,055004 (2008).

[84] N. Liebsch et al. “Phase II Study of High-Dose Photon/proton Radiotherapy in the Management of Spine Sarcomas”. *International Journal of Radiation Oncology, Biology, Physics* 74,732 (2009).

[85] *OncoRay Center for Radiation Research in Oncology.* URL: `(http://www.oncoray.de/)`.

[86] D. Margarone et al. “ELIMAIA: A Laser-Driven Ion Accelerator for Multidisciplinary Applications”. *Quantum Beam Sci.* 2,8 (2018).

[87] G. A. P. Cirrone et al. “ELIMED-ELIMAIA: The First Open User Irradiation Beamline for Laser-Plasma-Accelerated Ion Beams”. *Frontiers in Physics* 8,437 (2020).

[88] G. Aymar et al. “LhARA: The Laser-hybrid Accelerator for Radiobiological Applications”. *Frontiers in Physics* 8,432 (2020).

[89] S. Kar et al. “Modeling of laser-driven proton radiography of dense matter”. *High Energy Density Physics* 4,26 (2008).

[90] M. Barberio and P. Antici. “Laser-PIXE using laser-accelerated proton beams”. *Scientific Reports* 9,6855 (2019).

[91] M. Passoni et al. “Advanced laser-driven ion sources and their applications in materials and nuclear science”. *Plasma Physics and Controlled Fusion* 62,014022 (2019).

[92] M. H. Key. “Status of and prospects for the fast ignition inertial fusion concept”. *Physics of Plasmas* 14,055502 (2007).

[93] M. Tabak et al. “Ignition and high gain with ultrapowerful lasers*”. *Physics of Plasmas* 1,1626-1634 (1994).

[94] M. Roth et al. “Fast Ignition by Intense Laser-Accelerated Proton Beams”. *Phys. Rev. Lett.* 86,436 (2001).

[95] S. Atzeni, M. Temporal, and J.J. Honrubia. “A first analysis of fast ignition of precompressed ICF fuel by laser-accelerated protons”. *Nuclear Fusion* 42,L1 (2002).

[96] F. Consoli et al. “Diagnostic Methodologies of Laser-Initiated 11B(p,a)2a Fusion Reactions”. *Frontiers in Physics* 8,496 (2020).

[97] C. Labaune et al. “Fusion reactions initiated by laser-accelerated particle beams in a laser-produced plasma”. *Nature Communications* 4,2506 (2013).

[98] C. Baccou et al. “New scheme to produce aneutronic fusion reactions by laser-accelerated ions”. *Laser and Particle Beams* 33,117 (2015).

[99] D. Margarone et al. “Generation of alpha particle Beams With a Multi-KJ, Peta-Watt Class Laser System”. *Frontiers in Physics* 8,343 (2020).

[100] J. Gruenwald and C. Teodorescu. “Novel target design for a laser-driven aneutronic fusion reactor”. *Fusion Engineering and Design* 151,111397 (2020).

[101] V. S. Belyaev et al. “Observation of neutronless fusion reactions in picosecond laser plasmas”. *Physical Review E* 72,026406 (2005).

[102] S. Kimura, A. Anzalone, and A. Bonasera. “Comment on "Observation of neutronless fusion reactions in picosecond laser plasmas”. *Physical Review E* 79,038401 (2009).

[103] L. Giuffrida et al. “High-current stream of energetic α particles from laser-driven proton-boron fusion”. *Physical Review E* 101,013204 (2020).

[104] A. Karellas and B. R. Thomadsen. *Radiochromic Film, role and applications in radiation dosimetry*. Boca Raton, Florida: CRC press, taylor & Francis group, 2017.

[105] S. Vallières et al. “Low-energy proton calibration and energy-dependence linearization of EBT-XD radiochromic films”. *Review of Scientific Instruments* 90,083301 (2019).

[106] S. Yonai et al. “Experimental Evaluation of Dosimetric Characterization of Gafchromic EBT3 AND EBT-XD Films for Clinical Carbon Ion Beams”. *Radiation Protection Dosimetry* 180,314 (2018).

[107] S. Khachonkham et al. “Characteristic of EBT-XD and EBT3 radiochromic film dosimetry for photon and proton beams”. *Physics in Medicine and Biology* 63,065007 (2018).

[108] D. Kirby et al. “LET dependence of GafChromic films and an ion chamber in low-energy proton dosimetry”. *Physics in Medicine and Biology* 55,417 (2010).

[109] M. Vadrucci et al. “Calibration of GafChromic EBT3 for absorbed dose measurements in 5 MeV proton beam and 60Co γ-rays”. *Medical Physics* 42,4678 (2015).

[110] M. C. Battaglia et al. “Dosimetric response of radiochromic films to protons of low energies in the Bragg peak region”. *Physical Review of Accelerators and Beams* 19,064701 (2016).

[111] M. C. Battaglia et al. “EBT3 film calibrattion in the Bragg peak region for proton beams below 5 MeV”. *Nuclear Inst. and Methods in Physics research B* 444,117 (2019).

[112] A. S. Cucoanes et al. “Radiochromic film calibration at 9 MV accelerator of IFIN-HH”. *ACS photonics* 2,208 (2015).

[113] T. E. Cowan et al. “Ultralow Emittance, Multi-MeV Proton Beams from a Laser Virtual-Cathode Plasma Accelerator”. *Physical Review Letters* 92,204801 (2004).

[114] T. Bonnet et al. “Response functions of Fuji imaging plates to monoenergetic protons in the energy range 0.6–3.2 MeV”. *Review of Scientific Instruments* 84,013508 (2013).

[115] I. J. Paterson et al. “Image plate response for conditions relevant to laser–plasma interaction experiments”. *Measurement Science and Technology* 19,095301 (2008).

[116] A. Mančić et al. "Absolute calibration of photostimulable image plate detectors used as (0.5–20MeV) high-energy proton detectors". *Review of Scientific Instruments* 79,073301 (2008).

[117] N. Rabhi et al. "Calibration of imaging plate detectors to mono-energetic protons in the range 1-200 MeV". *Review of Scientific Instruments* 88,113301 (2017).

[118] C. G. Freeman et al. "Calibration of a Thomson parabola ion spectrometer and Fujifilm imaging plate detectors for protons, deuterons, and alpha particles". *Review of Scientific Instruments* 82,073301 (2011).

[119] F. Ingenito et al. "Directional Track Selection Technique in CR39 SSNTD for lowyield reaction experiments". *EPJ Web of Conferences* 167,05006 (2018).

[120] M. Kanasaki et al. "Application of CR-39 Solid State Nuclear Track Detectors to Laser-Driven Ion Acceleration Experiments". In: *Progress in Ultrafast Intense Laser Science XV*. Ed. by Kaoru Yamanouchi and Dimitrios Charalambidis. 133. Cham: Springer International Publishing, 2020.

[121] M. Seimetz et al. "Spectral characterization of laser-accelerated protons with CR-39 nuclear track detector". *Review of Scientific Instruments* 89,023302 (2018).

[122] I. Spencer et al. "Laser generation of proton beams for the production of short-lived positron emitting radioisotopes". *Nuclear Instruments and Methods in Physics Research Section B: Beam Interactions with Materials and Atoms* 183,449 (2001).

[123] J. M. Yang et al. "Nuclear reactions in copper induced by protons from a petawatt laser-foil interaction". *Applied Physics Letters* 84,675 (2004).

[124] M. M. Günther et al. "NAIS: Nuclear activation-based imaging spectroscopy". *Review of Scientific Instruments* 84,073305 (2013).

[125] J. Wiza et al. "Microchannel plate detectors". *Nuclear Instruments and Methods* 162,587 (1979).

[126] J.E. Ducret et al. "Calibration of the low-energy channel Thomson parabola of the LMJ-PETAL diagnostic SEPAGE with protons and carbon ions". *Review of Scientific Instruments* 89,023304 (2018).

[127] F. Consoli et al. "Study on a compact and adaptable Thomson Spectrometer for laser-initiated11B(p,a)8Be reactions and low-medium energy particle detection". *Journal of Instrumentation* 11,C05010 (2016).

[128] D. C. Carroll et al. "A modified Thomson parabola spectrometer for high resolution multi-MeV ion measurements—Application to laser-driven ion acceleration". *Nuclear Instruments and Methods in Physics Research Section A: Accelerators, Spectrometers, Detectors and Associated Equipment* 620,23 (2010).

[129] G. Di Giorgio et al. "Development of advanced Thomson spectrometers for nuclear fusion experiments initiated by laser". *Journal of Instrumentation* 15,C10013 (2020).

[130] Y. Zhang et al. "An angular-resolved multi-channel Thomson parabola spectrometer for laser-driven ion measurement". *Review of Scientific Instruments* 89,093302 (2018).

[131] E. Woryna et al. "Corpuscular diagnostics and processing methods applied in investigations of laser-produced plasma as a source of highly ionized ions". *Laser and Particle Beams* 14,293 (1996).

[132] M. Cipriani et al. "Spectral characterization by CVD diamond detectors of energetic protons from high-repetition rate laser for aneutronic nuclear fusion experiments". *Journal of Instrumentation* 14,C01027 (2019).

[133] G. Milluzzo et al. "A new energy spectrum reconstruction method for time-of-flight diagnostics of high-energy laser-driven protons". *Review of Scientific Instruments* 90,083303 (2019).

[134] V. Scuderi et al. "TOF diagnosis of laser accelerated, high-energy protons". *Nuclear Instruments and Methods in Physics Research Section A: Accelerators, Spectrometers, Detectors and Associated Equipment* 978,164364 (2020).

[135] D. Margarone et al. "Full characterization of laser-accelerated ion beams using Faraday cup, silicon carbide, and single-crystal diamond detectors". *Journal of Applied Physics* 109,103302 (2011).

[136] S. Nakamura et al. "Real-Time Optimization of Proton Production by Intense Short-Pulse Laser with Time-of-Flight Measurement". *Japanese Journal of Applied Physics* 45,L913 (2006).

[137] P. Bellido et al. "Characterization of protons accelerated from a 3-TW tabletop laser system". *Journal of Instrumentation* 12,T05001 (2017).

[138] R. Sussmann. *CVD diamond for electronic devices and sensors*. Wiley and Sons, 2009.

[139] A. Lo Giudice et al. "Average energy dissipated by mega-electron-volt hydrogen and helium ions per electron-hole pair generation in 4H-SiC". *Applied Physics Letters* 87,222105 (2005).

[140] G. L. Miller, W. M. Gidson, and P. F. Donovan. "Semiconductor Particle Detectors". *Annual Review of Nuclear Science* 12,189 (1962).

[141] G. Grosso and G. Parravicini. *Solid State Physics*. Oxford: Elsevier, 2013.

[142] W. Shockley. "Problems related to p-n junctions in silicon". *Solid-State Electronics* 2,35 (1961).

[143] C. A. Klein. "Bandgap Dependence and Related Features of Radiation Ionization Energies in Semiconductors". *Journal of Applied Physics* 39,2029 (1968).

[144] M. Pomorski et al. "Development of single-crystal CVD-diamond detectors for spectroscopy and timing". *physica status solidi (a)* 203,3152 (2006).

[145] R. C. Alig and S. Bloom. "Electron-Hole-Pair Creation Energies in Semiconductors". *Phys. Rev. Lett.* 35,1522 (1975).

[146] G. Bertuccio et al. "Silicon carbide detector for laser-generated plasma radiation". *Applied Surface Science* 272,128 (2013).

[147] D. M. Caughey and R. E. Thomas. "Carrier mobilities in silicon empirically related to doping and field". *Proceedings of the IEEE* 55,2192 (1967).

[148] K. Ng. Kwok. *Complete Guide to Semiconductor Devices*. New York: John Wiley and Sons, 2009.

[149] A. Lo Giudice et al. "Lateral IBIC characterization of single crystal synthetic diamond detectors". *physica status solidi (RRL) – Rapid Research Letters* 5,80 (2011).

[150] M. Marinelli et al. "Analysis of laser-generated plasma ionizing radiation by synthetic single crystal diamond detectors". *Applied Surface Science* 272,104 (2013).

[151] J. Forneris et al. "A 3-dimensional interdigitated electrode geometry for the enhancement of charge collection efficiency in diamond detectors". *EPL (Europhysics Letters)* 108,18001 (2014).

[152] W. Olthuis, W. Streekstra, and P. Bergveld. "Theoretical and experimental determination of cell constants of planar-interdigitated electrolyte conductivity sensors". *Sensors and Actuators B: Chemical* 24,252 (1995).

[153] J. F. Ziegler, M. D. Ziegler, and J. P. Biersack. "SRIM - The stopping power and range of ions in matter". *Nuclear Instruments and Methods Physics Research Section B. Beam Interaction with Matter and Atoms* 268,1818 (2010).

[154] M. Salvadori et al. "Accurate spectra for high energy ions by advanced time-of-flight diamond-detector schemes in experiments with high energy and intensity lasers". *Accepted for publication in Scientific Reports* volume,number (2020).

[155] M. B. H. Breese et al. "A review of ion beam induced charge microscopy". *Nuclear Instruments and Methods in Physics Research Section B: Beam Interactions with Materials and Atoms* 264,345 (2007).

[156] E. H. Rhoderick. "The physics of Schottky barriers". *Journal of Physics D: Applied Physics* 3,1153 (1970).

[157] C. Verona et al. "Comparison of single crystal diamond TOF detectors in planar and transverse configuration". *Journal of Instrumentation* 15,C09066 (2020).

[158] C. E. Nebel. "Electronic properties of CVD diamond". *Semiconductor Science and Technology* 18,S1 (2003).

[159] R. De Angelis et al. "High performance diagnostics for Time-Of-Flight and X ray measurements in laser produced plasmas, based on fast diamond detectors". *Journal of Instrumentation* 11,C12048 (2016).

[160] *Lecroy HDO 4104 specs*. URL: `https://teledynelecroy.com/oscilloscope/hdo4000a-high-definition-oscilloscopes/hdo4104a`.

[161] J. Raimbourg. "Electromagnetic compatibility management for fast diagnostic design". *Review of Scientific instruments* 4948,452 (2004).

[162] C. G. Brown et al. "Assessment and mitigation of electromagnetic pulse (EMP) impacts at short-pulse laser facilities". *Journal of Physics: Conference series* 244,032001 (2010).

[163] J. D. Jackson. *Clasical Electrodynamics, 3rd Edition*. New York: John Wiley and Sons, 1998.

[164] N. Marcuvitz. *Waveguide Handbook*. McGraw-Hill Book Company, Inc., 1951.

[165] F. Consoli et al. "EMP characterization at PALS on solid-target experiments". *Plasma Physics and Controlled Fusion* 60,105006 (2018).

[166] C. Mittermayer and A. Steininger. "On the determination of dynamic errors for rise time measurement with an oscilloscope". *IEEE Transactions on Instrumentation and Measurement* 48,1103 (1999).

[167] J. Fuchs et al. "Laser-driven proton scaling laws and new paths towards energy increase". *Nature Physics* 2,48 (2006).

[168] *Goodfellow website*. URL: `http://www.goodfellow.com/`.

[169] C. Strangio and A. Caruso. "Study on the hydrodynamical behavior of thin foils irradiated by near-field ISI smoothed beams". *Laser and Particle Beams* 16,45 (1998).

[170] F. Consoli et al. "Time-resolved absolute measurements by electro-optic effect of giant electromagnetic pulses due to laser-plasma interaction in nanosecond regime". *Scientific Reports* 6,27889 (2016).

[171] Bisesto F.G. et al. "The FLAME laser at SPARC LAB". *Nuclear Instruments and Methods in Physics Research Section A: Accelerators, Spectrometers, Detectors and Associated Equipment* 909,452 (2018). 3rd European Advanced Accelerator Concepts workshop (EAAC2017).

[172] I. Wilke et al. "Single-Shot Electron-Beam Bunch Length Measurements". *Phys. Rev. Lett.* 88,124801 (2002).

[173] R. Pompili et al. "Femtosecond dynamics of energetic electrons in high intensity laser-matter interactions". *Scientific Reports* 7,35000 (2016).

[174] F. G. Bisesto et al. "Ultrafast electron and proton bunches correlation in laser–solid matter experiments". *Optics Letters* 45,5575 (2020).

[175] M. Salvadori et al. "Assessment of sensitivity improvement for Time-Of-Flight schemes in experiments with high intensity lasers." *Journal of Instrumentation* 15,C10002 (2020).

[176] F. G. Bisesto et al. "Simultaneous observation of ultrafast electron and proton beams in TNSA". *High Power Laser Science and Engineering* 8,e23 (2020).

[177] F. G. Bisesto et al. "Single-shot electrons and protons time-resolved detection from high-intensity laser–solid matter interactions at SPARC-LAB". *High Power Laser Science and Engineering* 7,e53 (2019).

[178] M. Tampo et al. "Correlation between laser accelerated MeV proton and electron beams using simple fluid model for target normal sheath acceleration". *Physics of Plasmas* 17,073110 (2010).

[179] P. Antici et al. “Measuring hot electron distributions in intense laser interaction with dense matter”. *New Journal of Physics* 14,063023 (2012).

[180] C. Perego et al. “Target normal sheath acceleration analytical modeling, comparative study and developments”. *Review of Scientific Instruments* 83,02B502 (2012).

[181] M. Passoni et al. “Advances in target normal sheath acceleration theory”. *Physics of Plasmas* 20,060701 (2013).

[182] S. Vallières et al. “The laser-driven ion acceleration beamline on the ALLS 200 TW for testing nanowire targets”. In: *Laser Acceleration of Electrons, Protons, and Ions V*. Ed. by Eric Esarey, Carl B. Schroeder, and Jörg Schreiber. Vol. 11037. 1. International Society for Optics and Photonics. SPIE, 2019.

[183] S. Vallières et al. “Thomson Parabola and TOF detectors cross-calibration methodology on the ALLS 100 TW Laser-Driven ion acceleration beamline”. *Review of Scientific Instruments* 91,103303 (2020).

[184] A. Mancic et al. “Isochoric heating of solids by laser-accelerated protons: Experimental characterization and self-consistent hydrodynamic modeling”. *High Energy Density Physics* 6,21 (2010).

[185] P. Puyuelo Valdes. “Laser-driven ion acceleration with high-density gas-jet targets and application to elemental analysis”. Thèse de doctorat Astrophysique, Plasmas, nucléaire Institut national de la recherche scientifique (Québec, province) 2020. PhD thesis. 2020.

[186] F. Valle Brozas et al. “Laser-based X-ray and electron source for X-ray fluorescence studies”. *Applied Physics B* 122,220 (2016).

[187] B. Aurand et al. “A setup for studies of laser-driven proton acceleration at the Lund Lçaser Center”. *Laser and Particle Beams* 33,59 (2015).

[188] A. Andreev et al. “Efficient generation of fast ions from surface modulated nanostructure targets irradiated by high intensity short-pulse lasers”. *Physics of Plasmas* 18,103103 (2011).

[189] Y. Jinqing et al. “Laser-driven proton acceleration using a conical nanobrush target”. *Physics of Plasmas* 19,053108 (2012).

[190] J. Liangliang et al. “Exploring novel target structures for manipulating relativistic laser–plasma interaction”. *High Power Laser Science and Engineering* 5,e14 (2017).

[191] L. Fedeli et al. “Ultra-intense laser interaction with nanostructured near-critical plasmas”. *Scientific Reports* 8,3834 (2018).

[192] D. Margarone et al. “Laser-Driven Proton Acceleration Enhancement by Nanostructured Foils”. *Physical Review Letters* 109,234801 (2012).

[193] L. Giuffrida et al. “Manipulation of laser-accelerated proton beam profiles by nanostructured and microstructured targets”. *Physical review accelerators and beams* 20,081301 (2017).

[194] S. Bagchi et al. "Surface-plasmon-enhanced MeV ions from femtosecond laser irradiated, periodically modulated surfaces". *Physics of Plasmas* 19,030703 (2012).

[195] M. Passoni et al. "Toward high-energy laser-driven ion beams: Nanostructured double-layer targets". *Phys. Rev. Accel. Beams* 19,061301 (2016).

[196] S. Vallières et al. "Enhanced Laser-Driven Proton Acceleration Using Nanowire Targets". *Scientific Reports* 11,2226 (2021).

[197] V. Bagnoud et al. "Commissioning and early experiments of the PHELIX facility". *Applied Physics B* 100,137 (2010).

[198] F. Wagner et al. "Temporal contrast control at the PHELIX petawatt laser facility by means of tunable sub-picosecond optical parametric amplification". *Applied Physics B* 116,429 (2014).

[199] V. Bagnoud and F. Wagner. "Ultrahigh temporal contrast performance of the PHELIX petawatt facility". *High Power Laser Science and Engineering* 4,e39 (2016).

[200] O. N. Rosmej et al. "Interaction of relativistically intense laser pulses with long-scale near critical plasmas for optimization of laser based sources of MeV electrons and gamma-rays". *New Journal of Physics* 21,043044 (2019).

[201] O. N. Rosmej et al. "High-current laser-driven beams of relativistic electrons for high energy density research". *Plasma Physics and Controlled. Fusion* 62,115024 (2020).

[202] N. G. Borisenko et al. "Plastic Aerogel Targets and Optical Transparency of Undercritical Microheterogeneous Plasma". *Fusion Science and Technology* 51,655 (2007).

[203] G. Milluzzo et al. "Laser accelerated ion beam diagnostic with TOF detectors for ELIMED beam line". *Journal of instrumentation* 12,C02025 (2017).

[204] M. Salvadori et al. "A multi-layered diamond structure for energetic ions characterization". *paper in preparation* ().

[205] C. Verona et al. "Spectroscopic properties and radiation damage investigation of a diamond based Schottky diode for ion-beam therapy microdosimetry". *Journal of Applied Physics* 118,184503 (2015).

[206] B. Caiffi et al. "Proton Recoil Telescope Based on Diamond Detectors for the Measurement of Fusion Neutrons". *IEEE Transactions on Nuclear Science* 63,2409 (2016).

[207] S. Cesaroni et al. "DE-E single crystal diamond based telescope". *Nuclear Instruments and Methods in Physics Research Section A: Accelerators, Spectrometers, Detectors and Associated Equipment* 947,162744 (2019).

Ringraziamenti

Dopo il lungo viaggio che ha portato alla stesura di questa tesi, finalmente è arrivato anche uno dei momenti più piacevoli, quello di scrivere i ringraziamenti.

Da dove iniziare se non da un doveroso, ma non per questo meno sentito, grazie a Fabrizio che, insieme a tutto il gruppo ABC dell'ENEA, in questi tre anni mi ha sostenuta ed accolta come un componente attivo della squadra, credendo nelle mie capacità e permettendomi di vedere come sarebbe continuare a lavorare in questo campo. Ringrazio anche Claudio, per aver risposto alle mie centocinquantamila domande sui diamanti alle quali non si è mai stancato di rispondere.
Tuttavia non sarei mai entrata a far parte di questo gruppo se Danilo non mi avesse proposto, ormai quattro anni fa, di svolgere la tesi magistrale proprio li, a Frascati. Per questo e non solo, grazie !
Arrivando a Roma ho anche avuto modo di conoscere Mauro, che ringrazio per aver accettato di farmi da supervisor un po' a scatola chiusa, conoscendomi appena. Così come ringrazio Patrizio per avermi dato l'opportunità di imbarcarmi per il Canada per un dottorato in cotutela.
But my Canadian adventure would never have even started if Simon had not recruited me during JUAS. Together with Pilar we are the dream-team, Thank you both mes chers amis!

Tutto questo non sarebbe però stato possibile se non avessi avuto due genitori che mi hanno sempre incoraggiata e spronata a fare meglio (anche con la famigerata domanda "Perché non dieci?"), vi ringrazio per esserci stati ogni volta che ne ho avuto bisogno.
Un grazie va anche a mio fratello, che negli anni si è sempre dovuto sorbire le mie ripetizioni di presentazioni da portare per esami/conferenze e via dicendo e in questi mesi ha fatto da giudice e correttore per buona parte delle immagini presenti... Ecco, non ti ho messo fra gli autori ma il tuo contributo è riconosciuto nero su bianco!

Insieme con loro voglio ringraziare anche Mario, che in questo ultimo periodo di scrittura matta e disperatissima si è dovuto ingegnare per supportarmi, ma soprattutto sopportarmi 24h facendomi anche mantenere la sanità mentale!

...ed infine ringrazio me stessa, per aver scelto con cura le persone delle quali mi sono circondata.